

UNIVERSITÀ DEGLI STUDI DI NAPOLI FEDERICO II



DIPARTIMENTO DI INGEGNERIA CHIMICA, DEI MATERIALI E DELLA
PRODUZIONE INDUSTRIALE

SCUOLA DI DOTTORATO IN INGEGNERIA INDUSTRIALE

PHD PROGRAMME IN
PRODUCTION TECHNOLOGY AND SYSTEMS
COORDINATOR: PROF. LUIGI CARRINO
XXV CYCLE

PHD THESIS

**MULTI-SENSOR PROCESS MONITORING IN
TURNING OF NICKEL SUPERALLOYS**

TUTOR
PROF. ING. ROBERTO TETI

PHD CANDIDATE
ALESSANDRO SIMEONE

ACADEMIC YEAR 2012/2013



Contents

1.	Introduction.....	5
1.1.	Scope and purposes	5
1.2.	Publications review	6
1.3.	State of the Art.....	9
1.3.1.	Historical/philosophical background of sensorial perception	9
1.3.2.	Modern theories of sensorial perception.....	9
1.3.3.	Sensors and sensor systems for machining	9
1.3.4.	Advanced Signal Processing	13
1.3.5.	Monitoring scopes	17
1.3.6.	Decision making support systems and paradigms	19
1.3.7.	Sensor fusion technology	22
1.4.	ACCENT Project at a Glance	24
2.	Experimental Setup	27
2.1.	Machine Tool.....	27
2.2.	Work material.....	27
2.3.	Workpiece	29
2.4.	Cutting tools	29
3.	Experimental tests programme	31
3.1.	Experimental tests procedure.....	31
4.	Sensor Units.....	34
4.1.	Cutting Force Sensor	34
4.2.	Acoustic Emission Sensor	35
4.3.	Vibration Sensor	36
4.4.	Signal Acquisition.....	37
4.4.1.	Sampling Frequency	38
4.4.2.	RMS vs RAW	41
4.4.3.	Time constant	42
4.5.	Acquisition Software	44
5.	Tool wear.....	46
5.1.	Generalities	46
5.2.	Tool wear measurement	51
5.3.	Tool wear measurement during experimental tests.....	53
5.4.	Tool wear measurement reports	55
6.	Residual stress measurement	66

6.1.	Residual stress in machining.....	66
6.2.	X-ray diffraction technique	66
6.3.	Basic Procedure	72
6.4.	X-ray stress analyzer	78
6.5.	Residual stress measurement results	80
7.	Material characterization tests.....	83
7.1.	Test typologies	83
7.1.1.	Visual Inspection	83
7.1.2.	Fluorescent Penetrant Inspection	83
7.1.3.	Metallographic Tests	85
7.1.4.	Roughness measurement	88
7.1.5.	Micro-hardness	90
7.2.	Defects to be investigated.....	90
7.2.1.	Macro anomalies.....	90
7.2.2.	Micro anomalies	93
7.2.3.	Microstructure changes	95
7.3.	Reports and results.....	98
7.3.1.	Visual Inspection results	98
7.3.2.	FPI results.....	104
7.3.3.	Metallographic tests results	104
1.1.1.	Micro hardness results	115
1.1.2.	Roughness measurements reports	123
8.	Signal Processing and Features Extraction	129
8.1.	Pre – processing.....	129
8.1.1.	File format	129
8.1.2.	Signal segmentation	129
8.1.3.	Signal Subdivision	131
8.1.4.	Dataset Construction	132
8.2.	Conventional Features Extraction.....	133
8.3.	Principal Components Analysis	134
8.3.1.	Generalities	134
8.3.2.	Purposes	134
8.3.3.	Computation	134
8.4.	Results	141
9.	Neural Network based Pattern Recognition	142

9.1.	Pattern Recognition and Neural Networks	142
9.2.	Purposes	143
9.2.1.	Tool State Identification	143
9.2.2.	Residual Stress Assessment (worn tool)	143
9.2.3.	Residual Stress Assessment (fresh tool)	144
9.3.	Pattern Vectors	144
9.3.1.	Pattern Vectors from Conventional Features	144
9.3.2.	Pattern Vectors from PCA based Features	144
9.4.	Training Algorithms	145
9.4.1.	Levenberg-Marquardt (LM)	145
9.4.2.	Scaled Conjugate Gradient (SCG)	145
9.4.3.	Leave - k - Out (LKO)	146
9.5.	Matlab procedure	146
10.	Results	150
10.1.	Tool State Identification	150
10.1.1.	Standards Tests	150
10.1.2.	Standard Tests + Severe Cutting Conditions Tests	156
10.2.	Residual Stress Assessment (worn tool)	163
10.2.1.	Standard Tests	163
10.2.2.	Standard Tests + Severe Cutting Conditions Tests	170
10.3.	Residual Stress Assessment (fresh tool)	177
10.3.1.	Standard Tests	177
10.3.2.	Standard Tests + Severe Cutting Conditions Tests	183
10.4.	Summary plots	190
11.	Conclusions / Considerations	194
	List of references	197

Background

1. Introduction

1.1. Scope and purposes

This thesis work was developed in conjunction with the activities of the EC FP7 *Adaptive Control of Manufacturing Processes for a New Generation of Jet Engine Components* (ACCENT) Project (See section 1.4).

Most of the experimental activities were carried out at AVIO SpA facilities, Pomigliano d'Arco, Naples; Avio SpA is an industrial partner in the EC FP7 ACCENT Project.

The goals of this thesis work are explained below.

First of all, the design and realization of an experimental campaign of turning tests on a nickel base alloy of aeronautical interest (Inconel 718) was carried out in an industrial environment.

A multi sensor monitoring system, endowed with diverse sensing units was designed, assembled, calibrated and employed during machining tests in order to acquire different sensor signals on an online basis.

Raw signals acquired were subjected to conventional and advanced signal analysis methods in order to extract significant features useful for decision making on process conditions.

This thesis work includes material characterization tests carried out to investigate the surface integrity of the workpiece as well as the state of the tool wear with the scope of correlating these conditions to sensor signals features.

By the implementation of a decision making support system, sensor signal features extracted by signal processing techniques were utilized for the identification of defects in the workpiece due to the machining process, as revealed by the material characterization tests.

Decision making was carried out by diverse Neural Network pattern recognition paradigms, designed and implemented for the purpose.

The organization of the activities carried out in this thesis can be summarized as in the flow chart reported in Fig. 1.1.

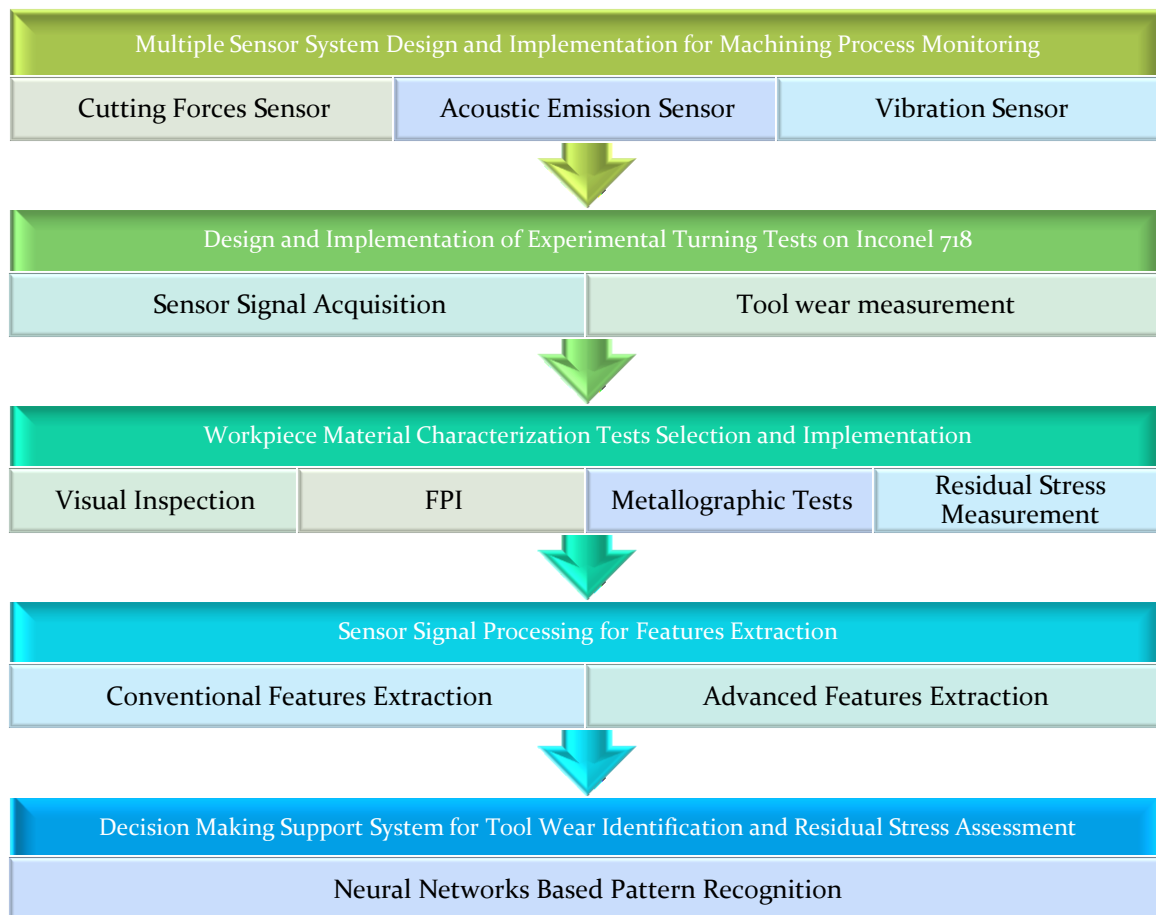


Fig. 1.1 Activities flow chart

1.2. Publications review

In [1] tool wear progress estimation for optimal tool life utilisation in turning of Inconel 718 aircraft engine products, under industrial manufacturing conditions, was achieved through cognitive modeling of tool wear growth based on supervised neural network data processing.

Low prediction errors were obtained for the lower cutting speeds, whereas large forecast errors were verified for the highest cutting speed value. However, under the latter condition, the flank wear safe machining limit (SML) was exceeded, which represents an industrially unacceptable event. If this instance is disregarded as technologically improper, the estimation errors are low enough to deem the Neural Network modelling able to provide a dependable tool wear curve trend for all realistic Inconel 718 turning conditions.

In [2] sensor fusion of digital signals obtained during sensor monitoring of longitudinal turning operations carried out on C45 carbon steel was investigated with the aim to achieve the reliable chip form categorization. Advanced signal processing, characterization and feature extraction was performed through the Principal Component Analysis (PCA) algorithm and cognitive decision making was carried out using neural network based pattern recognition.

The Neural Network success rates in chip form recognition were always higher than 80%, validating the capability of PCA in extracting valuable sensory features for chip form monitoring.

The favourable/unfavourable chip type identification yielded higher NN SR values than the single chip form classification, as a four classes (four chip forms) recognition effort is undoubtedly harder than a two-classes (favourable/unfavourable chip form) discrimination task.

The Neural Network Success Rates values for the 4-element feature vectors are higher than for the 3-element feature vectors cases, confirming that sensor fusion of sensorial data of different kinds can be positively valuable for pattern recognition.

In [3] a multiple sensor monitoring approach for tool wear identification during the orthogonal cutting of diverse composite materials (GFRP, SMC, CFRP) was carried out through the detection of cutting force and acoustic emission sensor signals. Signal data processing was performed through the Principal Component Analysis (PCA) procedure in order to lessen the high dimensionality of sensor signals and extract significant signal features to utilize for pattern recognition based decision making on tool wear state identification.

The results obtained by applying the PCA procedure showed that the first principal component is strongly related to AE signal, the second principal component to the cutting force component F_y , and the third principal component to the cutting force component F_z , for all three examined composite materials.

The 3 principal components were used as inputs to a neural network (NN) based pattern recognition paradigm to identify the correlations between sensory data and tool wear state. For all composite materials, the NN success rate was comprised between 70% and 88%, representing a medium to high NN performance for decision making on cutting tool conditions during composite materials machining.

[4] discusses an enhanced strategy for process monitoring of machining processes, based on industrial needs and incentives. Through subdividing the feature to be monitored e.g. a hole, different actions can be set for each section. Thus an Adaptive Process Monitor.

The concept is implemented in an industrial environment, however on a laboratory scale, from which the results in this paper are collected.

It is shown that by the implementation of the adaptive concept, anomalies like tool run-out can be detected prior to any gross malfunction of the process e.g. prior to any scrapping.

Furthermore, measures can be taken to create a uniform Probability of Detection (POD), in particular for deep holes.

In [5] multiple sensor monitoring for tool wear state classification was carried out during turning of Inconel 718 through simultaneous detection of cutting force, acoustic emission and vibration sensor signals.

Sensor fusion signal data processing was performed through Principal Component Analysis (PCA) to reduce the high dimensionality of sensorial data and extract significant signal features to utilize for NN based pattern recognition aimed at decision making on tool wear state.

The PCA approach allowed to extract principal components features from multi sensor fusion data sets that yielded NN success rates in tool wear classification much higher than for signal features obtained from single sensors or combinations of two sensors.

As regards the correlation between sensor signals and principal components provided by the PCA algorithm, the acceleration signal features, strongly related to the first 3 principal components, provided lower NN success rates for tool wear identification than in the case of cutting force signal features related to higher order principal components.

In [6] multiple sensor monitoring for tool wear state assessment was carried out during turning of Inconel 718 through simultaneous detection of cutting force, acoustic emission and vibration sensor signals.

Feature extraction through linear predictive analysis (LPA) was applied in order to obtain 4 element feature vectors.

Sensor fusion technology based neural network paradigm was implemented by combining the 4 feature vectors. In particular, the fusion of sensorial data was applied considering the integration of two sensor signal specimens ($[F_x + F_y + F_z + AERMS]$ or $[AERMS + a_x + a_y + a_z]$) and the all sensorial data specimens ($[F_x + F_y + F_z + AERMS + a_x + a_y + a_z]$).

The obtained results showed that the NN SR values in the assessment of tool wear is higher by resorting to sensor fusion of 3 sensorial data (cutting force, acceleration and AE) instead of using the combinations of two sensors (cutting force and AE or acceleration components and AE).

This emphasizes the NN capability to realize the concept of sensor fusion.

In [7], tool wear development during turning of a difficult-to-machine Ni-base alloy (Inconel 718) was investigated.

An experimental programme was implemented according to a DoE procedure and cutting tests were carried out for different cutting conditions with stepwise measurements of tool flank wear.

The experimental data were processed through 3-layers back-propagation feed-forward NNs with the aim to predict tool wear in the case of unknown process conditions.

The good NN prediction performance obtained for all feed rates is allowed for convenient data processing conditions of the corresponding trained NN that are asked to provide output values interpolated with respect to the NN training set: this is a task at which feed-forward backpropagation NN are typically very good.

In [8] multiple sensor monitoring for residual stress assessment was carried out during turning of Inconel 718 through simultaneous detection of cutting force, acoustic emission and vibration sensor signals.

Sensor fusion signal data processing was performed through two different methodologies, a conventional one and the Principal Component Analysis (PCA), to reduce the high dimensionality of sensorial data and extract significant signal features to utilize for NN based pattern recognition aimed at decision making on residual stress condition. As regards the correlation between sensor signals and principal components provided by the PCA algorithm, the acceleration signal features, strongly related to the first 3 principal components, provided higher NN success rates for tool wear identification than in the case of cutting force signal features related to higher order principal components.

1.3. State of the Art

In the cognitive sciences, sensorial perception is the process of attaining awareness or understanding of sensory information. It is a task far more complex than was imagined in the ‘50s–19s’, when it was predicted that building perceiving machines would take about a decade, a goal which is still very far from fruition [10].

1.3.1. Historical/philosophical background of sensorial perception

Since the times of early ancient Greek philosophy, a number of interesting considerations concerning Sensorial Perception (SP), knowledge achievement and truth identification have emerged. The diverse concepts, views and theories regarding SP and knowledge acquisition may be grouped into a few categories that, along with the predominant cultural tendency in the course of epochs, attribute to SP a higher or lower role (Table 1.1)[10].

Table 1.1: Concepts of sensorial perception (SP) and its role in knowledge acquisition and truth identification during the different epochs.

SP role	Authors of concepts/theories of SP in the course of epochs
Trivial, minor or no value	Heraclitus (535–475 B.C.); Parmenides (515–450 B.C.) and the Eleatics; Pyrrho (360–320 B.C.) and the Sceptics
Initiates cognition	Empedocles (490–430 B.C.); Democritus (460–370 B.C.) and the Atomists
Supports cognition	Plato (427–347 B.C.); Plotinus (205–270 A.D.); St. Augustine (354–430 A.D.); Hegel (1770–1831) and the Idealists
Indispensible for cognition	Aristotle (384–322 B.C.); St. Thomas Aquinas (1221–1274); Ockam (1280–1349); Spinoza (1632–1677); Leibniz (1646–1716); Locke (1632–1704) and the Empyrist; Kant (1724–1804); Peirce (1839–1914) and the Pragmatists
Basis of all knowledge acquisition	Epicurus (341–270 B.C.); Zeno (334–262 B.C.) and the Stoics; L. da Vinci (1452–1519); Telesio (1509–1588); Galilei (1564–1642); F. Bacon (1561–1626); Newton (1642–1727); Descartes (1596–1650) and the theory of passive perception; Condillac (1714–1780) and the Sensists; Stuart Mill (1806–1873), Comte (1798–1857) and the Positivists
Continuous adaptation of sensing to environment	Darwin (1809–1882), Avenarius (1843–1900), Mach (1838–1916) and the Empiriocritics; Dewey (1859–1952) and the Instrumentalists; Bergson (1859–1941); Gregory [6–8] and the theory of active perception

1.3.2. Modern theories of sensorial perception

Passive perception, initially conceived by R. Descartes and surmised as a “static” sequence of events: surrounding → input (senses) → processing (brain) → output (reaction), is still supported by mainstream philosophers, psychologists, neurologists and scientists. However, it is a theory nowadays largely losing momentum. The theory of active perception has emerged from extensive research of sensory misapprehensions, most notably the works of Gregory [11][12]. This theory, which is increasingly gaining experimental support, can be surmised as the “dynamic” relationship between description (in the brain) ↔ senses ↔ surrounding, all of which holds true to the linear concept of experience. For more information on the implications of active perception theory for science and technology see [13].

1.3.3. Sensors and sensor systems for machining

The measuring techniques for the monitoring of machining operations have traditionally been categorised into two approaches: direct and indirect. In the direct approach the actual quantity of

the variable, e.g. tool wear, is measured. Examples of direct measurement in this case are the use of cameras for visual inspection, radioactive isotopes, laser beams, and electrical resistance. Many direct methods can only be used as laboratory techniques. This is largely due to the practical limitations caused by access problems during machining, illumination and the use of cutting fluid. However, direct measurement has a high degree of accuracy and has been employed extensively in research laboratories to support the investigations of fundamental measurable phenomena during machining processes. Through indirect measurement approaches, auxiliary quantities such as the cutting force components can be measured. The actual quantity is subsequently deduced via empirically determined correlations. Indirect methods are less accurate than direct ones but are also less complex and more suitable for practical applications. In contrast to the traditional detection of tool conditions, the approach is that machining processes are being continuously monitored via sensing devices to quantify the process performance or provide information for process optimization using sensors. Sensors that are commonly used for online measurement are summarised in Fig. 1.2.[10]

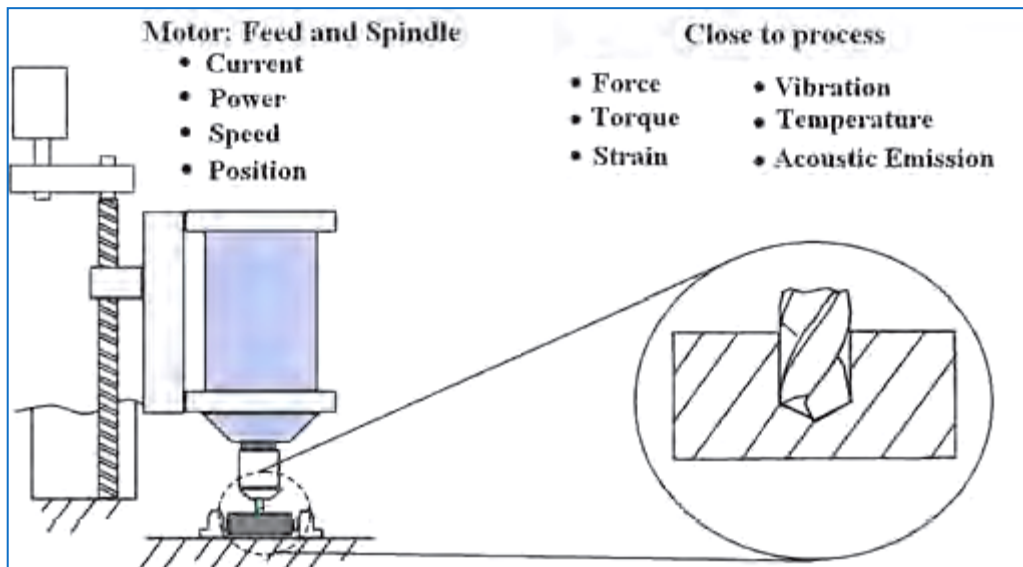


Fig. 1.2. Measurable phenomena for online sensor monitoring

Force and Torque

Any cutting operation requires a certain force to separate and remove the material. The monitoring of cutting forces in machining for the validation of analytical process models, the detection of tool failure, etc., has been used extensively by researchers [14]. This is due to the high sensitivity and rapid response of force signals to changes in cutting states. Torque sensors, like force sensors, also consist of a mechanical structure that responds to a deformation but in this case the applied load is torsional. The underlying force measurement technology is often identical but the application of torque sensors and the method of signal transmission from rotating tool holders are different. Force and torque sensors generally employ sensing elements that convert the applied force or torsional load into deformation of an elastic element. The two main sensor types used are piezoelectric based and strain based sensors.

Piezoelectric sensors

Direct force measurement using piezoelectric sensors is possible when the force transducer is mounted in line with the force path. In cases where more measurement flexibility is required, multi-

component force transducers have been developed and are used extensively in lab based applications. Rotating cutting force dynamometers are also available that contain the force sensing elements capable to measure 3 components of force and torque. The data is transmitted from the rotating part of the sensor to a stator via telemetry. Rotating cutting force dynamometers can operate at speeds of up to 20,000 rpm and have been used for high speed milling of aerospace materials. Developments like the integration of force sensors into the machine structure have taken place over the last 10 years with concepts developed for drilling [15] and milling [24]. Fig. 1.3 shows sensors integrated into the main force flux of the motor spindle. These concepts have been slow to transfer into practice because the spindle or structure itself must be characterised and strategies to isolate process phenomena from spindle and machine dynamics must be developed [17][24][26][27][21].

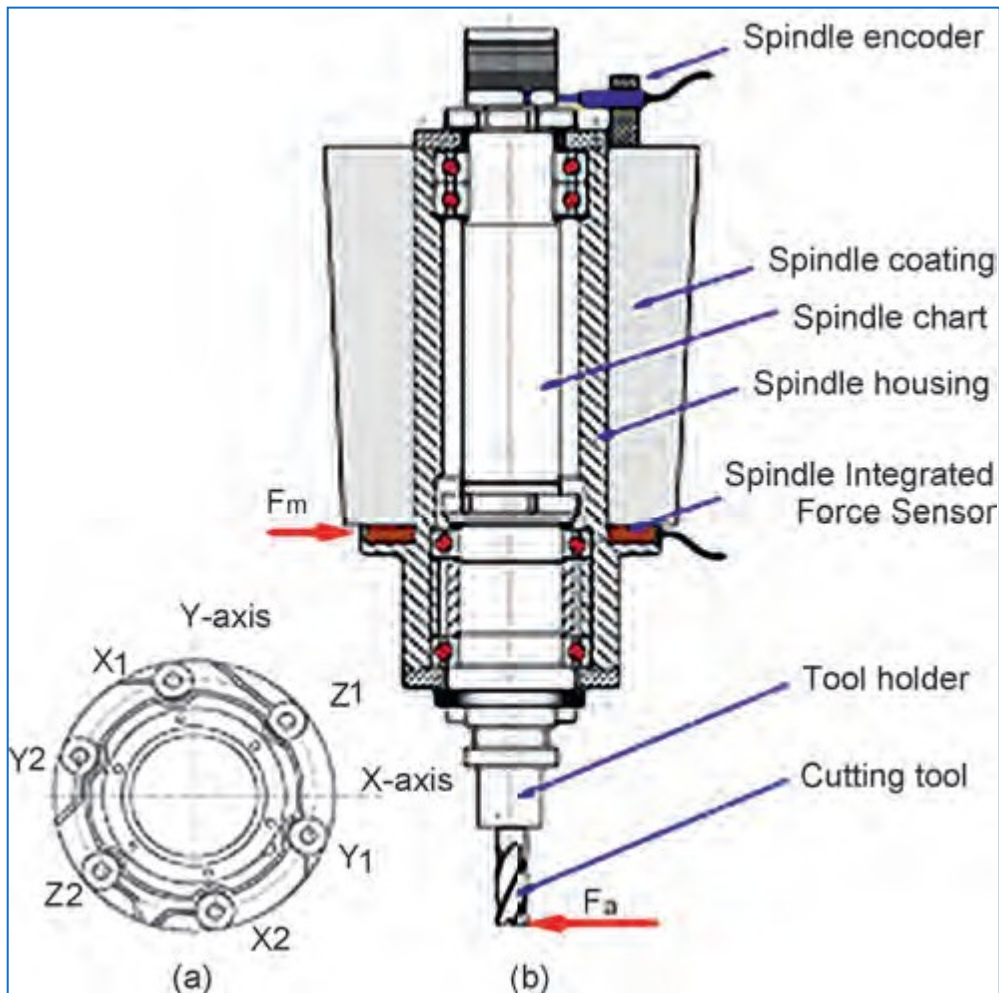


Fig. 1.3 - Integrated force sensors in motor spindle [22]

Acoustic emission measuring technology and sensors

Piezoelectric sensor technology is particularly suitable for measuring acoustic emission (AE) [23][24] in machining process monitoring. With very wide sensor dynamic bandwidth from 100 to 900 kHz, AE can detect most of the phenomena in machining, though significant data acquisition and signal processing is required [25] (Fig. 1.4). This presents problems for signal processing and bandpass filters usually provide great flexibility for AE detection by selecting appropriate frequency ranges. The output signal from the AE sensor is fed through a preamplifier that has a high input impedance and low output impedance. A root mean square (RMS) converter, gain selection unit and filters are

also typically contained within the preamplifier housing. The capacitance principle can also be used for detecting AE, as the capacitance of two parallel plates changes with the distance between plates. The accuracy of this AE detection method is higher than many other techniques and capacitance based AE sensors are used for calibrating other AE sensors. However, capacitance type displacement sensors for AE are very sensitive to sensor position and surface mounting. Thus, they are not suitable for machining process monitoring where the operating environment is often quite severe on the sensor [26].

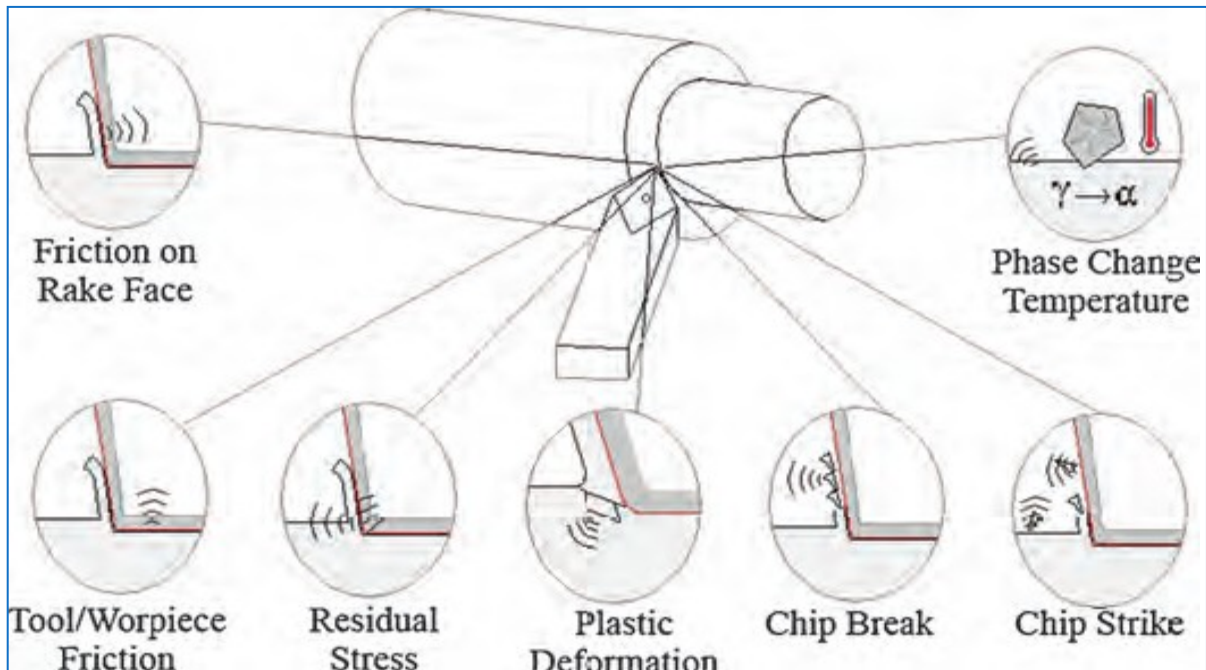


Fig. 1.4 - Sources of AE in machining [25]

Another sensing method for AE detection is the application of a piezoelectric thin film sensor deposited on a shim and located between cutting insert and tool holder. The coating materials can be AlN or ZnO. The sensor is reported to have advantages over commercially available AE sensors: it is located close to the cutting process and is characterised by a very large frequency bandwidth. Good signal quality has been reported, particularly in the high frequency range, with less interference and lower geometrical propagation loss and absorption rate [27]. An alternative approach using fibre optics was investigated in [28] [29]. This sensing method has reported advantages over conventional AE sensors such as a broader bandwidth, flat frequency response and absolute calibration. More significantly, the fibre optic interferometer is a noncontacting method of signal transmission from source to sensor. The latter two methods have largely only been developed in the laboratory and have not been significantly used in industrial applications.

The high frequency and low amplitude nature of AE means that signal transmission via a coupling fluid is possible. By the location of the AE sensor on the coolant supply nozzle, the coolant can be used as transmission path [30]. Hutton and Hu [31] used a nonintrusive coupling fluid to couple the AE sensor to the spindle drive shaft, similar to Li et al. [33]. These signal transmission methods had a distinct advantage for rotating tools such as in milling and drilling. Various other methods of signal transmission from AE sensor to AE coupler/signal processor are common to other sensing applications, including slip rings, inductive coupling, and radio frequency transmission [30][33]. Jemielniak [34] investigated aspects of AE signal processing in machining and proposed that in the machine tool environment the AE signal is repeatedly reflected from the inner surfaces of the

structure where the sensor is mounted. This resulted in prolonged duration of the signal recorded by the sensor. AE sensor mounting requires a couplant between sensor and material surface. The latter should be free from dirt, paint, and any other barrier that may influence the acoustic coupling. The farther the sensor is placed from the AE source, the greater the signal attenuation. This has significant implications for measuring AE during machining. If the AE sensor is mounted on the workpiece side, the changing distance between sensor and source during machining is a factor that requires consideration. This sensor location also presents difficulties regarding sensor mounting, e.g. should the AE sensor be located on the workpiece or on some stationary part of the machine tool [35].

Vibration and other sensor types

A large variety of sensing principles are used for sensing vibration. However, piezoelectric transduction is the most common type in vibration sensing of machining operations. Vibrations that occur during metal cutting can be divided into two groups: (i) dependant and (ii) independent of the cutting process. The two groups are not mutually exclusive. Vibration independent of metal cutting include forced vibration caused by other machines or machine components, e.g. vibration transmitted through foundations, unbalance of rotating parts, inertia forces of reciprocating parts and kinematic inaccuracies of drives. Vibration dependant on metal cutting can demonstrate a number of characteristics as a function of the process, e.g. interrupted cutting. The varying cutting forces that occur during metal cutting may result from non-homogeneity and properties variations in the work material. Tool engagement conditions during machining play a notable role in the vibration produced. The self excited vibration characteristic known as chatter is the most renowned type of vibration in machining and is detrimental to surface finish and tool life. Chatter mainly occurs due to the waviness regeneration caused by the interaction between material surface and tool at particular spindle rotational frequencies, and by mode coupling where relative vibration between workpiece and tool occurs concurrently in two directions in the plane of cut[10].

1.3.4. Advanced Signal Processing

It is generally acknowledged that reliable process condition monitoring based on a single signal feature (SF) is not feasible. Therefore, the calculation of a sufficient number of SFs related to the tool and/or process conditions [36][37][38][38] is a key issue in machining monitoring systems. This is obtained through signal processing methods that comprise the stages shown in Fig. 1.5. First, pre-processing (filtering, amplification, A/D conversion, and segmentation) including, on occasion, signal transformation into frequency or time–frequency domain (Fourier transform, wavelet transform, etc.). The next stage is the extraction of signal or signal transform features changing with tool or process conditions. There are many diverse descriptors from different sensor signals, but most cannot be easily related with the process being monitored. Thus, feature selection is of critical importance and the identified relevant features are finally integrated into the tool or process condition diagnosis system.

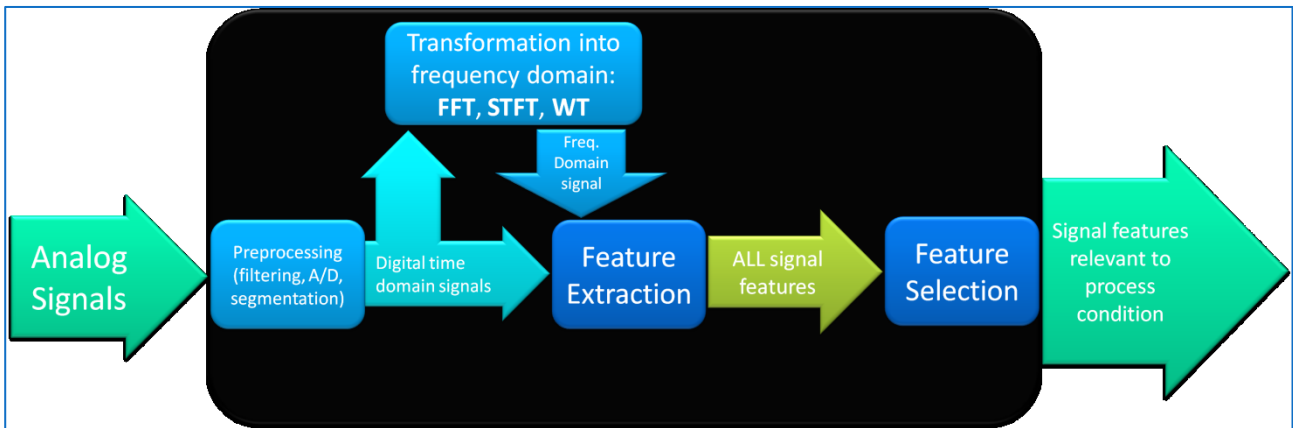


Fig. 1.5. Signal processing logical scheme[1]

Signal pre-processing

The analog signal from the sensor usually cannot be connected directly to the A/D converter but needs pre-processing by a conditioner specific to the sensor (piezotron coupler, charge amplifier, etc.). For example, a typical procedure of analog AE signal pre-processing follows the pattern schematically shown in Fig. 1.6.

The piezoelectric AE sensor is usually placed as close as possible to the cutting zone, e.g. on the tool shank, the tool post, the head stock or the spindle. Because of its high impedance, the sensor must be directly connected to a buffer amplifier which converts the charge signal from the sensor into a proportional voltage signal. This is typical also of other piezoelectric sensors such as dynamometers or accelerometers. The analog signal should be filtered to keep it within the range of the frequency response of the sensor, suppress high frequency noise or continuous biases. The filtered signal is then subjected to further processing and/or recording. The frequency range of the raw AE reaches 1 MHz (typically 80–700 kHz) so dealing with it requires a high sampling frequency (>1 MS/s) and large memory resources with high computing costs. Thus, in many cases the AE signal is demodulated to RMS (AERMS) to obtain a low frequency variable, which can be further processed with less expensive signal processing devices [10].

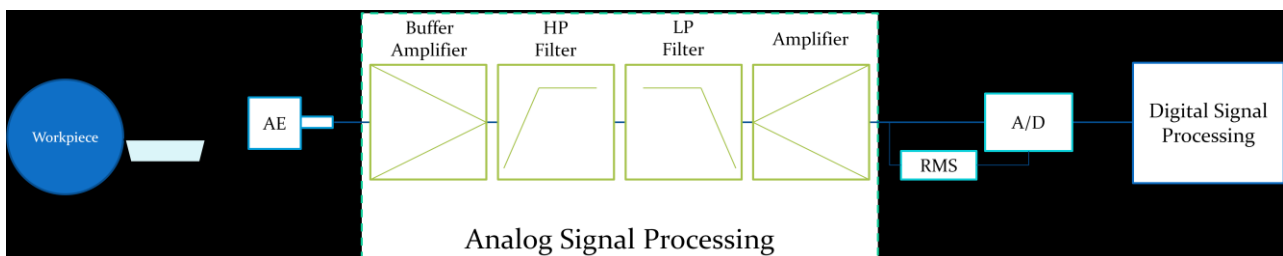


Fig. 1.6. Typical measuring chain for AE detection during machining[10]

The integration time constant of the RMS converter should be carefully selected, depending on the subsequent SF extraction. Signal averages can be calculated with other features such as burst rate, event counts, etc. In such cases, the integration time constant should be 10 times shorter than the typical burst duration, which is approximately 2 ms [34]. The AE energy from the cutting zone can be considerable. Because of the pre-processing units characteristics, these high amplitude signals may cause overloading of the buffer amplifier and signal saturation. High-pass filtering of saturated signals results in temporal vanishing of the signal value [40]. This can often result in misleading data evaluation. It should be noted that this signal distortion cannot be detected in the AE_{RMS} signal and,

in this case, such signals must be considered completely distorted and useless. To avoid these problems, the gain of the buffer amplifier should be as small as possible and any further necessary amplification should be done after signal filtering. This is critically important when AERMS is used instead of AEr_{aw} [40]. Just before conversion into digital form, for the highest possible accuracy, the signal is usually amplified so that the signal maximum voltage range equals the maximum input range of the A/D converter. The digital signal is often subjected to further pre-processing. Digital filtering reduces frequency bands not correlated with the monitored process or extracts information necessary for specific pattern recognition stages. For example while using a spindle-integrated force sensor system on a machining center, the cutting force signals are distorted when the spindle speed harmonics coincide with the spindle natural modes. Kalman filters eliminate the influence of structural modes on force measurement and significantly increase the frequency bandwidth of the force measurement system [41]. Scheffer and Heyns [42] investigated possible SFs related to tool wear in interrupted cutting. They applied digital filters to separate two frequency ranges of cutting force signals: the low frequency range was an indication of static cutting forces and the high-frequency range of the natural frequencies of the toolholder which resulted from the excitation of the cutting operation. Jemielniak [43] used low-pass filtering of cutting force signals for catastrophic tool failure detection in turning based on the detection of sudden force value changes. The filtering allowed a much lower tolerance band on the limit set on force value. In many applications, a digital signal is filtered to prevent high frequency noise and signal oscillations due to transient mechanical events [44][45]. Another sensor signal pre-processing method is segmentation. Signal information should be extracted when the tool is actually removing metal in a steady state, since only this signal portion contains information about process or tool conditions [46][47]. Dong et al. [48] calculated SFs from force samples in one spindle rotation, instead of one tooth period, to reduce the influence of runout. Similarly in [49], where tool failure detection in interrupted turning was analyzed, the data points taken into consideration contained the AE data from at least one full workpiece revolution. Jemielniak et al. [50] noted that, despite constant cutting conditions in single micro-milling cut, AE was not constant; thus, separate SFs were calculated for all the cut and for the 1st and the 2nd third of the cut.

Features extraction in time domain

From the sensor signal, SFs need to be derived that can describe the signal adequately and maintain the relevant information about the process or tool conditions. There are several SFs that can be extracted from any time domain signal. The most common are: (i) arithmetic mean, average value, magnitude [44][48][51][52][53][54][55][56][57][58][59]; (ii) effective value (root mean square – RMS) [44][48][51][53][54][55][57][59][60]; (iii) variance (or standard deviation) [44][45][52][53][54][57][60][61]; (iv) skewness [45][53][54][55][56][57][61]; (v) kurtosis [45][53][54][55][56][57][61][62]; (vi) signal power [46][57][61]; (vii) peak-to-peak, range, or peak-to-valley amplitude, [42][44][45][51][53][57]; (viii) crest factor [45][51][54][55][57]; and (ix) ratios of the signals, signal increments [51][63].

Acoustic emission time domain features.

Some features are applicable only to vibration and AE signals: (a) ring down count or pulse rate: number of times AE_{raw} signal crosses the threshold level [37][40][59][60][64]; (b) pulse width: the percentage of time during which AE_{raw} remains above the threshold level [40][64]; (c) burst rate number of times AE_{RMS} signal exceeds preset thresholds per second [37][40][57]; and (d) burst width

– percentage of time AE_{RMS} signal remains above each threshold [40][64]. Kannatey-Asibu and Dornfeld [65] assumed that AE_{RMS} signal has a b distribution. They showed that skew and kurtosis are sensitive to both the stick-slip transition for chip contact along the tool rake face and progressive tool wear on the flank of the cutting tool. Jemielniak and Otman [49][66] applied these parameters to catastrophic tool failure detection.

Time series modeling.

Three main time series modeling techniques are frequently used in machining monitoring: Auto Regressive (AR), Moving Average (MA) and Auto Regressive Moving Average (ARMA) [37][45][54][67]. Early research work developed AR models of high order, up to the 28th order [67]. These were considered of little practical use because of the high computing load inadequate for online process monitoring. Thus, the 1st or the 1st and the 2nd AR, MA or ARMA coefficients were used as features [37][45][54]; sometimes higher AR coefficients of the 3rd–5th order [68]. Recently, Suprock et al. [68] applied the 100th order AR model for failure prediction in endmilling. They noticed that, while lower-order models may achieve “adequacy”, as defined in statistical terms, higher-order models produce more stable trends.

Principal Component Analysis.

Principal component analysis (PCA), also known as the Karhunen–Loeve transformation, has been widely used in system identification and dimensionality reduction in dynamic systems. Shi and Gindy [69] investigated the PCA technique to extract features from multiple sensory signals treated as a high-dimensional multivariate random matrix, composed of several vectors formed by the signals. By implementation of PCA, the signals can be reduced to a new reduced-size feature vector. Shi and Gindy used two perpendicular cutting force signals for tool wear monitoring in broaching. The pattern of cutting forces in the 2D space orbit diagram (Fig. 1.7) formed as scatter ellipse and was closely related to tool wear. This relation was quantitatively evaluated by PCA through the length of the major/minor axes (a/b) and the ellipse inclination angle (θ). Moreover, the origin (F_y , F_z) of the scatter ellipse was related to the average value of the cutting force in two orthogonal directions and could also be included in the feature set. Finally, the feature set normalized elements were specified as $\{F_y, F_z, a, b, \theta\}$ and fed to the tool wear prediction model. Abellan-Nebot and Subiron [70] extracted several standard SFs from cutting force signals, applied PCA to reduce the number of SF and constructed a new set of features that were a combination of the original SFs.

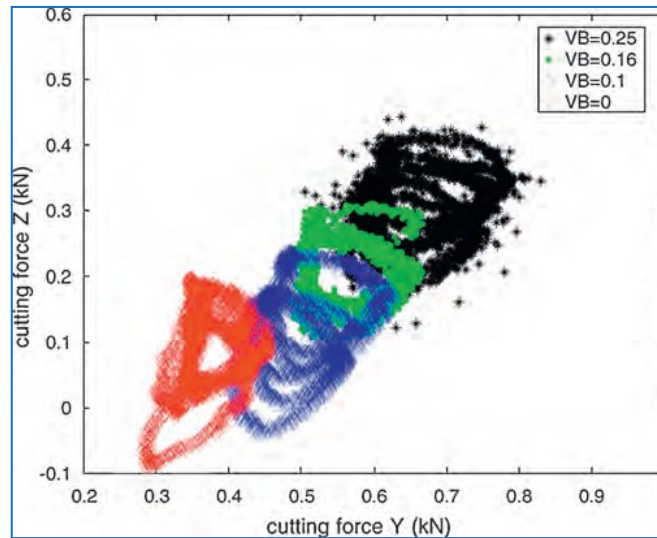


Fig. 1.7. Orbit diagram of cutting force signals in dual directions measured by integrated force sensors for different level of tool wear [69]

1.3.5. Monitoring scopes

In this section, a survey of applications related to the main goals of advanced monitoring of machining operations is presented.

Tool conditions

Kuljanic et al. [71] focus on the application of AE for tool wear estimation in milling using WPD to build an automatic tool wear classification system. Axinte and Gindy [72] try to correlate broaching tool conditions to output signals of multiple sensors: AE, vibration, cutting force and broaching machine hydraulic pressure. In [73], they assess the use of spindle power signal for TCM in milling, drilling and turning: this method is successful for continuous turning and drilling while it shows low sensitivity for discontinuous milling. Teti and Baciú [74] apply an intelligent monitoring system based on audible sound energy for in-process tool state recognition in band sawing of Al alloy and low C steel. Lee et al. [75] present a real-time tool breakage monitoring system for milling based on cutting force indirect measurement through feed drive AC motor current, whose sensitivity is sufficient to identify tool breakage. Ryabov et al. [76] develop an online tool geometry measurement system based on a laser displacement meter. Ahn et al. build up a vision system to detect small diameter tap breaks hardly perceived by indirect in-process monitoring methods as AE, torque and motor current; in [77], they propose an online drill wear estimation method based on spindle motor power signal during drilling. Arrazzola [78] uses micro-scale thermal imaging to identify effects of steel machinability change on cutting zone temperature and related tool wear mechanisms. In [79], he analyses and compares cost effective methods for tool breakage detection by performing trials on an ultra-precision micro-milling machine.

Chip conditions

Govekar et al. [80] use filtered AE spectrum components for chip form classification. Kim and Ahn [52] propose a method of chip disposal state monitoring in drilling based on spindle motor power features. Teti et al. [81][82][83] apply WPT and spectral estimation of cutting force signals for chip form recognition. Venuvinod et al. [84] use a variety of sensors to obtain stable clusters of chip form under varying dry cutting conditions through geometric transformations of the control variables: they aimed at recognising chip entanglements, chip size (including continuity), and chip shape.

Andreasen and De Chiffre [85] develop and test a laboratory system for automatic chip breaking detection via frequency analysis of cutting forces.

Process Conditions

Brophy et al. [86] classify drilling operations as 'normal' or 'abnormal' (tool breakage or missing tool) using spindle power signals. Mezentsev et al. [87] develop a method for fault detection in tapping based on torque and radial force; the method allows to identify typical faults of tapping operations: axial misalignment, tap runout, tooth breakage both singly and in a combined way. Axinte et al. [88] develop an online machining monitoring system based on PXI and LabVIEW platforms experimentally validated for broaching, turning and milling of aero engine materials. Teti et al. [89][90][91] use a process monitoring system based on inexpensive sound energy sensors, audible sound frequency analysis and neural network processing of audible sound SFs to identify variable process conditions in Al alloy milling. Chen et al. [92] implement a generalised internet-based process monitoring facility to provide clients with a virtual manufacturing process optimisation facility combining process simulation software with a Remote Machine Monitoring System (RMMS). In [93], state monitoring in the slicing of quartz glass ferrules is studied using AE detected during normal and abnormal states and extracting SFs for each symptom: a monitoring algorithm is proposed to reliably discriminate abnormal from normal states even under noisy circumstances. In [94], a polishing expert system integrated with sensory information is proposed which can modify even the polishing conditions initially recommended by the system itself, depending on the on-site polishing status; a real system using AE signals is developed. Pujana et al. [95] report on a new method to assess cutting variables (shear angle, chip thickness, tool vibration amplitude, strain, strain rate) and chip topology by means of high speed photography combined with laser printed square grid patterns on the workpiece at industrial cutting speeds and feeds.

Surface integrity

Azouzi and Guillot [96] apply cutting parameters and two cutting force components for online estimation of surface finish and dimensional deviations. Huang and Chen [58] employ a statistical approach to correlate surface roughness and cutting force in endmilling operations. Abouelatta and Madl [97] develop a method of surface roughness prediction in turning based on cutting parameters and FFT analysis of tool vibrations. Salgado et al. [98] use singular spectrum analysis to decompose the vibration signals for in-process prediction of surface roughness in turning. Song et al. [99] investigate time series analysis of vibration acceleration signals measured during cutting operations for real-time prediction of surface roughness. Axinte et al. [100] try to correlate the quality of the machined surface after broaching, in terms of geometrical accuracy, burr formation, chatter marks and surface anomalies, and the output signals from multiple sensors: AE, vibration, cutting force; the former proved efficient to detect small surface anomalies such as plucking, laps and smeared material. Guo and Ammala [59] investigate the sensitivity of a broad range of AE parameters to white layer, surface finish and tool wear in hard machining: AE_{RMS} , frequency and count rate have good correlation with white layer formation and may be used to monitor surface integrity factors. Kwak and Song [60] apply AE signal analysis to recognise grinding burns in cylindrical plunge grinding processes. Chang et al. [101] develop a method for inprocess surface roughness prediction based on the displacement signal of spindle motion. Axinte et al. [102][103], using AE signals backed up by cutting force data, report on process monitoring to detect surface anomalies when abusively broaching and milling difficult-to-machine aerospace materials. In [104], they report on the dynamics of broaching of complex part features: force and acceleration signal analysis revealed that damped coupled vibrations, resulting in tilted chatter surface marks, occur due to specific geometry

of cutting edges that enable coupling of 3D vibrations. In [105][106], the detection of workpiece surface discontinuities, plucking, and smearing is attempted through an array of 3 AE sensors during multiple cutting edge machining. Rawat and Attia [107] investigate the effect of cutting speed and feed rate on the quality features of drilled holes in carbon fiber composites (delamination, geometric errors, surface finish) by recording cutting forces with a dynamometer and inserting two K type thermocouples inside the drill.

1.3.6. Decision making support systems and paradigms

In monitoring and control activities for modern untended manufacturing systems, the role of cognitive computing methods employed in the implementation of intelligent sensors and sensorial systems is a fundamental one [108]. A conspicuous number of schemes, techniques and paradigms have been used to develop decision making support systems functional to come to a conclusion on machining process conditions based on sensor signals data features.

Neural Networks

An artificial neural network (NN) is a computational model of the human brain that assumes that computation is distributed over several simple interconnected processing elements, called neurons or nodes, which operate in parallel [109]. A NN provides a mapping through which points in the input space are associated with corresponding points in an output space on the basis of designated attribute values, of which class membership can be one. NN can capture domain knowledge from examples, do not archive knowledge in an explicit form such as rules or databases, can readily handle both continuous and discrete data, and have a good generalisation capability. NN can be employed as mapping devices, pattern classifiers or patterns completers. For more information on NN, see [110][111]. Knowledge is built into a NN by training. Some NN can be trained by feeding them with typical input patterns and expected output patterns. The error between actual and expected outputs is used to modify the weight of the connections between neurons. This method is known as supervised training. Other NN are trained in an unsupervised mode where only the input patterns are provided during training: the NN learns automatically to cluster them in groups with similar features.

Supervised learning

Among supervised learning paradigms, backpropagation (BP) NN, which are multiple-layered feedforward (FF) NN [109], have been very popular for their performance. Jemielniak et al. [64] noticed that conventional training of FF BP NN very soon leads to overtraining and deterioration of the NN response. Training of these NN depends very much on the initial weight values. A good way to obtain satisfactory results is to introduce random distortions to the weight system, which efficiently push the NN out of local minima of testing errors. An even more effective method is to employ temporary shifts in the weights, alternately negative and positive.

This brings the NN to a balance between training and testing errors and enables a notable reduction in the number of hidden nodes. Further supervised NN approaches are also considered here due to their use in decision making during monitoring of machining: probabilistic NN (PNN) [112], recurrent NN (RNN) [113][114][115], artificial cellular NN (ACNN) [116], fuzzy logic NN (FLNN) or neurofuzzy systems (NFS) combining NN and FL methods to integrate the benefits of both paradigms [117].

Unsupervised learning.

In unsupervised learning, only input stimuli are shown to the NN that organises itself internally so that each hidden processing element responds strongly to a different set or closely related group of stimuli. These sets of stimuli represent clusters in the input space which typically stand for distinct real concepts. Among unsupervised learning paradigms, the self-organising map (SOM) NN has been largely used for their performance [118]. The SOM NN creates a 2D feature map of input data so that order is preserved: if two input vectors are close, they will be mapped to processing elements that are close together in the 2D layer that represents the features or clusters of the input data.

NN applications to sensor monitoring of machining

The use of PNN for automated classification of broaching tool conditions utilising cutting force data is described in [119]. Trials with short broaching tools that simulate the roughing stage of industrial broaching were carried out to produce square profile slots while detecting cutting force signals. To reproduce real industrial tool failures, where both tool wear and single tooth chipping or breakage may randomly occur, the broaching tools had cutting teeth in different conditions: fresh, worn, chipped tooth, broken tooth. The push-off force F_y was selected as the most sensitive to tool conditions. Tool failure recognition was based on the extraction of a set of N characteristic points from the F_y plot by repetitive selection of local maxima to construct N -elements feature vectors (pattern vectors). Pattern vectors for different tool conditions were used as inputs to a PNN with 4 tool state classes: fresh, worn, chipped, broken. The success rate achieved was as high as 92%. A scheme of the tool failure recognition paradigm is shown in Fig. 1.8. Recurrent NN with simple architecture were used in [120][121][122][123][124] for the evaluation of tool wear in turning. In [120], features from wavelet representation of AE signals were related to flank wear. Using RNN data processing, accurate flank wear estimations were obtained for the operating conditions adopted in the experimentation [121]. In [122], fractal dimensions were used as input features to a RNN for flank wear land estimation [123]. The development of this estimator comprised four stages: (i) signal representation, (ii) signal separation, (iii) feature extraction, and (iv) state estimation (flank wear land). In stage (i), a compact Suboptimal Wavelet Packet Representation (SWPR) [121], superior to other wavelet-based signal representation schemes, was used. In stage (ii), a method for suppressing noise components from measured time series data, called Modified Wavelet Method (MWM) [124], was selected for signal separation due to its high performance.

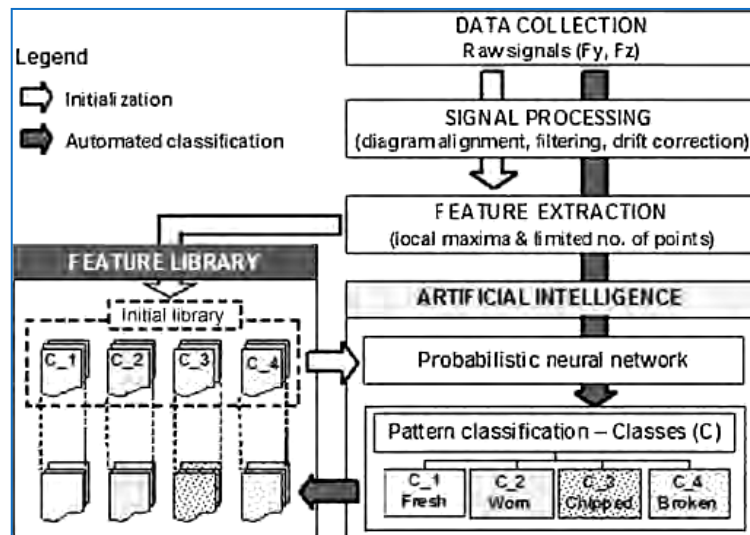


Fig. 1.8. Schematic of the tool condition recognition system.[10]

The capacity, correlation and information fractal dimensions were extracted as features of a 4D time series vector formed by combining cutting force and vibration signals. The extracted features were related to flank wear land using a trained RNN that out-performed earlier tool wear estimators in terms of architecture simplicity and estimation accuracy. Due to the high signal sampling rate, this estimator may be used for real-time flank wear estimation at time epochs of few milliseconds, which can help with early detection of undue tool wear and related machining process faults [122].

Particular attention was paid to industrial needs: (a) no reduction in machine stiffness; (b) compatibility with pallet and tool changers; (c) no restriction on tools, parts and cutting parameters; (d) robustness against sensing units failures; and (d) independence from cutting conditions and system dynamics. To evaluate the system capability for a broad application range, different test setups with diverse milling machines, toolings, sensor systems and work materials were used. A NN approach was used for decision making, comprising an ACNN [116] applied to acceleration signals and a fuzzy NN [117] for axial force signals. Good levels of NN accuracy were obtained with all single sensor signals. To realise the concept of multi-sensor chatter detection, the NN outputs for each single sensor signal were combined through: (i) linear combination of single sensor chatter indicators; (ii) a separate NN for multi-sensor classification; (iii) fuzzy logic classification (Sugeno fuzzy model); and (iv) statistical inference classification based on conditional probability, i.e. the probability that the system is unstable for a specific combination of single chatter indicators. The accuracy of the first three approaches was very high: 95–96%. But residual accuracy in case of sensing unit malfunctions dropped notably: 50–75%. The behaviour of the fourth approach was quite different: accuracy was slightly lower, 94%, but insensitivity to malfunctions was extremely robust: 90–92%. Thus, the statistical inference multi-sensor chatter indicator, combining NN data processing and statistical methods to achieve both high accuracy and high robustness, was assessed as the most suitable for industrial milling applications. In [125], a sensor monitoring method, based on spindle motor power sensing and NN processing, was evaluated for chip disposal state detection in drilling. Spindle motor power measurements have the advantage of being easily realised during machining. From them, selected features such as variance/mean, mean absolute deviation, gradient, and event count were calculated to form input vectors to a FF BP NN for decision making on chip disposal state. The selected features were experimentally shown to be sensitive to changes in chip disposal state and relatively insensitive to changes in drilling conditions. So, the proposed

monitoring system could effectively recognize chip disposal states over a wide range of drilling parameters, even if training was carried out under diverse process conditions.

Among the various sensing techniques, audible sound energy appears as one of the most practical ones since it can replace the traditional ability of the operator, based on his experience and senses (mainly vision and hearing), to determine the process state and react adequately to any machine performance decay [126]. This monitoring technology, however, has not been exhaustively investigated for process monitoring in machining, even though it is extensively used by machine tool operators for real-time decision making. In [77][89][90][91], audible sound energy generated by milling and band sawing of Al alloy and C steel under different process and tool conditions was analysed in the frequency domain by a real-time spectrum analyser to develop an automatic process monitoring system based on inexpensive sound sensors. Signal analysis was carried out by suppressing the noise generated by the machine and the environment from the sound emitted during machining. Classification of audible sound SFs was performed by a NN approach that could successfully identify the process and tool conditions solely on the basis of sound sensor monitoring.

1.3.7. Sensor fusion technology

Sensor fusion concepts and paradigms

When measuring a particular variable, a single sensory source for that variable may not be able to meet all the required performance specifications. A solution to this problem is sensor fusion that combines sensory data from disparate sources so that the resulting information is better than would be possible when these sources are used individually. The term “better” can mean more accurate, more complete, more dependable, more robust, or refer to the result of an emerging view, such as stereoscopic vision that calculates depth information by combining 2D images from two cameras at slightly different viewpoints. One can distinguish direct fusion, indirect fusion and fusion of the outputs of the former two. Direct fusion is the fusion of sensor data from a set of heterogeneous or homogeneous sensors, soft sensors, and history values of sensor data, while indirect fusion uses information sources like a priori knowledge about the environment and human input [127][128][129].

Reconfigurable monitoring system for sensor fusion research

Sensor fusion for machining process monitoring has been extensively investigated in [130][131][132][133][134] within a multi-annual project aiming at the implementation of a reconfigurable multisensory monitoring system (Fig. 1.9), endowed with cutting force, vibration, AE, motor current, audible sound and optical sensors, for application to diverse machining processes (orthogonal cutting, turning, milling, drilling, and broaching), work materials (steels, composite materials, Ti alloys, Ni alloys, Ni-Ti alloys) and monitoring scopes (tool wear, chip form, process conditions, work material state, and machinability assessment). Sensor signal characterisation is based on frequency domain analysis, accomplishing sensor signal spectral estimation through a parametric method that allows for feature extraction from the signal frequency content [135]. In this procedure, the signal spectrum is assumed to take on a specific functional form, the parameters of which are unknown. The spectral estimation problem, therefore, becomes one of estimating these unknown parameters of the spectrum model rather than the spectrum itself [136]. From each signal specimen (measurement vector), p features $\{a_1, \dots, a_p\}$ (feature vector), characteristic of the spectrum model, are obtained through Linear Predictive Analysis (LPA) by applying Durbin's algorithm [137]. The details of this procedure are given in [138].



Fig. 1.9. Reconfigurable multi-sensor monitoring system [10]

Feature vectors are used to construct input pattern vectors for pattern recognition paradigms [139]. If single signal specimens are utilised as inputs, the feature vector and pattern vector coincide. If signal specimens' inputs come from two or more diverse sensor signals, input patterns are complex vectors integrating sensory data from diverse sources to realise the concept of sensor fusion. Pattern recognition and decision making in the reconfigurable multi-sensor monitoring system is carried out by three layers FF BP NN whose architecture is automatically configured as a function of the monitoring application. The constructed input pattern vectors are the input of the first NN layer that, accordingly, assumes a number of nodes equal to the number of input pattern vector elements. The hidden layer takes up a number of nodes as a function of the number of input nodes. The output layer contains one or more nodes, yielding coded values associated with the monitored process variables that need to be recognised. For NN learning, the leave-k-out method, particularly useful when dealing with relatively small training sets, is typically utilised [140]: one homogeneous group of k patterns, extracted from the training set, is held back in turn for testing and the rest of the patterns is used for training. The NN output is correct if the actual output, O_a , is equal to the desired output, O_d , $\pm 50\%$ of the difference between the numerical codes for different process conditions.

By setting error $E = (O_a - O_d)$, process conditions identification is correct if $-0.5 \leq E \leq +0.5$; otherwise, a misclassification case occurs. The ratio of correct classifications over total training cases yields the NN success rate.

Sensor fusion application to machining process monitoring

The NN pattern recognition paradigm of the reconfigurable multi-sensor monitoring system proved able to effectively realize the concept of sensor fusion for a broad range of machining process monitoring applications, yielding satisfactory results also under unfavourable situations by synergically combining the knowledge extracted from multiple sources of information. In [132][141][142] the system was applied to process condition and machinability evaluation during cutting of difficult-to-machine materials such as Ti alloys and NiTi alloys, using cutting force and acceleration signals through both single signal and sensor fusion data analysis.

Training sets with input pattern vectors of different size and nature were built: (a) signal specimen feature vectors of single cutting force or acceleration component: F_x , F_y , F_z , a_x , a_y , a_z ; (b) integrated pattern vectors of the 3 cutting force or acceleration components:

$[F] = [F_x \ F_y \ F_z]$; $[A] = [a_x \ a_y \ a_z]$; (c) sensor fusion pattern vectors combining cutting force and acceleration pattern vectors:

$[S] = [F \ A] = [F_x \ F_y \ F_z \ a_x \ a_y \ a_z]$. The NN outputs were coded values to evaluate process condition and machinability. Results showed that the use of single component signal data as pattern inputs provided acceptable accuracy: 78–85%. If the integrated 3 acceleration or 3 cutting force components signal data are used as inputs, accuracy improves notably: 92–97%. By applying sensor fusion technology to fully combine information from cutting force and acceleration signal data, a very high accuracy is obtained: 99–100%.

In Teti and Segreto [131], sensor monitoring during cutting of plastic matrix fibre reinforce composites was performed for consistent and reliable identification of tool state. AE and cutting force signals were subjected to the NN based sensor fusion paradigm. The superior classification results found by merging cutting force and AE data stressed sensor fusion aptitude for data analysis enhancement and decision making reinforcement [81][143].

It is worth noting that the above results were achieved via sensor fusion of multimodal data which is far less common than fusion of data from the same sensor type. This highlights the NN ability to efficiently realize the concept of sensor fusion as well as to deal with incomplete or noisy data sets, yielding satisfactory results also under adverse situations by synergically combining knowledge extracted from multiple sources of information. In [144], the combination of a direct sensor (vision) and an indirect sensor (force) is proposed to create an intelligent integrated TCM system for online monitoring of tool wear and breakage in milling, using the complementary strengths of the two types of sensors. For tool flank wear, images of the tool are captured and processed in-cycle using successive moving-image analysis. Two features of the cutting force, which closely indicate flank wear, are extracted in-process and appropriately preprocessed. A SOM network is trained in a batch mode after each cutting pass, using the two features from the cutting force, and measured wear values obtained by interpolating the vision-based measurements. The trained SOM network is applied to the succeeding machining pass to estimate the flank wear in-process. The in-cycle and in-process procedures are employed alternatively for the online monitoring of flank wear. To detect tool breakage, two time domain features from cutting force are used, and their thresholds are determined dynamically. Again, vision is used to verify any breakage identified in-process through cutting force monitoring. Experimental results show that this sensor fusion scheme is feasible and effective to implement online TCM in milling and is independent of cutting conditions [10].

1.4. ACCENT Project at a Glance

The manufacture of safety critical rotating components in modern aero engines is by nature very conservative. In order to achieve the required engine performance, thermal and mechanical stresses are pushed to the maximum, which in turn leaves the choice of materials to exotic super alloys. These materials are classed as difficult to machine under normal circumstances, but when added to the changes in mechanical properties which occur naturally from part to part, consequently variable and often unpredictable tool life, and the ever present possibility of random and unexpected process anomalies, machining processes can never be fully optimised. Stringent legislative controls are

placed on safety critical component manufacture to ensure that parts entering service will function correctly and safely to a declared service life, and in declaring the service life for such a part, the machinability issues stated above have to be taken into consideration. Hence manufacturing process parameters are often reduced or tools are changed early to ensure part surface integrity. The industry method adopted, is to “freeze” to process following process qualification to first article inspection, and successful part validation via laboratory examination and testing. Once frozen, no changes to process parameters are permitted without time consuming and costly re-validation.

Objectives

ACCENT aimed at allowing the European Aero Engine manufacturers to improve their competitiveness by applying adaptive control techniques to the manufacture of their components. Being able to adapt the machining process to the constantly changing tool and component conditions whilst operating in a multi-dimensional “approved process window”, processes can be optimised to the prevailing conditions and no longer “frozen”. Benefits can be seen in terms of reduced part manufacturing process time, more consistent part quality in terms of geometry, surface and sub-surface properties, tool usage optimisation, elimination of costly part re-validation due to small process changes, and the possibility to improve component design due to optimised machined surfaces.

Description of Work

The project is divided into five work packages (WP).

- WP1: project management.
- WP2: ensures that a standard procedure is generated to define multi-dimensional parameter windows for the machining process and material combinations. The outcome will be a specification which defines how a machining process has to be established and controlled in order to satisfy a defined surface integrity level.
- WP3: is focused on developing the Standard Procedure for Adaptive Control. The work package will deliver an understanding of how to use process monitoring systems in a closed-loop adaptive control system that keeps the process within a defined process window.
- WP4: will bring together those elements that have a direct effect on the component performance in terms of life and fitness for purpose. The interaction between the surface integrity generated as a result of the machining process parameters, cutting tool and machine tool condition, material characteristics, etc. will be investigated and understood.
- WP5: exploitation and dissemination.

The knowledge gained by the Project allows for the design function to understand the effect of machining processes on part quality and subsequent component service, and thus allows the component design to be optimised. With the new validation procedure, new demands can be placed on storage and retrieval of related data.

Expected Results

For the manufacture of critical aero-engine components, ACCENT aimed at developing a standard procedure for defining process parameter windows and methods whereby components manufactured within these process parameter windows are validated to meet the demands of design and surface integrity requirements. It aimed to provide a new manufacturing methodology that can allow significant reduction in recurring validation costs and develop a novel standard procedure for

adaptive control based on process monitoring techniques. It took account of factors responsible for producing variable part quality and provide aero-engine manufacturers with a methodology that can be adapted to individual company procedures, thus allowing the design and manufacture of critical components to be optimised. As the majority of Europe's aero-engine companies are project partners, increased contacts led to new collaboration opportunities and consolidation of the aero-engine sector in Europe. ACCENT involved world-leading experts from both universities and companies in Europe, thus helping to increase the synergy between academia and industry, and helped to secure a supply of highly skilled young aero-engine engineers in Europe.

Related Info

- Acronym: ACCENT
- Name of proposal: Adaptive Control of Manufacturing Processes for a New Generation of Jet Engine Components
- Grant Agreement: 213855
- Instrument: CP - FP
- Total cost: 8 196 673 €
- EU contribution: 5 374 684 €
- Call: FP7-AAT-2007-RTD-1
- Starting date: 01/07/2008
- Ending date: 30/06/2012
- Duration: 48 months
- Technical domain: Design Tools and Production
- Coordinator: Mr. David Bone Dave.Bone@rolls-royce.com

Partners

- WZL-RWTH Aachen DE
- MTU Aero Engines GmbH DE
- Avio SpA IT
- Snecma FR
- Volvo Aero Corporation SE
- Industria de Turbo Propulsores, S.A. ES
- Turbomeca FR
- L'Ecole Nationale d'Ingénieurs de Tarbes FR
- Société d'Etudes et de Recherches de l'ENSAM FR
- Technical University of Kosice SK
- Mondragon Goi Eskola Politeknikoa S. Coop. ES
- Advanced Prototype Research IT
- University of Naples IT

Experimental Activities

2. Experimental Setup

2.1. Machine Tool

The machine tool employed for experimental campaign is a VDF CNC horizontal lathe as reported in Fig. 2.1.



Fig. 2.1 – VDF CNC Horizontal Lathe machine tool

2.2. Work material

The material used for the experimental activities is INCONEL 718.

Inconel 718 is a precipitation-hardenable nickel-chromium alloy containing significant amounts of iron, niobium, and molybdenum along with lesser amounts of aluminum and titanium. It combines corrosion resistance and high strength with outstanding weldability, including resistance to postweld cracking. The alloy has excellent creep-rupture strength at temperatures up to 700 °C. Used in gas turbines, rocket motors, spacecraft, nuclear reactors, pumps, and tooling.[146].

Typical analysis in percent

Table 2.1

Ni(+Co):	50 - 55	Cr:	17 - 21
Fe:	bal	Co:	1
Mo:	2.3 - 3.3	Nb (+Ta)	4.75 - 5.5
Ti	0.65 - 1.15	Al:	0.2 - 0.8
C:	0.08	Mn	0.35
Si:	0.35	B:	0.006
Cu:	0.3		

Physical properties

Table 2.2. Inconel 718 physical properties

Density	8.19 g/cm ³
Melting point range:	1260 - 1336 °C
Specific heat:	435 J/kg·K
Average Coefficient of Thermal Expansion:	13.0 µm/m·K
Thermal Conductivity:	11.4 W/m·K
Electrical Resistivity:	1250 n·m
Curie Temperature:	-112 °C

Typical mechanical properties:

Table 2.3. Inconel 718 mechanical properties

At room temperature	
Ultimate tensile strength	1240 MPa
Yield strength	1036 MPa
Elongation in 50 mm	12 %
Elastic modulus (Tension)	211 GPa
Hardness	36 HRC

2.3. Workpiece

The experimental campaign was carried out by turning an Inconel 718 cylindrical shaft, as shown in Fig. 2.2



Fig. 2.2 Inconel 718 Cylindrical shaft utilized as work material

2.4. Cutting tools

The cutting tools utilized for the experimental tests are **Kennametal CNMG120408-K313** rhombic uncoated carbide tools as the one shown in figure below.

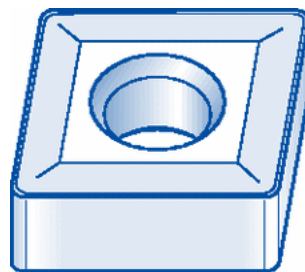
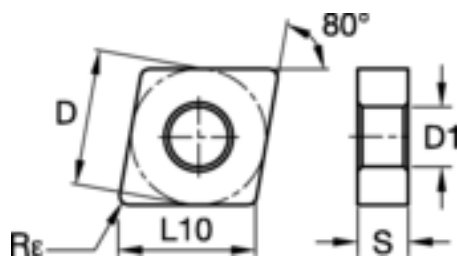


Fig. 2.3 - Kennametal cutting tool



D	L10	S	Re	D1
12.70	12.90	4.76	0.8	5.16

dimensions in millimeters

Fig. 2.4. Cutting tool dimensions

The tool holder is a customized compatible holder as shown in figure 2.5.

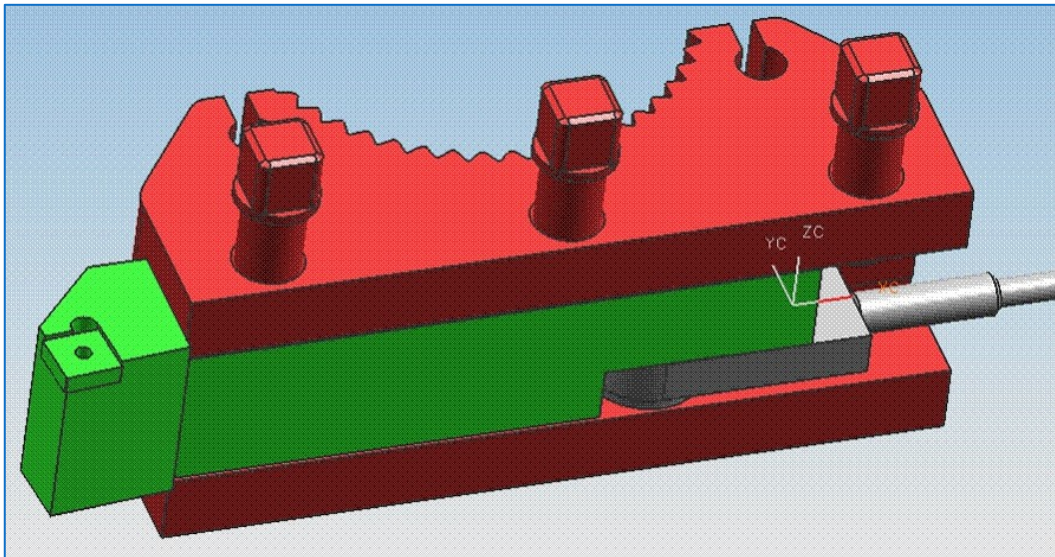


Fig. 2.5 – Customized tool holder

3. Experimental tests programme

On the basis of common cutting parameters adopted for turning of Inconel 718 workpieces, three cutting speed values were considered for the experimental programme, respectively 45, 50 and 55 m/min, this last value is close to the maximum acceptable cutting speed, fixed at 56 m/min in case of cutting with carbide inserts.

Three feed rates were considered: 0.10, 0.125 and 0.15 mm/rev according to the literature and the common shop floor values.

Table 3.1. Standard Tests experimental programme

Test ID	V (m/min)	f (mm/rev)
#1	45	0.10
#2	45	0.125
#3	45	0.15
#4	50	0.10
#5	50	0.125
#6	50	0.15
#7	55	0.10
#8	55	0.125
#9	55	0.15

The depth of cut (a_p) is kept constant and equal to 0.3 mm for every cutting test.

An additional experimental programme has been carried out in order to increase the probabilities in generating surface defects.

For this purpose, severe cutting conditions were chosen, increasing both the cutting speed (up to 80 – 100 m/min) and the feed rate (up to 0.30 mm/rev). The turning tests were carried out both in cooled and in dry conditions as reported in the table below.

Table 3.2. Severe cutting conditions tests experimental programme

Test ID	V (m/min)	f (mm/rev)	Cutting Fluid
#1H	80	0.15	On
#2H	80	0.30	On
#3H	100	0.15	On
#4H	100	0.30	On
#5H	80	0.15	Off
#6H	80	0.30	Off
#7H	100	0.15	Off
#8H	100	0.30	Off

3.1. Experimental tests procedure

The experimental tests begin with turning the external diameter for 120 seconds setting a depth of cut equal to 0.3 mm. In this way the external diameter will be reduced by 0.6 mm at every step.

After every step, the tool wear measurement by a profile projector is carried out. If the tool wear has reached the 0.3 mm value, considered the maximum recommended acceptable value, then the test is completed otherwise there will be another 120 seconds turning step.

For the severe cutting conditions tests, the single turning step lasts 30 seconds while the tool wear threshold value is 0.5 mm. The experimental procedures can be summarized by the flow charts reported below.

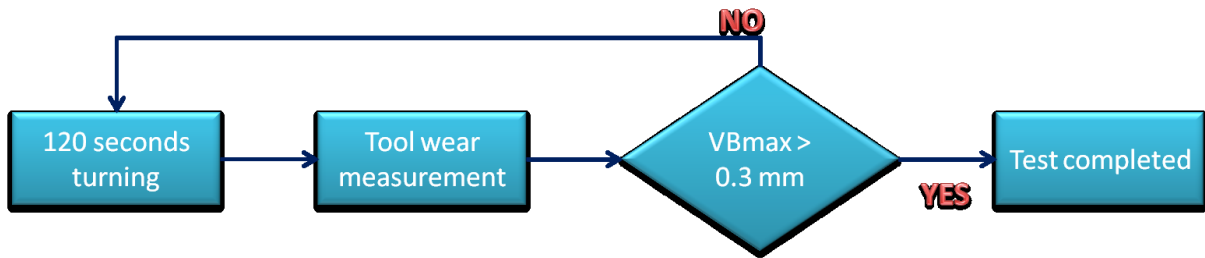


Fig.3.1.Experimental procedure flow chart for standard tests

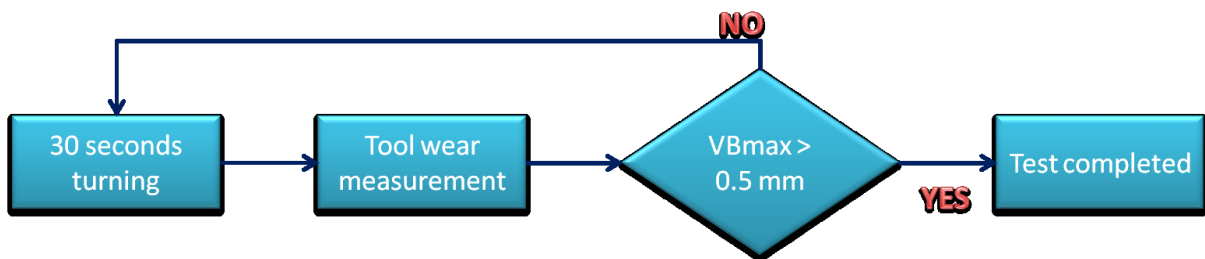


Fig. 3.2 Experimental procedure flow chart for Severe Cutting Conditions tests

In order to have 2 minutes step (or 30 seconds for Severe Cutting Conditions Tests) regardless the several cutting speeds, the cutting length Z (illustrated in Fig. 3.3), was calculated as follows:

V _c	Cutting Speed	m/min
T	Cutting Time	min
D	Diameter	mm
f	Feed Rate	mm/rev
n	Number of revolutions	

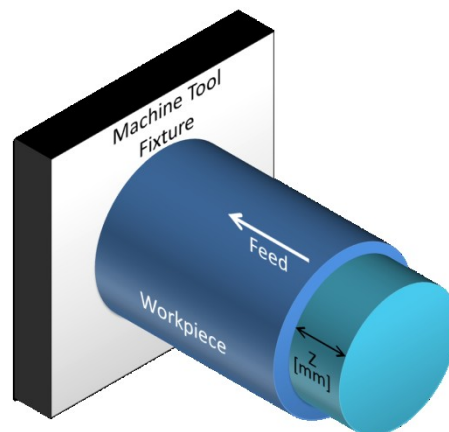


Fig. 3.3. Cutting length

$$T = \frac{Z}{n \cdot f}$$

$$Z = T \cdot n \cdot f$$

$$n = \frac{V_c \cdot 1000}{\pi \cdot D}$$

$$Z = T \cdot \frac{V_c \cdot 1000}{\pi \cdot D} \cdot f$$

At every step, the workpiece diameter decreases by 0.6 mm ($2 \cdot a_p$), consequently the cutting length increases. Hence, after calculating Z for every step, an average value was considered and used in the CNC code.

$$\tilde{Z} = \frac{\sum Z_{step}}{\text{number of steps}}$$

4. Sensor Units

4.1. Cutting Force Sensor

The cutting force sensor used for process monitoring is **MONTRONIX FS-ICA** shown in Fig. 4.1 a.

The cutting force sensor signal is then amplified by a **Montronix TSFA₃-ICA Force Amplifier** (Fig. 4.1 b)

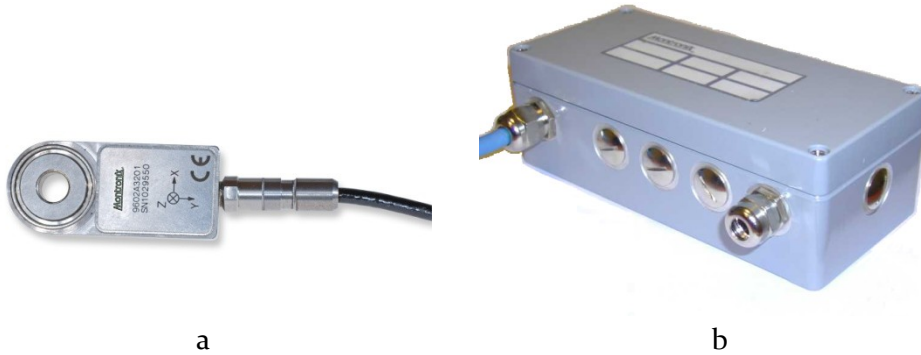


Fig. 4.1. Cutting force sensor (a) and amplifier (b)

The force amplifier was configured with the following settings, shown in Fig. 4.2 and explained in Table 4.1.

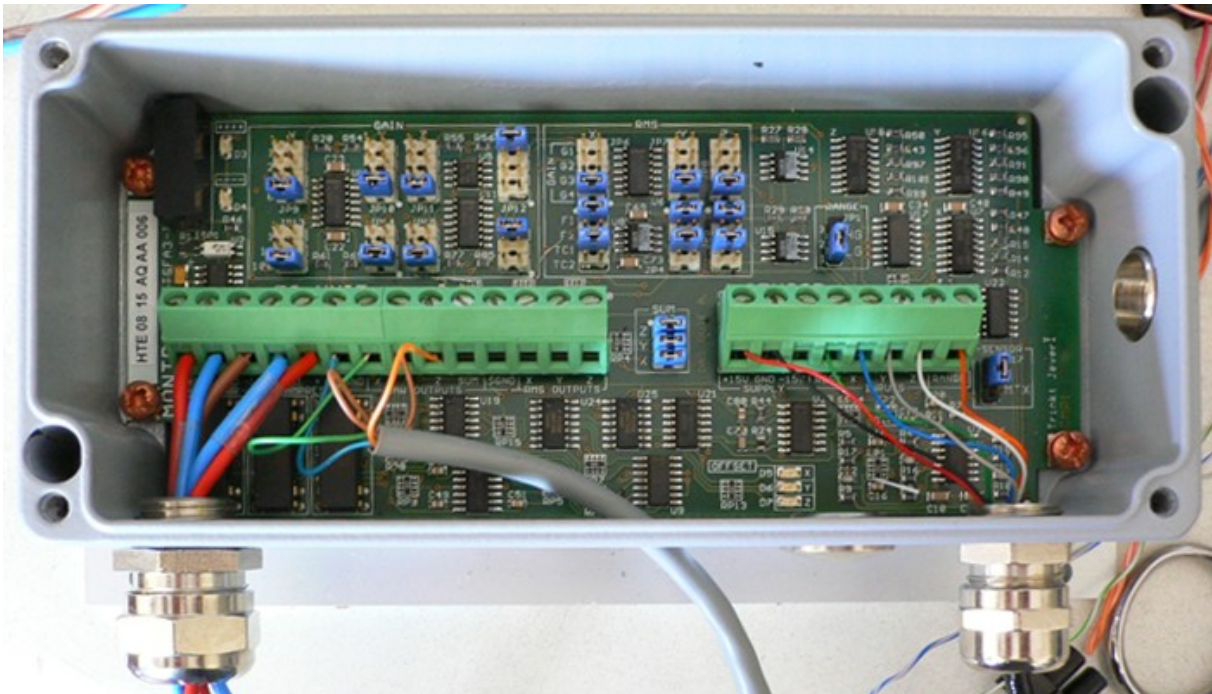


Fig. 4.2. Cutting Force amplifier settings

Table 4.1. Cutting force amplifier specifications

Cutting Forces Amplifier Specifications	
Gain Settings	1, 2, 4, 8, 10, 20, 40, 80, 100, 200, 400, 800
Gain Error	±2%
Power Provided to Sensor	±15 VDC
Amplifier Power Requirements	+15 VDC @ 70mA, -15 VDC @ -20 mA
Temperature Range	0° to 60° C
Connectors	PG9 threated fittings, sensor-specific
Weight	700
Sensor Inputs	1, 2 or 3

Table 4.2. Cutting forces sensor signal pre-conditionings

Cutting Forces Sensor Signal pre-conditioning	
Type of signal:	analog signal
Selected gain:	8 x 100 = 800
Frequency band:	0 – 2500 Hz
Static Part of Force Signal (Fx, Fy, Fz):	3 times ±10V
Digitalisation:	through National Instruments USB-6221 A/D converter using sampling rate = 10 kHz

4.2. Acoustic Emission Sensor

The acoustic emission sensor used for process monitoring is **MONTRONIX BV-100 Series** shown in Fig. 4.3.

The analogue acoustic emission sensor signal is then amplified by a **Montronix TSVA4G AE Amplifier**.

The RMS signal is obtained by using a **SHORT** time constant equal to 0.12 ms.



Fig. 4.3. Acoustic Emission sensor (a) and amplifier (b)

The Acoustic Emission amplifier was configured with the following settings, shown in Fig. 4.4 and explained in Table 4.3.

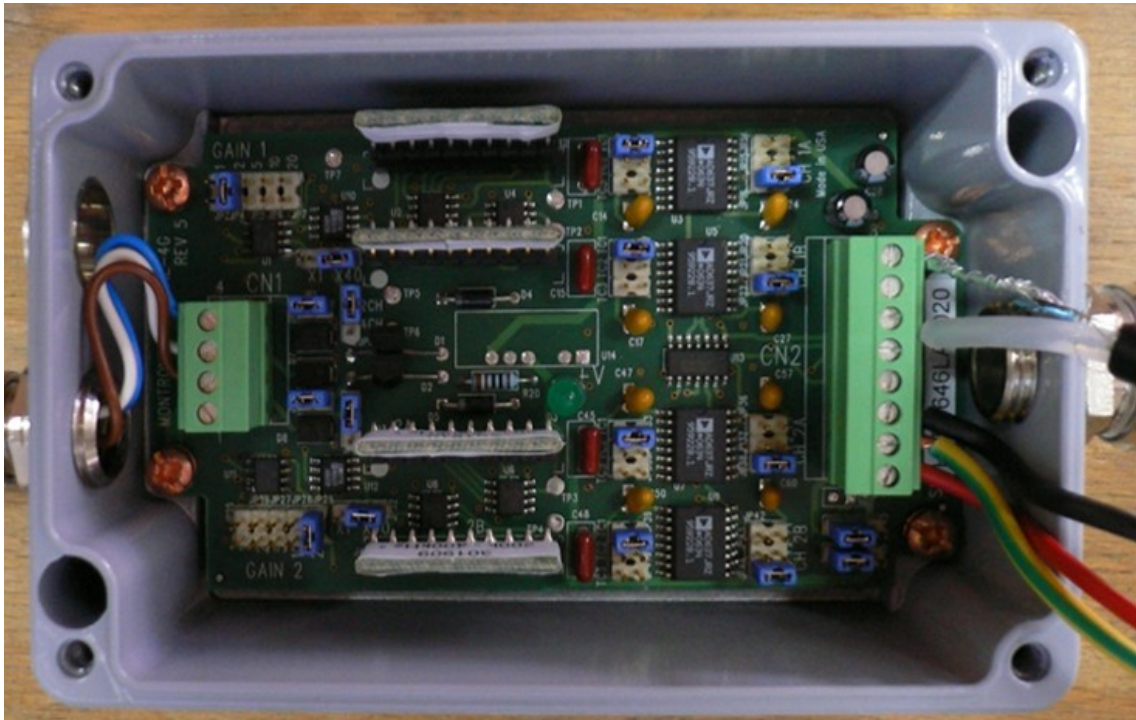


Fig. 4.4. AE amplifier settings

Table 4.3. AE amplifier specifications

AE Amplifier Specifications	
Gain Settings	1, 2, 5, 10, 20, 40, 80, 200, 400, 800
Gain Error	±2%
Output Voltage	0 to 10 V
Power provided to Sensor	+ 15 VDC @ 4mA constant current
Amplifier Power Requirements	+15 VDC @ 80mA, -15 VDC @ -60 mA
Temperature Range	0° to 60° C
Connectors	PG9 threaded fittings, sensor-specific
Weight	680 g

Table 4.4. AE sensor signal pre-conditioning

AE Sensor Signal pre-conditioning	
Type of signal:	analog RMS signal
Time average:	Short (0.12 ms)
Selected gain:	20 x 40 = 800
Frequency band:	0 – 2500 Hz
Digitalisation:	through National Instruments USB-6221 A/D converter using sampling rate = 10 kHz

4.3. Vibration Sensor

The vibration sensor used for this experimental campaign was a Montronix SpectraPulse provided by direct USB connection, shown in Fig. 4.5.

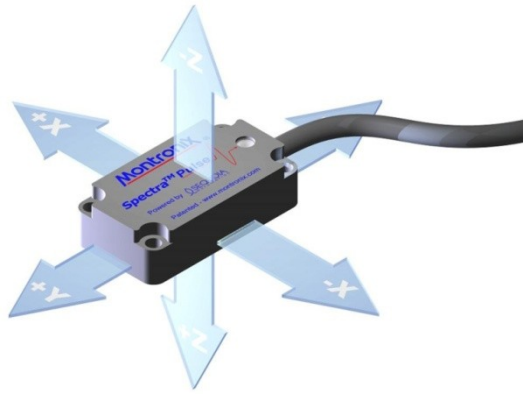


Fig. 4.5. Montronix SpectraPulse USB Vibration Sensor

Vibration sensor technical specifications are reported in the table below

Table 4.5. Vibration sensor technical specifications

Vibration sensor technical specifications	
Frequency range:	DC 0 to 2500 Hz
Measuring range:	± 18 g
Shock Resistance:	1000 g
Weight:	55 g
Dimensions (mm):	55 x 30 x 15
Connection:	USB

4.4. Signal Acquisition

A customized amplification board was assembled in order to handle the multi-sensor system for the experimental campaign. A power supply box is connected to the two amplifiers (Forces and Acoustic Emission). In order to avoid signal drift phenomena, the force amplifier is connected to a secondary power switch, in order to reset the sensor before every sensing session.

The power box, the amplifiers and the switch are screwed on a metallic board. A scheme of the amplification board is shown in Fig. 4.6, and a picture is reported in Fig.4.7.

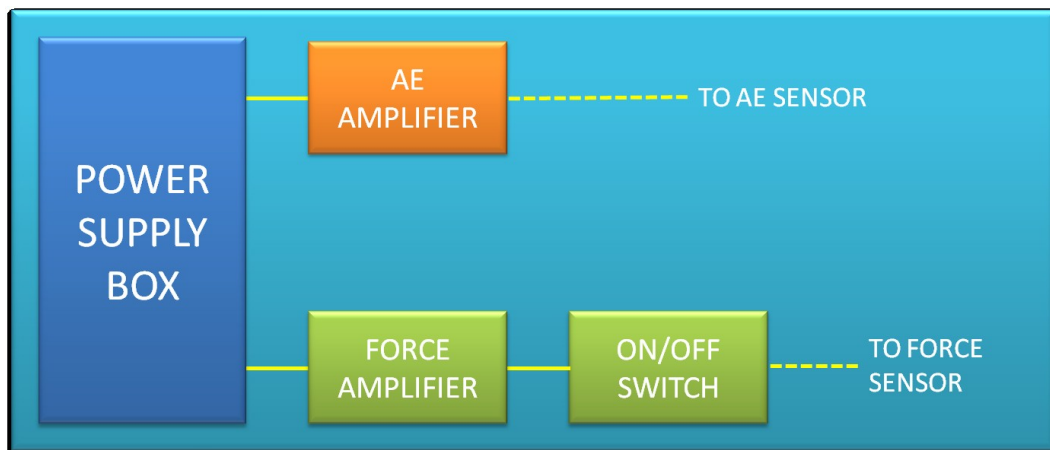


Fig. 4.6. Amplification board scheme



Fig. 4.7. Custom Amplification Board

The analogue signal from the Cutting Force sensor and AE sensor have to be digitized by a National Instruments USB-6221 A/D

Specifications	
Channels	16 analog input channels (8 differential channels)
Resolution	16 bits
Sample Rate	250 kS/s
Maximum Voltage Range	10 V , 10 V
Maximum Voltage Range Accuracy	3100 μ V
Maximum Voltage Range Sensitivity	97.6 μ V
Minimum Voltage Range	-200 mV , 200 mV
Minimum Voltage Range Accuracy	112 μ V
Minimum Voltage Range Sensitivity	5.2 μ V



Fig. 4.8. National Instrument Data Acquisition Device

4.4.1. Sampling Frequency

Nyquist-Shannon theory

The Nyquist sampling theorem provides a prescription for the nominal sampling interval required to avoid aliasing. It may be stated simply as follows:

The sampling frequency should be at least twice the highest frequency contained in the signal.

Or in mathematical terms:

$$f_s \geq 2 \cdot f_c$$

Where f_s is the sampling frequency (how often samples are taken per unit of time or space), and f_c is the highest frequency contained in the signal. That this is so is really quite intuitive.

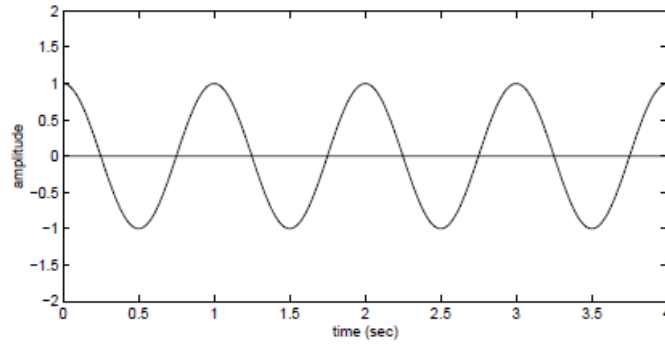


Fig. 4.9.

Consider for example a signal composed of a single sinewave at a frequency of 1 Hz:

Sampling this waveform at 2 Hz (as dictated by the Nyquist theorem) is sufficient to capture each peak and trough of the signal:

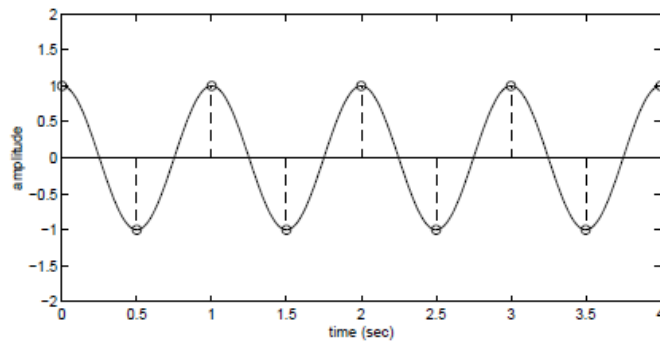


Fig. 4.10.

By sampling at a frequency higher than this, for example 3 Hz, there are more than enough samples to capture the variations in the signal:

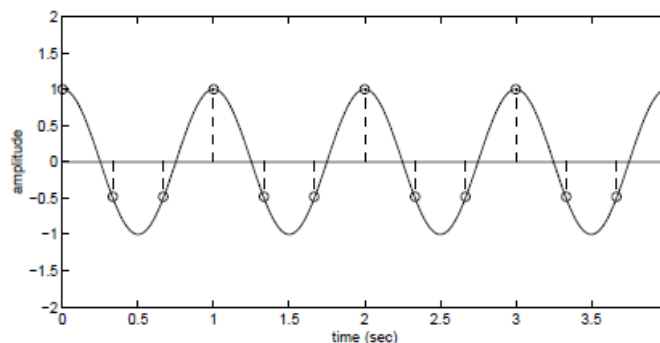


Fig. 4.11.

However, sampling at a frequency lower than 2 Hz, for example at 1.5 Hz, there will not be enough samples to capture all the peaks and troughs in the signal:

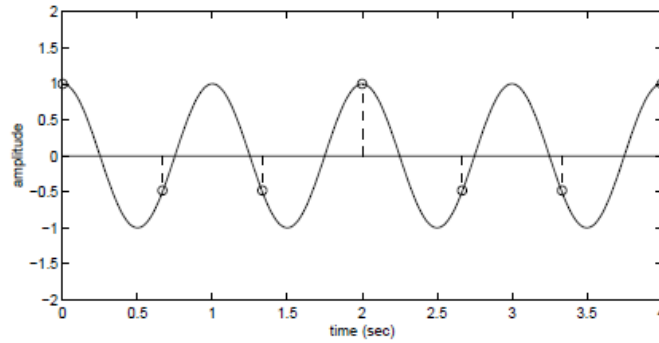


Fig. 4.12.

Note here that here there is not only a loss of information, but the information about the signal is wrong. The person receiving these samples, without any previous knowledge of the original signal, may well be misled into thinking that the signal has quite a different form:

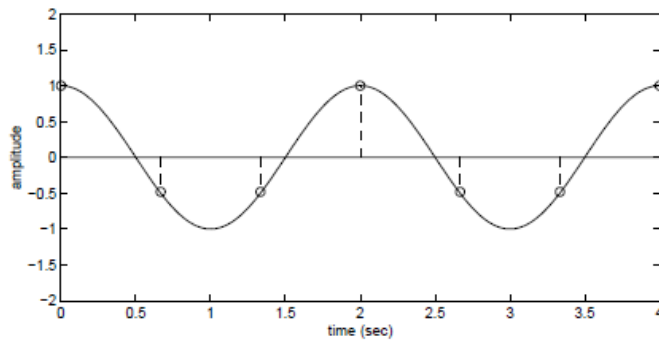


Fig. 4.13.

From this example, it's possible to see the reason for the term aliasing. That is, the signal now takes on a different "persona", or a false presentation, due to being sampled at an insufficiently high frequency.

Now we are ready to think about the sampling of a complex signal composed of many frequency components. By Fourier's theorem, it's known that any continuous signal may be decomposed in terms of a sum of sines and cosines at different frequencies.

For example, the following waveform was composed by adding together sinewaves at frequencies of 1 Hz, 2 Hz, and 3 Hz:

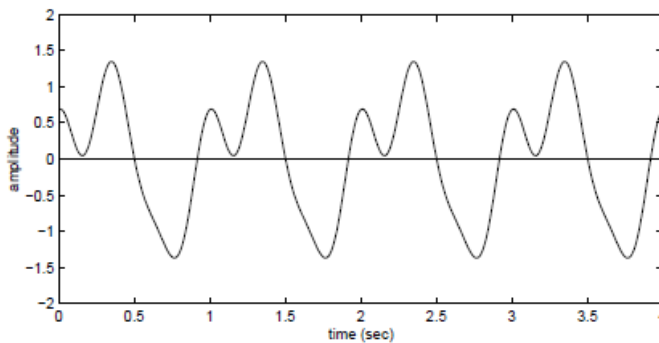


Fig. 4.14.

According to the Nyquist sampling theorem, the signal must be sampled at twice the highest frequency contained in the signal. In this case, we have $f_c=3$ Hz, and so the Nyquist theorem tells that the sampling frequency, f_s , must be at least 6 Hz. And sure enough, this appears to be sufficient:

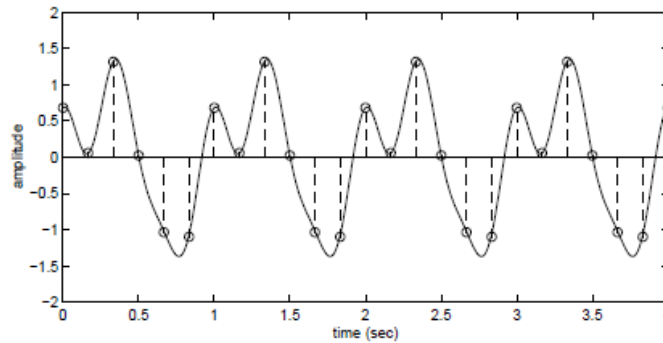


Fig. 4.15.

Thus, when a signal contains not just one but many different frequencies added together, the minimal sampling rate needed to avoid aliasing is just twice whatever the highest frequency is, irrespective of how many other frequency components there are [147].

4.4.2. RMS vs RAW

The RAW information from the monitoring is a collection of positive and negative electrical signals, their frequency (how often they occur), and their amplitude give information about the stress generated i.e. by the elastic waves in case of acoustic emission [148].

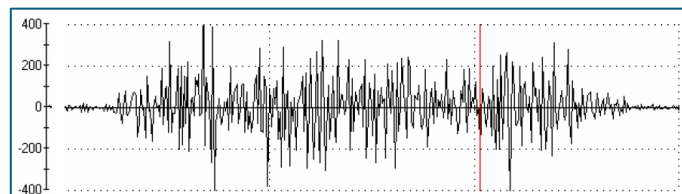


Fig. 4.16. Raw signal

In the raw graph (Fig. 4.16) the X axis displays time and the Y axis displays amplitude in V (Volts), both positive and negative about the axis which is zero. This 3 second sample of data has an amplitude of 400V.

RMS or Root Mean Square is a technique for rectifying the RAW signal and converting it to an amplitude envelope, which is easier to view, to make it easier to view. The rectification process converts all the numbers into positive values rather than positive and negative. The RMS graph of the same 3 seconds of signal is shown below in Fig. 4.17.

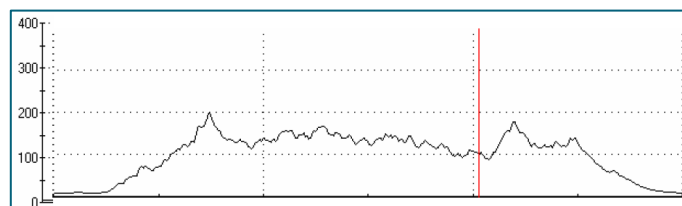


Fig. 4.17. RMS Signal

The RMS of a collection of n values $\{x_1, x_2, \dots, x_n\}$ is

$$x_{RMS} = \sqrt{\frac{1}{N} \sum_{i=1}^N x_i^2} = \sqrt{\frac{x_1^2 + x_2^2 + \dots + x_N^2}{N}}$$

The corresponding formula for a continuous function $f(t)$ defined over the interval $T_1 \leq t \leq T_2$ is

$$f_{RMS} = \sqrt{\frac{1}{T_2 - T_1} \cdot \int_{T_1}^{T_2} [f(t)]^2 dt}$$

And the RMS for a function over all time is

$$f_{RMS} = \lim_{T \rightarrow \infty} \sqrt{\frac{1}{2T} \int_{-T}^T [f(t)]^2 dt}$$

4.4.3. Time constant

RMS and Noise calculations are always performed through an average of the instantaneous voltages over a period of time called the Time Constant. The shorter the time constant, the closer the RMS value is to the instantaneous peak value.

The figures below illustrate the difference in peak signal sampling using two different time constants. In case of using $\tau_{RMS} = 1.2$ ms the width of the peak basis is circa 2000 samples (0.4 s at 5 kHz- Fig. 4.18), while using $\tau_{RMS} = 0.12$ ms it is circa 700 samples (0.14 s at 5 kHz – Fig. 4.19) [149].

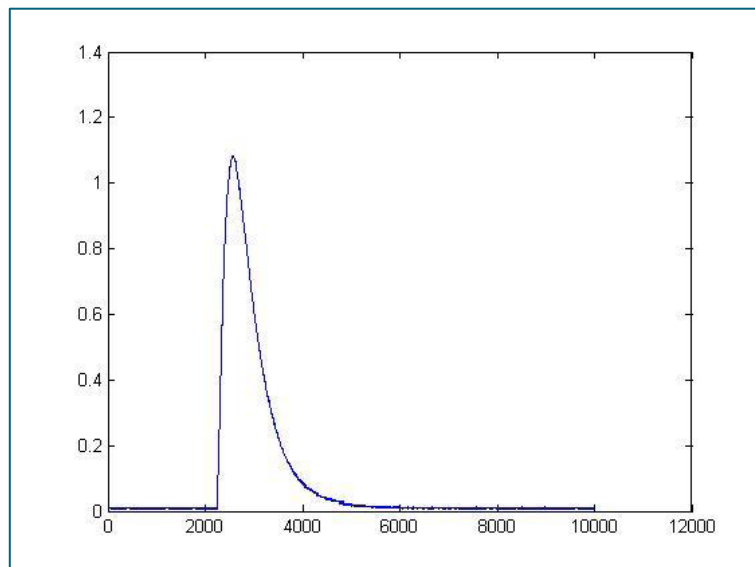


Fig. 4.18. Peak signal sampled with Time Constant $\tau_{RMS} = 1.2$ ms

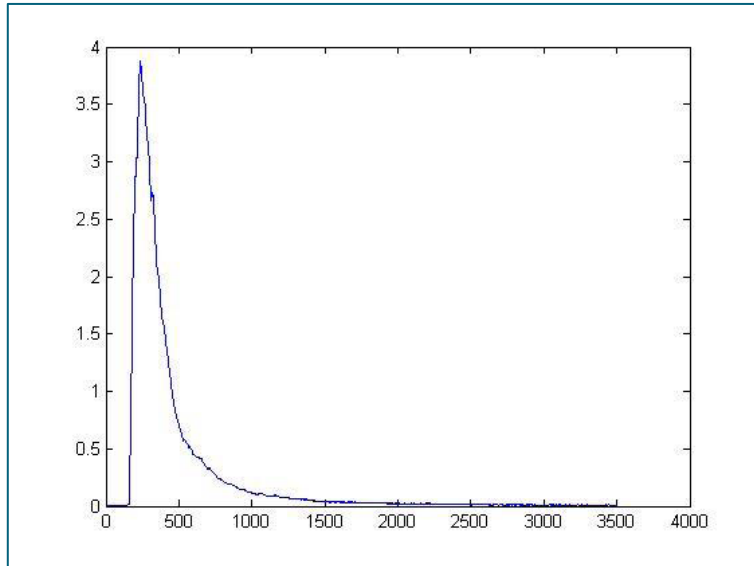


Fig. 4.19. Peak signal sampled with Time Constant $\tau_{RMS} = 0.12 \text{ ms}$

According to Nyquist theorem and taking into account the natural frequencies of the available equipment, and bearing in mind the purposes of this research, it has been decided to use as sampling frequency the following values:

Table 4.6. Sampling frequencies

Sensor Unit	Sampling Frequency
Cutting Forces	10 kHz
Acoustic Emission RMS	
Power	
Vibration	3 kHz

In this way it is possible to easily handle the arrays of data for all the application needed without any loss of quality in terms of precision and reliability.

4.5. Acquisition Software

For the Cutting Forces, Acoustic Emission and Power, the signal acquisition software is **LABview**.

For the vibration signal, the specific **VIBRALOG** software has been used.

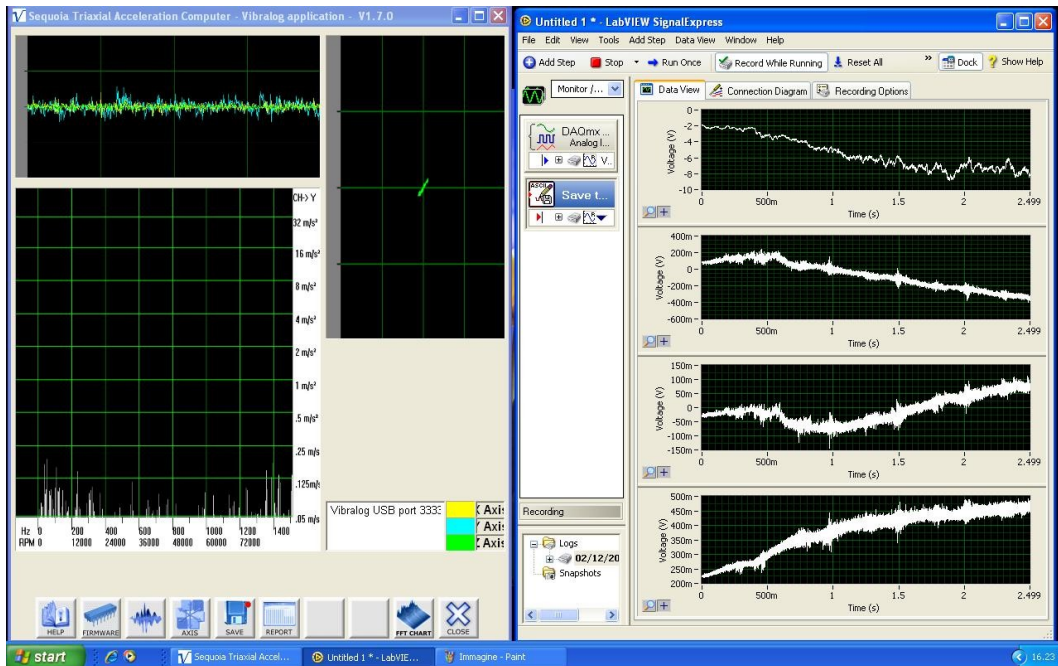


Fig. 4.20. Vibralog and Labview screenshotGeneral Scheme

In Fig. 4.21 a general schema of the multi sensor monitoring system applied to the machine tool is reported.

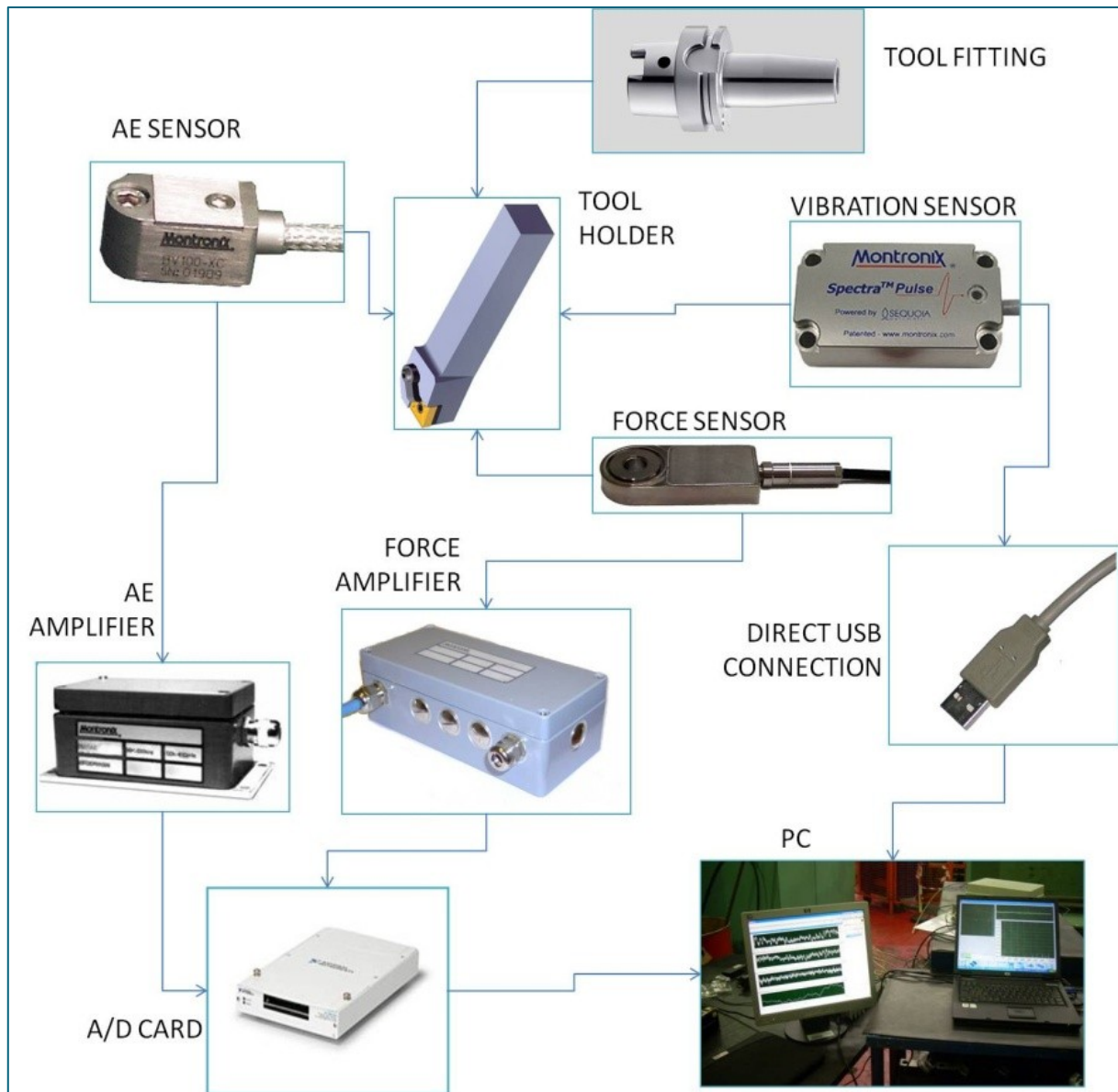
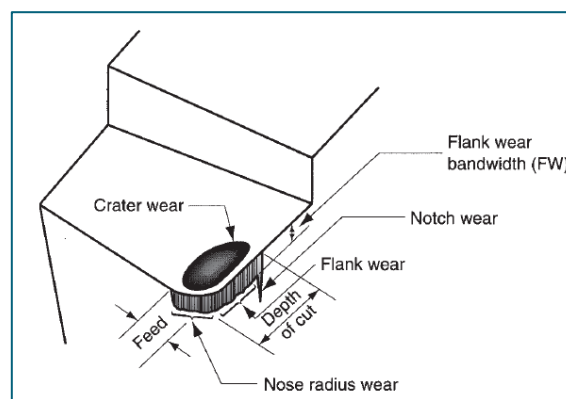


Fig. 4.21. Sensor Monitoring General Setup Scheme

5. Tool wear

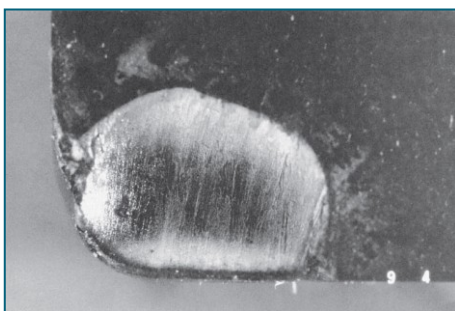
5.1. Generalities

Gradual wear occurs at two principal locations on a cutting tool: the top rake face and the flank. Accordingly, two main types of tool wear can be distinguished: crater wear and flank wear, illustrated in Figs. 5.1 and 5.2. A single-point tool is used to explain tool wear and the mechanisms that cause it. **Crater wear**, Fig. 5.2(a), consists of a cavity in the rake face of the tool that forms and grows from the action of the chip sliding against the surface. High stresses and temperatures characterize the tool–chip contact interface, contributing to the wearing action. The crater can be measured either by its depth or its area. **Flank wear**, Fig. 5.2(b), occurs on the flank, or relief face, of the tool. It results from rubbing between the newly generated work surface and the flank face adjacent to the cutting edge. **Flank wear** is measured by the width of the wear band, FW. This wear band is sometimes called the flank wear land [150].

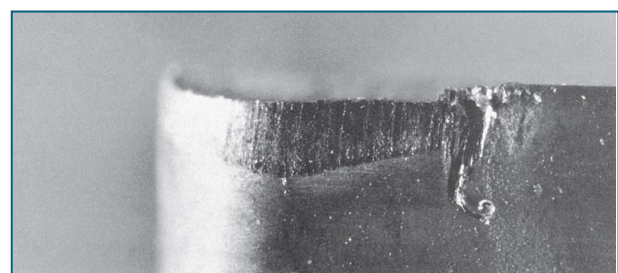


5.1. Diagram of worn cutting tool, showing the principal locations and types of wear that occur

Certain features of flank wear can be identified. First, an extreme condition of flank wear often appears on the cutting edge at the location corresponding to the original surface of the workpart. This is called notch wear. It occurs because the original work surface is harder and/or more abrasive than the internal material, which could be caused by work hardening from cold drawing or previous machining, sand particles in the surface from casting, or other reasons. As a consequence of the harder surface, wear is accelerated at this location. A second region of flank wear that can be identified is **nose radius wear**; this occurs on the nose radius leading into the end cutting edge.



(a)



(b)

Fig. 5.2. (a) Crater wear and (b) flank wear on a cemented carbide tool, as seen through a toolmaker's microscope. (Courtesy of Manufacturing Technology Laboratory, Lehigh University, photos by J. C. Keefe.)

The mechanisms that cause wear at the tool–chip and tool–work interfaces in machining can be summarized as follows:

- **Abrasion.** This is a mechanical wearing action caused by hard particles in the work material gouging and removing small portions of the tool. This abrasive action occurs in both flank wear and crater wear; it is a significant cause of flank wear.
- **Adhesion.** When two metals are forced into contact under high pressure and temperature, adhesion or welding occur between them. These conditions are present between the chip and the rake face of the tool. As the chip flows across the tool, small particles of the tool are broken away from the surface, resulting in attrition of the surface.
- **Diffusion.** This is a process in which an exchange of atoms takes place across a close contact boundary between two materials. In the case of tool wear, diffusion occurs at the tool-chip boundary, causing the tool surface to become depleted of the atoms responsible for its hardness. As this process continues, the tool surface becomes more susceptible to abrasion and adhesion. Diffusion is believed to be a principal mechanism of crater wear.
- **Chemical reactions.** The high temperatures and clean surfaces at the tool-chip interface in machining at high speeds can result in chemical reactions, in particular, oxidation, on the rake face of the tool. The oxidized layer, being softer than the parent tool material, is sheared away, exposing new material to sustain the reaction process.
- **Plastic deformation.** Another mechanism that contributes to tool wear is plastic deformation of the cutting edge. The cutting forces acting on the cutting edge at high temperature cause the edge to deform plastically, making it more vulnerable to abrasion of the tool surface. Plastic deformation contributes mainly to flank wear.

Most of these tool-wear mechanisms are accelerated at higher cutting speeds and temperatures. Diffusion and chemical reaction are especially sensitive to elevated temperature [150].

Tool life and the Taylor tool life equation

As cutting proceeds, the various wear mechanisms result in increasing levels of wear on the cutting tool. The general relationship of tool wear versus cutting time is shown in Fig. 5.3. Although the relationship shown is for flank wear, a similar relationship occurs for crater wear. Three regions can usually be identified in the typical wear growth curve. The first is the break-in period, in which the sharp cutting edge wears rapidly at the beginning of its use. This first region occurs within the first few minutes of cutting. The break-in period is followed by wear that occurs at a fairly uniform rate. This is called the steady-state wear region. In our figure, this region is pictured as a linear function of time, although there are deviations from the straight line in actual machining. Finally, wear reaches a level at which the wear rate begins to accelerate. This marks the beginning of the failure region, in which cutting temperatures are higher, and the general efficiency of the machining process is reduced. If allowed to continue, the tool finally fails by temperature failure.

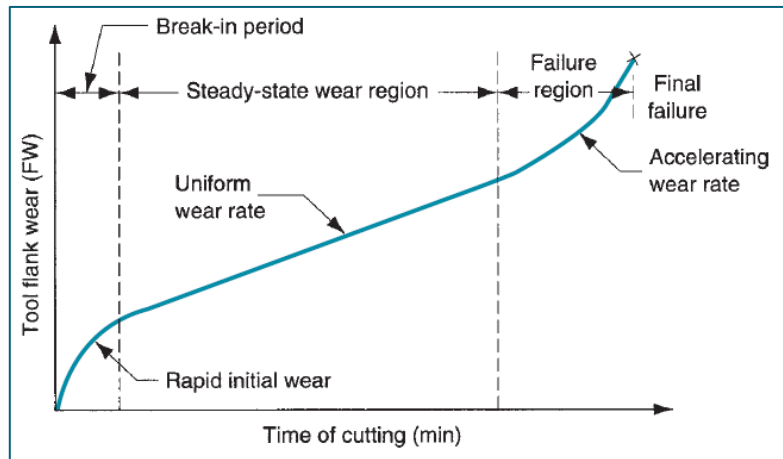


Fig. 5.3. Tool wear as a function of cutting time. Flank wear (FW) is used here as the measure of tool wear. Crater wear follows a similar growth curve.

The slope of the tool wear curve in the steady-state region is affected by work material and cutting conditions. Harder work materials cause the wear rate (slope of the tool wear curve) to increase. Increased speed, feed, and depth of cut have a similar effect, with speed being the most important of the three. If the tool wear curves are plotted for several different cutting speeds, the results appear as in Fig. 5.4. As cutting speed is increased, wear rate increases so the same level of wear is reached in less time.

Tool life is defined as the length of cutting time that the tool can be used. Operating the tool until final catastrophic failure is one way of defining tool life. This is indicated in Fig. 5.4. by the end of each tool wear curve. However, in production, it is often a disadvantage to use the tool until this failure occurs because of difficulties in sharpening the tool and problems with work surface quality. As an alternative, a level of tool wear can be selected as a criterion of tool life, and the tool is replaced when wear reaches that level. A convenient tool life criterion is a certain flank wear value, such as 0.5 mm, illustrated as the horizontal line on the graph. When each of the three wear curves intersects that line, the life of the corresponding tool is defined as ended. If the intersection points are projected down to the time axis, the values of tool life can be identified [150].

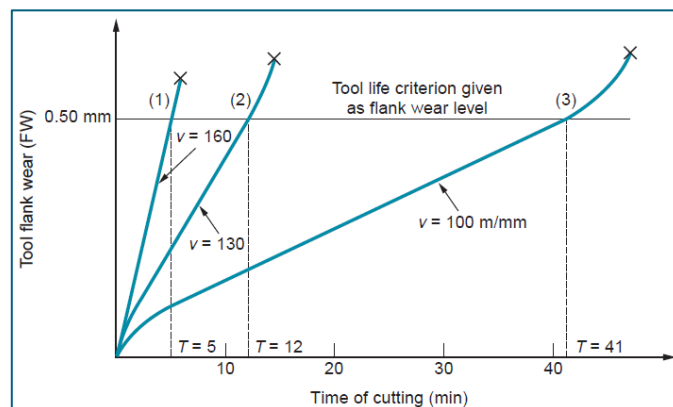


Fig. 5.4. Effect of cutting speed on tool flank wear for three cutting speeds. Hypothetical values of speed and tool life are shown for a tool life criterion of 0.50 mm flank wear

Taylor Tool Life Equation

If the tool life values for the three wear curves in Fig. 5.4. are plotted on a natural log–log graph of cutting speed versus tool life, the resulting relationship is a straight line as shown in Fig. 5.5. The

discovery of this relationship around 1900 is credited to F.W. Taylor. It can be expressed in equation form and is called the Taylor tool life equation:

$$vT^n = C \tag{5.1}$$

where v = cutting speed, m/min; T = tool life, min; and n and C are parameters whose values depend on feed, depth of cut, work material, tooling (material in particular), and the tool life criterion used.

The value of n is relative constant for a given tool material, whereas the value of C depends on tool material, work material, and cutting conditions.

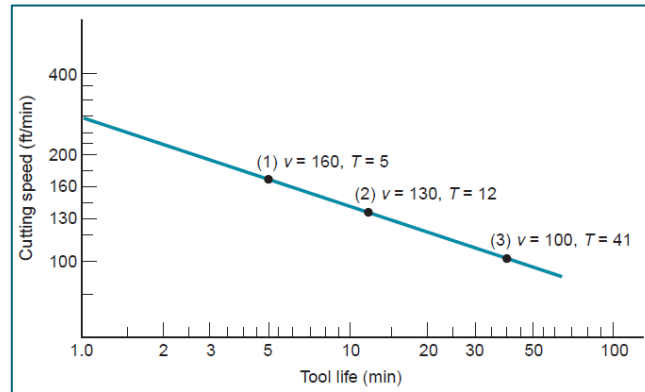


Fig. 5.5. Natural log-plot of cutting speed vs- tool life

Basically, Eq. 5.1 states that higher cutting speeds result in shorter tool lives. Relating the parameters n and C to Fig. 5.5, n is the slope of the plot (expressed in linear terms rather than in the scale of the axes), and C is the intercept on the speed axis. C represents the cutting speed that results in a 1-min tool life. The problem with Eq. 5.1 is that the units on the right-hand side of the equation are not consistent with the units on the left-hand side. To make the units consistent, the equation should be expressed in the form

$$vT^n = C(T_{ref}^n) \tag{5.2}$$

where T_{ref} = a reference value for C . T_{ref} is simply 1 min when m/min (ft/min) and minutes are used for v and T , respectively. The advantage of Eq. 5.2 is seen when it is desired to use the Taylor equation with units other than m/min (ft/min) and minutes—for example, if cutting speed were expressed as m/sec and tool life as sec. In this case, T_{ref} would be 60 sec and C would therefore be the same speed value as in Eq. 5.1, although converted to units of m/sec. The slope n would have the same numerical value as in Eq. 5.1.

An expanded version of Eq. 5.2 can be formulated to include the effects of feed, depth of cut, and even work material hardness:

$$vT^n f^m d^p H^q = K T_{ref}^n f_{ref}^m d_{ref}^p H_{ref}^q \tag{5.3}$$

where f = feed, mm; d = depth of cut, mm; H = hardness, expressed in an appropriate hardness scale; m , p , and q are exponents whose values are experimentally determined for the conditions of the operation; K = a constant analogous to C in Eq. 5.2; and f_{ref} , d_{ref} , and H_{ref} are reference values for feed, depth of cut, and hardness.

The values of m and p , the exponents for feed and depth, are less than 1.0. This indicates the greater effect of cutting speed on tool life, because the exponent of v is 1.0. After speed, feed is next in importance, so m has a value greater than p . The exponent for work hardness, q , is also less than 1.0.

Perhaps the greatest difficulty in applying Eq. 5.3 in a practical machining operation is the tremendous amount of machining data that would be required to determine the parameters of the equation. Variations in work materials and testing conditions also cause difficulties by introducing statistical variations in the data. Eq. 5.3 is valid in indicating general trends among its variables, but not in its ability to accurately predict tool life performance. To reduce these problems and make the scope of the equation more manageable, some of the terms are usually eliminated. For example, omitting depth and hardness reduces Eq. 5.3 to the following:

$$vT^n f^m = KT_{ref}^n f_{ref}^m \quad 5.4$$

where the terms have the same meaning as before, except that the constant K will have a slightly different interpretation.

Tool Life Criteria in Production

Although flank wear is the tool life criterion in our previous discussion of the Taylor equation, this criterion is not very practical in a factory environment because of the difficulties and time required to measure flank wear. Following are nine alternative tool life criteria that are more convenient to use in a production machining operation, some of which are admittedly subjective [150]:

- Complete failure of the cutting edge (fracture failure, temperature failure, or wearing until complete breakdown of the tool has occurred). This criterion has disadvantages, as discussed earlier.
- Visual inspection of flank wear (or crater wear) by the machine operator (without a toolmaker's microscope). This criterion is limited by the operator's judgment and ability to observe tool wear with the naked eye.
- Fingernail test across the cutting edge by the operator to test for irregularities.
- Changes in the sound emitting from the operation, as judged by the operator.
- Chips become ribbony, stringy, and difficult to dispose of.
- Degradation of the surface finish on the work.
- Increased power consumption in the operation, as measured by a wattmeter connected to the machine tool.
- Workpiece count. The operator is instructed to change the tool after a certain specified number of parts have been machined.
- Cumulative cutting time. This is similar to the previous workpiece count, except that the length of time the tool has been cutting is monitored. This is possible on machine tools controlled by computer; the computer is programmed to keep data on the total cutting time for each tool.

5.2. Tool wear measurement

[ISO 3685:1993 \(E\)](#)

Particles adhering to the flank directly under the wear land can give the appearance of a larger width of the wear land. Also a deposit in the crater results in lower values of the crater depth. Loose material shall be removed carefully but chemical etchants shall not be used except at the end of the test.

For the purpose of the wear measurements, the major cutting edge is considered to be divided into four zones as shown in Fig. 5.6.

- **Zone C** is the curved part of the cutting edge at the tool corner.
- **Zone B** is the remaining straight part of the cutting edge between zone C and zone A.
- **Zone A** is the quarter of the worn cutting edge length b farthest away from the tool corner.
- **Zone N** extends beyond the area of mutual contact between the tool and workpiece for approximately 1 mm to 2 mm along the major cutting edge. The wear is of notch type.

The width of the flank wear land VB_B shall be measured within zone B in the tool cutting edge plane P_s (the plane containing the major cutting edge and the assumed direction of primary motion) perpendicular to the major cutting edge. The width of the flank wear land shall be measured from the position of the original major cutting edge [151].

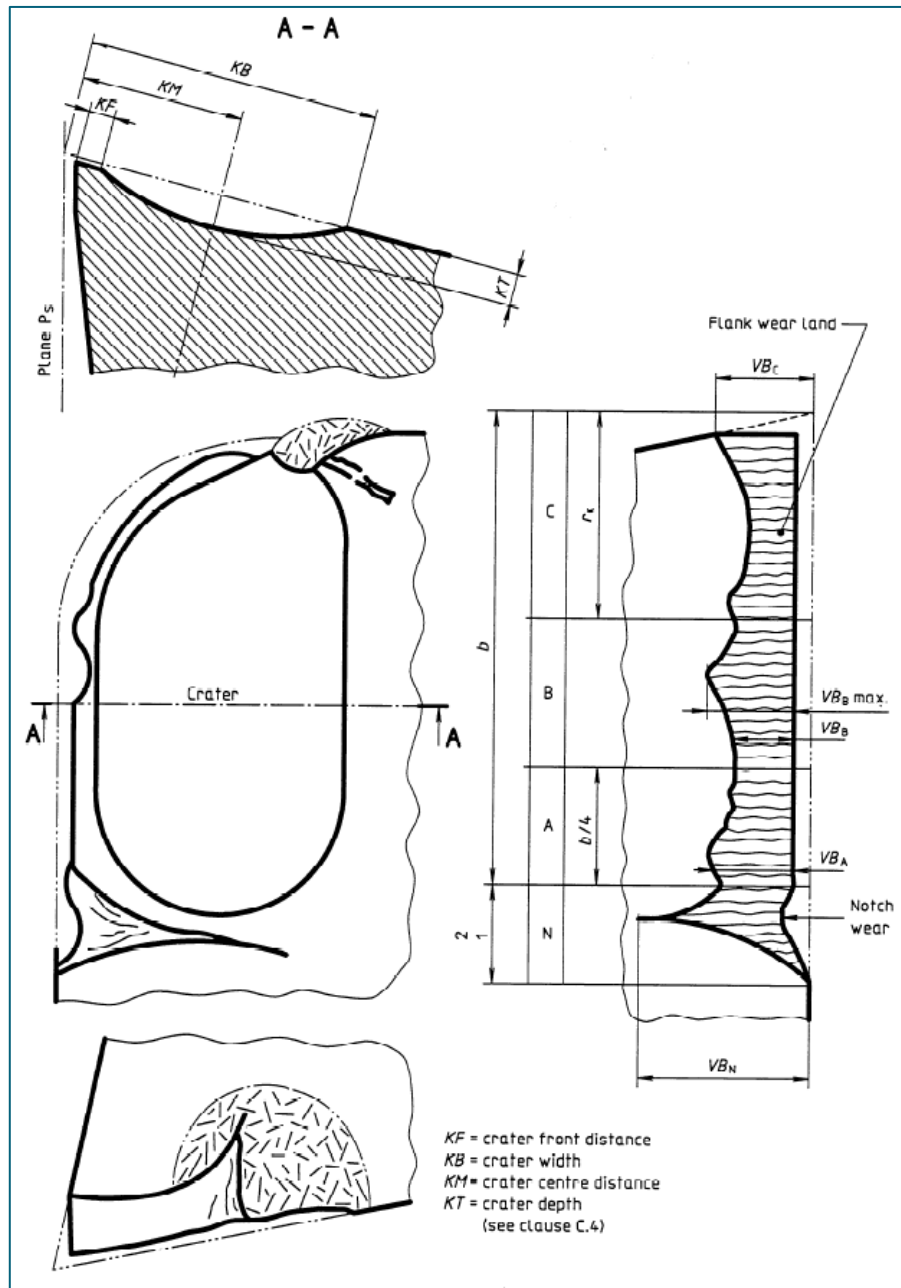
Flank wear

This is the best known type of tool wear (Fig. 5.6). In many cases the flank wear land has a rather uniform width along the middle portion of the straight part of the major cutting edge. The width of the flank wear land is relatively easy to measure. The growing width of the flank wear land leads to a reduction in the quality of the tool. All cutting tool materials normally have a high initial rate of flank wear which usually decreases considerably after a short time of cutting, unless excessive cutting speeds are used. The flank wear of high-speed steel frequently develops differently from the wear of sintered carbide and ceramic tools.

High-speed steel tools may have prolonged periods of very little measurable increase of flank wear. This phenomenon occurs especially at low cutting speeds when machining ductile materials. At higher cutting speeds the increase of flank wear of all cutting tool materials is usually approximately uniform, subsequent to the initial high wear rate. The final portion of the flank wear versus time graph often shows an accelerated rate of wear which leads to catastrophic failure. The width of the flank wear land VB_{max} . (Fig. 5.6) is a suitable tool wear measure and a predetermined value of VB_{max} . is regarded as a good tool-life criterion [151].

Notch wear

This is a special type of combined flank and face wear which occurs adjacent to, but outside, the point where the major cutting edge intersects the work surface, and may under certain circumstances make the change of tools necessary. The profile and the length of the wear notch VB_N (Fig. 5.6) depend to a great extent on the accuracy of repeated depth settings. For these reasons the notch wear is excluded from the evaluation of the width of the flank wear land (see 8.3). In special cases where the notch wear is predominant over all other tool wear phenomena, the length of the wear notch may be used as the tool wear measure. In such cases the value for VB_B may be used as the tool-life criterion [151].



5.6. Some types of wear on turning tool

Wear of the face

Crater wear is the most commonly occurring type of face wear. The depth of the crater KT (Fig. 5.6) may be used as a tool wear measure and a predetermined value of KT may be selected as a tool-life criterion. Crater wear is more important for carbide tools than for ceramic and high-speed steel. The position of the crater relative to the cutting edge has also some importance. A deep, wide crater far away from the cutting edge can be less dangerous to the tool than a less deep, narrow crater close to the cutting edge.

The distance from the front edge of the crater to the major cutting edge is sometimes a useful criterion which if limited can eliminate catastrophic failure. This is one of the reasons why the values for KT as a tool-life criterion are given in relation to the feed. For special purposes, the crater centre distance KM and the crater width KB may be measured as additional information. However, they should not be used as tool-life criteria.

The crater centre distance KM (the distance between the original major cutting edge and the deepest point of the crater) is measured in zone B parallel to the face and perpendicular to the major cutting edge (Fig. 5.6).

The crater width KB (the distance between the original major cutting edge and the rear side of the crater) is measured parallel to the face in zone B and perpendicular to the major cutting edge (Fig. 5.6). As the crater centre distance KM depends not only on feed but also on work material and tool material, the crater ratio $K = \frac{KT}{KM}$ is sometimes calculated.

A chosen value may then be used as the tool-life criterion and the value K approximately 0.1 is recommended [151].

5.3. Tool wear measurement during experimental tests

In order to built tool wear curves development it is necessary to carry out tool wear measurement after every 2 minutes turning step.

It has been chosen as tool life criteria, the VB_{max} value, it means the maximum value of flank wear as explained in § 5.2. The maximum acceptable value was set at 0.3 mm for standard tests and 0.5 mm for severe conditions cutting tests.

The first step for tool wear measurement is to remove the tool insert from the tool holder on the lathe, and clean it to remove chip parts.

The insert is then positioned in an identical tool holder located on the profile projector..

Then, the insert is enlightened by two radial light (Fig.5.7) in a dark environment.

On the profile projector screen, the enlarged image of the tool flank is visualized. A correct visualization depends on the adjustment of the two radial lights.

Once the tool is positioned and enlightened adjustment is done, the measuring starting point, zero, is set in correspondence of the top edge of the insert, as shown in Fig 5.8.

By a joystick the system is moved until the flank wear lower edge is reached and the measurement is recorded.

By repeating this procedure after every turning step, it is possible to track the tool wear curves development for every experimental test.

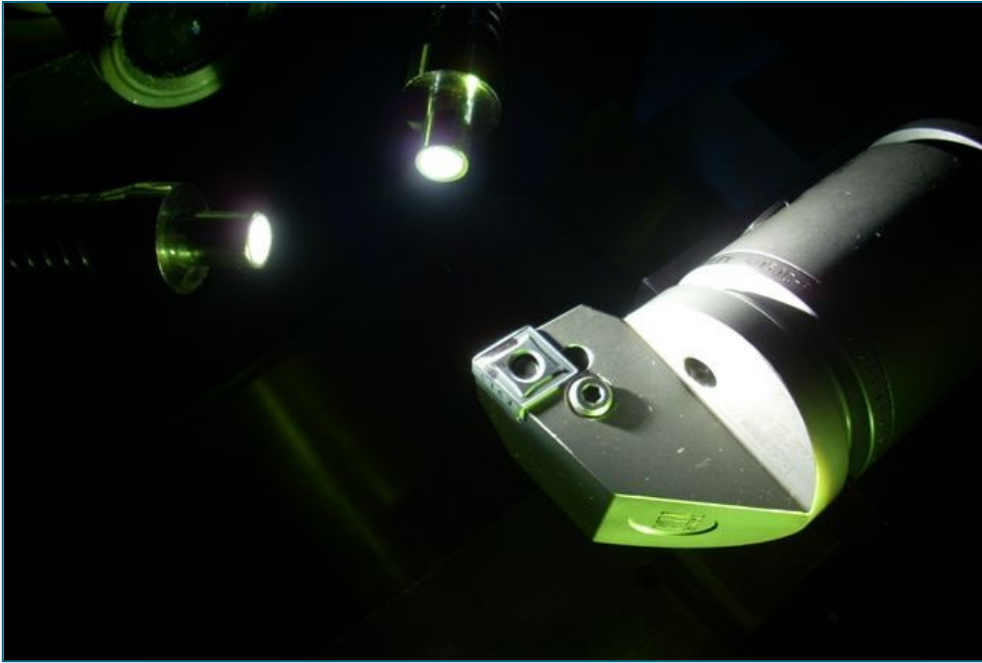


Fig. 5.7. Cutting tool positioned in the profile projector

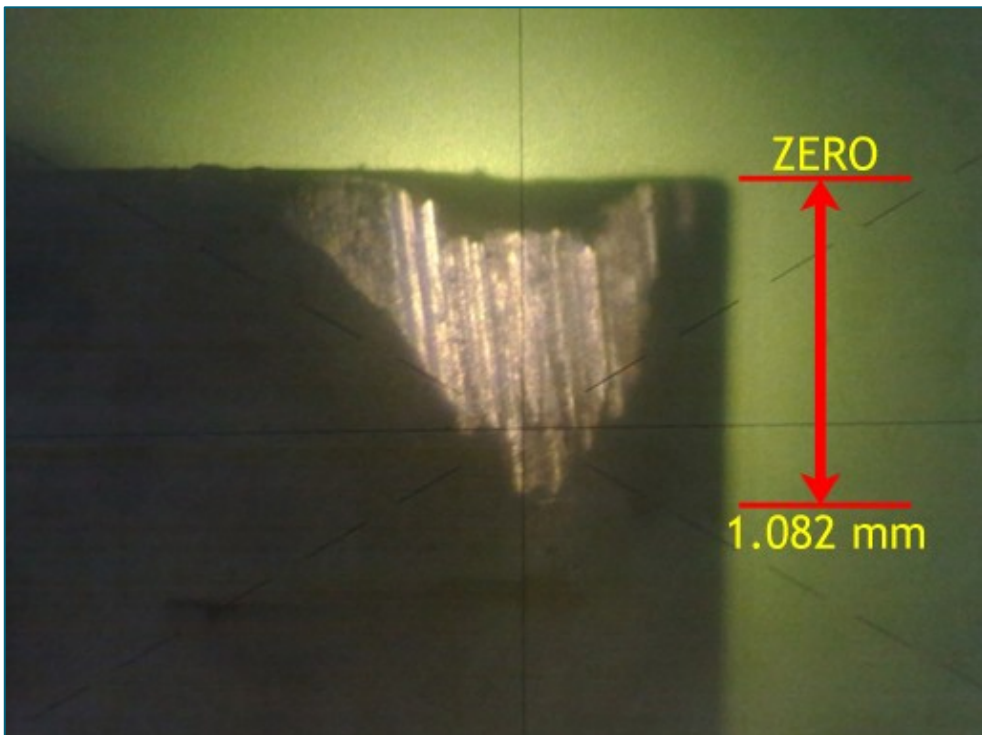


Fig. 5.8. Tool flank wear VBmax as visualized on the profile projector screen, for T8_H test.

5.4. Tool wear measurement reports

Test #1

Test #1				
	Vc	45	m/min	
	f	0.1	mm/rev	
	ap	0.3	mm	
	Z	28.5	mm	
Step	n (rev/min)	D (mm)	T (s)	VBmax (mm)
1	140	102.4	120	0.083
2	141	101.8	240	0.129
3	142	101.2	360	0.146
4	142	100.6	480	0.160
5	143	100	600	0.172
6	144	99.4	720	0.186
7	145	98.8	840	0.202
8	146	98.2	960	0.215
9	147	97.6	1080	0.229
10	148	97	1200	0.239
11	149	96.4	1320	0.253
12	150	95.8	1440	0.267
13	150	95.2	1560	0.285
14	151	94.6	1680	0.301

Test #1r

Test #1r				
	Vc	45	m/min	
	f	0.1	mm/rev	
	ap	0.3	mm	
	Z	34.5	mm	
Step	n (rev/min)	D (mm)	T (s)	VBmax (mm)
1	170	84.25	120	0.108
2	171	83.65	240	0.132
3	172	83.05	360	0.143
4	174	82.45	480	0.156
5	175	81.85	600	0.171
6	176	81.25	720	0.180
7	178	80.65	840	0.188
8	179	80.05	960	0.195
9	180	79.45	1080	0.203
10	182	78.85	1200	0.220
11	183	78.25	1320	0.231
12	184	77.65	1440	0.244
13	186	77.05	1560	0.256
14	187	76.45	1680	0.273
15	189	75.85	1800	0.300

Test #2

	Vc	45 m/min		
	f	0.125 mm/rev		
	ap	0.3 mm		
	Z	35.5 mm		
Step	n (rev/min)	D (mm)	T (s)	VBmax (mm)
1	140	102.4	120	0.100
2	141	101.8	240	0.136
3	142	101.2	360	0.152
4	142	100.6	480	0.170
5	143	100	600	0.184
6	144	99.4	720	0.192
7	145	98.8	840	0.203
8	146	98.2	960	0.214
9	147	97.6	1080	0.223
10	148	97	1200	0.242
11	149	96.4	1320	0.256
12	150	95.8	1440	0.270
13	150	95.2	1560	0.285
14	151	94.6	1680	0.310

Test #2r

	Vc	45 m/min		
	f	0.125 mm/rev		
	ap	0.3 mm		
	Z	43 mm		
Step	n (rev/min)	D (mm)	T (s)	VBmax (mm)
1	170	84.25	120	0.112
2	171	83.65	240	0.128
3	172	83.05	360	0.144
4	174	82.45	480	0.159
5	175	81.85	600	0.178
6	176	81.25	720	0.185
7	178	80.65	840	0.191
8	179	80.05	960	0.206
9	180	79.45	1080	0.215
10	182	78.85	1200	0.230
11	183	78.25	1320	0.242
12	184	77.65	1440	0.256
13	186	77.05	1560	0.278
14	187	76.45	1680	0.300

Test #3

Vc	45 m/min			
f	0.15 mm/rev			
ap	0.3 mm			
Z	42.5 mm			
Step	n (rev/min)	D (mm)	T (s)	VBmax (mm)
1	140	102.4	120	0.104
2	141	101.8	240	0.138
3	142	101.2	360	0.157
4	142	100.6	480	0.170
5	143	100	600	0.188
6	144	99.4	720	0.210
7	145	98.8	840	0.224
8	146	98.2	960	0.248
9	147	97.6	1080	0.262
10	148	97	1200	0.289
11	149	96.4	1320	0.306

Test #3r

Vc	45 m/min			
f	0.15 mm/rev			
ap	0.3 mm			
Z	39 mm			
Step	n (rev/min)	D (mm)	T (s)	Vbmax (mm)
1	130	110.25	120	0.107
2	131	109.65	240	0.132
3	131	109.05	360	0.156
4	132	108.45	480	0.179
5	133	107.85	600	0.192
6	134	107.25	720	0.226
7	134	106.65	840	0.249
8	135	106.05	960	0.280
9	136	105.45	1080	0.300

Test #4

Vc	50 m/min			
f	0.1 mm/rev			
ap	0.3 mm			
Z	40 mm			
Step	n (rev/min)	D (mm)	T (s)	VBmax (mm)
1	x	x	120	0.120
2	x	x	240	0.132
3	x	x	360	0.154
4	x	x	480	0.176
5	x	x	600	0.205
6	x	x	720	0.224
7	x	x	840	0.232
8	x	x	960	0.250
9	x	x	1080	0.276
10	x	x	1200	0.307

Test #4r

Vc	50 m/min			
f	0.1 mm/rev			
ap	0.3 mm			
Z	31.5 mm			
Step	n (rev/min)	D (mm)	T (s)	Vbmax (mm)
1	155	102.4	120	0.122
2	156	101.8	240	0.151
3	157	101.2	360	0.181
4	158	100.6	480	0.203
5	159	100	600	0.222
6	160	99.4	720	0.253
7	161	98.8	840	0.281
8	162	98.2	960	0.313

Test #4rr

Vc	50 m/min			
f	0.1 mm/rev			
ap	0.3 mm			
Z	28.8 mm			
Step	n (rev/min)	D (mm)	T (s)	Vbmax (mm)
1	144	110.25	120	0.110
2	145	109.65	240	0.132
3	146	109.05	360	0.166
4	147	108.45	480	0.194
5	148	107.85	600	0.225
6	148	107.25	720	0.249
7	149	106.65	840	0.278
8	150	106.05	960	0.303

Test #5

Vc	50 m/min			
f	0.125 mm/rev			
ap	0.3 mm			
Z	50 mm			
Step	n (rev/min)	D (mm)	T (s)	Vbmax (mm)
1	x	x	120	0.126
2	x	x	240	0.150
3	x	x	360	0.164
4	x	x	480	0.192
5	x	x	600	0.232
6	x	x	720	0.268
7	x	x	840	0.292
8	x	x	960	0.332

Test #5r

Vc	50 m/min			
f	0.125 mm/rev			
ap	0.3 mm			
Z	43.5 mm			
Step	n (rev/min)	D (mm)	T (s)	Vbmax (mm)
1	173	92.05	120	0.101
2	174	91.45	240	0.128
3	175	90.85	360	0.147
4	176	90.25	480	0.177
5	178	89.65	600	0.200
6	179	89.05	720	0.230
7	180	88.45	840	0.263
8	181	87.85	960	0.308

Test #6

Vc	50 m/min			
f	0.15 mm/rev			
ap	0.3 mm			
Z	59.5 mm			
Step	n (rev/min)	D (mm)	T (s)	Vbmax (mm)
1	x	x	120	0.114
2	x	x	240	0.142
3	x	x	360	0.175
4	x	x	480	0.212
5	x	x	600	0.250
6	x	x	720	0.286
7	x	x	840	0.315

Test #6r

Vc	50 m/min			
f	0.15 mm/rev			
ap	0.3 mm			
Z	52 mm			
Step	n (rev/min)	D (mm)	T (s)	Vbmax (mm)
1	173	92.05	120	0.136
2	174	91.45	240	0.187
3	175	90.85	360	0.222
4	176	90.25	480	0.256
5	178	89.65	600	0.301

Test #7

Vc	55 m/min			
f	0.1 mm/rev			
ap	0.3 mm			
Z	44 mm			
Step	n (rev/min)	D (mm)	T (s)	VBmax (mm)
1	x	x	120	0.131
2	x	x	240	0.154
3	x	x	360	0.173
4	x	x	480	0.217
5	x	x	600	0.243
6	x	x	720	0.282
7	x	x	840	0.318

Test #7r

Vc	55 m/min			
f	0.1 mm/rev			
ap	0.3 mm			
Z	38.5 mm			
Step	n (rev/min)	D (mm)	T (s)	VBmax (mm)
1	190	92.05	120	0.161
2	191	91.45	240	0.223
3	193	90.85	360	0.278
4	194	90.25	480	0.349

Test #7rr

Vc	55 m/min			
f	0.1 mm/rev			
ap	0.3 mm			
Z	35 mm			
Step	n (rev/min)	D (mm)	T (s)	VBmax (mm)
1	173	101.37	120	0.128
2	174	100.77	240	0.171
3	175	100.17	360	0.229
4	176	99.57	480	0.282
5	177	98.97	600	0.326

Test #8

Vc	55 m/min			
f	0.125 mm/rev			
ap	0.3 mm			
Z	52 mm			
Step	n (rev/min)	D (mm)	T (s)	VBmax (mm)
1	206	85.1	120	0.108
2	207	84.5	240	0.205
3	209	83.9	360	0.262
4	210	83.3	480	0.320

Test #8r

Vc	55 m/min			
f	0.125 mm/rev			
ap	0.3 mm			
Z	48 mm			
Step	n (rev/min)	D (mm)	T (s)	VBmax (mm)
1	190	92.05	120	0.192
2	191	91.45	240	0.261
3	193	90.85	360	0.316

Test #8rr

Vc	55 m/min			
f	0.125 mm/rev			
ap	0.3 mm			
Z	43.5 mm			
Step	n (rev/min)	D (mm)	T (s)	VBmax (mm)
1	173	101.37	120	0.181
2	174	100.77	240	0.257
3	175	100.17	360	0.329

Test #9

Vc	55 m/min			
f	0.125 mm/rev			
ap	0.3 mm			
Z	62 mm			
Step	n (rev/min)	D (mm)	T (s)	VBmax (mm)
1	206	85.1	120	0.200
2	207	84.5	240	0.283
3	209	83.9	360	0.363

Test #9r

Vc	55 m/min			
f	0.15 mm/rev			
ap	0.3 mm			
Z	52 mm			
Step	n (rev/min)	D (mm)	T (s)	VBmax (mm)
1	173	101.37	120	0.252
2	174	100.77	240	0.332

Test #9rr

Vc	55 m/min			
f	0.15 mm/rev			
ap	0.3 mm			
Z	48 mm			
Step	n (rev/min)	D (mm)	T (s)	VBmax (mm)
1	159	110.43	120	0.223
2	159	109.83	240	0.305

On the basis of the tool wear measurements listed above, it was possible to draw the tool wear curves development, as reported in Fig. 5.9 for Standard Tests

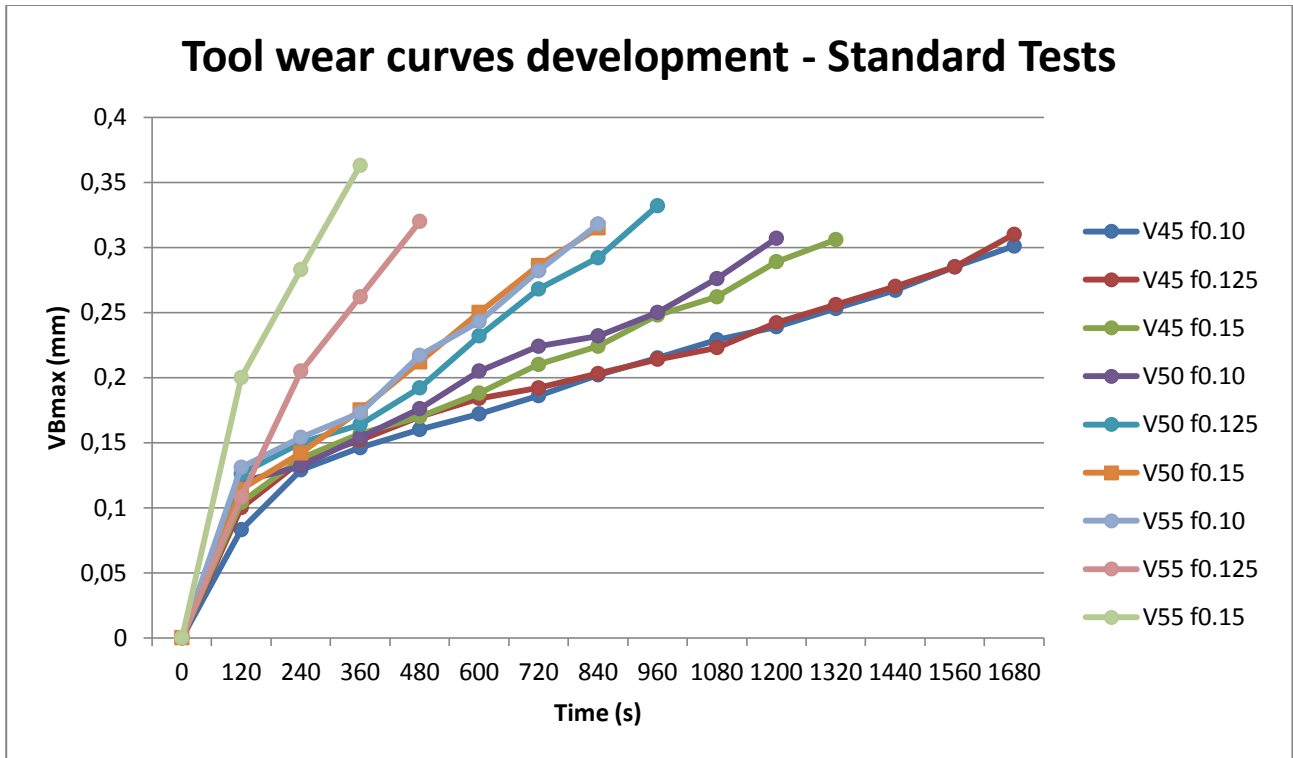


Fig. 5.9. Tool wear curves for standard tests

Test #1H

Vc	80 m/min	Fluid: on		
f	0.15 mm/rev			
ap	0.3 mm			
Z	17.4 mm			
Step	n (rev/min)	D (mm)	T (s)	VBmax (mm)
1	231	110.25	30	0.198
2	232	109.65	60	0.278
3	234	109.05	90	0.345
4	235	108.45	120	0.437
5	236	107.85	150	0.557

Test #2H

Vc	80 m/min	Fluid: on		
f	0.3 mm/rev			
ap	0.3 mm			
Z	34.7 mm			
Step	n (rev/min)	D (mm)	T (s)	VBmax (mm)
1	231	110.25	30	0.230
2	232	109.65	60	0.305
3	234	109.05	90	0.415
4	235	108.45	120	0.540

Test #3H

Vc	100 m/min	Fluid: on		
f	0.15 mm/rev			
ap	0.3 mm			
Z	21.7 mm			
Step	n (rev/min)	D (mm)	T (s)	VBmax (mm)
1	289	110.25	30	0.285
2	290	109.65	60	0.348
3	292	109.05	90	0.865

Test #4H

Vc	100 m/min	Fluid: on		
f	0.3 mm/rev			
ap	0.3 mm			
Z	43.4 mm			
Step	n (rev/min)	D (mm)	T (s)	VBmax (mm)
1	289	110.25	30	0.593
2	290	109.65	60	0.765

Test #5H

Vc	80 m/min	Fluid: off		
f	0.15 mm/rev			
ap	0.3 mm			
Z	17.4 mm			
Step	n (rev/min)	D (mm)	T (s)	VBmax (mm)
1	231	110.25	30	0.198
2	232	109.65	60	0.280
3	234	109.05	90	0.390
4	235	108.45	120	0.507

Test #6H

Vc	80 m/min	Fluid: off		
f	0.3 mm/rev			
ap	0.3 mm			
Z	34.7 mm			
Step	n (rev/min)	D (mm)	T (s)	VBmax (mm)
1	231	110.25	30	0.244
2	232	109.65	60	0.304
3	234	109.05	90	0.378
4	235	108.45	120	0.601

Test #7H

Vc	100 m/min	Fluid: off		
f	0.15 mm/rev			
ap	0.3 mm			
Z	21.7 mm			
Step	n (rev/min)	D (mm)	T (s)	VBmax (mm)
1	289	110.25	30	0.285
2	290	109.65	60	0.348
3	292	109.05	90	0.865

Test #8H

Vc	100 m/min	Fluid: off		
f	0.3 mm/rev			
ap	0.3 mm			
Z	43.4 mm			
Step	n (rev/min)	D (mm)	T (s)	VBmax (mm)
1	289	110.25	30	1.082

On the basis of the tool wear measurements listed above, it was possible to draw the tool wear curves development, for Severe Cutting Conditions Tests, as reported in Fig. 5.10 and Fig. 5.11 for cooled tests and dry tests respectively.

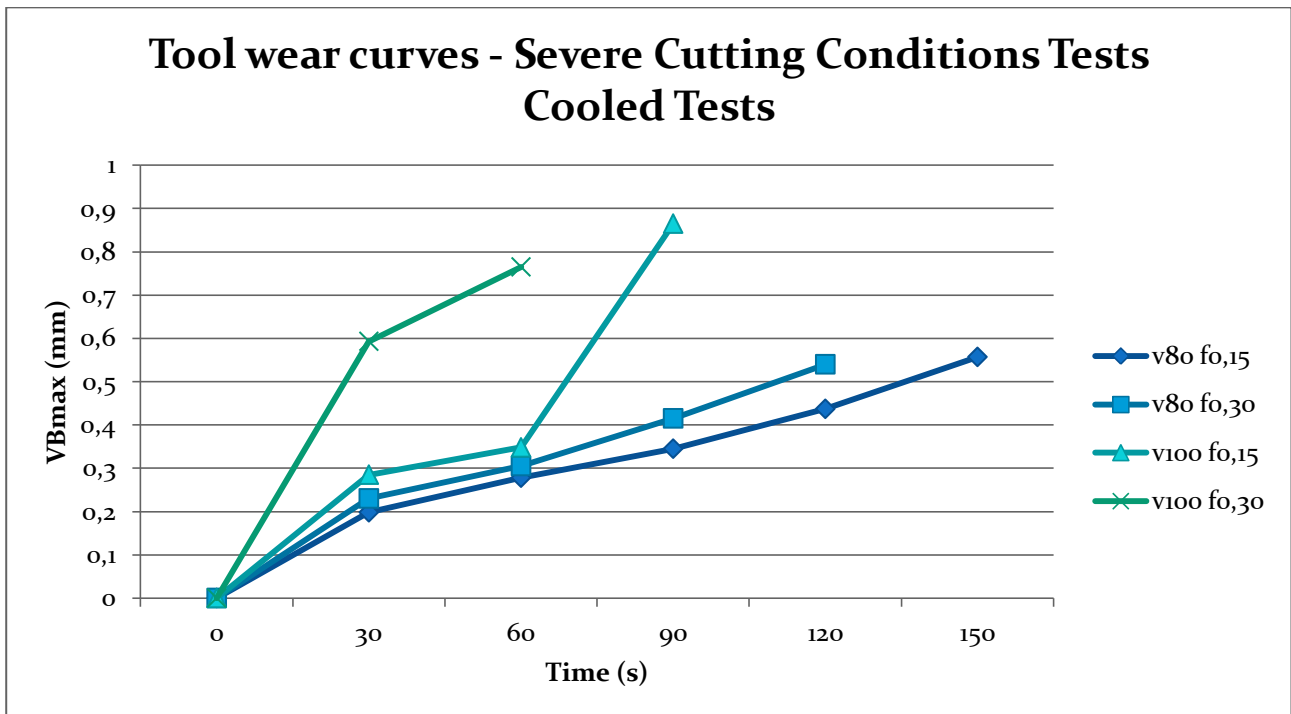


Fig. 5.10. Tool wear curves for Severe Conditions Cutting Tests (Cooled Tests)

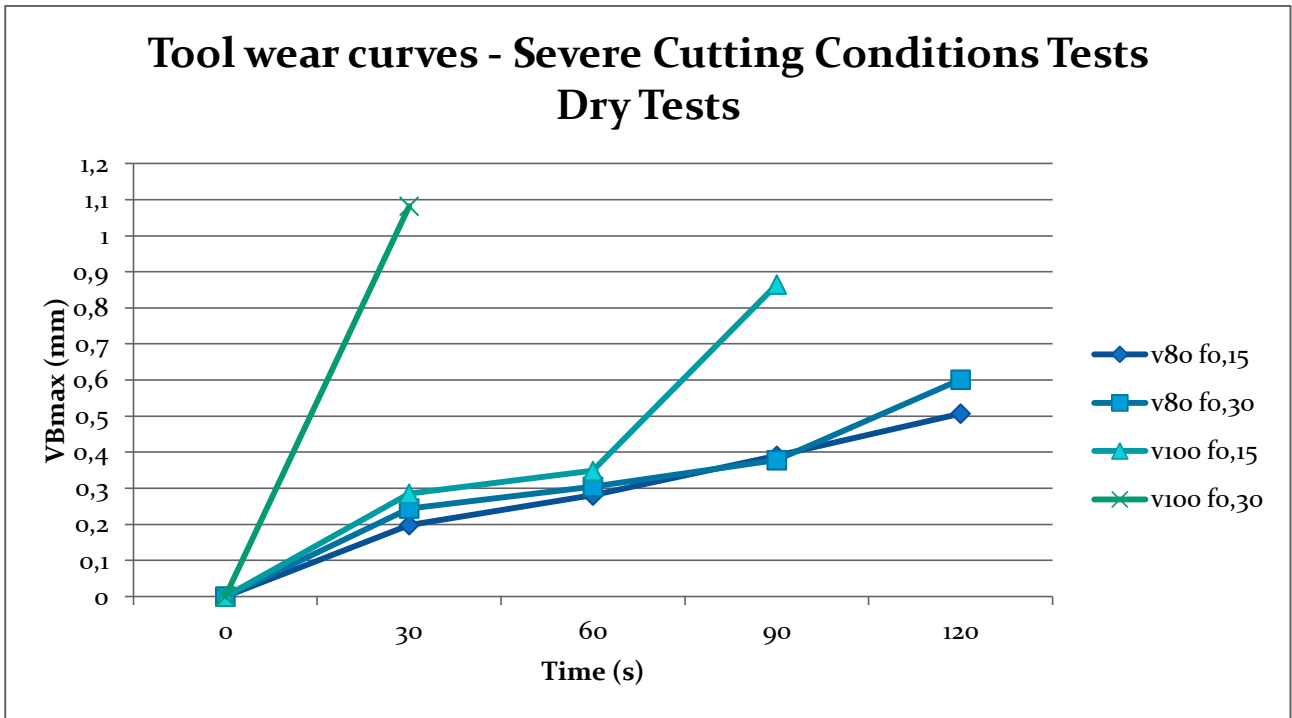


Fig. 5.11. Tool wear curves for Severe Conditions Cutting Tests (Dry Tests)

6. Residual stress measurement

6.1. Residual stress in machining

It is probably true to say that all engineering components contain stresses (of variable magnitude and sign) before being subjected to service loading conditions owing to the history of the material prior to such service. These stresses, produced as a result of mechanical working of the material, heat treatment, chemical treatment, joining procedure, etc., are termed residual stresses and they can have a very significant effect on the fatigue life of components. These residual stresses are “locked into” the component in the absence of external loading and represent a datum stress over which the service load stresses are subsequently superimposed. If, by fortune or design, the residual stresses are of opposite sign to the service stresses then part of the service load goes to reduce the residual stress to zero before the combined stress can again rise towards any likely failure value; such residual stresses are thus extremely beneficial to the strength of the component and significantly higher fatigue strengths can result. If, however, the residual stresses are of the same sign as the applied stress, e.g. both tensile, then a smaller service load is required to produce failure than would have been the case for a component with a zero stress level initially; the strength and fatigue life in this case is thus reduced. Thus, both the magnitude and sign of residual stresses are important to fatigue life considerations, and methods for determining these quantities are introduced below [152].

6.2. X-ray diffraction technique

[\[PAUL S. PREVÉY, LAMBDA RESEARCH, INC\]](#)

In x-ray diffraction residual stress measurement, the strain in the crystal lattice is measured, and the residual stress producing the strain is calculated, assuming a linear elastic distortion of the crystal lattice. Although the term stress measurement has come into common usage, stress is an extrinsic property that is not directly measurable. All methods of stress determination require measurement of some intrinsic property, such as strain or force and area, and the calculation of the associated stress. Mechanical methods (dissection techniques) and nonlinear elastic methods (ultrasonic and magnetic techniques) are limited in their applicability to residual stress determination. Mechanical methods are limited by assumptions concerning the nature of the residual stress field and sample geometry. Mechanical methods, being necessarily destructive, cannot be directly checked by repeat measurement. Spatial and depth resolution are All nonlinear elastic methods are subject to major error from preferred orientation, cold work, temperature, and grain size. All require stress-free reference samples, which are otherwise identical to the sample under investigation. Nonlinear elastic methods are generally not suitable for routine residual stress determination at their current state of development. In addition, their spatial and depth resolutions are orders of magnitude less than those of x-ray diffraction.

To determine the stress, the strain in the crystal lattice must be measured for at least two precisely known orientations relative to the sample surface. Therefore, xray diffraction residual stress measurement is applicable to materials that are crystalline, relatively fine grained, and produce diffraction for any orientation of the sample surface. Samples may be metallic or ceramic, provided a diffraction peak of suitable intensity and free of interference from neighboring peaks can be produced in the high back-reflection region with the radiations available. X-ray diffraction residual stress measurement is unique in that macroscopic and microscopic residual stresses can be determined nondestructively [153].

Macroscopic stresses, or macrostresses, which extend over distances that are large relative to the grain size of the material, are of general interest in design and failure analysis. Macrostresses are tensor quantities, with magnitudes varying with direction at a single point in a body. The macrostress for a given location and direction is determined by measuring the strain in that direction at a single point. When macrostresses are determined in at least three known directions, and a condition of plane stress is assumed, the three stresses can be combined using Mohr's circle for stress to determine the maximum and minimum residual stresses, the maximum shear stress, and their orientation relative to a reference direction. Macrostresses strain many crystals uniformly in the surface. This uniform distortion of the crystal lattice shifts the angular position of the diffraction peak selected for residual stress measurement.

Microscopic stresses, or microstresses, are scalar properties of the sample, such as percent of cold work or hardness, that are without direction and result from imperfections in the crystal lattice. Microstresses are associated with strains within the crystal lattice that traverse distances on the order of or less than the dimensions of the crystals. Microstresses vary from point to point within the crystal lattice, altering the lattice spacing and broadening the diffraction peak. Macrostresses and microstresses can be determined separately from the diffraction peak position and breadth.

Fig. 6.1 shows the diffraction of a monochromatic beam of x-rays at a high diffraction angle (2θ) from the surface of a stressed sample for two orientations of the sample relative to the x-ray beam. The angle ψ , defining the orientation of the sample surface, is the angle between the normal of the surface and the incident and diffracted beam bisector, which is also the angle between the normal to the diffracting lattice planes and the normal to sample surface [153].

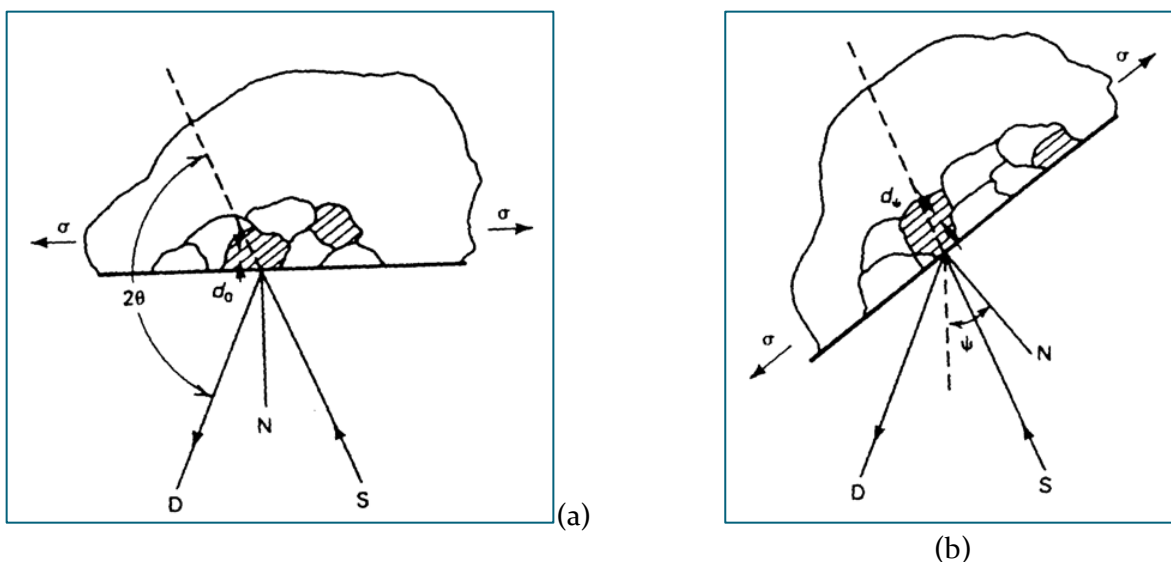


Fig. 6.1. (a) $\psi = 0$. (b) $\psi = \psi$ (sample rotated through some known angle ψ).
D, x-ray detector; S, x-ray source; N, normal to the surface.

Diffraction occurs at an angle 2θ , defined by Bragg's Law: $n\lambda = 2d \sin \theta$, where n is an integer denoting the order of diffraction, λ is the x-ray wavelength, d is the lattice spacing of crystal planes, and θ is the diffraction angle. For the monochromatic x-rays produced by the metallic target of an x-ray tube, the wavelength is known to 1 part in 10⁵. Any change in the lattice spacing, d , results in a corresponding shift in the diffraction angle 2θ .

Fig. 6.1 (a) shows the sample in the $\psi = 0$ orientation. The presence of a tensile stress in the sample results in a Poisson's ratio contraction, reducing the lattice spacing and slightly increasing the diffraction angle, 2θ . If the sample is then rotated through some known angle ψ (Fig.6.1(b)), the tensile stress present in the surface increases the lattice spacing over the stress-free state and decreases 2θ . Measuring the change in the angular position of the diffraction peak for at least two orientations of the sample defined by the angle ψ enables calculation of the stress present in the sample surface lying in the plane of diffraction, which contains the incident and diffracted x-ray beams. To measure the stress in different directions at the same point, the sample is rotated about its surface normal to coincide the direction of interest with the diffraction plane.

Because only the elastic strain changes the mean lattice spacing, only elastic strains are measured using x-ray diffraction for the determination of macrostresses. When the elastic limit is exceeded, further strain results in dislocation motion, disruption of the crystal lattice, and the formation of microstresses, but no additional increase in macroscopic stress. Although residual stresses result from nonuniform plastic deformation, all residual macrostresses remaining after deformation are necessarily elastic.

The residual stress determined using x-ray diffraction is the arithmetic average stress in a volume of material defined by the irradiated area, which may vary from square centimeters to square millimeters, and the depth of penetration of the x-ray beam. The linear absorption coefficient of the material for the radiation used governs the depth of penetration, which can vary considerably.

However, in iron, nickel, and aluminum-base alloys, 50% of the radiation is diffracted from a layer approximately 0.005 mm (0.0002 in.) deep for the radiations generally used for stress measurement. This shallow depth of penetration allows determination of macro and microscopic residual stresses as functions of depth, with depth resolution approximately 10 to 100 times that possible using other methods. Although in principle virtually any interplanar spacing may be used to measure strain in the crystal lattice, availability of the wavelengths produced by commercial x-ray tubes limits the choice to a few possible planes. The choice of a diffraction peak selected for residual stress measurement impacts significantly on the precision of the method. The higher the diffraction angle, the greater the precision. Practical techniques generally require diffraction angles, 2θ , greater than 120° .

Table 6.1 lists recommended diffraction techniques for Nickel base alloys. The relative sensitivity is shown by the value of K_{45} , the magnitude of the stress necessary to cause an apparent shift in diffraction-peak position of 1° for a $45^\circ\psi$ tilt. As K_{45} increases, sensitivity decreases.

Table 6.1. Inconel 718 Diffraction technique

Alloy	Radiation	Lattice Plane (hkl)	Angle (2θ), degrees	Elastic constants(a)		Bulk Error (%)	$K_{45}(b)$		Linear Absorption Coefficient (μ)	
				(E/1-v) GPa (10^5 psi)	Bulk		MPa	ksi	cm^{-1}	In.^{-1}
Nickel-base alloys										
Inconel 718	Cu $K\alpha$	(420)	145.0	140.0±2.1	156.5	-8.9	772	112.0	1232	3127

(a) Constants determined from four-point bending tests. (b) K_{45} is the magnitude of the stress necessary to cause an apparent shift in diffraction-peak position of 1° for 45° angle tilt

Plane-Stress Elastic Model

X-ray diffraction stress measurement is confined to the surface of the sample. Electropolishing is used to expose new surfaces for subsurface measurement. In the exposed surface layer, a condition of plane stress is assumed to exist. That is, a stress distribution described by principal stresses σ_1 and σ_2 exists in the plane of the surface, and no stress is assumed perpendicular to the surface, $\sigma_3 = 0$. However, a strain component perpendicular to the surface ϵ_3 exists as a result of the Poisson's ratio contractions caused by the two principal stresses (Fig. 6.2).

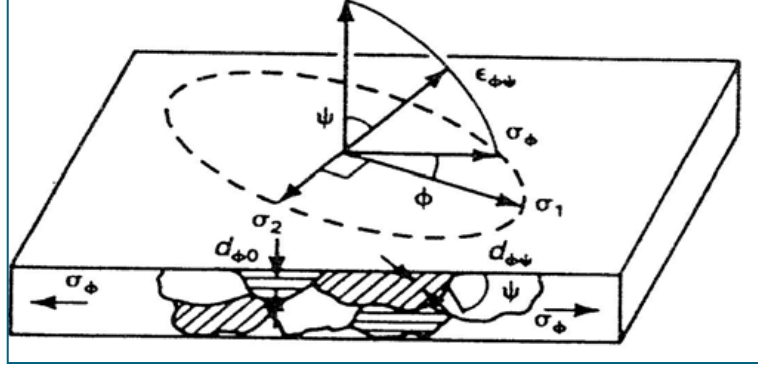


Fig. 6.2. Plane stress elastic model

The strain, $\epsilon_{\phi\psi}$ in the direction defined by the angles ϕ and ψ is:

$$\epsilon_{\phi\psi} = \left[\frac{1+\nu}{E} (\sigma_1 \sigma_1^2 + \sigma_2 \sigma_2^2) \right] - \left[\frac{\nu}{E} (\sigma_1 + \sigma_2) \right] \quad \text{Eq. 6.1}$$

where E is the modulus of elasticity, ν is the Poisson's ratio, and α_1 and α_2 are the angle cosines of the strain vector:

$$\alpha_1 = \cos \phi \sin \psi \quad \text{Eq. 6.2}$$

$$\alpha_2 = \sin \phi \sin \psi$$

Substituting for the angle cosines in Eq. 6.1 and simplifying enables expressing the strain in terms of the orientation angles:

$$\epsilon_{\phi\psi} = \left[\frac{1+\nu}{E} (\sigma_1 \cos^2 \phi + \sigma_2 \sin^2 \phi) \sin^2 \psi \right] - \left[\frac{\nu}{E} (\sigma_1 + \sigma_2) \right] \quad \text{Eq. 6.3}$$

If the angle ψ is taken to be 90° , the strain vector lies in the plane of the surface, and the surface stress component, σ_ϕ is:

$$\sigma_\phi = (\sigma_1 \cos^2 \phi) + (\sigma_2 \sin^2 \phi) \quad \text{Eq. 6.4}$$

Substituting Eq. 6.4 into Eq. 6.3 yields the strain in the sample surface at an angle ϕ from the principal stress σ_1 :

$$\epsilon_{\phi\psi} = \left[\frac{1+\nu}{E} (\sigma_{\phi}) \sin^2\psi \right] - \left[\frac{\nu}{E} (\sigma_1 + \sigma_2) \right] \quad \text{Eq. 6.5}$$

Equation 5 relates the surface stress σ_{ϕ} , in any direction defined by the angle ψ , to the strain, ϵ , in the direction (ϕ, ψ) and the principal stresses in the surface.

If $d_{\phi\psi}$ is the spacing between the lattice planes measured in the direction defined by ϕ and ψ , the strain can be expressed in terms of changes in the linear dimensions of the crystal lattice:

$$\epsilon_{\phi\psi} = \frac{\Delta d}{d_0} = \frac{d_{\phi\psi} - d_0}{d_0}$$

where d_0 is the stress-free lattice spacing. Substitution into Eq 6.5 yields:

$$\frac{d_{\phi\psi} - d_0}{d_0} = \left[\left(\frac{1+\nu}{E} \right)_{(hkl)} \sigma_{\phi} \sin^2\psi \right] - \left[\left(\frac{\nu}{E} \right)_{(hkl)} (\sigma_1 + \sigma_2) \right] \quad \text{Eq. 6.6}$$

where the elastic constants $\left(\frac{1+\nu}{E} \right)_{(hkl)}$ and $\left(\frac{\nu}{E} \right)_{(hkl)}$ are not the bulk values but the values for the crystallographic direction normal to the lattice planes in which the strain is measured as specified by the Miller indices (hkl) . Because of elastic anisotropy, the elastic constants in the (hkl) direction commonly vary significantly from the bulk mechanical values, which are an average over all possible directions in the crystal lattice.

The lattice spacing for any orientation, then, is:

$$d_{\phi\psi} = \left[\left(\frac{1+\nu}{E} \right)_{(hkl)} \sigma_{\phi} d_0 \sin^2\psi \right] - \left[\left(\frac{\nu}{E} \right)_{(hkl)} d_0 (\sigma_1 + \sigma_2) \right] + d_0 \quad \text{Eq. 6.7}$$

Eq. 6.7 describes the fundamental relationship between lattice spacing and the biaxial stresses in the surface of the sample. The lattice spacing $d_{\phi\psi}$, is a linear function of $\sin^2\psi$.

Fig. 6.3 shows the actual dependence of $d(311)$ for ψ , ranging from 0 to 45° for shot peened 5056-O aluminum having a surface stress of -148 MPa (-21.5 ksi), to which a straight line has been fitted by least squares regression.

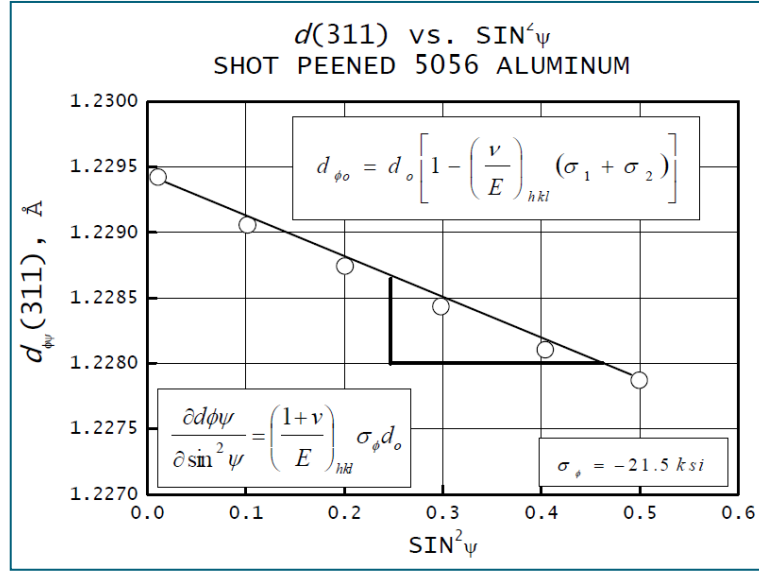


Fig. 6.3. A $d(311)$ versus $\sin^2\psi$ plot for a shot peened 5056-O aluminum alloy having a surface stress of -148 MPa

The intercept of the plot at $\sin^2\psi = 0$ is:

$$d_{\phi_0} = d_0 - \left(\frac{\nu}{E}\right)_{(hkl)} d_0 (\sigma_1 + \sigma_2) = d_0 \left[1 - \left(\frac{\nu}{E}\right)_{(hkl)} (\sigma_1 + \sigma_2) \right] \quad \text{Eq. 6.8}$$

which equals the unstressed lattice spacing, d_0 , minus the Poisson's ratio contraction caused by the sum of the principal stresses. The slope of the plot is:

$$\frac{\partial d_{\phi\psi}}{\partial \sin^2\psi} = \left(\frac{1+\nu}{E}\right)_{(hkl)} \sigma_{\phi} d_0$$

which can be solved for the stress σ_{ϕ} :

$$\sigma_{\phi} = \left(\frac{E}{1+\nu}\right)_{(hkl)} \frac{1}{d_0} \left(\frac{\partial d_{\phi\psi}}{\partial \sin^2\psi}\right) \quad \text{Eq. 6.9}$$

The x-ray elastic constants can be determined empirically, but the unstressed lattice spacing, d_0 , is generally unknown. However, because $E \gg (\sigma_1 + \sigma_2)$, the value of d_{ϕ_0} from Eq 6.8 differs from d_0 by not more than $\pm 1\%$, and σ_{ϕ} may be approximated to this accuracy using:

$$\sigma_{\phi} = \left(\frac{E}{1+\nu}\right)_{(hkl)} \frac{1}{d_{\phi_0}} \left(\frac{\partial d_{\phi\psi}}{\partial \sin^2\psi}\right) \quad \text{Eq. 6.10}$$

The method then becomes a differential technique, and no stress-free reference standards are required to determine d_0 for the biaxial stress case. The three most common methods of x-ray diffraction residual stress measurement, the single-angle, two-angle, and $\sin^2\psi$ techniques, assume plane stress at the sample surface and are based on the fundamental relationship between lattice spacing and stress given in Eq 6.7.

The $\sin^2\psi$ technique

The $\sin^2\psi$ technique [154] is identical to the two-angle technique, except lattice spacing is determined for multiple ψ tilts, a straight line is fitted by least squares regression (as shown for the shot peened aluminum sample in Fig. 6.3), and the stress is calculated from the slope of the best fit line using Eq 6.10. The method, a standard procedure in Japan and Germany, provides no significant improvement in precision over the two-angle technique if the two data points are selected at the extreme ends of the $\sin^2\psi$ range.

The primary advantage of the $\sin^2\psi$ technique, considering the additional time required for data collection, is in establishing the linearity of d as a function of $\sin^2\psi$ to demonstrate that x-ray diffraction residual stress measurement is possible on the sample of interest.

6.3. Basic Procedure

Sample preparation

Sample preparation, if the geometry of the sample does not interfere with the incident or diffracted x-ray beams, is generally minimal. Preparation of the sample surface depends on the nature of the residual stresses to be determined. If the stresses of interest are produced by such surface treatments as machining, grinding, or shot peening, the residual stress distribution is usually limited to less than 500 μm of the sample surface. Therefore, the sample surface must be carefully protected from secondary abrasion, corrosion, or etching. Samples should be oiled to prevent corrosion and packed to protect the surface during handling. Secondary abrasive treatment, such as wire brushing or sand blasting, radically alters the surface residual stresses, generally producing a shallow, highly compressive layer over the original residual stress distribution.

If the stresses of interest are those produced by carburizing or heat treatment, it may be advisable to electropolish the surface of the sample, which may have undergone finish grinding or sand blasting after heat treatment. Electropolishing eliminates the shallow, highly stressed surface layer, exposing the subsurface stresses before measurement.

To measure the inside surface of tubing, in bolt holes, between gear teeth, and other restrictive geometries, the sample must be sectioned to provide clearance for the incident and diffracted x-ray beams. Unless prior experience with the sample under investigation indicates that no significant stress relaxation occurs upon sectioning, electrical resistance strain-gage rosettes should be applied to the measurement area to record the strain relaxation that occurs during sectioning. Unless the geometry of the sample clearly defines the minimum and maximum directions of stress relaxation, a full rectangular strain-gage rosette should be used to calculate the true stress relaxation in the direction of interest from the measured strain relaxation.

Following x-ray diffraction residual stress measurements, the total stress before sectioning can be calculated by subtracting algebraically the sectioning stress relaxation from the x-ray diffraction results. If only near-surface layers are examined on a massive sample, a constant relaxation correction can be applied to all depths examined. If a significant volume of material is removed, as in determination of the stress distribution through the carburized case of a thin bearing race, a more accurate representation of sectioning relaxation can be achieved by applying strain-gage rosettes to the inner and outer surfaces and by assuming a linear relaxation of stress through the sample.

Sample Positioning.

Because the diffraction angles must be determined to accuracies of approximately $\pm 0.01^\circ$, the sample must be positioned in the x-ray beam at the true center of rotation of the ψ and 2θ axes, and the angle ψ must be constant throughout the irradiated area.

Therefore, extremely precise positioning of the sample to accuracies of approximately 0.025 mm (0.001 in.) is critical. Further, the size of the irradiated area must be limited to an essentially flat region on the sample surface. Small diameter samples or such sample geometries as small-radius fillets, the roots of threads, and fine-pitched gears may contribute to major sources of error if the x-ray beam is not confined to an essentially flat region at a known ψ tilt on the curved surface. If the irradiated area is allowed to span a curved surface, ψ will not be constant during determination of lattice spacing. These restrictions imposed by the sample geometry may prohibit x-ray diffraction residual stress measurement in many areas of primary concern, such as the roots of notches.

Irradiated Area and Measurement Time.

The residual stress determined by x-ray diffraction is the arithmetic average stress in the area defined by the dimensions of the x-ray beam. Consideration must be given to an appropriate beam size for the nature of the stress to be investigated. If average stresses over significant areas are of interest, the maximum beam size allowed by the geometry of the sample would be an appropriate choice. If local variations in residual stress, such as those produced by individual passes of a grinding wheel, are of interest, a smaller irradiated area with a geometry appropriate for the investigation should be selected. Practical dimensions of the irradiated area may range from circular zones 1.25 mm (0.050 in.) in diameter to a range of rectangular geometries from approximately 0.5 to 13 mm (0.020 to 0.5 in.). The maximum irradiated area generally feasible is approximately 13 x 8 mm (0.5 x 0.3 in.).

As the irradiated area is increased, the data collection time necessary to achieve adequate precision for residual stress measurement diminishes. The precision with which the diffracted intensity can be determined varies as the inverse of the square root of the number of x-rays collected. To determine the intensity to an accuracy of 1% at a single point on the diffraction peak, 10^4 x-rays must be counted, regardless of the time required. With diffracted intensities typically available on a fixed slit diffractometer system, this may require collection times of approximately 30 s for each point on the diffraction peak. If seven data points are collected on each diffraction peak for a two-angle technique, total measurement time may be 10 to 15 min. Reducing the irradiated area sufficiently to decrease the diffracted intensity by an order of magnitude increases the data collection time proportionally for the same precision in measurement. If fluorescence is not a problem, position-sensitive detectors can be used to collect data simultaneously at numerous points across the diffraction peak, with some sacrifice in angular precision, reducing data collection time by an order of magnitude [153].

Diffraction-Peak Location.

The transition metal target x-ray tubes used for stress measurement produce a continuous spectrum of white radiation and three monochromatic high-intensity lines. The three lines are the $K\alpha_1$, $K\alpha_2$, and $K\beta$ characteristic radiations with wavelengths known to high precision. The $K\alpha_1$ and $K\alpha_2$ lines differ too little in wavelength to allow separation of the diffraction peaks produced. The $K\alpha_1$ line, the highest intensity, is nominally twice that of the $K\alpha_2$ line. The $K\beta$ line is produced at a substantially shorter wavelength and can generally be separated from the $K\alpha$ lines by filtration, the use of high-

energy resolution detectors, or crystal monochromators. The $K\beta$ line is typically one fifth the intensity of the $K\alpha$ line and is generally too weak for practical x-ray diffraction residual stress measurement on plastically deformed surfaces.

Because the $K\alpha$ doublet is generally used for residual stress measurement, the diffraction peaks produced consist of a superimposed pair of peaks, as shown in Fig. 6.3 for four cases, indicating the various degrees of broadening that may be encountered. The variable blending of the $K\alpha$ doublet typical of an annealed sample is indicated by curve A; a fully hardened or cold-worked sample, curve D. Because the accuracy of x-ray diffraction residual stress measurement depends on the precision with which the diffraction peak can be located, the method used to locate broadened doublet peaks is of primary importance.

Precise determination of the position of the diffraction peak at each ψ tilt begins with collection of raw intensity data at several points on the peak. The diffracted intensity (x-rays counted per unit time) or inverse intensity (time for a fixed number of x-rays to be counted) is determined to a precision exceeding 1% at several fixed diffraction angles, 2θ , spanning the diffraction peak. Depending on the method to be used for peak location, 3 to 15 individual data points and 2 background points are measured using standard diffractometer techniques. If data are collected using a position-sensitive detector, the diffracted intensity can be determined at dozens of data points spanning the diffraction peak. Sharp diffraction peaks, such as those shown in curve A in Fig. 6.4, may be located using intensity data of lower precision than that required for broad peaks, as shown in curve D. The number of x-rays to be collected, and therefore the time required for stress measurement to a fixed precision, increases as the diffraction peaks broaden.

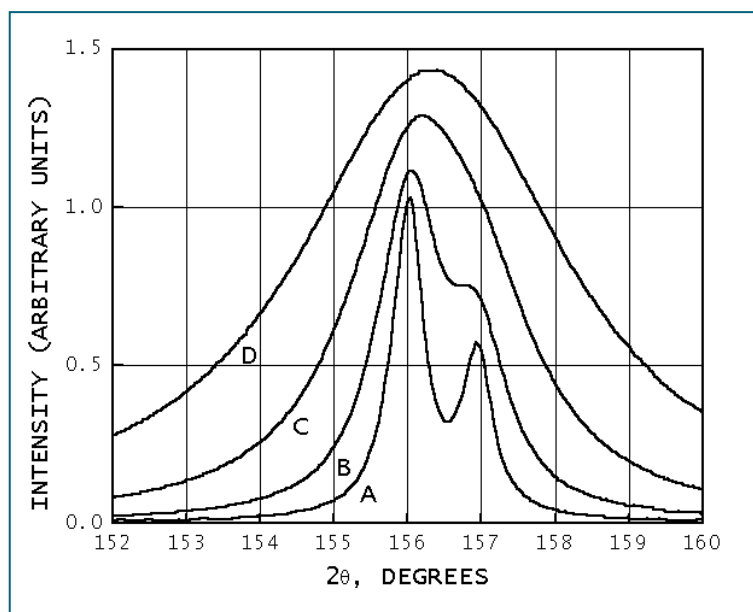


Fig. 6.4. Range of $K\alpha$ doublet blending for a simulated steel (211) Cr $K\alpha$ peak at 156.0° . A, fully annealed, B and C, intermediate hardness; D, fully hardened

Before determining a diffraction-peak position, the raw measured intensities must be corrected for Lorentz polarization and absorption. A sloping background intensity is then corrected by subtracting the background, assuming a linear variation beneath the diffraction peak. Various numerical methods are available to calculate the position of the diffraction peak. The simplest method,

incorporated in early automated diffraction equipment, is to locate 2θ positions on either side of the peak at which the intensity is equal and assume the peak position to be at the midpoint. A straight line can be fitted to the opposing sides of the diffraction peak and the point of intersection of the two lines taken as a peak position [155]. Early SAE literature recommends calculating the vertex of the parabola defined by three points confined to the top 15% of the peak [156]. A significant improvement in precision can be achieved, approaching the 0.01° resolution of most diffractometers, by collecting 5 to 15 data points in the top 15% and fitting a parabola by least squares regression before calculation of the peak vertex.

If the intensity is measured at many points ranging across the entire $K\alpha$ doublet, the peak position can be calculated as the centroid of the area above the background or by autocorrelation. Both of these area-integration methods are independent of the peak shape, but are extremely sensitive to the precision with which the tails of the diffraction peak can be determined.

All the above methods are effective, regression fit parabola being superior, if applied to a single symmetrical diffraction peak profile, such as the simple $K\alpha_1$ peak shown in curve A in Fig. 6.4 or the fully combined doublet shown in curve D. All can lead to significant error in the event of partial separation of the doublet, as shown in curve B (Fig. 6.4). Partial separation commonly results from defocusing as the sample is tilted through a range of ψ angles. If residual stresses are measured as a function of depth, diffraction peaks can vary from breadths similar to curve D (Fig. 6.4) at the cold-worked surface through a continuous range of blending to complete separation beneath the cold-work layer, as shown in curve A. All the techniques of peak location discussed can lead to significant error in stress measurement as the degree of doublet separation varies. The Rachinger correction [157] can be applied to separate the $K\alpha$ doublet before fitting parabolas, but the precision of the correction diminishes on the $K\alpha_2$ side of the combined profile and is generally inadequate for precise residual stress measurement. Fitting Pearson VII distribution functions (Cauchy to Gaussian bell-shaped, as described in [158] and [159]) separately to the $K\alpha_1$ and $K\alpha_2$ diffraction peaks, assuming a doublet separation based on the difference in wavelength, provides a method of peak location that overcomes most of the problems outlined above.

Figs. 6.5 and 6.6 show the effect of the peak-location method on the results obtained. Fig. 6.5 illustrates comparison of the same data reduced using Pearson VII distribution functions and a five-point least squares parabolic fit for ground Ti-6Al-4V using the (21.3) planes for residual stress measurement. Apparent nonlinearities in d versus $\sin^2\psi$ for the parabola fit are due to inaccurate diffraction-peak location in the presence of partial blending of the $K\alpha$ doublet. Fig. 6.6 shows the errors in stress measurement by the two methods of peak location applied to the identical data for the entire stress profile. The errors for the distribution function fit are smaller than the plotting symbols at all depths.

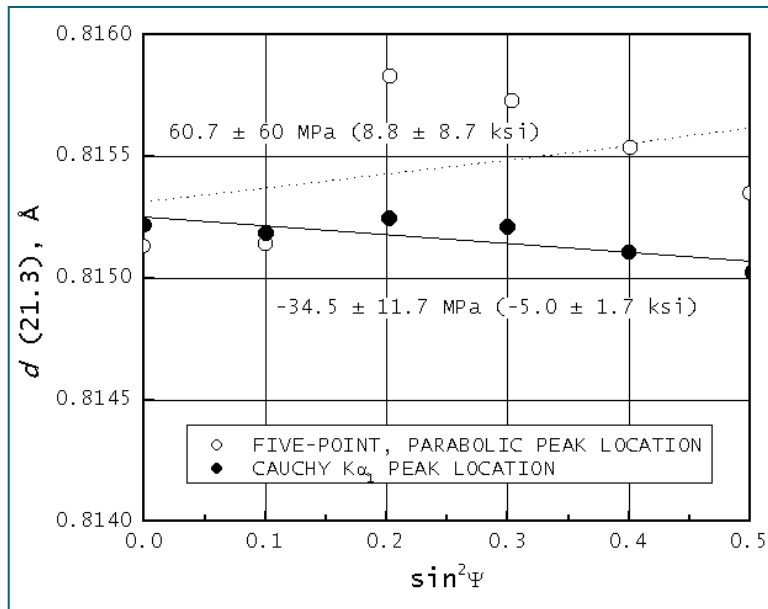


Fig. 6.5. Comparison of $d(21.3)$ versus $\sin^2\psi$ data taken 0.176 mm below the surface for a ground Ti-6Al-4V sample using two diffraction peak location methods

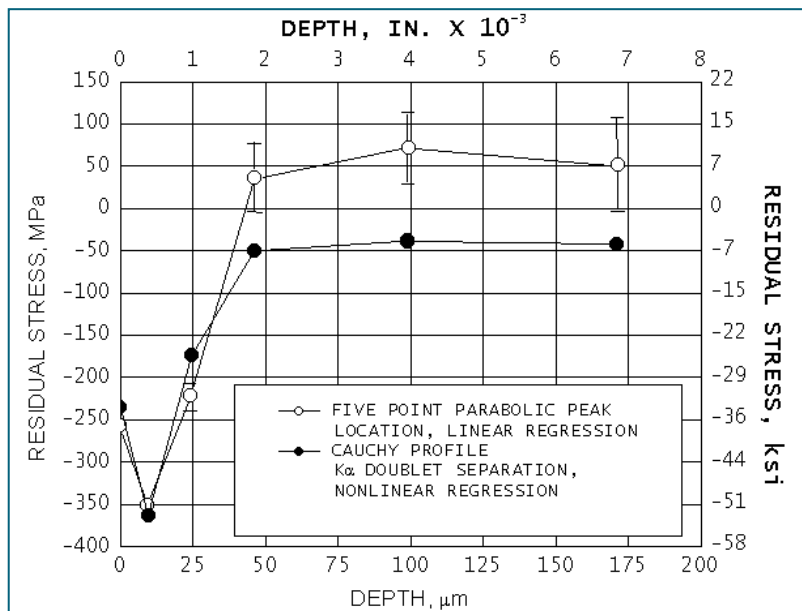


Fig. 6.6. Comparison of residual stress patterns derived using Cauchy and parabolic peak location for a ground Ti-6Al-4V sample using a six-angle $\sin^2\psi$ technique. Errors in stress measurement by two methods of diffraction-peak location are shown.

Microstress Determination and line Broadening.

Diffraction peak broadening caused by microstresses in the crystal lattice can be separated into components due to strain in the crystal lattice and crystallite size. Separation of the broadening, which is of instrumental origin, from that due to lattice strain and crystallite size is performed using Fourier analysis of the diffraction-peak profile and data collection sufficient to define precisely the shape of the entire diffraction peak. Analysis of the Fourier series terms allows separation of the components of the broadening attributable to lattice strain from that caused by reduction in the crystallite size. However, this method requires extensive data collection and depends on the

precision with which the tails of the diffraction peak can be separated from the background intensity.

For most routine analyses of microstresses associated with cold working or heat treatment for which separation of the strain and size components is not necessary, much simpler determinations of diffraction-peak breadth are adequate. The diffraction-peak width can be quantified precisely as the integral breadth (total area under the peak divided by diffraction-peak height) or the width at half the height of the diffraction peak. The width of the diffraction peak can be measured directly from strip-chart recordings or calculated from the width of the function fitted to the diffraction-peak profile during macrostress measurement. Microstresses and macrostresses can then be determined simultaneously from the peak breadth and position.

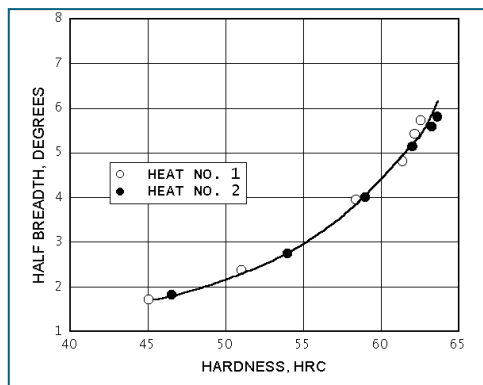


Fig. 6.7. Diffraction-peak breadth at half height for the (211) peak for M50 high-speed tool steel as a function of Rockwell hardness.

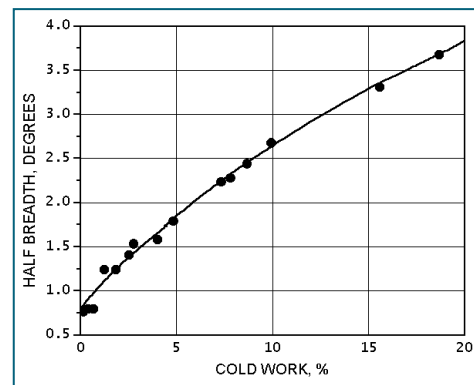


Fig. 6.8. Diffraction-peak breadth at half height for the (420) peak for Rene 95 as a function of cold-working percentage

Figs 6.7 and 6.8 show empirical relationships established between diffraction-peak breadth at half height for the (211) peak for M50 high-speed tool steel as a function of hardness and for the (420) peak breadth as a function of percent cold work for Rene 95, respectively. These empirical curves can be used to calculate the hardness or cold work in conjunction with macroscopic residual stress measurement. For the preparation of the hardness curve, a series of coupons are quenched and tempered to known hardness. The peak breadth is then measured using the same slit system and peak-location method used for macrostress measurement. For the percent cold work curve, samples are heat treated, then pulled in tension to produce a series of coupons with various known amounts of cold work. Because the initial heat treatment may alter significantly the initial peak breadth before cold work, the coupons must receive the same heat treatment as the samples to be measured before inducing known amounts of cold work [153].

Sample fluorescence

Sample fluorescence complicates the selection of radiation to be used for residual stress measurement. The radiation necessary for the highest precision techniques may cause fluorescence of the elements present in the sample under investigation. The use of Cu K α radiation for residual stress measurement in alloys containing iron, chromium, or titanium can result in fluorescent background intensities many times as intense as the diffracted radiation, greatly reducing the signal-to-noise ratio. Problems with fluorescence may be overcome in some cases by use of metal foil filters, but generally require use of a crystal monochromator or high energy resolution solid-state detector. Failure to eliminate fluorescence can degrade severely the precision with which the diffraction peak

can be located accurately, increasing random experimental error significantly. Diffracted beam monochromators and solid-state detectors can be used only on standard laboratory diffractometers. The position-sensitive detectors available for residual stress measurement are the gas-filled proportional counter or fluorescence screen type and have insufficient energy resolution to overcome fluorescence [153].

6.4. X-ray stress analyzer

The instrument used for the residual stress measurement is an “XSTRESS 3000” X-ray stress analyzer produced by Stresstech, as shown in Fig. 6.9.

The most important features are reported below [160]:



Fig. 6.9. Stresstech XSTRESS3000

Technical Specifications

Main Unit X3000

- High voltage power supply (generator) for X-ray tube continuously variable within 5 to 30 kV / 0 up to 10 mA.
- Ultra-compact design.
- Electrical
- 90 to 260 VAC, 48 to 62 Hz, 600 VA
- Cooling
- Self-contained recirculating water cooling with heat exchanger for X-ray tube and
- power supply. No external water supply needed.

Goniometer

- Xstress 3000 goniometer type G2 mounted on a tripod with magnetic anchoring as a standard.
- χ -inclination: Programmable -45° to $+45^\circ$ (standard)
- χ -oscillation: Programmable 0° to $\pm 6^\circ$.

- Distance between goniometer and the measurement point automatically adjusted to ± 0.003 mm accuracy.

Detectors

- Dual position sensitive MOS Linear Image Sensors in symmetrical modified χ (side inclination) geometry.
- Angular resolution: $0.029^\circ/\text{pixel}$, 512 pixels/0.5 in.
- 2θ -angle is instantly adjustable by sliding the detectors manually to the desired angular position along arc-shaped detector holder.
- 2θ -range of the detectors is continuously adjustable within $+100^\circ$ to 165°

X-ray Tube

- Miniature, 30 kV, 10 mA, 300 W, Cr, Cu, Co, Fe, V, Ti, Mn. Cr-tube provided as a standard. Tube can be replaced in less than 10 minutes without special tools.

Cables

- 5 meters standard.

Collimator

- Replaceable, to provide 1, 2, 3, 4, and 5 millimeter spot sizes. Special collimators available as an option.

6.5. Residual stress measurement results

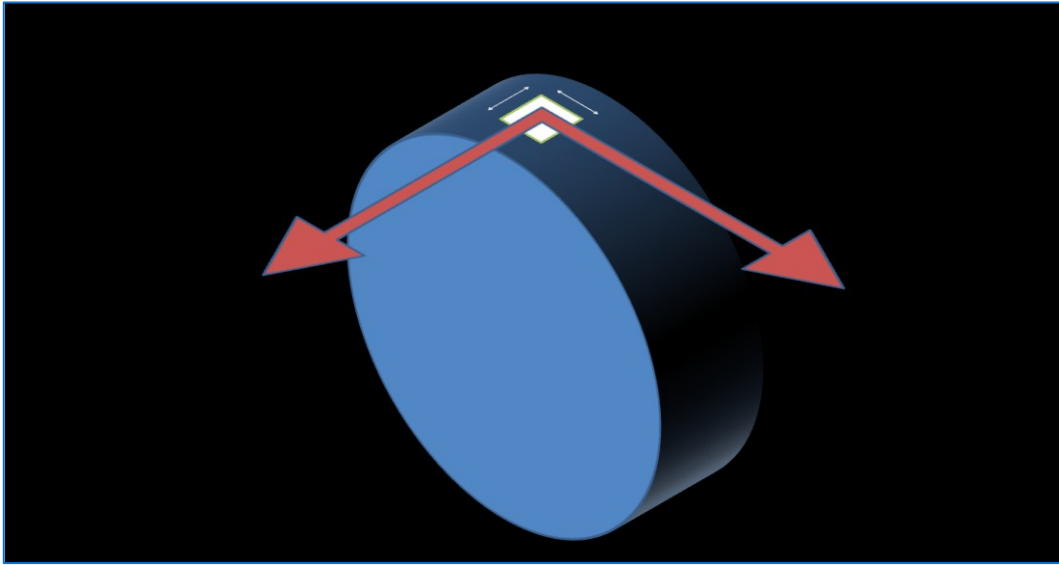


Fig. 6.10. Residual stress measurement directions on a test sample

In Fig. 6.10 a residual stress measurement scheme is reported. The blue ring represent the test workpiece, and the white square is representative of the test surface (1 mm x 1 mm). The two red arrows show the two measurement directions: the cutting speed direction and the feed direction respectively.

Table 6.2. Residual stress measurement results

	Test ID	RS (MPa) direction 1	RS (MPa) direction 2
Standard Tests	T_1	379	-176
	T_2	182	-287
	T_3	455	-65
	T_4	309	-111
	T_5	644	35
	T_6	767	205
	T_7	378	-9
	T_8	662	252
	T_9	1009	725
Severe Cutting Condition Tests	T_1H	1228	635
	T_2H	1515	1206
	T_3H	1376	882
	T_4H	1521	1172
	T_5H	1387	934
	T_6H	1473	965
	T_7H	1277	689
	T_8H	1412	1187

In Table 6.2 all the residual stress measurements are reported, for all the tests and for both the measurement directions. In bold the values that exceed the acceptance threshold, set at 850 MPa.

In Fig. 6.11 the residual stress measured values are reported in a 3D plot. As reported in the graph, for standard tests only the test T_9 produces unacceptable residual stress value (over the grey plan threshold). Figs. 6.12 and 6.13 show the residual stress measurement results for the Severe Cutting Conditions Tests, cooled and dry respectively. It is clear that for both series of tests, all the measurements showed unacceptable residual stress values, over 850 MPa.

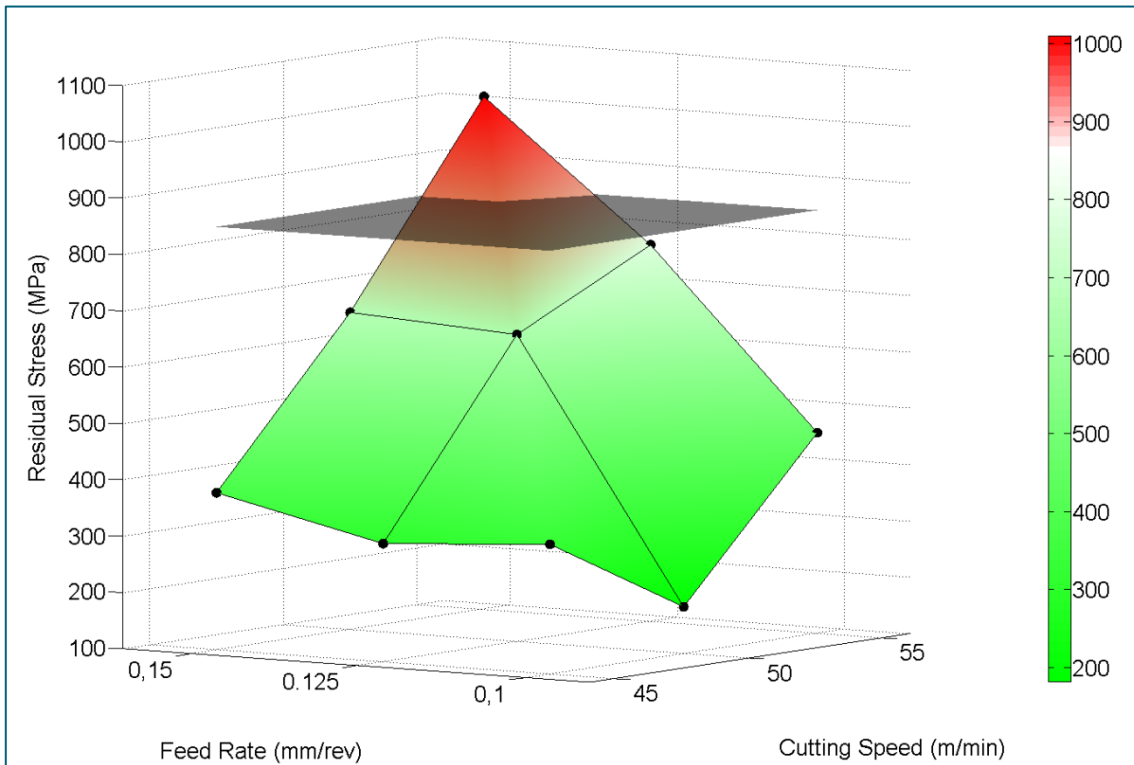


Fig. 6.11. Residual stress plot of Standard Tests

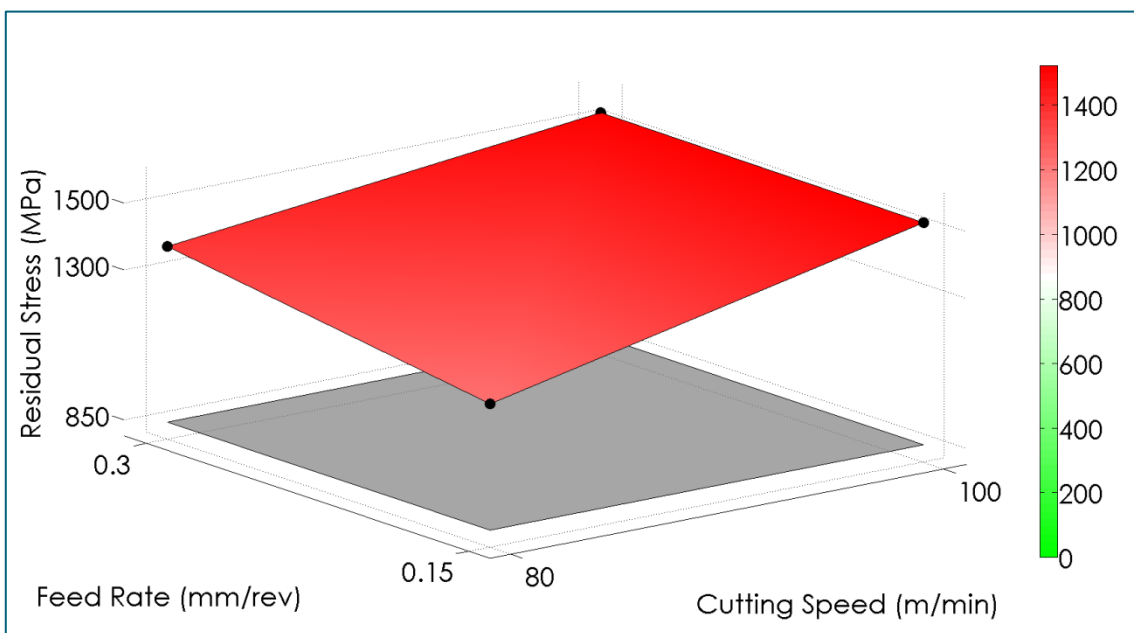


Fig. 6.12. Residual stress measurement for Severe Cutting Conditions Tests (Cooled tests)

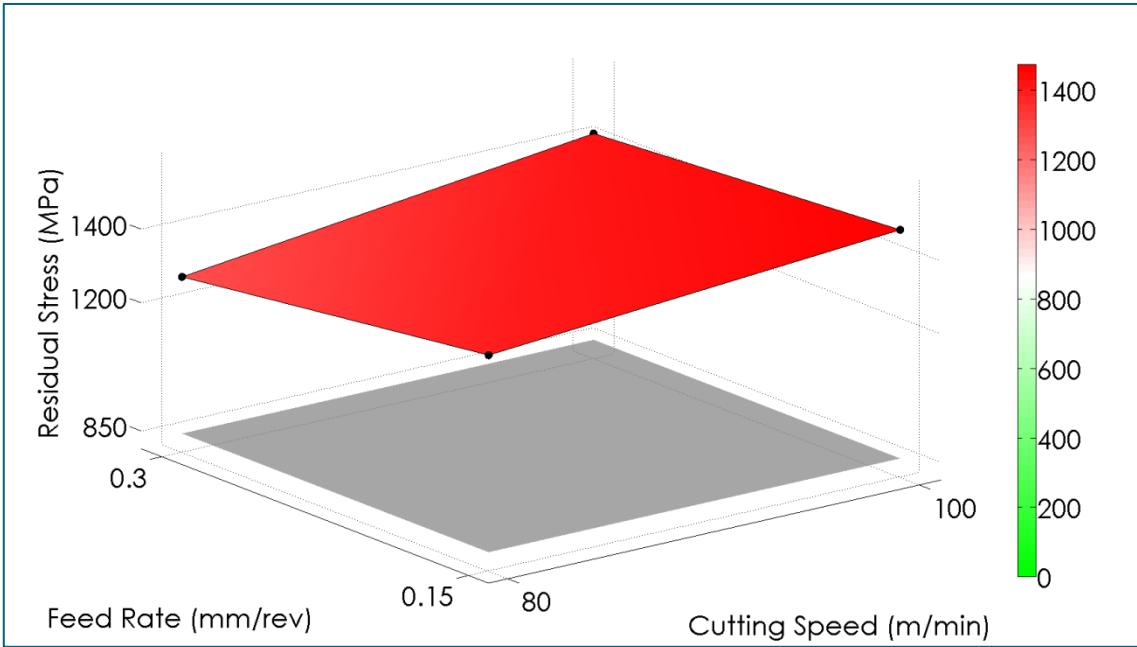


Fig. 6.13. Residual stress measurement for Severe Cutting Conditions Tests (Dry tests)

7. Material characterization tests

7.1. Test typologies

7.1.1. Visual Inspection

Visual inspection is the most basic and common inspection method, and involves getting the inspector to "see" where one normally couldn't. This is done with the use of tools such as fiberscopes, borescopes, magnifying glasses and mirrors. Successful use of the technique requires good lighting and vision for best sensitivity, as well as training & experience which are vital for accurate interpretation of features.[161]

Advantages of Visual Inspection

- Inspection performed rapidly and at low cost
- Ability to inspect complex sizes and shapes of any material
- Minimum part preparation required

Limitations of Visual Inspection

- Surface to be inspected must somehow be accessible to inspector or visual aids
- Surface finish, roughness and cleanliness can interfere with inspection
- Only surface defects are detectable

7.1.2. Fluorescent Penetrant Inspection

In Fluorescent Penetrant Inspection (FPI), a fluid with high capillary potential is applied to a sample and drawn into surface breaking flaws. The excess is removed after a period of time and an appropriate developer is applied to draw the penetrant back out. As it bleeds out laterally on the part surface, it is visually noted due to contrast with the developer. A penetrant that fluoresces under UV light may also be used to generate dramatic visualization of the flaws.

It may be used on any non-porous material and is used to find surface flaws, sometimes to detect leaks. Equipment for FPI can be as simple as a collection of aerosol spray cans, or may be a fully automated system. There are considerable choices of penetrant, remover, and developer materials. Selection is based on the required sensitivity, portability requirements, and the nature of the material to be tested with respect to compatibility issues [162].

Procedure

Surface Preparation: One of the most critical steps of a liquid penetrant inspection is the surface preparation. The surface must be free of oil, grease, water, or other contaminants that may prevent penetrant from entering flaws. The sample may also require etching if mechanical operations such as machining, sanding, or grit blasting have been performed. These and other mechanical operations can smear metal over the flaw opening and prevent the penetrant from entering.

Penetrant Application: Once the surface has been thoroughly cleaned and dried, the penetrant material is applied by spraying, brushing, or immersing the part in a penetrant bath.

Penetrant Dwell: The penetrant is left on the surface for a sufficient time to allow as much penetrant as possible to be drawn from or to seep into a defect. Penetrant dwell time is the total time that the penetrant is in contact with the part surface. Dwell times are usually recommended by the penetrant

producers or required by the specification being followed. The times vary depending on the application, penetrant materials used, the material, the form of the material being inspected, and the type of defect being inspected for. Minimum dwell times typically range from five to 60 minutes. Generally, there is no harm in using a longer penetrant dwell time as long as the penetrant is not allowed to dry. The ideal dwell time is often determined by experimentation and may be very specific to a particular application

Excess Penetrant Removal: This is the most delicate part of the inspection procedure because the excess penetrant must be removed from the surface of the sample while removing as little penetrant as possible from defects. Depending on the penetrant system used, this step may involve cleaning with a solvent, direct rinsing with water, or first treating the part with an emulsifier and then rinsing with water.

Developer Application: A thin layer of developer is then applied to the sample to draw penetrant trapped in flaws back to the surface where it will be visible. Developers come in a variety of forms that may be applied by dusting (dry powdered), dipping, or spraying (wet developers).

Indication Development: The developer is allowed to stand on the part surface for a period of time sufficient to permit the extraction of the trapped penetrant out of any surface flaws. This development time is usually a minimum of 10 minutes. Significantly longer times may be necessary for tight cracks.

Inspection: Inspection is then performed under appropriate lighting to detect indications from any flaws which may be present.

Clean Surface: The final step in the process is to thoroughly clean the part surface to remove the developer from the parts that were found to be acceptable [163].

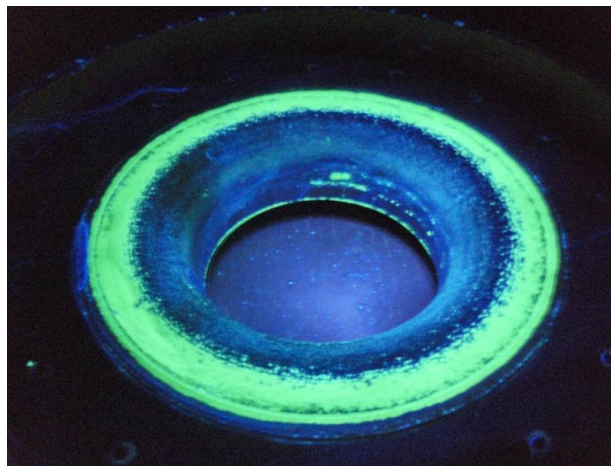


Fig. 7.1. Example of FPI Testing Sample

Advantages of FPI

- Large areas or volumes of parts/materials can be inspected rapidly and at low cost
- Parts with complex geometries are routinely inspected
- Indications are produced directly on surface of the part, providing a visual image of the discontinuity
- Equipment investment can be quite low
- Aerosol spray cans can make testing very portable

Limitations of FPI

- Only detects surface breaking defects
- Test material must be nonporous
- Precleaning is critical - contaminants can mask defects
- Post cleaning is sometimes necessary to remove chemicals
- Requires multiple operations under controlled conditions
- Chemical handling precautions may be necessary
- Metal smearing from machining, grinding and other operations inhibits detection
- Some materials may need to be etched prior to inspection [162].

7.1.3. Metallographic Tests

Optical metallography, entails examination of materials using visible light to provide a magnified image of the micro- and macrostructure.

Microscopy (microstructural examination) involves magnifications of approximately 50x or higher; macroscopy (macrostructural examination), 50 x or lower.

Optical microscopy is used to characterize structure by revealing grain boundaries, phase boundaries, inclusion distribution, and evidence of mechanical deformation.

Because the macro- and microstructure of metals and alloys often determine the behavior of the material, characterization of the effects of composition, processing, service conditions, and other such variables on the macro- and microstructure is frequently required. Typical structure-property relationships that have been established using optical metallography include:

- A general increase in yield strength and hardness of a metal with decreasing grain size
- A general tendency for a decreased ductility with increasing inclusion content
- Correlations of weld penetration, heataffected zone (HAZ) size, and welddefect density with the nature and character of the welding
- Evaluation of such surface treatments as carburizing and induction hardening by determinations of the depth and microstructural characteristics of the hardened region
- Correlations of fatigue crack growth rates and fracture-toughness parameters with such structural variables as inclusion content and distribution
- Association of failure initiation sites with microstructural inhomogeneities, such as second-phase particles
- Correlations of anisotropic mechanical behavior with elongated grains and/or preferred grain orientations

The microstructures of metals and alloys are determined by composition, solidification processes, and thermomechanical treatment. Therefore, these process variables determine the response of metals and alloys to laboratory and service environments. Because of the relationships between structure and properties, metallographic characterization is used in materials specification, quality control, quality assurance, process control, and failure analysis.

Optical metallography is applicable to studies ranging from fundamental research to production evaluations [164].

Specimen preparation

The first step in metallographic analysis is to select a sample that is representative of the material to be evaluated. This step is critical to the success of any subsequent study. The second, equally important step is to correctly prepare a metallographic specimen.

The region of the sample that is of interest must be sectioned from the component. Each of the samples would be mounted to facilitate handling. Selected surfaces would then be ground flat, polished, and etched to reveal the specific structure or structures of interest.

Sectioning

Sectioning of a metallographic sample must be performed carefully to avoid altering or destroying the structure of interest. The most widely used sectioning device is the abrasive cutoff machine, ranging from units using thin diamond-rimmed wafering blades to those using wheels that are more than 1.5 mm thick, 30 to 45 cm in diameter, containing silicon carbide particles. Heat is generated during abrasive cutting, and the material just below the abraded surface is deformed. To minimize burning and deformation, a lubricant or coolant is typically used. Wet cutting yields a flat relatively smooth surface. However, because of the abrasion associated with cutting, the structure of the metal or alloy is damaged to a depth of approximately 1 mm.

Mounting

Mounting facilitates handling of the specimen. A procedure that does not damage the specimen should be selected. Because large specimens are generally more difficult to prepare than small ones, specimen size should be minimized. Standard or typical specimen mounts are right circular cylinders 25 to 50 mm in diameter. Mounting mediums should be compatible with the specimen regarding hardness and abrasion resistance. Two common mounting materials are thermosetting phenolics, such as Bakelite, and thermoplastic materials, such as methyl methacrylate (Lucite). A thermosetting polymer develops a rigid three-dimensional structure upon being heated and held at 200 to 300 °C. A thermoplastic polymer softens when held at elevated temperatures. Mounting involves placing the specimen in a mold and surrounding it with the appropriate powders. The mold and its contents are then heated under pressure to the thermal setting or the softening temperature. Once the powder sets, thermosetting mounts can be removed from the mold without lowering the temperature; thermoplastic mounts must be cooled to ambient temperature before removal. Mounting pressure or temperature may alter the structure of low melting temperature or soft and/or fragile specimens; therefore, castable (cold-mounting) techniques have been developed.

Plastics that set at room temperature are referred to as castable (cold-mounting) materials. The most widely used materials are epoxy resins. Epoxies resist acids and strong solvents effectively, a desirable characteristic in any mounting material. Epoxies and thermoplastic materials are relatively soft mounting materials, and the specimen in such a mount must often be surrounded by a hard material, for example, hardened steel balls Fig. 7.2. This material helps retain the edges of the sample by maintaining a flat surface during grinding and polishing [164].

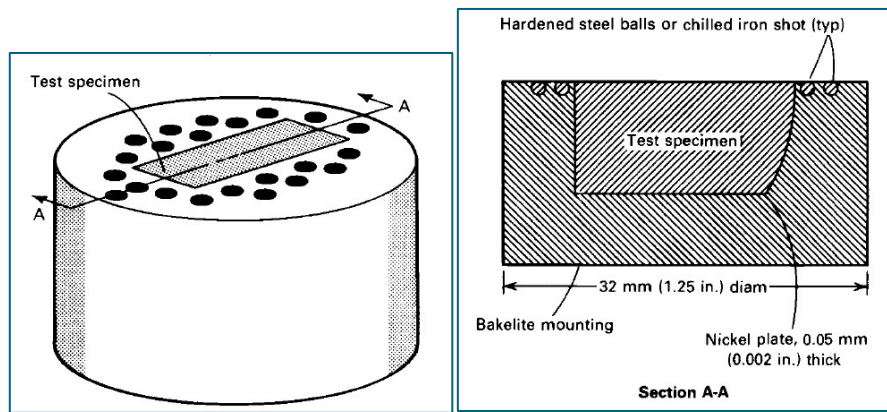


Fig. 7.2. One method of mounting the sample to retain flatness for metallographic examination

Grinding

Grinding is generally considered the most important step in specimen preparation. Care must be taken to minimize mechanical surface damage. Grinding is generally performed by the abrasion of the specimen surface against water-lubricated abrasive wheels (assuming water does not adversely affect the metal). Grinding develops a flat surface with a minimum depth of deformed metal and usually is accomplished by using progressively finer abrasive grits on the grinding wheels. A typical sequence might begin with 120- or 180-grit papers and proceed to 240, 320, 400, and 600 grits. Scratches and damage to the specimen surface from each grit must be removed by the next finer grinding step. The surface damage remaining, on the specimen after grinding must be removed by polishing. If this disturbed or deformed metal at the surface is not removed, microstructural observations may be obscured.

Polishing

Polishing of the metallographic specimen generally involves rough polishing and fine polishing. In rough polishing, the cloth covering on a wheel is impregnated with a fine (often as small as $1\ \mu\text{m}$) diamond paste or a slurry of powdered $\alpha\text{-Al}_2\text{O}_3$ in water, and the specimen is held against the rotating wheel. The cloth for rough polishing is frequently napless, providing easy access of the polishing abrasive to the specimen surface. Fine polishing is conducted similarly, but with finer abrasives (down to $0.05\ \mu\text{m}$ in diameter) on a napped cloth. Although often automated, polishing can be performed by hand. Vibratory polishing and electropolishing techniques have also been developed for many metals and alloys. Polishing should yield a scratch-free specimen surface, in which inclusions and other second-phase articles may be visible. Polishing damage, should be recognized and avoided when preparing metallographic specimens.

Etching

Etching includes any process used to reveal the microstructure of a metal or alloy. Because many microstructural details are not observable on an as-polished specimen, the specimen surface must be treated to reveal such structural features as grains, grain boundaries, twins, slip lines, and phase boundaries. Etchants attack at different rates areas of different crystal orientation, crystalline imperfections, or different composition. The resulting surface irregularities differentially reflect the incident light, producing contrast, coloration, polarization, etc. Various etching techniques are available, including chemical attack, electrochemical attack, thermal treatments, vacuum cathodic etching, and mechanical treatments. Chemical and electrochemical attack are the most frequently used. Metallography involves many steps that can obscure or alter the structure observed during examination, leading to erroneous conclusions. Therefore, specimen preparation is not necessarily

straightforward, and care must be taken to ensure that the structure observed is not an artifact. Good metallography is necessary in developing a correlation between the structure and the properties of metals and alloys [164].

7.1.4. Roughness measurement

([DIN EN ISO 4287:1998](#) AND [DIN EN ISO 11562:1998](#))

Every surface has some form of texture which will vary according to the way it has been manufactured. Surface characteristics can be quantified by the use of parameters, the most popular of which are described here [165].

Amplitude Parameters

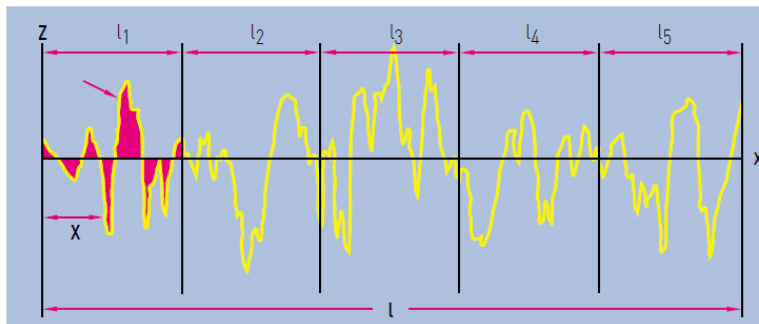


Fig. 7.3. R_a , R_q , W_a , W_q , P_a , P_q

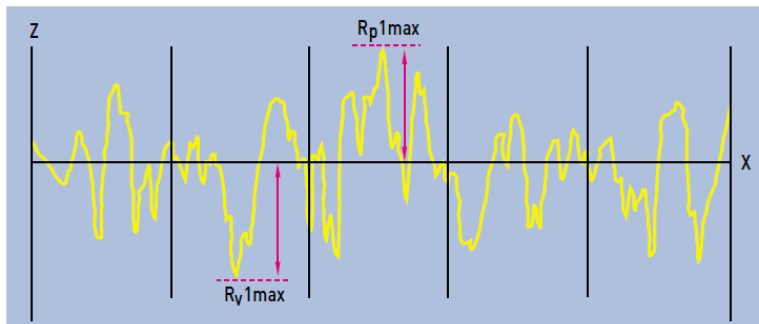


Fig. 7.4. R_v , R_p , R_t , W_v , W_p , W_t , P_v , P_p , P_t

- R_a is the arithmetic mean of the absolute departures of the roughness profile from the mean line. It is universally recognized and is the most often used international parameter of roughness.
- R_q (sometimes referred to as RMS) is the rms parameter corresponding to R_a .

$$R_a = \frac{1}{l} \int_0^l |z(x)| dx$$

$$R_q = \sqrt{\frac{1}{l} \int_0^l z^2(x) dx}$$

- W_a , W_q , P_a and P_q are the corresponding parameters from the waviness and primary profiles, respectively.
- R_v is the maximum depth of the profile below the mean line within the sampling length.
- R_p is the maximum height of the profile above the mean line within the sampling length.
- R_t is the maximum peak to valley height of the profile in the assessment length.
- R_{pmax} is the largest of the individual peak to mean from each sample length.

- R_{v1max} is the largest of the individual mean to valleys from each sample length.
- W_v , W_p , W_t , P_v , P_p , and P_t are the corresponding parameters from the waviness and primary profiles, respectively.

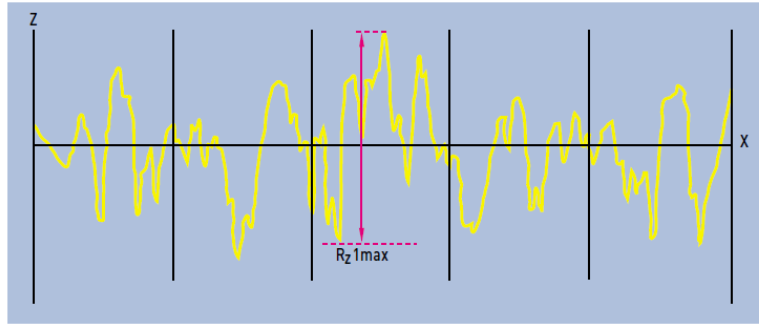


Fig. 7.5. R_z , W_z , P_z

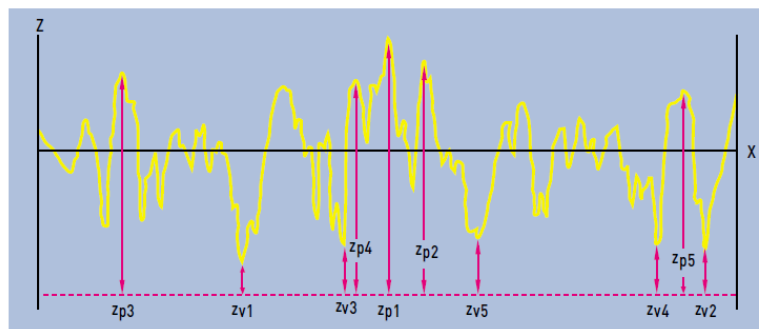


Fig. 7.6. $R_{z(JIS)}$, $P_{z(JIS)}$

- $R_z = R_p + R_v$ and is the maximum peak to valley height of the profile within a sampling length.
- R_{z1max} is the largest of the individual peak to valleys from each sample length.
- W_z , P_z are the corresponding parameters from the waviness and primary profiles respectively.
- $R_{z(JIS)}$ (also known as the ISO 10 point height parameter in ISO 4287/1-1984) is measured on the roughness and primary profiles only and is numerically the average height difference between the five highest peaks and the five lowest valleys within the sampling length.

$$R_{z(JIS)} = \frac{(zp1 + zp2 + zp3 + zp4 + zp5) - (zv1 + zv2 + zv3 + zv4 + zv5)}{5}$$

- $P_{z(JIS)}$ is the corresponding parameter from the primary profile.

Cut-off, Evaluation and Sample lengths

A cut-off is a filter that uses electronic or mathematical means to remove or reduce unwanted data in order to look at wavelengths in the region of interest. Sample lengths are equal to the filter cut-off length λ_c (Table 7.1) and are long enough to include a statistically reliable amount of data.

The evaluation length (l) is defined as the length of profile used for the measurement of surface roughness parameters. It usually contains several sample lengths with five consecutive sample lengths taken as standard. Almost all parameters are defined over one sample length, however in practice more than one sample length is assessed (usually five) and the mean is calculated. This provides a better statistical estimate of the parameter's measured value [165].

Selecting the proper cut-off length [165]

Table 7.1. Recommended cut-off according to ISO-4288/1997

RECOMMENDED CUT-OFF ISO 4288-1997

PERIODIC PROFILES	NON-PERIODIC PROFILES		CUT-OFFS	SAMPLING LENGTH / EVALUATION LENGTH
Spacing Sm (mm)	R _z (μm)	Ra (μm)	λc (μm)	λc/L (mm)
>0.013 to 0.04	(0.025) to 0.1	(0.006) to 0.02	0.08	0.08 / 0.4
>0.04 to 0.13	>0.1 to 0.5	>0.02 to 0.1	0.25	0.25 / 1.25
>0.13 to 0.4	>0.5 to 10	>0.1 to 2	0.8	0.8 / 4
>0.4 to 1.3	>10 to 50	>2 to 10	2.5	2.5 / 12.5
>1.3 to 4	>50 to 200	>10 to 80	8	8 / 40

7.1.5. Micro-hardness

Microhardness testing is a useful tool for the microstructural analysis of a finished surface. Information such as phase identification and fracture toughness data can be determined. Hardness is defined as the resistance to penetration by an indenter, and the Knoop and Vickers measurements are the most common [166].

A Knoop hardness number (HK) is obtained by:

$$HK = \frac{P}{A_p} = 14.229 \frac{P}{d^2}$$

where P is the load in kilogram force, A_p is the projected area of indentation in millimeters, and d is the length of the longest diagonal in millimeters.

The Vickers hardness number (HV) is obtained by:

$$HV = \frac{P}{A_s} = 1.8544 \frac{P}{d^2}$$

where P is the load in kilogram force, A_s is the surface area of indentation in millimeters, and d is the length of the longest diagonal in millimeters. Surface preparation is typically required before hardness testing to ensure that accurate reproducible results can be obtained. The surface finish used depends on the load to be applied to the indenter. For microhardness testing (1 to 1000 gf), a final polish is recommended. Microhardness testing is a useful technique in characterizing different phases, and it has also been used to determine the fracture toughness in brittle materials. Fracture toughness is determined by initiating a controlled crack, then breaking the specimen, or by measuring crack lengths and applying fracture toughness equations [167][168][169][170].

7.2. Defects to be investigated

7.2.1. Macro anomalies

Scores

Scoring is surface damage due to accumulated small seizures caused by sliding under improper lubrication or severe operating conditions. Linear damage appears circumferentially on the raceway

and roller surfaces. Cycloidal shaped damage on the roller ends and Scoring on the rib surface contacting roller ends also occur. Scores' depth maximum allowable value: 0.013 mm. [171].



Fig. 7.7. Scores

Scratches

Grooves produced in a solid surface by the cutting and/or plowing action of a sharp particle or protuberance moving along that surface.

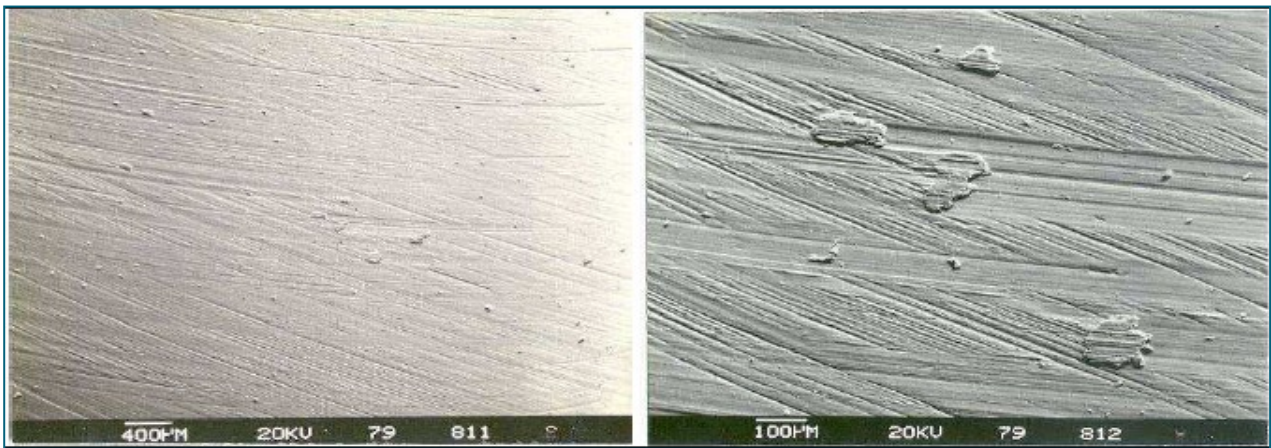


Fig. 7.8. Scratches

Orange peel

Dull or cloudy spots appear on surface along with light Wear. From such dull spots, tiny Cracks are generated downward to a depth of 5-10 μm . Small particles fall off and minor Flaking occurs widely.



Fig. 7.9. Orange Peel

Chatter

Chatter is a self-excited vibration that can occur during machining operations and become a common limitation to productivity and part quality.

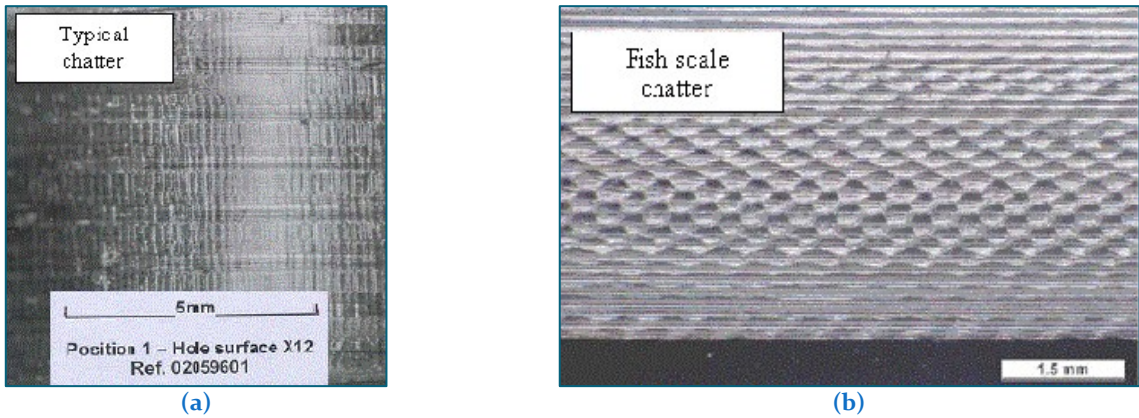


Fig. 7.10. (a) Typical Chatter (b) Fish Scale Chatter

Cracks

Cracks are external or internal separations with sharp outlines. Cracks requiring a magnification of 10x or higher to be seen by a naked eye are called microcracks.



Fig. 7.11. Cracks

Inclusion

A physical and mechanical discontinuity occurring within a material or part, usually consisting of solid, encapsulated foreign material. Inclusions are often capable of transmitting some structural stresses and energy fields, but to a noticeably different degree than from the parent material [172].

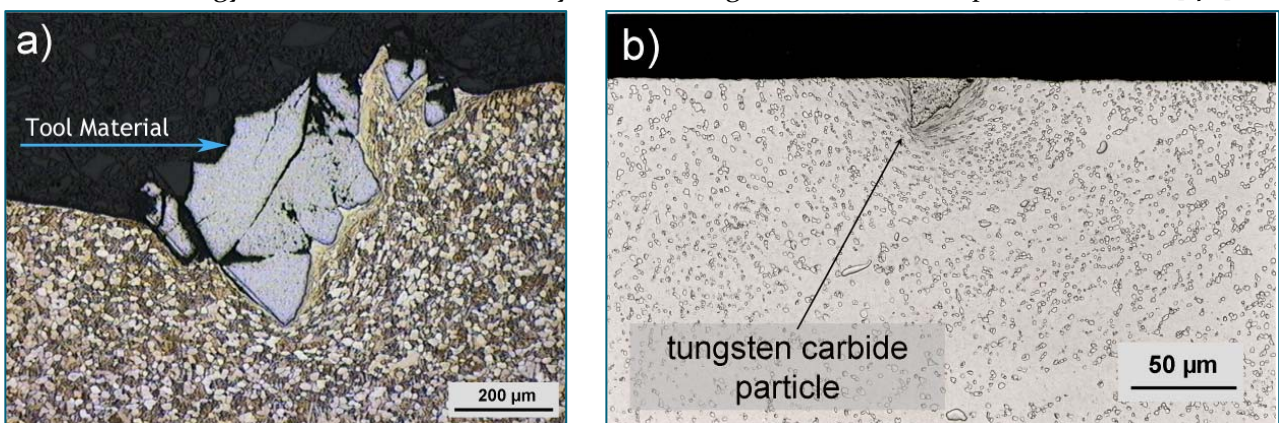


Fig. 7.12. Inclusions: (a) Micro section of broken tungsten carbide cutting insert in TiAl6V4 matrix showing microstructural distortion and phase transformation through adiabatic shear; (b) broken inclusion in Waspaloy after rework.[173]

Discoloration

A change in the appearance from shiny bright metal. Localized heating takes place at the surface of the hole. Colour intensity can be used to predict temperature reached.



Fig. 7.13. Discoloration

Burr

A burr is a body created on a workpiece surface during the manufacturing of a workpiece, which extends over the intended and actual workpiece surface and has a slight volume in comparison with the workpiece, undesired, but to some extent, unavoidable [174].

Typically burrs occurring in turning operations are Poisson burrs (Fig. 7.14). They form when the cutting edge of a tool extends past the workpiece edge. Yet, if the cutting tool passes over a groove or cutting is interrupted due to other geometric features of the workpiece, a rollover burr forms. In turning operations, most burrs are created as a rollover burr at the side of the workpiece when the tool exits from cutting [175][176].

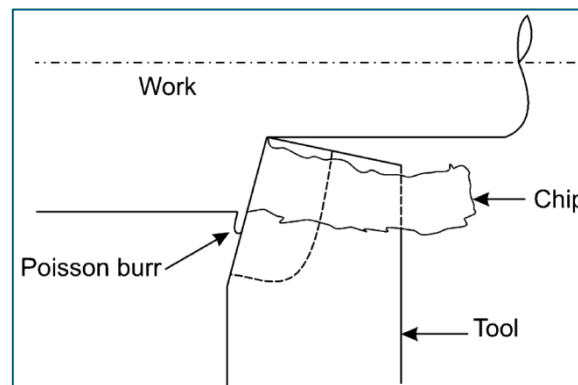


Fig. 7.14. Poisson burr formed when cutting edge of tool extends past edge of workpiece

7.2.2. Micro anomalies

Flaking

Flaking occurs when small pieces of bearing material are split off from the smooth surface of the raceway or rolling elements due to rolling fatigue, thereby creating regions having rough and coarse texture[177].



Fig. 7.15. Flaking

Laps

Laps (or seams) are surface defects which result from overlapping of the material during processing.



Fig. 7.16. Laps

Plucking

Plucking is a phenomenon where small volumes of material are torn out of the surface. This leads to very small surface depressions, which are open to the surface and so not reliably detected by penetrant inspection. Plucking is mainly observed on machined surfaces using aggressive cutting parameters [181].

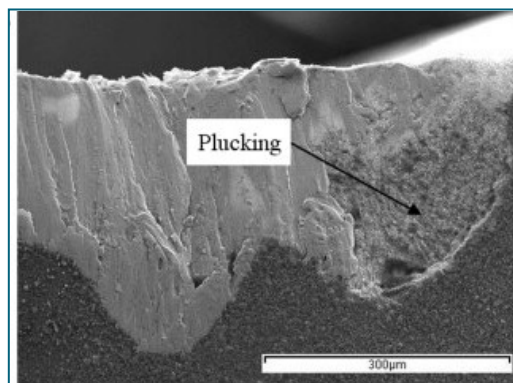


Fig. 7.17. Plucking [180]

Smearing

A condition that causes a tool to leave burrs on a workpiece when it is not properly lubricated during machining. Smearing causes a poor surface finish [178].

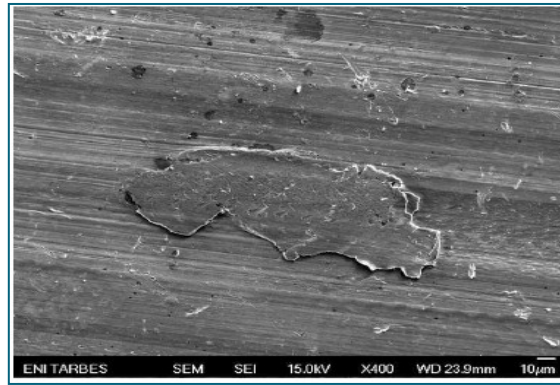


Fig. 7.18. Smearing

7.2.3. Microstructure changes

Recast Layer

The recast layer is a surface layer made up of molten metal particles that have been re-deposited onto the surface of the workpiece [179].

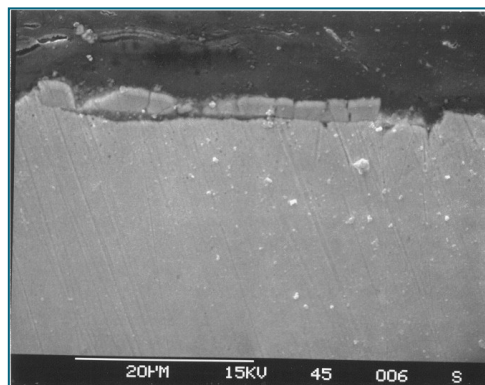


Fig. 7.19. SEM of recast layer on cut surface

White etching layer (WEL)

A generic term referring to a layer of material that may be hard and brittle and because of its resistance to etching in comparison to the bulk material, appears featureless and white under light microscopes. WEL is normally found in association with a plastically deformed layer that results from the heat and stresses generated during metal removal operations

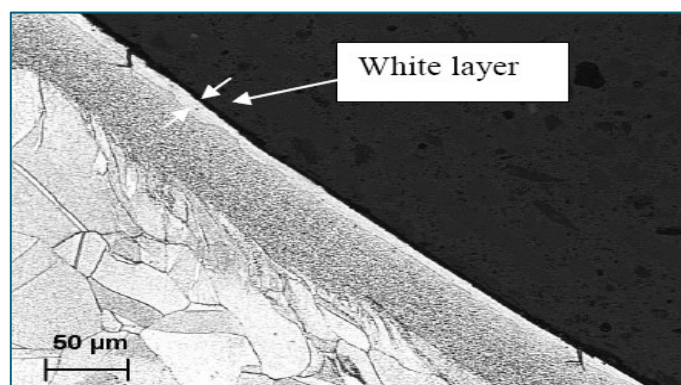


Fig. 7.20. White Layer

Table 7.2. WEL Acceptance criteria

White Etching Layer		
Acceptable	Continuous areas	$\leq 2.54 \mu\text{m}$
	Isolated areas provided they are no deeper than:	$1.27 \mu\text{m}$
Rejectable	White layer in excess of acceptable requirements	

Distorted Surface Structure

Slightly Distorted Surface Structure

Microstructure is distorted however grain and/or phase boundaries are definable.

Severely Distorted Surface Structure

A microstructure distorted to the extent where grain and/or phase boundaries become undefinable.

Acceptance criteria

Table 7.3. Distorted surface acceptance criteria

Distorted Surface Structure		
Acceptable	Distortion-free	---
	Slightly distorted	$15.24 \mu\text{m}$
	Severely distorted	$7.62 \mu\text{m}$
Rejectable	Distorted structures in excess of acceptable requirements	

Table 7.4. Defect frequency

Frequency	% of investigated surface with defect
Isolated	< 5
Occasional	$5 - 15$
Intermittent	$> 15 - 40$
Predominant	$> 40 - 90$
Continuous	> 90

Recrystallized Layer

The change from one crystal structure to another, as occurs on heating or cooling through a critical temperature.

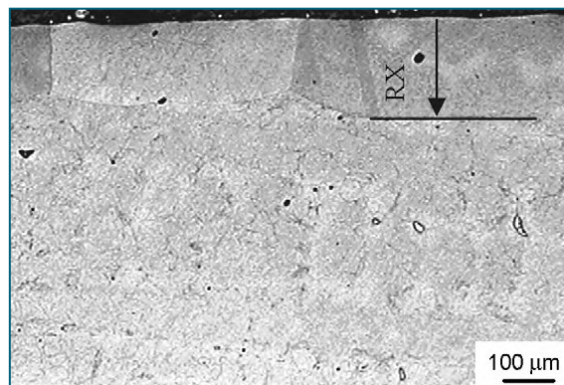


Fig. 7.21. Schematic diagram of the measurement of the recrystallized depth [182]

Re-deposited Layer

Programming errors or tool selection errors can lead to contact of non cutting tool parts with the machined surface. This usually rare event could lead to overheating and/or microstructural distortion and even cracks at the component surface. Another reason for overheating may be the absence of coolant or out of range cutting parameters. Fig. 7.22 presents the result of intended abusive cutting conditions at the surface of a hole. The micro-structure is heavily distorted and parent material is redeposited. Provided that such events will of course be noticed it must be taken into account that there could remain some damage after rework of the surface [173].

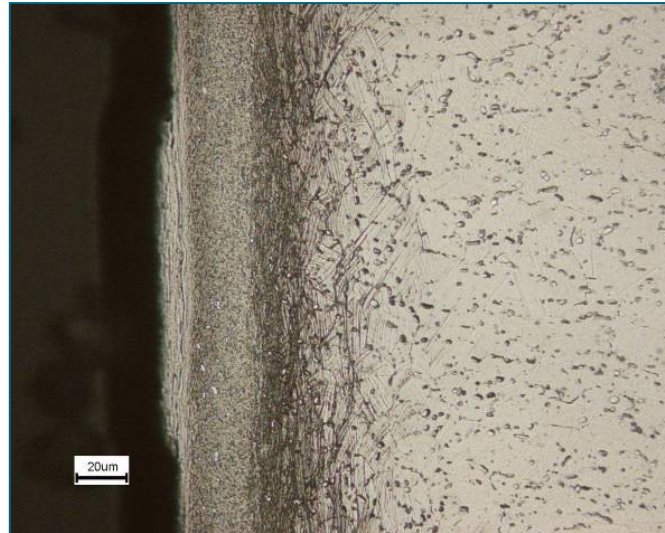


Fig. 7.22. Redeposited layer [173]

7.3. Reports and results

7.3.1. Visual Inspection results

Standard Tests

T_1		
V45	Fo.10	Ap 0.3
Defect type	Detected	Entity
Scores	N	
Scratches	Y	few
Orange Peel	N	
Chatter	N	
Cracks	N	
Inclusion	N	
Discoloration	N	
Burr	N	
Final Evaluation: 12/15		

T_2		
V45	Fo.125	Ap 0.3
Defect type	Detected	Entity
Scores	N	
Scratches	N	
Orange Peel	N	
Chatter	N	
Cracks	N	
Inclusion	N	
Discoloration	N	
Burr	N	
Final Evaluation: 14/15		

T_3		
V45	Fo.15	Ap 0.3
Defect type	Detected	Entity
Scores	N	
Scratches	N	
Orange Peel	N	
Chatter	N	
Cracks	N	
Inclusion	N	
Discoloration	N	
Burr	N	
Final Evaluation: 14/15		

T_4		
V50	Fo.10	Ap 0.3
Defect type	Detected	Entity
Scores	N	
Scratches	N	
Orange Peel	N	
Chatter	N	
Cracks	N	
Inclusion	N	
Discoloration	N	
Burr	N	
Final Evaluation: 14/15		

T_5		
V50	Fo.125	Ap 0.3
Defect type	Detected	Entity
Scores	N	
Scratches	N	
Orange Peel	N	
Chatter	N	
Cracks	N	
Inclusion	N	
Discoloration	N	
Burr	N	
Final Evaluation: 14/15		

T_6		
V50	Fo.15	Ap 0.3
Defect type	Detected	Entity
Scores	Y	Due to handling
Scratches	N	
Orange Peel	N	
Chatter	N	
Cracks	N	
Inclusion	N	
Discoloration	N	
Burr	N	
Final Evaluation: 12/15		

T_7		
V55	Fo.10	Ap 0.3
Defect type	Detected	Entity
Scores	N	
Scratches	N	
Orange Peel	N	
Chatter	N	
Cracks	N	
Inclusion	N	
Discoloration	N	
Burr	N	
Final Evaluation: 14/15		

T_8		
V55	Fo.125	
Defect type	Detected	Entity
Scores	N	
Scratches	Y	~10
Orange Peel	N	
Chatter	N	
Cracks	N	
Inclusion	N	
Discoloration	N	
Burr	N	
Final Evaluation: 11/15		

T_9		
V55	Fo.15	
Defect type	Detected	Entity
Scores	N	
Scratches	N	
Orange Peel	N	
Chatter	N	
Cracks	N	
Inclusion	N	
Discoloration	N	
Burr	N	
Final Evaluation: 14/15		

Severe Cutting Conditions Tests

T_1H		
V80	Fo.15	Cool
Defect type	Detected	Entity
Scores	Y	(?)
Scratches	N	
Orange Peel	N	
Chatter	N	
Cracks	N	
Inclusion	N	
Discoloration	N	
Burr	N	
Final Evaluation: 8/15		

T_2H		
V80	Fo.30	Cool
Defect type	Detected	Entity
Scores	Y	In some parts of circumference, not deep
Scratches	Y	Very superficial
Orange Peel	N	
Chatter	N	
Cracks	N	
Inclusion	N	
Discoloration	N	
Burr	N	
Final Evaluation: 7/15		

T_3H		
V100	Fo.15	Cool
Defect type	Detected	Entity
Scores	N	
Scratches	Y	Superficial
Orange Peel	N	
Chatter	N	
Cracks	N	
Inclusion	N	
Discoloration	N	
Burr	N	
Final Evaluation: 10/15		

T_4H		
V100	Fo.30	Cool
Defect type	Detected	Entity
Scores	N	
Scratches	Y	Superficial
Orange Peel	N	
Chatter	N	
Cracks	N	
Inclusion	N	
Discoloration	N	
Burr	N	
Final Evaluation: 10/15		

T_5H		
V80	Fo.15	Dry
Defect type	Detected	Entity
Scores	N	
Scratches	Y	Deeper than usual
Orange Peel	N	
Chatter	N	
Cracks	N	
Inclusion	N	
Discoloration	N	
Burr	N	
Final Evaluation: 11/15		

T_6H		
V80	Fo.30	Dry
Defect type	Detected	Entity
Scores	Y	All along the circumference
Scratches	Y	Superficial
Orange Peel	N	
Chatter	N	
Cracks	N	
Inclusion	N	
Discoloration	N	
Burr	N	
Final Evaluation: 8/15		

T_7H		
V100	Fo.15	Dry
Defect type	Detected	Entity
Scores	Y	All along the circumference
Scratches	Y	Superficial
Orange Peel	N	
Chatter	N	
Cracks	N	
Inclusion	N	
Discoloration	N	
Burr	N	
Final Evaluation: 7/15		

T_8H		
V100	Fo.30	Dry
Defect type	Detected	Entity
Scores	Y	All along the circumference
Scratches	Y	Superficial
Orange Peel	N	
Chatter	N	
Cracks	N	
Inclusion	N	
Discoloration	N	
Burr	N	
Final Evaluation: 6/15		

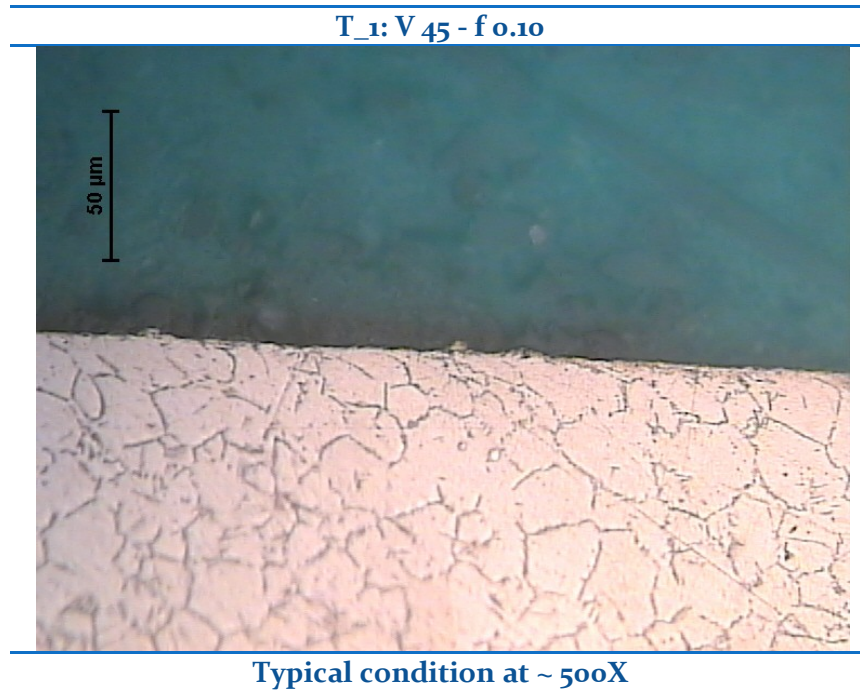
7.3.2. FPI results

FPI Tests did NOT evidence any surface defect, neither in Standard Tests nor in Severe cutting conditions tests.

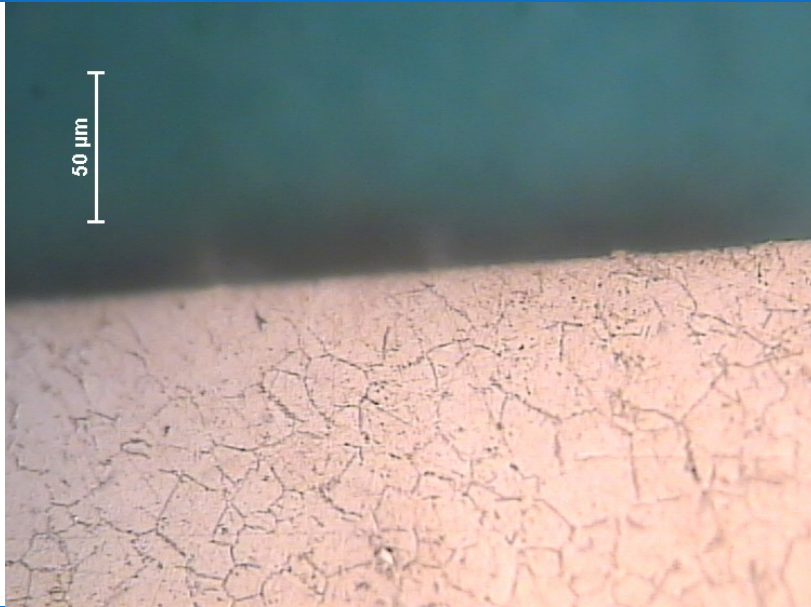
7.3.3. Metallographic tests results

Standard Tests

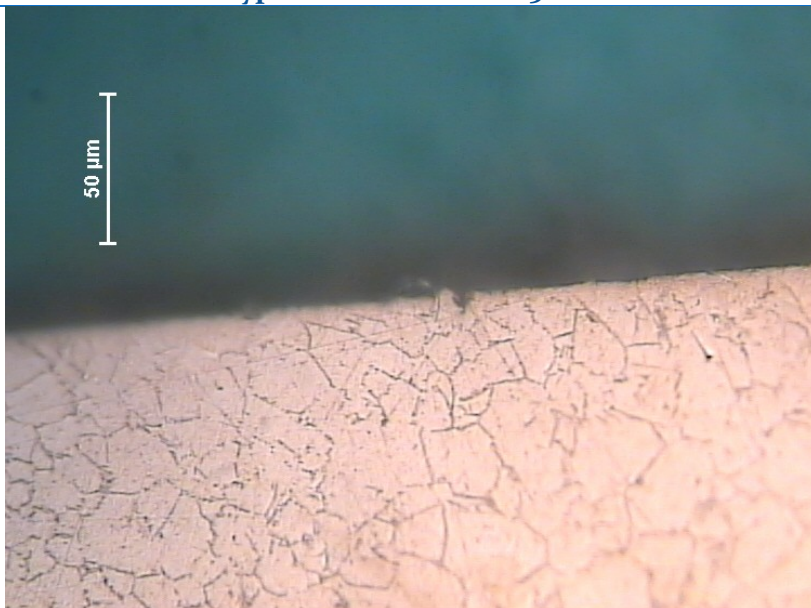
Tests carried out by Aviogroup SpA



T_2: V 45 - f 0.125

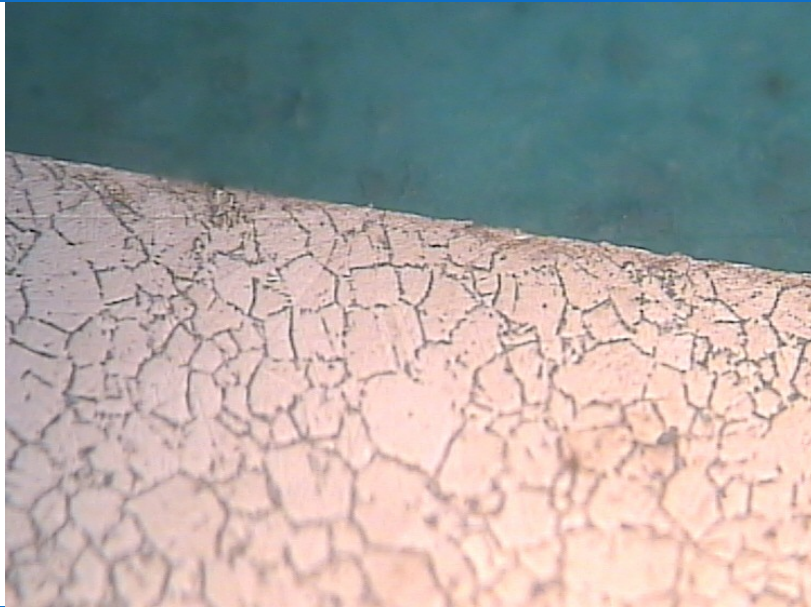


Typical condition at ~ 500X

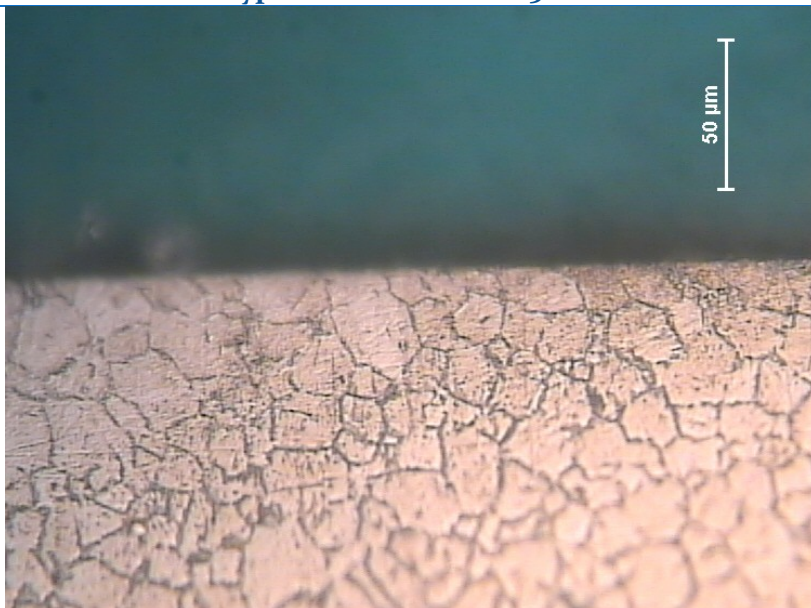


Worst condition at ~ 500X

T₃: V₄₅ - f 0.15

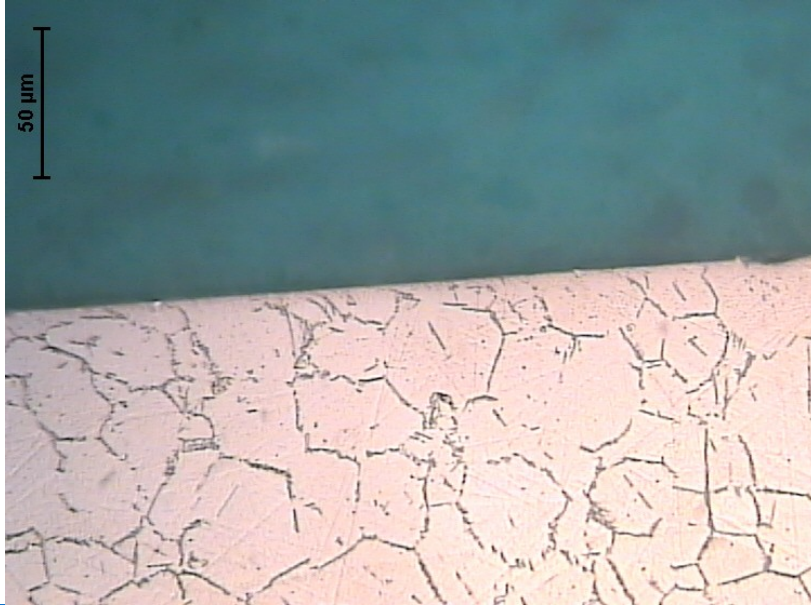


Typical condition at ~ 500X



Worst condition at ~ 500X

T_4: V 50 - f 0.10

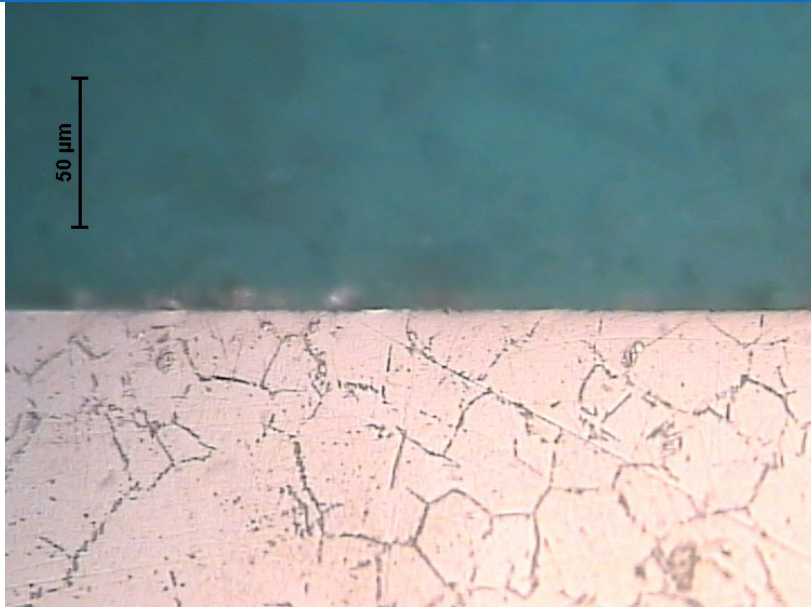


Typical condition at ~ 500X



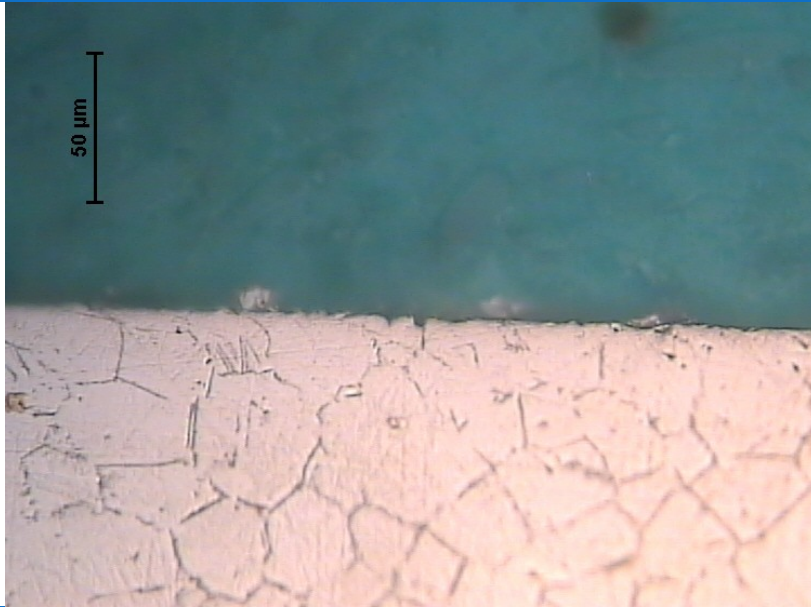
Worst condition at ~ 500X

T_5: V 50 - f 0.125

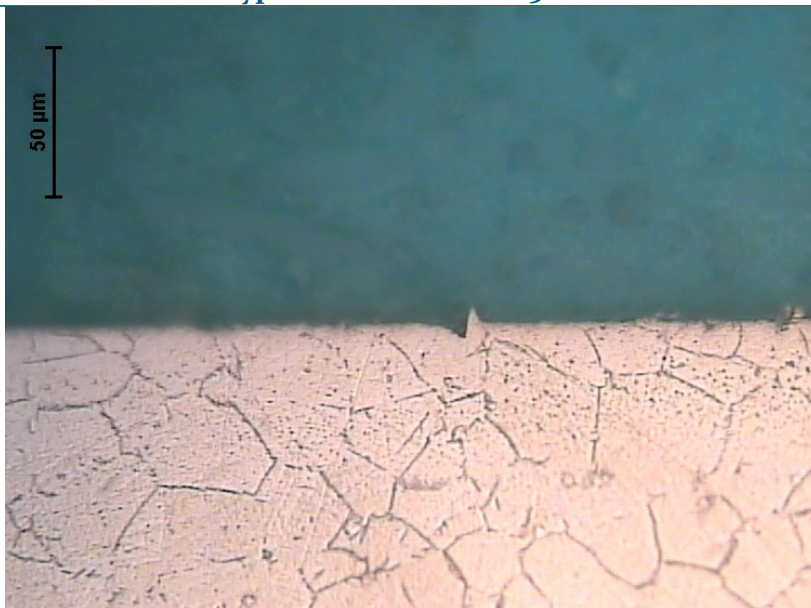


Typical condition at ~ 500X

T_6: V50 - f 0.15



Typical condition at ~ 500X



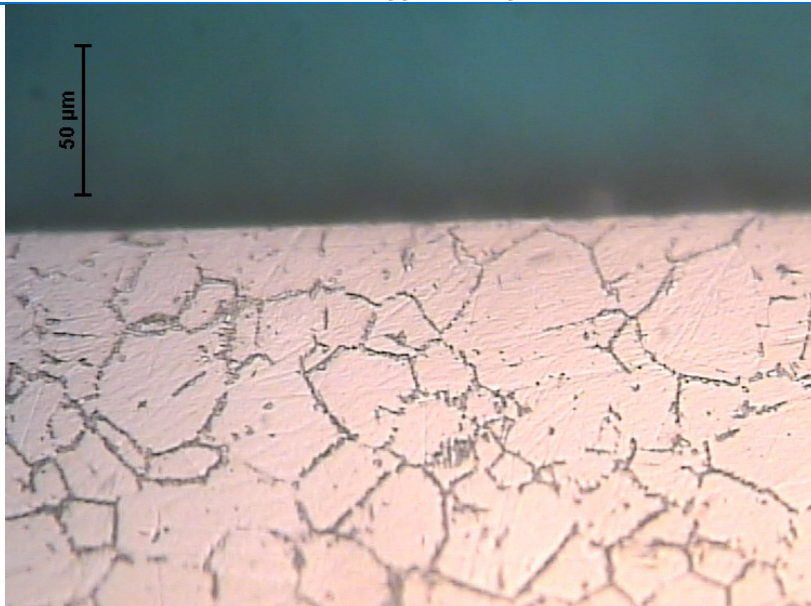
Worst condition at ~ 500X

T_7: V 55 - f 0.10



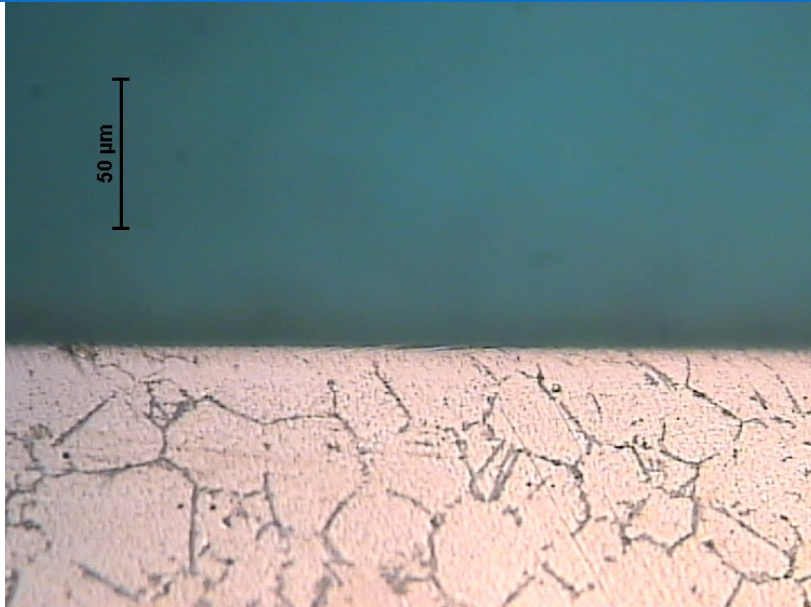
Typical condition at ~ 500X

T_8: V 55 - f 0.125



Typical condition at ~ 500X

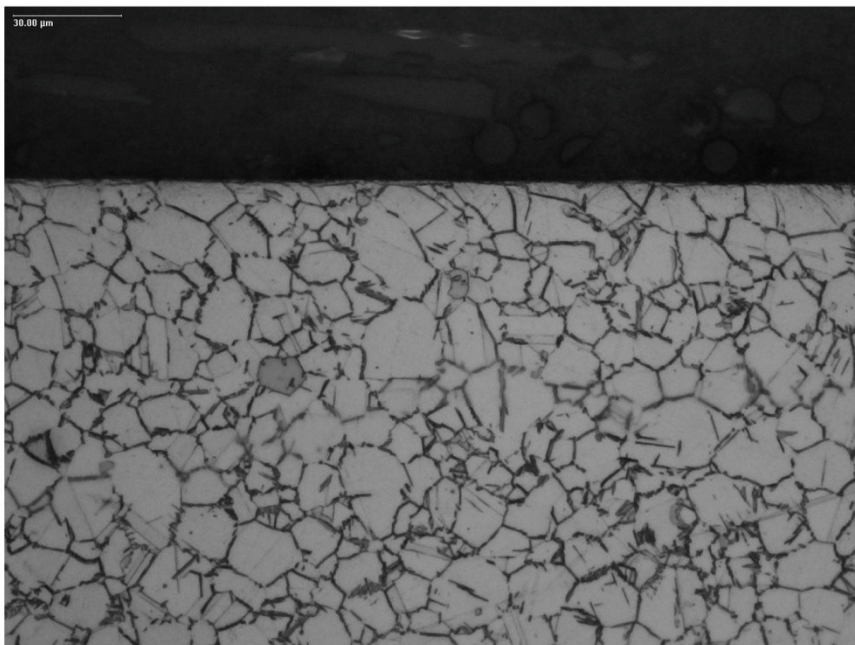
T_9: V 55 - f 0.15



Typical condition at ~ 500X

Severe Cutting Conditions Tests

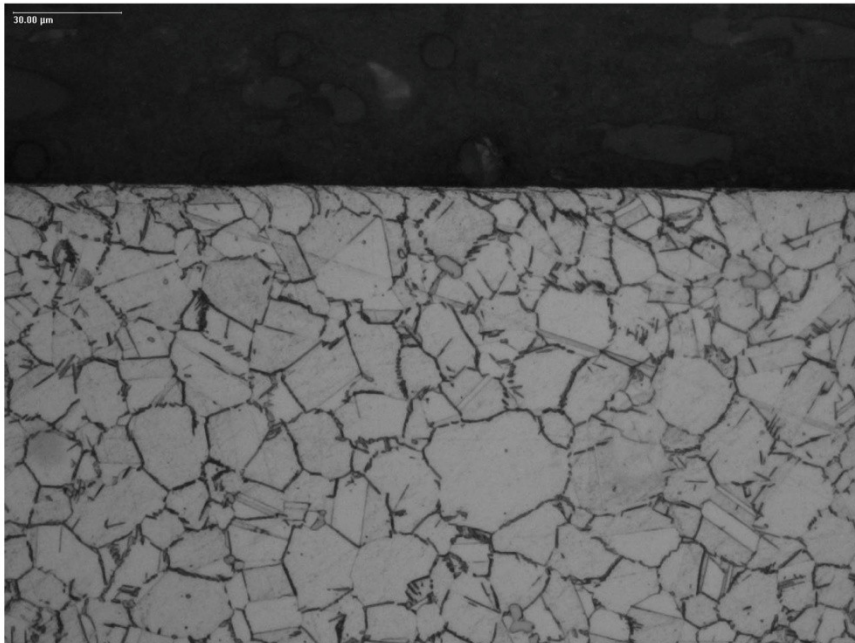
Tests carried out by Aviogroup SpA



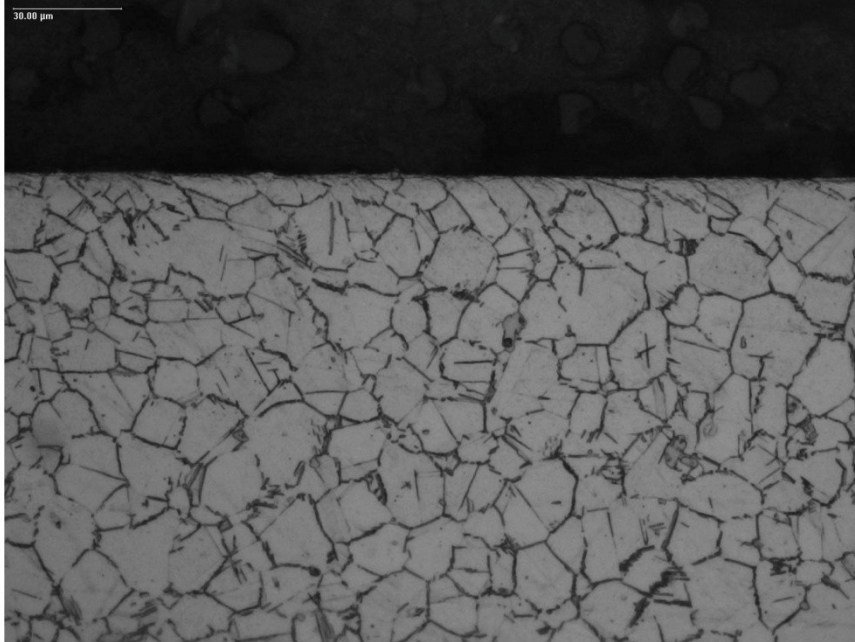
Test T_1H [v=80 m/min, f=0.15 mm/rev, cooled]
1.5 μm isolated WEL, 11 μm intermittent Distorted Structure



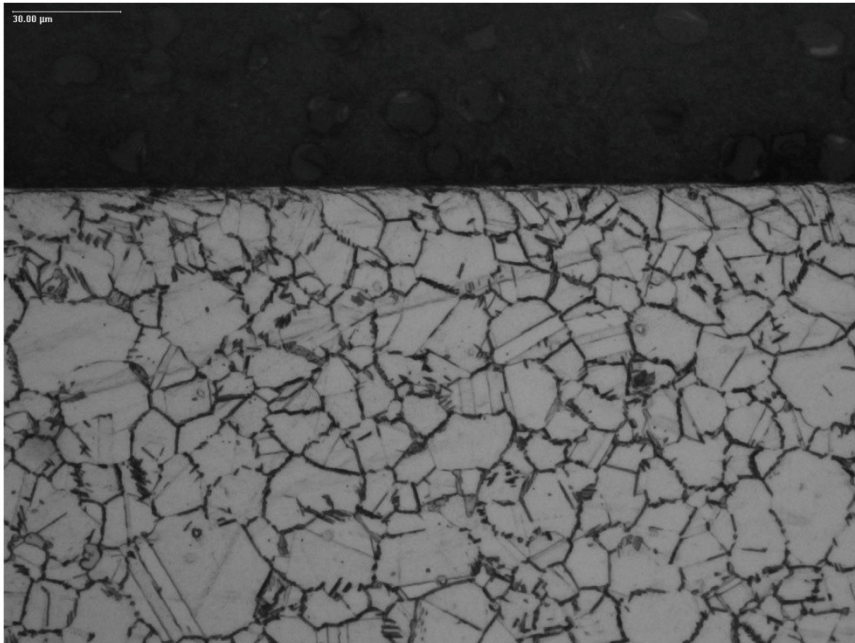
Test T_2H [$v=80$ m/min, $f=0.30$ mm/rev, cooled]
1 μm isolated WEL, 6 μm occasional Distorted Structure



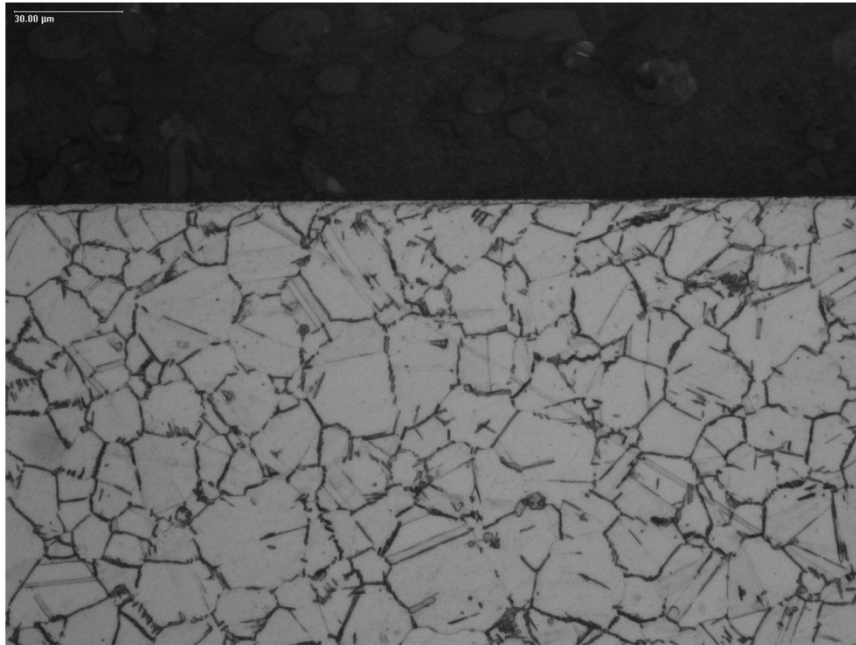
Test T_3H [$v=100$ m/min, $f=0.15$ mm/rev, cooled]
1.5 μm isolated WEL, 9 μm intermittent Distorted Structure



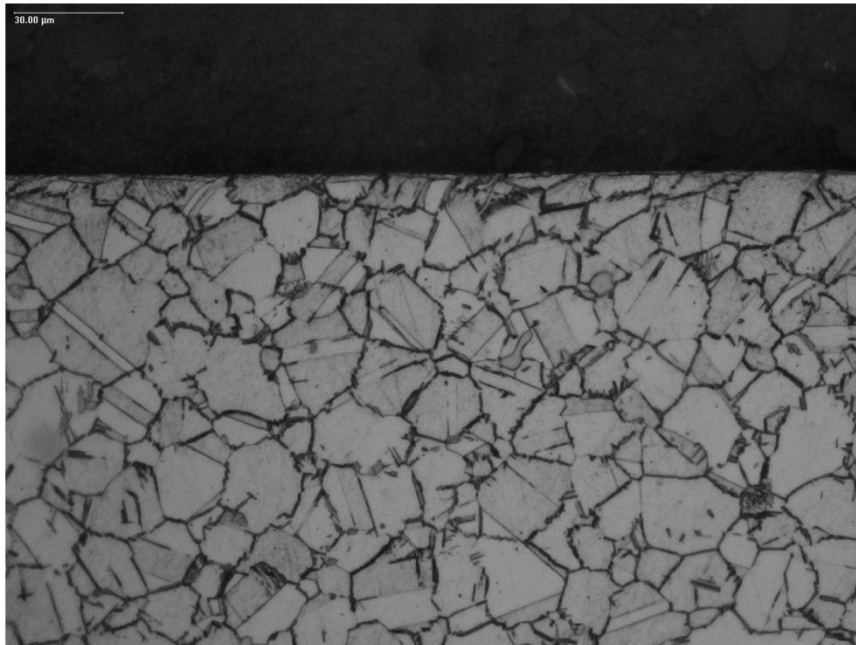
Test T_4H [$v=100$ m/min, $f=0.30$ mm/rev, cooled]
1.5 μm isolated WEL, 12 μm intermittent Distorted Structure



Test T_5H [$v=80$ m/min, $f=0.15$ mm/rev, dry]
1 μm intermittent WEL, 9 μm intermittent Distorted Structure



Test T_6H [$v=80$ m/min, $f=0.30$ mm/rev, dry]
1.5 μm occasional WEL, 12 μm intermittent Distorted Structure



Test T_7H [$v=100$ m/min, $f=0.15$ mm/rev, dry]
1.5 μm occasional WEL, 12 μm intermittent Distorted Structure



Test T_8H [$v=100$ m/min, $f=0.30$ mm/rev, dry]
 $0 \mu\text{m}$ WEL, $9\mu\text{m}$ intermittent Distorted Structure

1.1.1. Micro hardness results

Notations

Hardness Tests (Vickers 300g)

d = Arithmetic mean of the two diagonals, d_1 and d_2 in mm

D = distance from edge

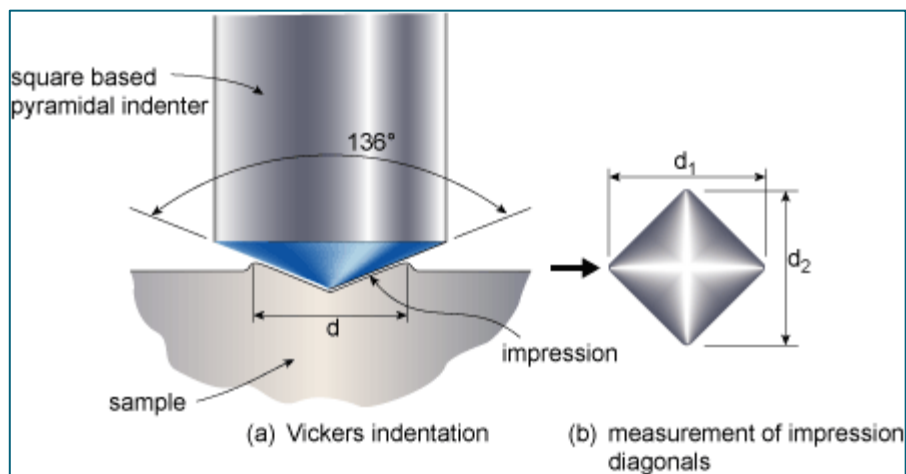


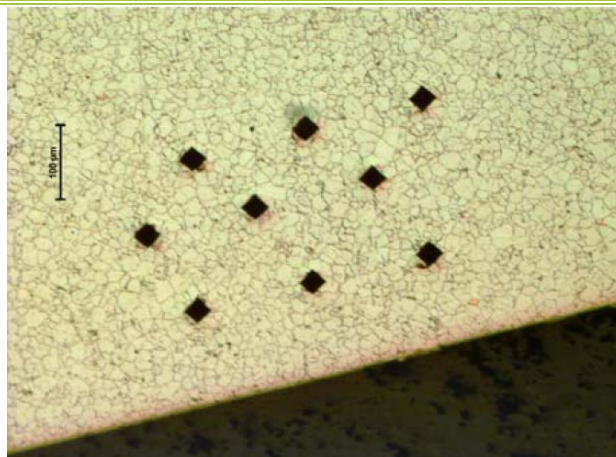
Fig. 7.23.

Standard Tests

T ₁ : V ₄₅ - f 0.10				
d(μm)	HV	D(μm)	Row	HV average
34.7	462	107	1	458
34.9	457	112	1	
35.0	454	113	1	
34.5	467	193	2	467
34.4	470	216	2	
34.6	465	229	2	
34.5	467	319	3	467
34.4	470	326	3	
34.6	465	340	3	

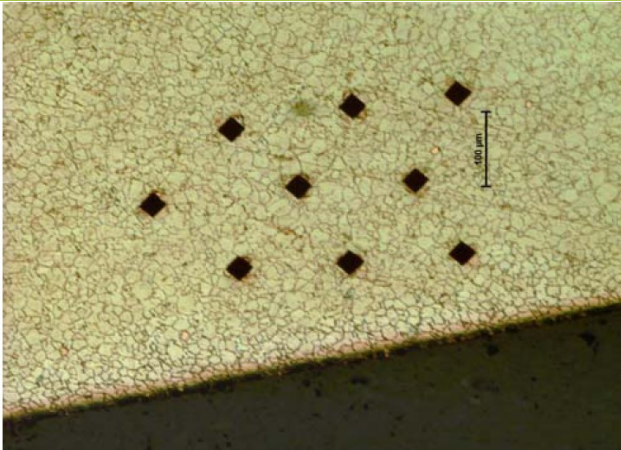
T ₂ : V ₄₅ - f 0.125				
d(μm)	HV	D(μm)	Row	HV average
34.3	473	114	1	473
34.3	473	105	1	
34.3	473	91	1	
34.7	462	229	2	471
34.9	457	206	2	
33.6	493	220	2	
34.6	465	297	3	459
34.9	457	324	3	
35.0	454	341	3	

T ₃ : V ₄₅ - f 0.15				
d(μm)	HV	D(μm)	Row	HV average
34.3	473	126	1	474
33.8	487	128	1	
34.7	462	127	1	
34.3	473	243	2	473
34.5	467	244	2	
34.1	478	242	2	
34.7	462	331	3	472
34.0	481	330	3	
34.3	473	328	3	



Hardness Impressions @100X

T_4: V 50 - f 0.10				
d(μm)	HV	D(μm)	Row	HV average
33.9	484	108	1	478
34.2	476	121	1	
34.3	473	142	1	
33.9	484	217	2	489
33.8	487	236	2	
33.5	496	247	2	
34.9	457	318	3	474
34.2	476	328	3	
33.7	490	330	3	



Hardness Impressions @100X

T_5: V 50 - f 0.125				
d(μm)	HV	D(μm)	Row	HV average
34.1	478	77*	1	468
34.6	465	119	1	
34.7	462	106	1	
34.0	481	210	2	474
34.3	473	205	2	
34.5	467	205	2	
34.8	459	270	3	467
34.4	470	265	3	
34.3	473	266	3	

* distance from edge less than 2,5 times diagonal lenght

T_6: V ₅₀ - f 0.15				
d(μm)	HV	D(μm)	Row	HV average
34.5	470	95	1	467
34.1	478	105	1	
35.0	454	106	1	
34.3	473	194	2	469
34.5	467	200	2	
34.5	467	204	2	
34.2	476	283	3	473
34.1	478	268	3	
34.6	465	290	3	

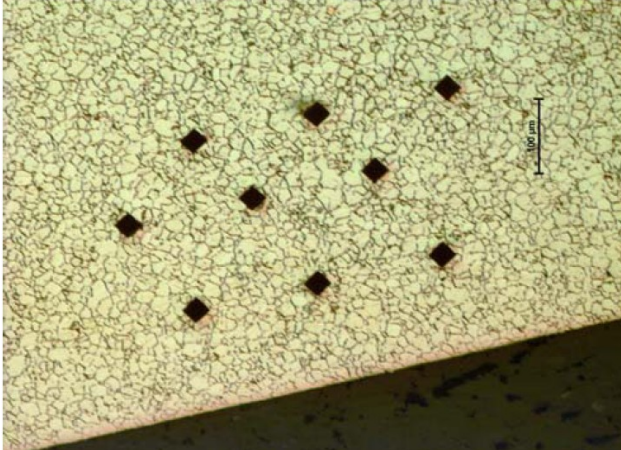
T_7: V ₅₅ - f 0.10				
d(μm)	HV	D(μm)	Row	HV average
34.5	467	95	1	469
34.4	470	111	1	
34.4	470	89	1	
34.2	476	237	2	473
34.5	467	267	2	
34.2	476	241	2	
34.3	473	369	3	470
34.6	465	378	3	
34.3	473	376	3	

T_8: V ₅₅ - f 0.125				
d(μm)	HV	D(μm)	Row	HV average
34.5	467	75	1	465
34.7	462	100	1	
34.6	465	117	1	
34.2	476	191	2	471
34.4	470	207	2	
34.5	467	198	2	
34.3	473	313	3	473
34.4	470	296	3	
34.2	476	288	3	

T_9: V ₅₅ - f 0.15				
d(μm)	HV	D(μm)	Row	HV average
34.8	459	132	1	474
33.9	484	115	1	
34.1	478	110	1	
34.5	467	234	2	466
34.6	465	230	2	
34.6	465	230	2	
34.2	476	350	3	473
34.3	473	372	3	
34.0	470	363	3	

Severe Cutting Conditions Tests Microhardness Measurements

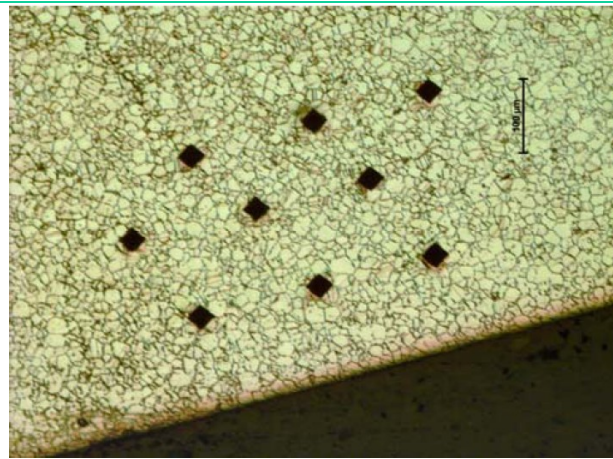
T_1H: V 80 - f 0.15 - Cooled				
d(μm)	HV	D(μm)	Row	HV average
34.4	470	136	1	470
34.3	473	135	1	
34.5	467	137	1	
34.5	467	267	2	465
34.8	459	266	2	
34.4	470	267	2	
34.9	457	353	3	465
34.4	470	358	3	
34.5	467	358	3	



Hardness Impressions @100X

T₂H: V 80 - f 0.30 - Cooled

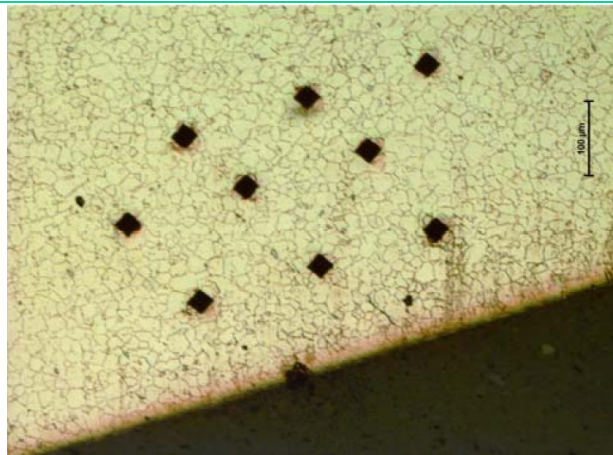
d(μm)	HV	D(μm)	Row	HV average
34.7	462	128	1	464
34.3	473	128	1	
34.9	457	131	1	
34.3	473	250	2	467
34.5	467	251	2	
34.7	462	254	2	
34.0	481	345	3	475
34.5	467	345	3	
34.1	478	343	3	



Hardness Impressions @100X

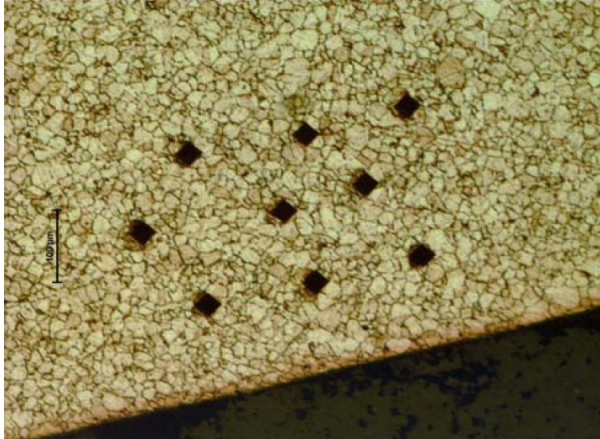
T₃H: V 100 - f 0.15 - Cooled

d(μm)	HV	D(μm)	Row	HV average
33.8	487	138	1	475
34.3	473	137	1	
34.6	465	136	1	
34.7	462	265	2	471
33.9	484	267	2	
34.5	467	262	2	
34.8	459	352	3	466
34.3	473	358	3	
34.5	467	355	3	



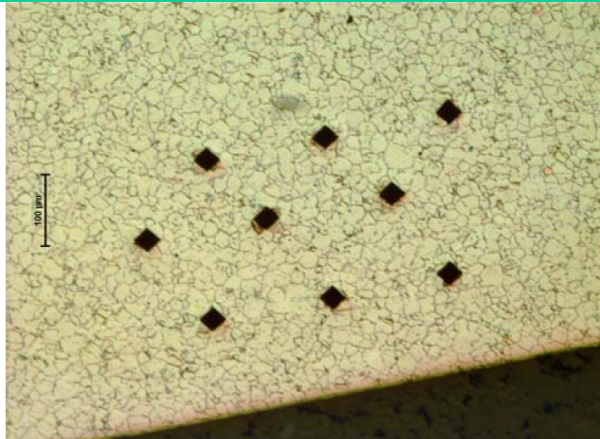
Hardness Impressions @100X

T_4H: V 100 - f 0.3 - Cooled				
d(μm)	HV	D(μm)	Row	HV average
34.0	481	125	1	476
34.6	465	123	1	
34.0	481	126	1	
34.6	465	239	2	461
35.1	451	230	2	
34.5	467	242	2	
35.3	446	330	3	445
35.2	449	326	3	
35.5	441	335	3	



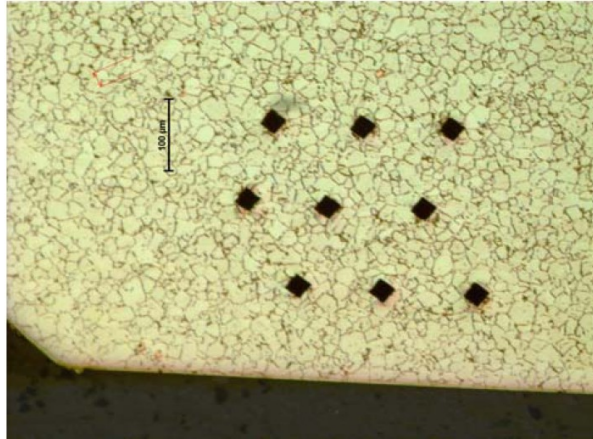
Hardness Impressions @100X

T_5H: V 80 - f 0.15 - Dry				
d(μm)	HV	D(μm)	Row	HV average
34.9	457	137	1	461
34.8	459	135	1	
34.5	467	137	1	
34.5	467	262	2	467
34.3	473	262	2	
34.7	462	264	2	
34.3	473	359	3	471
34.4	470	359	3	
34.4	470	359	3	



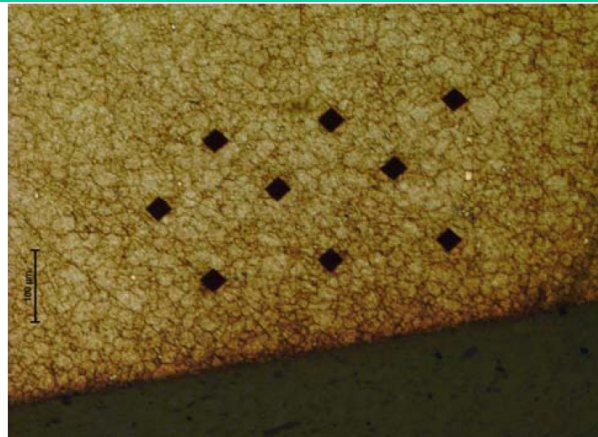
Hardness Impressions @100X

T_6H: V 80 - f 0.15 - Dry				
d(μm)	HV	D(μm)	Row	HV average
34.2	476	131	1	477
34.1	478	129	1	
34.2	476	133	1	
34.2	476	251	2	474
34.5	467	245	2	
34.1	478	249	2	
34.0	481	361	3	470
34.5	467	358	3	
34.7	462	363	3	



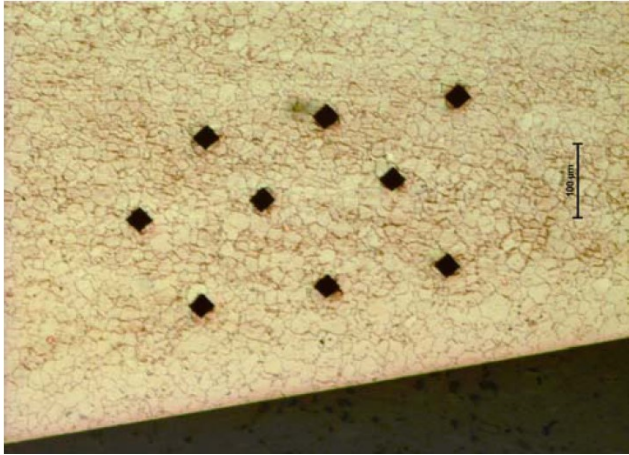
Hardness Impressions @100X

T_7H: V 100 - f 0.15 - Dry				
d(μm)	HV	D(μm)	Row	HV average
34.3	473	118	1	470
34.2	476	120	1	
34.7	462	121	1	
34.9	457	229	2	466
34.5	467	228	2	
34.3	473	232	2	
34.1	478	307	3	474
34.7	462	311	3	
34.0	481	312	3	



Hardness Impressions @100X

T_8H: V ₁₀₀ - f 0.30 - Dry				
d(μm)	HV	D(μm)	Row	HV average
33.5	496	136	1	504
33.1	508	137	1	
33.1	508	138	1	
33.2	505	264	2	497
33.5	496	264	2	
33.7	490	267	2	
33.4	499	359	3	499
33.1	508	360	3	
33.7	490	358	3	



Hardness Impressions @100X

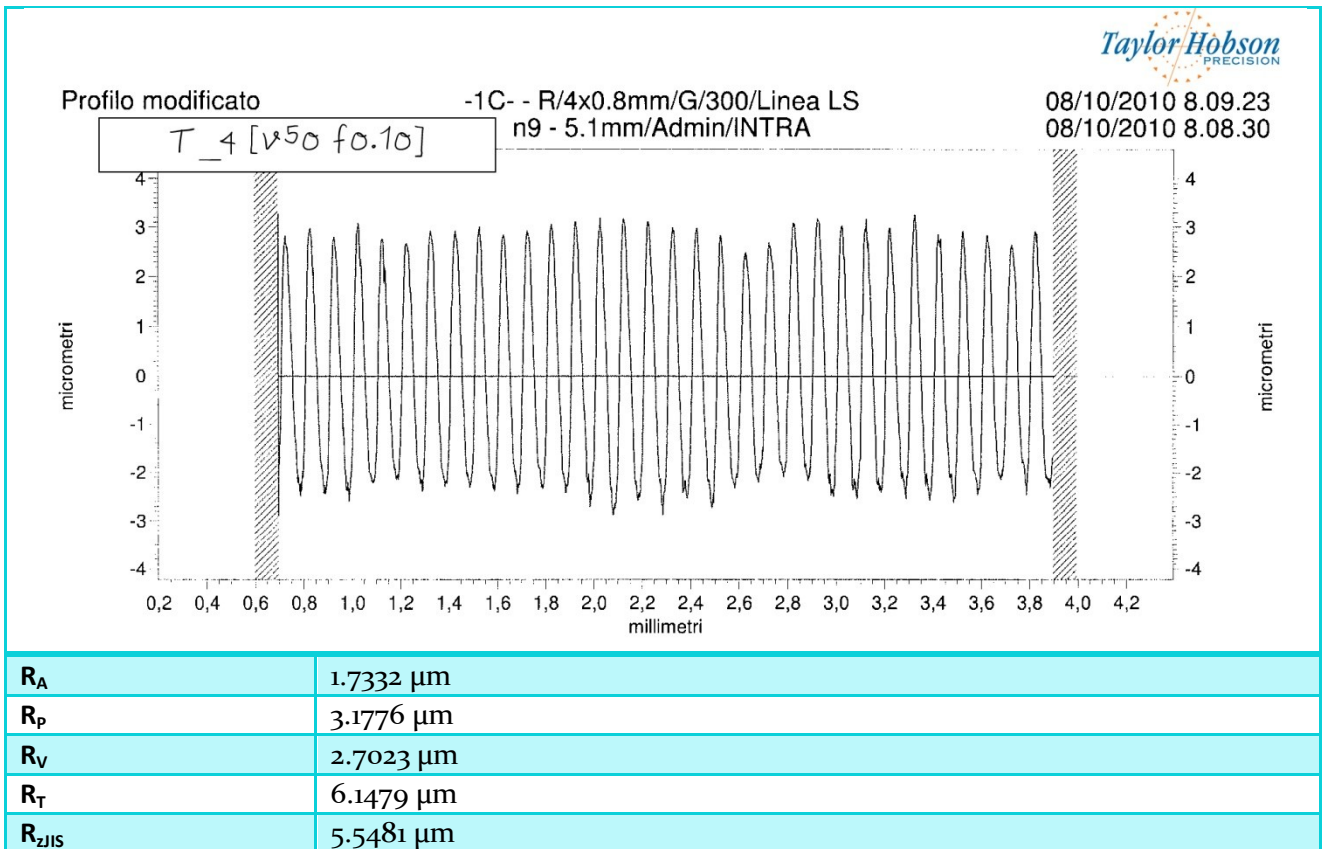
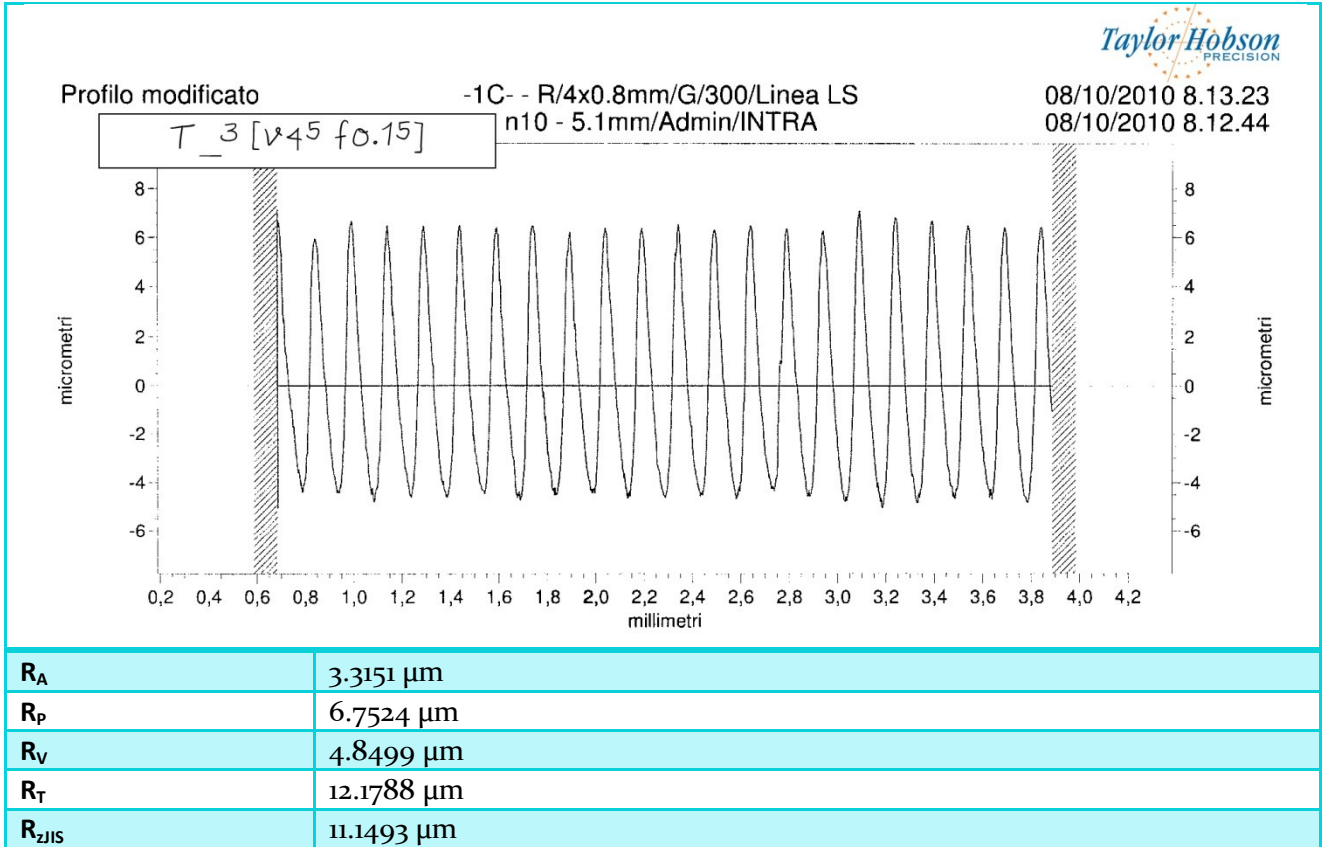
1.1.2. Roughness measurements reports

Roughness measurements are carried out on samples by using a Taylor Hobson roughness tester. The results are reported in the tables below.

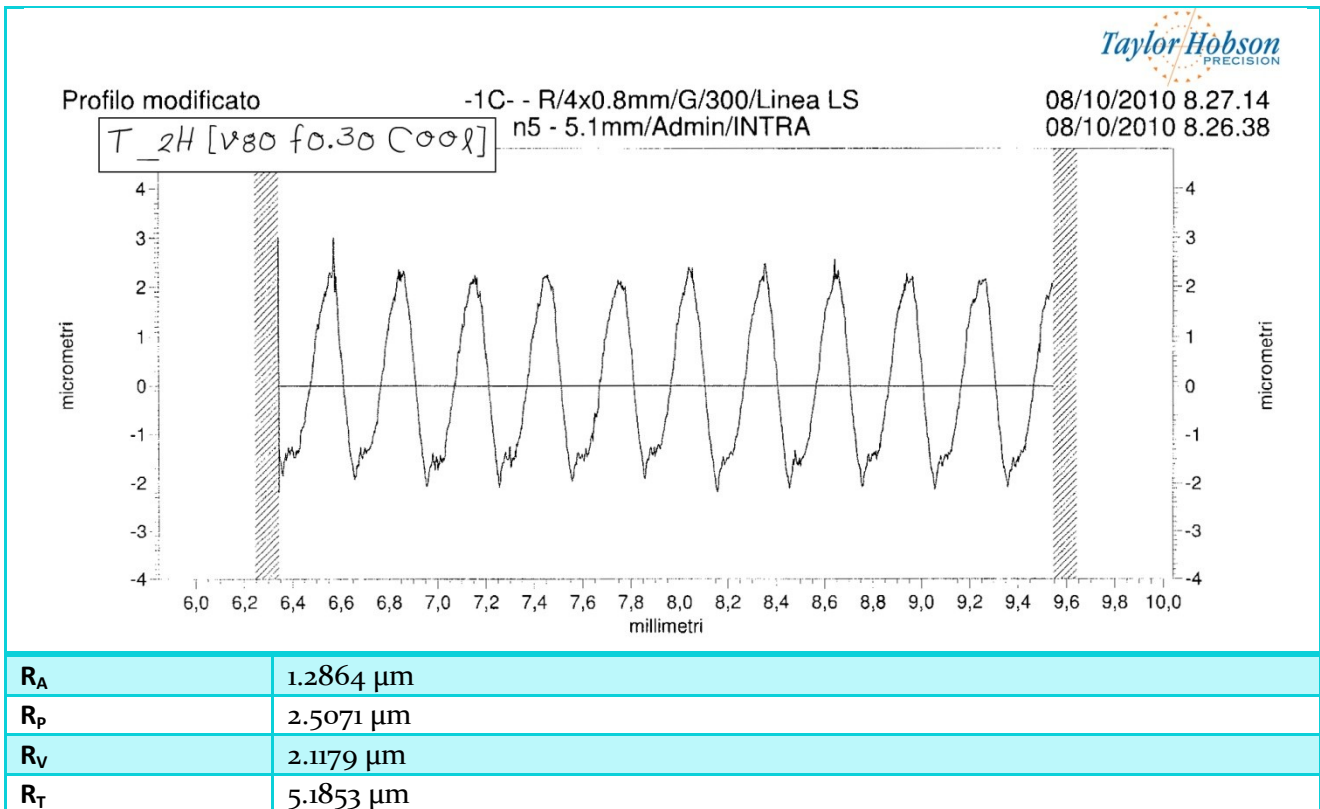
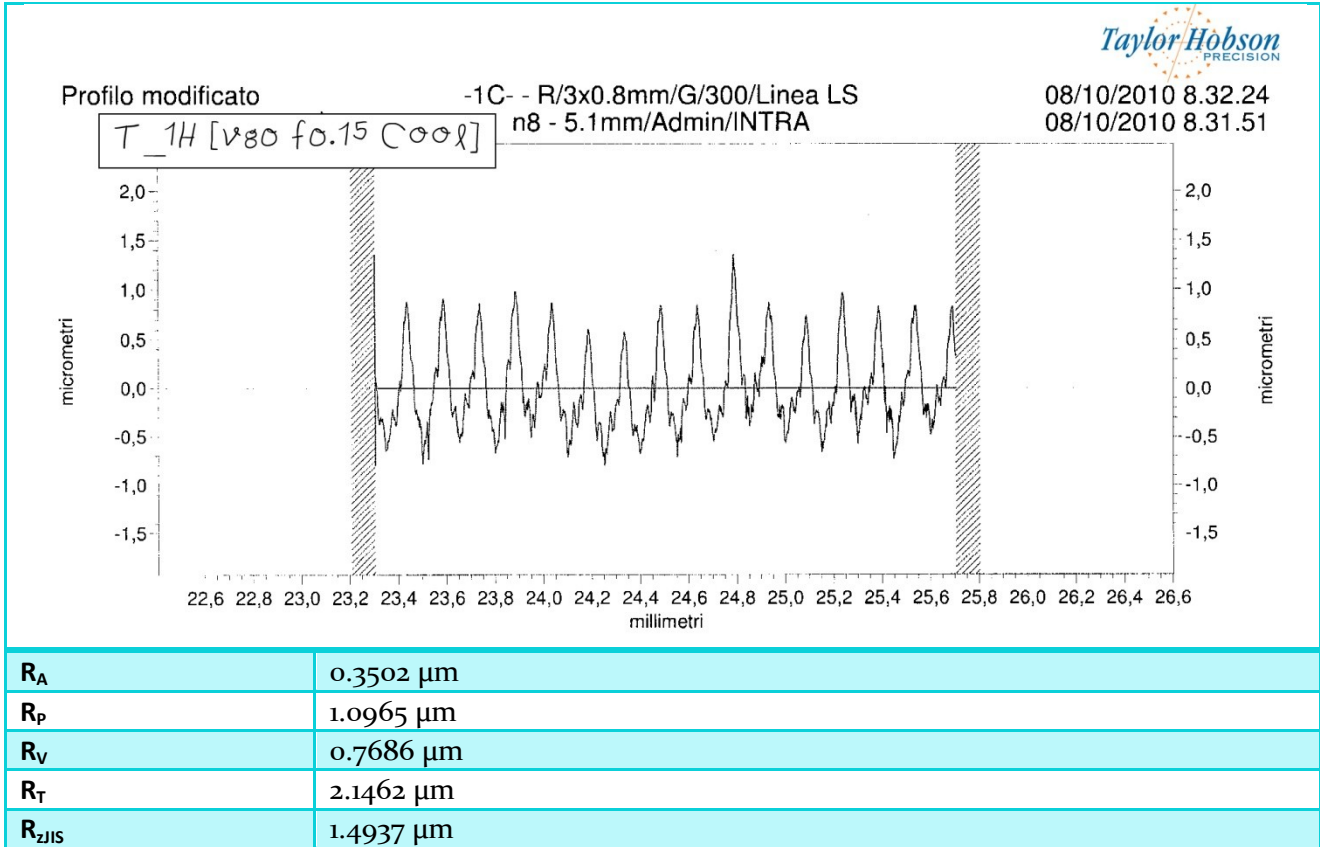
Table 7.5. Roughness parameters

Roughness parameters	
R _A	Arithmetic average of absolute values
R _p	Maximum peak height
R _v	Maximum valley depth
R _T	Maximum Height of the Profile
R _{ZJIS}	Japanese Industrial Standard for Rz, based on the five highest peaks and lowest valleys over the entire sampling length

Standard Tests



Severe Cutting Conditions Tests

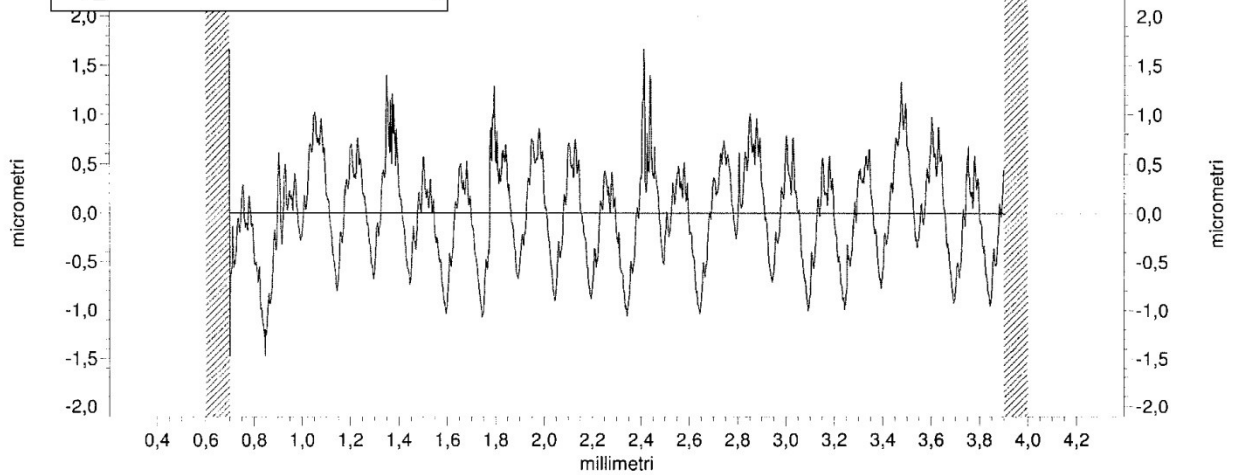


Profilo modificato

-1C- - R/4x0.8mm/G/300/Linea LS
n4 - 5.1mm/Admin/INTRA

08/10/2010 8.25.55
08/10/2010 8.25.21

T_3H [v100 fo.15 Cool]



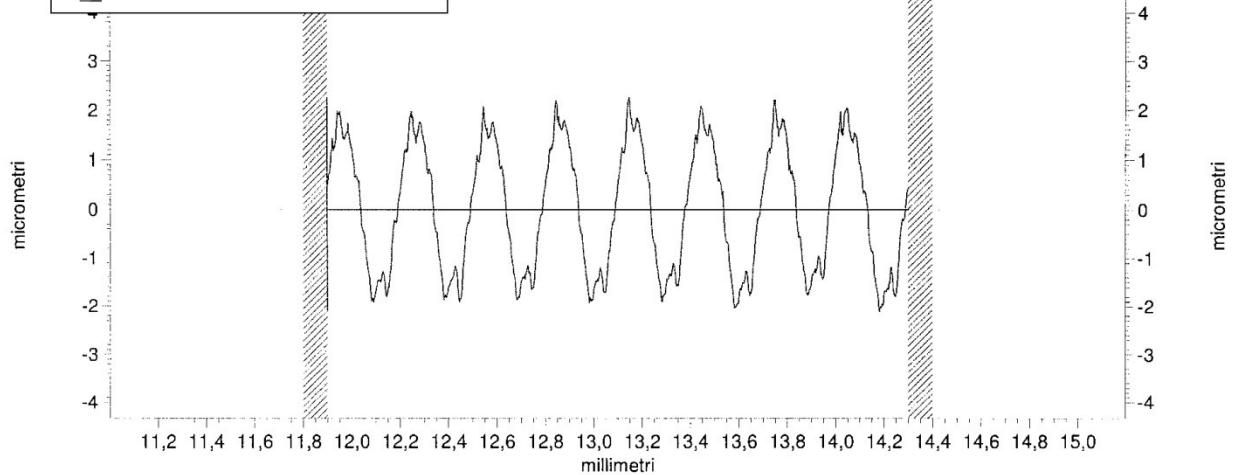
R_A	0.4279 μm
R_P	1.4225 μm
R_V	1.1493 μm
R_T	3.1398 μm
R_{Z15}	1.7243 μm

Profilo modificato

-1C- - R/3x0.8mm/G/300/Linea LS
n3 - 5.1mm/Admin/INTRA

08/10/2010 8.22.09
08/10/2010 8.21.35

T_4H [v100 fo.30 Cool]



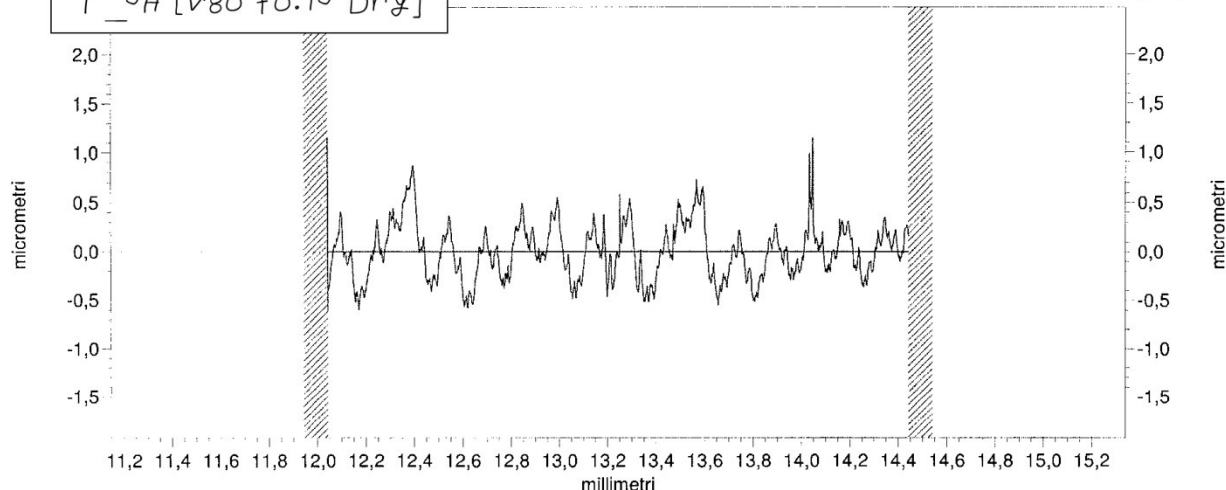
R_A	1.1726 μm
R_P	2.1774 μm
R_V	1.9801 μm
R_T	4.3643 μm

Profilo modificato

-1C- - R/3x0.8mm/G/300/Linea LS
n6 - 5.1mm/Admin/INTRA

08/10/2010 8.29.20
08/10/2010 8.28.45

T_5H [v80 f0.15 Dry]



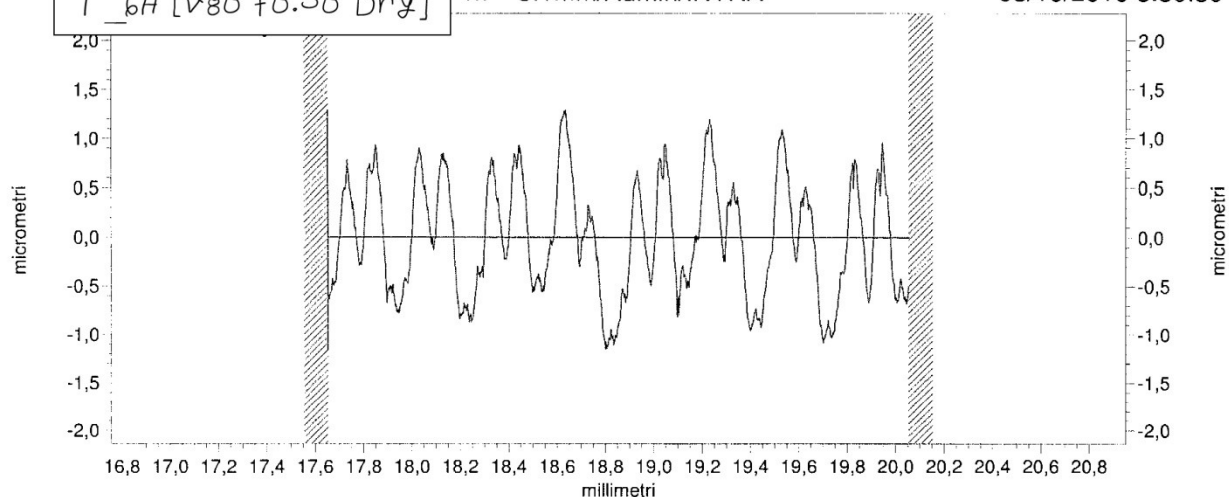
R_A	0.2258 μm
R_p	0.9111 μm
R_v	0.5554 μm
R_T	1.7409 μm
R_{zJIS}	0.9051 μm

Profilo modificato

-1C- - R/3x0.8mm/G/300/Linea LS
n7 - 5.1mm/Admin/INTRA

08/10/2010 8.31.02
08/10/2010 8.30.30

T_6H [v80 f0.30 Dry]



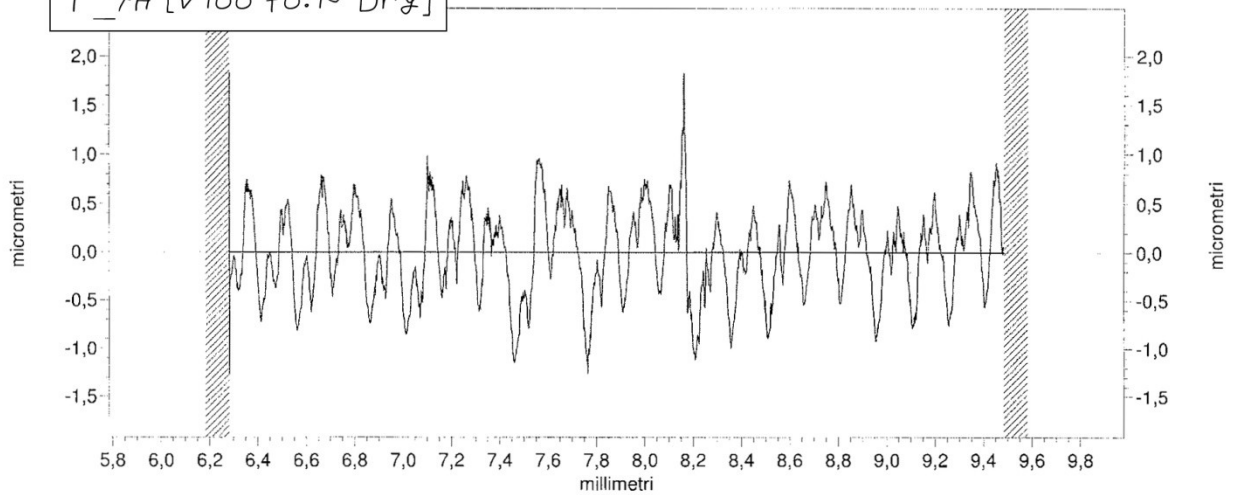
R_A	0.4978 μm
R_p	1.1037 μm
R_v	1.0371 μm
R_T	2.4434 μm
R_{zJIS}	1.4467 μm

Profilo modificato

-1C- - R/4x0.8mm/G/300/Linea LS
n2 - 5.1mm/Admin/INTRA

08/10/2010 8.20.33
08/10/2010 8.19.56

T_7H [v100 f0.15 Dry]



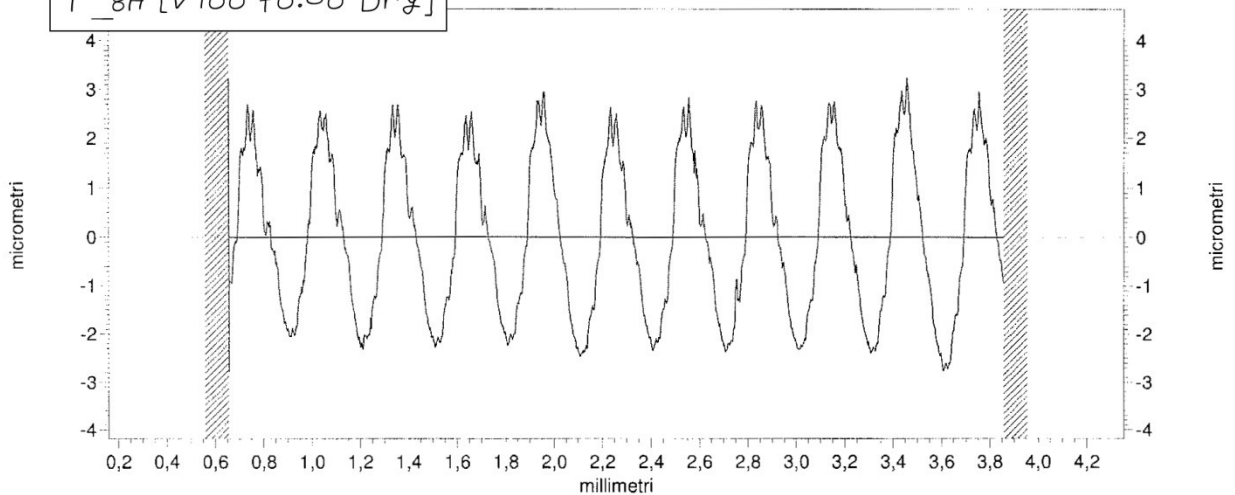
R_A	0.3786 μm
R_P	1.1270 μm
R_V	1.0380 μm
R_T	3.0915 μm
R_{Z15}	1.4958 μm

Profilo modificato

-1C- - R/4x0.8mm/G/300/Linea LS
n1 - 5.1mm/Admin/INTRA

08/10/2010 8.18.15
08/10/2010 8.17.34

T_8H [v100 f0.30 Dry]



R_A	1.4443 μm
R_P	2.9257 μm
R_V	2.4814 μm
R_T	5.9946 μm

8. Signal Processing and Features Extraction

8.1. Pre – processing

8.1.1. File format

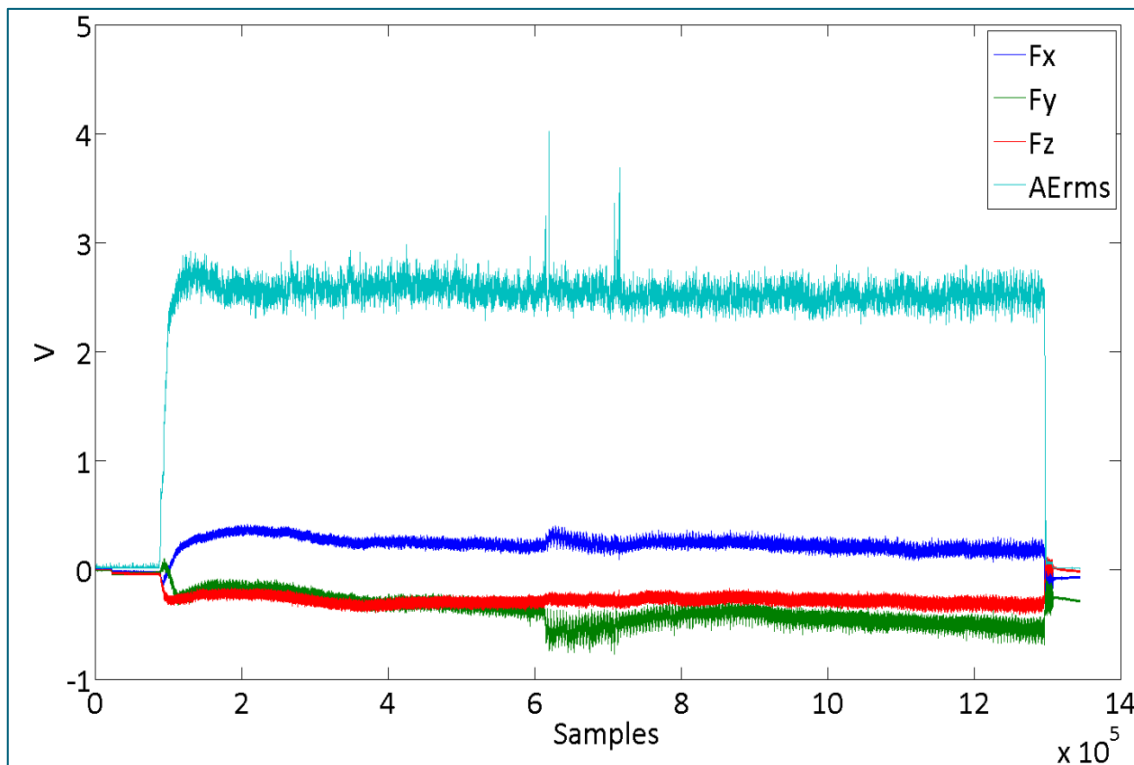
Labview allows to save the acquired signals in *.txt file compatible with all the operative systems. Nevertheless, Matlab needs a conversion in order to store the data in the workspace.

Among the Matlab resources, a file converter is available, txt2mat.m downloadable at [183], it quickly converts ascii files containing m-by-n numeric data, allowing for header lines.

For the Vibralog output files, the file format is *.dat. A file conversion is hence needed in order to process the signals in Matlab.

8.1.2. Signal segmentation

The raw signals (Fig. 8.1) coming from the stored data, needs to be pre-processed in order to be handled for further analysis.



8.1. Examples of raw signals

Signal head and tail were removed from each component of the whole signals. This operation is carried out manually, evaluating time by time the samplings to be removed.

After this preliminary operation, signals appear as in Fig. 8.2.

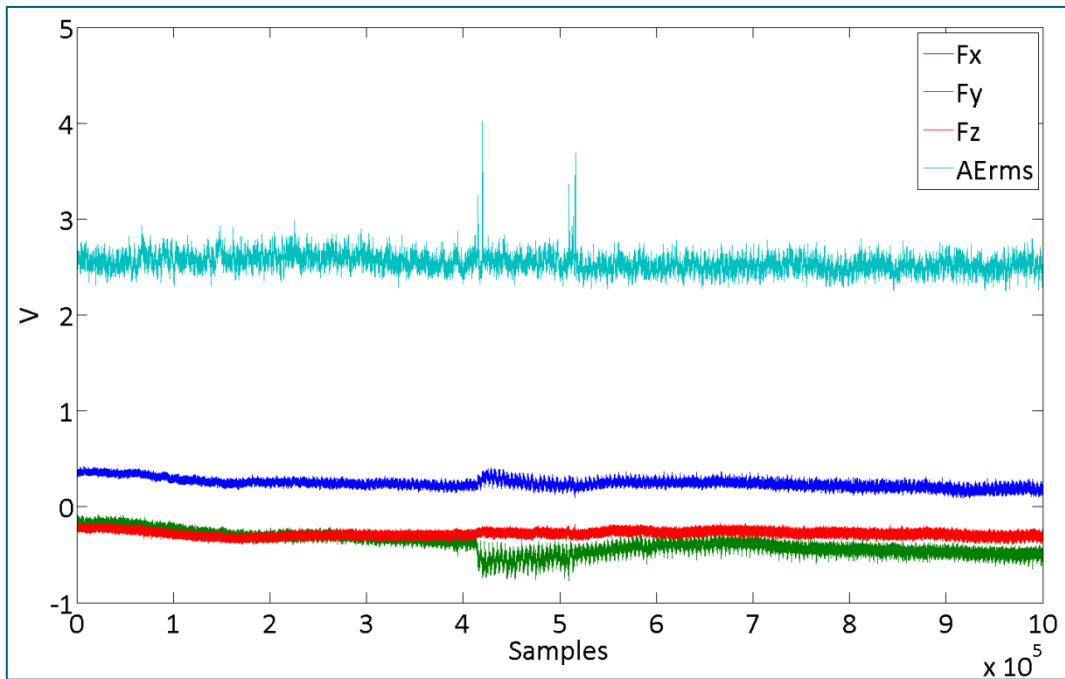
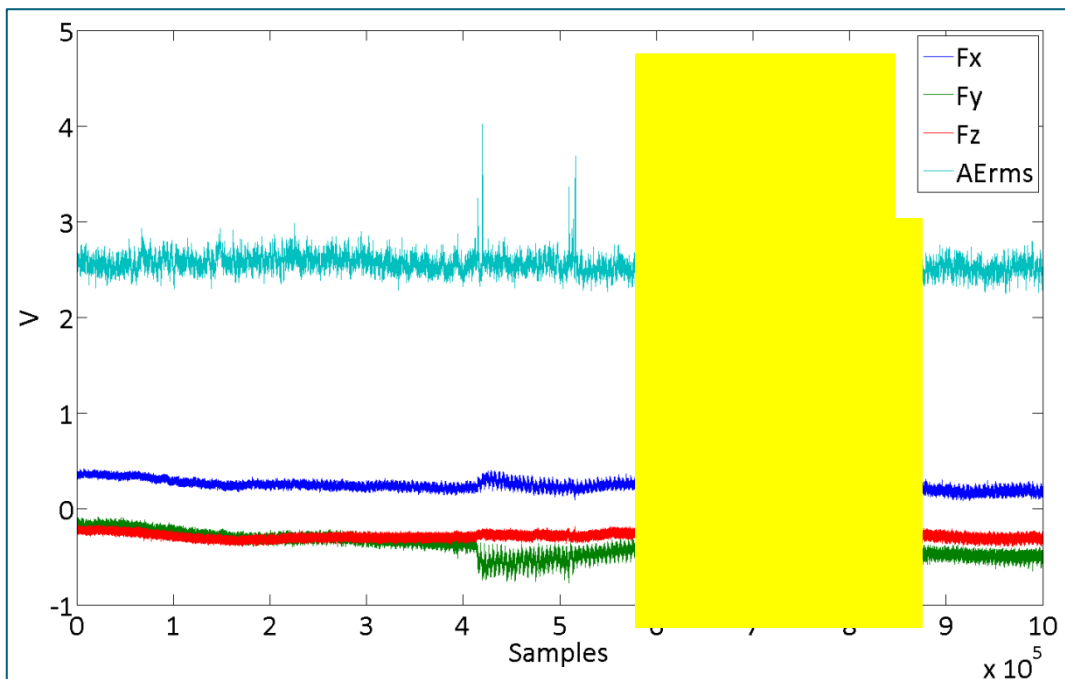


Fig. 8.2. First signal segmentation (head and tail removed)

Signal segmentation has been carried out by extracting a portion of signal as highlighted in Fig. 8.3. This operation is required in order to process an homogenous segment of signal. The number of samples per portion varies for each test and step.



8.3. Fig. Selected signal portion for segmentation (in yellow)

The signal segmentation has been carried out for all the signal components: F_x , F_y , F_z , AE_{RMS} , A_x , A_y , A_z , respectively for each experimental test and each step.

The file name to be given to each segmented signal set is made up in the following way:

- Test number, according to Tables 3.1 and 3.2.

- Step number

So, for example, the file related to the first step of Test #1 is `Test1_step1.mat`

8.1.3. Signal Subdivision

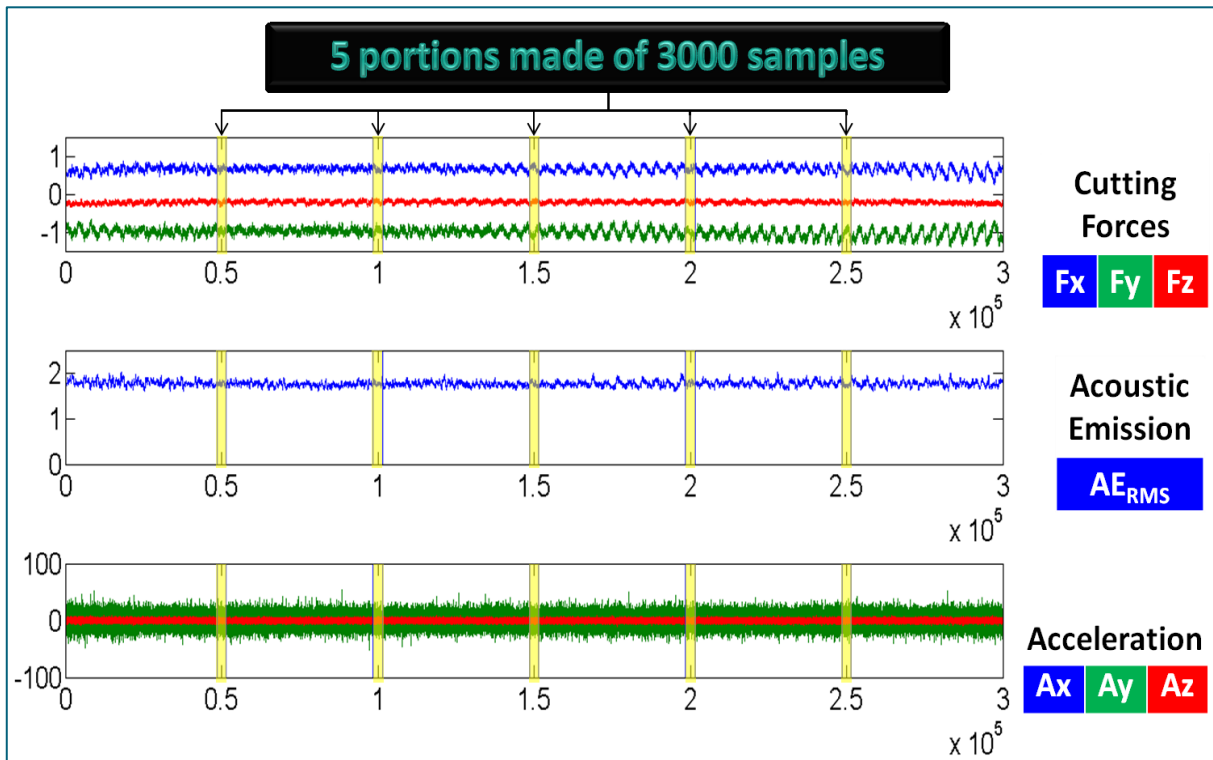


Fig. 8.4. Signal subdivision

Signal subdivision is carried out by isolating five portions made of 3000 samples each, as highlighted in yellow in Fig. 8.4.

The five portions are uniformly distributed along the signal length resulting from the previous segmentation. This procedure is automatically carried out through Matlab® ad-hoc code written for this purpose. Below an example of such code written for test case Test_1:

```
Test_1_I=Test_1(((length(Test_1)/6)-1499):((length(Test_1)/6)+1500),:);
Test_1_II=Test_1(((length(Test_1)/3)-1499):((length(Test_1)/3)+1500),:);
Test_1_III=Test_1(((length(Test_1)/2)-1499):((length(Test_1)/2)+1500),:);
Test_1_IV=Test_1((4*(length(Test_1)/6)-1499):(4*(length(Test_1)/6)+1500),:);
Test_1_V=Test_1((5*(length(Test_1)/6)-1499):(5*(length(Test_1)/6)+1500),:);
```

Where Test_1_I, Test_1_II, Test_1_III, Test_1_IV and Test_1_V are respectively the five selected portions of the signal.

In this way, the files are renamed in order to classify the signals according to their experimental test, step number and portion.

For example, the first portion of the first step of the first test case is named:

`Test1_step1_I`

Test₁_step₁_II is the second portion, and so on

The dataset coming out from this operation appears as it follows:

Table 8.1. Example of dataset (T₁_I)

Sampling	Fx	Fy	Fz	AERMS	Ax	Ay	Az
1	0,6444	-0,6031	-0,1491	1,7085	3,6908	-8,9871	0,6727
2	0,6483	-0,6021	-0,1326	1,7075	0,0358	-1,3501	1,5047
...	0,6528	-0,5920	-0,1841	1,7065	-3,5602	-12,8791	0,2567
3000	0,9276	-0,9763	-0,1776	1,8261	0,8078	10,5959	-4,0513

8.1.4. Dataset Construction

Due to drift phenomena occurred during the acquisition phases, it can happen that vibration signals have non-zero mean value, while, for their very nature, vibrations should oscillate around zero. To bring back the signal mean value to zero, the following Matlab® code was implemented (the example is referred to test case Test₁_I)

```
means_I=mean(Test_1_I); %calculates the mean value of each variable
columns=size(Test_1_I,2); %calculate the number of columns of dataset
for i = 5:columns;

Test_1_I(:,i)= Test_1_I(:,i)-means_I(i); % mean subtraction from the vibration columns
end
```

The vibration columns are 5, 6 and 7, respectively Ax, Ay and Az

The final dataset used for signal processing is hence made of a 3000 x 7 matrix, in which the 3000 rows are the signal specimens and the 7 columns represent the signal variables: Fx, Fy, Fz, AERms, Ax, Ay and Az respectively. The last 3 columns (related to the three acceleration components) are normalized and have zero mean value.

In this way, five dataset for each experimental test case step have been created.

8.2. Conventional Features Extraction

The conventional features to be extracted from each dataset are statistical features: means and variances

The features extracted are:

- Mean Fx;
- Mean Fy;
- Mean Fz;
- Variance Fx;
- Variance Fy;
- Variance Fz;
- Mean AErms;
- Variance AErms;
- Variance Ax;
- Variance Ay;
- Variance Az;

For the acceleration components obviously the mean is not calculated as it is zero by definition.

By implementing the following Matlab® code, the 11 features have been extracted.

```
clear workspace
load ../Dataset/Test1_step1.mat
conv_I=[mean(Test1_step1_I(:,1:3)),var(Test1_step1_I(:,1:3)),mean(Test1_step1_I(:,4)),var
(Test1_step1_I(:,4)),var(Test1_step1_I(:,5:7))];
conv_II=[mean(Test1_step1_II(:,1:3)),var(Test1_step1_II(:,1:3)),mean(Test1_step1_II(:,4))
,var(Test1_step1_II(:,4)),var(Test1_step1_II(:,5:7))];
conv_III=[mean(Test1_step1_III(:,1:3)),var(Test1_step1_III(:,1:3)),mean(Test1_step1_III(:,
4)),var(Test1_step1_III(:,4)),var(Test1_step1_III(:,5:7))];
conv_IV=[mean(Test1_step1_IV(:,1:3)),var(Test1_step1_IV(:,1:3)),mean(Test1_step1_IV(:,4))
,var(Test1_step1_IV(:,4)),var(Test1_step1_IV(:,5:7))];
conv_V=[mean(Test1_step1_V(:,1:3)),var(Test1_step1_V(:,1:3)),mean(Test1_step1_V(:,4)),var
(Test1_step1_V(:,4)),var(Test1_step1_V(:,5:7))];

box_conv=[conv_I;conv_II;conv_III;conv_IV;conv_V];

save conv_Test1_step1.mat
```

In this way, a 5x11 matrix is created, in which the five rows are the five signal portions and the 11 columns are the 11 conventional features extracted.

As an example the conventional features related to Test1_step1 are reported in the table below

Table 8.2. Conventional features extracted from T_1_1

ID TEST	Mean Fx	Mean Fy	Mean Fz	Var Fx	Var Fy	Var Fz	Mean AE	Var AE	Var Ax	Var Ay	Var Az
Test1_step1_I	0,3630	-0,1751	-0,2245	0,0001	0,0004	0,0002	2,5985	0,0069	7,0708	164,7952	3,1242
Test1_step1_II	0,3575	-0,1709	-0,2243	0,0002	0,0004	0,0002	2,5218	0,0058	8,2219	178,4524	3,1371
Test1_step1_III	0,3468	-0,1787	-0,2354	0,0002	0,0004	0,0002	2,5590	0,0040	9,8744	175,4386	3,7511
Test1_step1_IV	0,3349	-0,1999	-0,2573	0,0002	0,0004	0,0002	2,6263	0,0071	9,8561	180,3695	3,5059
Test1_step1_V	0,3199	-0,2237	-0,2735	0,0002	0,0004	0,0002	2,6555	0,0041	11,2864	201,7403	3,8425

8.3. Principal Components Analysis

8.3.1. Generalities

Advances in computing and sensor technology allow the collection and storage of large amounts of measurements from many chemical manufacturing processes. These measured data are a rich source of information, which when used effectively can greatly enhance the performance of these processes. The information embedded in data can be efficiently extracted by constructing accurate models that describe, summarize, and predict the process behavior [184].

Principal Component Analysis (PCA) is a popular modeling technique used to extract information from process data by relating its variables. PCA has been found useful in many applications, such as process monitoring [185][186], data filtering, [187] compression and regression. It transforms the process variables by rotating their axes of representation to capture the variation of the original variables in a lower dimension space. The new axes of rotation are represented by the projection directions or principal component loadings [184].

8.3.2. Purposes

The goals of PCA [188] are to:

- extract the most important information from the data table;
- compress the size of the data set by keeping only this important information;
- simplify the description of the data set;
- analyze the structure of the observations and the variables.

In order to achieve these goals, PCA computes new variables called *principal components* which are obtained as linear combinations of the original variables.

The first principal component is required to have the largest possible variance (*i.e.*, inertia and therefore this component will "explain" or "extract" the largest part of the inertia of the data table). The second component is computed under the constraint of being orthogonal to the first component and to have the largest possible inertia. The other components are computed likewise. The values of these new variables for the observations are called *scores*, these scores can be interpreted geometrically as the *projections* of the observations onto the principal components [188].

8.3.3. Computation

The Principal Components Analysis procedure can be summarized in the following flow chart:



8.3.3.1. Normalization

To implement the Principal Components Analysis on the dataset, the first step to carry out is the data normalization, which consists to bring all the signal variables to zero-mean values. In order to perform this normalization, the following Matlab® code was created:

```
means_I=mean(Test1_step1_I);
columns=size(Test1_step1_I,2);
for i = 1:columns;

Test1_step1_I(:,i)=Test1_step1_I(:,i)-means_I(i);
end
%-----
means_II=mean(Test1_step1_II);
columns=size(Test1_step1_II,2);
for i = 1:columns;

Test1_step1_II(:,i)=Test1_step1_II(:,i)-means_II(i);
end
%-----
means_III=mean(Test1_step1_III);
columns=size(Test1_step1_III,2);
for i = 1:columns;

Test1_step1_III(:,i)=Test1_step1_III(:,i)-means_III(i);
end
%-----
means_IV=mean(Test1_step1_IV);
columns=size(Test1_step1_IV,2);
for i = 1:columns;

Test1_step1_IV(:,i)=Test1_step1_IV(:,i)-means_IV(i);
end
%-----
means_V=mean(Test1_step1_V);
columns=size(Test1_step1_V,2);
for i = 1:columns;

Test1_step1_V(:,i)=Test1_step1_V(:,i)-means_V(i);
end
%-----
```

In this way, the mean value of each variable has been subtracted from the related column.

The dataset is now ready for the next PCA steps.

8.3.3.2. Covariance Matrix Calculation

The Covariance matrix is a matrix formed from the pairwise covariances of several random variables; more precisely, for the k -dimensional vector $X = (X_1, \dots, X_k)$ the covariance matrix is the square matrix $\Sigma = E[(X - EX)(X - EX)^T]$, where $EX = (EX_1, \dots, EX_k)$ is the vector of mean values.

The components of the covariance matrix are:

$$\sigma_{ij} = E[(X_i - EX_i)(X_j - EX_j)] = \text{cov}(X_i, X_j)$$

$$i, j = 1, \dots, k$$

and for $i = j$ they are the same as $DX_i (= \text{Var}(X_i))$ (that is, the variances of the X_i lie on the principal diagonal). The covariance matrix is a symmetric positive semi-definite matrix. If the covariance matrix is positive definite, then the distribution of X is non-degenerate; otherwise it is degenerate. For the random vector X the covariance matrix plays the same role as the variance of a random variable [189].

The covariance matrix of each dataset is calculated along the all seven variables

Table 8.3. Example of covariance matrix (Test T_1_I)

0,0255	-0,0306	-0,0005	0,0089	-0,0036	0,0276	-0,0030
-0,0306	0,0388	0,0011	-0,0104	0,0043	-0,0504	0,0036
-0,0005	0,0011	0,0011	0,0003	-0,0021	-0,0020	0,0006
0,0089	-0,0104	0,0003	0,0056	-0,0009	0,0184	0,0017
-0,0036	0,0043	-0,0021	-0,0009	13,6935	-2,7606	3,1376
0,0276	-0,0504	-0,0020	0,0184	-2,7606	88,8354	1,3861
-0,0030	0,0036	0,0006	0,0017	3,1376	1,3861	4,0516

8.3.3.3. Eigenvectors Calculation

Eigenvectors are a special set of vectors associated with a linear system of equations (i.e., a matrix equation) that are sometimes also known as characteristic vectors, proper vectors, or latent vectors [190].

The determination of the eigenvectors and eigenvalues of a system is extremely important in physics and engineering, where it is equivalent to matrix diagonalization and arises in such common applications as stability analysis, the physics of rotating bodies, and small oscillations of vibrating systems, to name only a few. Each eigenvector is paired with a corresponding so-called eigenvalue. Mathematically, two different kinds of eigenvectors need to be distinguished: left eigenvectors and right eigenvectors. However, for many problems in physics and engineering, it is sufficient to consider only right eigenvectors. The term "eigenvector" used without qualification in such applications can therefore be understood to refer to a right eigenvector.

The decomposition of a square matrix A into eigenvalues and eigenvectors is known in this work as eigen decomposition, and the fact that this decomposition is always possible as long as the matrix consisting of the eigenvectors of A is square is known as the eigen decomposition theorem.

Define a right eigenvector as a column vector X_R satisfying

$$AX_R = \lambda_R X_R \tag{8.1}$$

Where A is a matrix, so

$$(A - \lambda_R I)X_R = \mathbf{0} \quad (8.2)$$

which means the right eigenvalues must have zero determinant, i.e.,

$$\det(A - \lambda_R I) = 0 \quad (8.3)$$

Similarly, define a left eigenvector as a row vector X_L satisfying

$$X_L A = \lambda_L X_L \quad (8.4)$$

Taking the transpose of each side gives

$$(X_L A)^T = \lambda_L X_L^T \quad (8.5)$$

which can be rewritten as

$$A^T X_L^T = \lambda_L X_L^T \quad (8.6)$$

Rearrange again to obtain

$$(A^T - \lambda_L I) = 0 \quad (8.7)$$

which means

$$\det(A^T - \lambda_L I) = 0 \quad (8.8)$$

Rewriting gives

$$0 = \det(A^T - \lambda_L I) = \det(A^T - \lambda_L I^T) \quad (8.9)$$

$$0 = \det(A - \lambda_L I)^T \quad (8.10)$$

$$0 = \det(A - \lambda_L I) \quad (8.11)$$

where the last step follows from the identity

$$\det(A) = \det(A^T) \quad (8.12)$$

Equating equations (8.9) and (8.11), which are both equal to 0 for arbitrary A and X , therefore requires that $\lambda_R = \lambda_L \equiv \lambda$, i.e., left and right eigenvalues are equivalent, a statement that is not true for eigenvectors.

Let X_R be a matrix formed by the columns of the right eigenvectors and X_L be a matrix formed by the rows of the left eigenvectors. Let

$$D \equiv \begin{bmatrix} \lambda_1 & \cdots & 0 \\ \vdots & \ddots & \vdots \\ 0 & \cdots & \lambda_n \end{bmatrix} \quad (8.13)$$

Then

$$AX_R = X_R D \quad (8.14)$$

$$X_L A = D X_L \quad (8.15)$$

And

$$X_L A X_R = X_L X_R D \quad (8.16)$$

$$X_L A X_R = D X_L X_R \quad (8.17)$$

So

$$X_L X_R D = D X_L X_R \quad (8.18)$$

But this equation is of the form

$$C D = D C \quad (8.19)$$

where D is a diagonal matrix, so it must be true that $C \equiv X_L X_R$ is also diagonal. In particular, if A is a symmetric matrix, then the left and right eigenvectors are simply each other's transpose, and if A is a self-adjoint matrix (i.e., it is Hermitian), then the left and right eigenvectors are adjoint matrices.

Eigenvectors may not be equal to the zero vector. A nonzero scalar multiple of an eigenvector is equivalent to the original eigenvector. Hence, without loss of generality, eigenvectors are often normalized to unit length.

While an $n \times m$ matrix always has n eigenvalues, some or all of which may be degenerate, such a matrix may have between 0 and n linearly independent eigenvectors. For example, the matrix $\begin{bmatrix} 1 & 1 \\ 0 & 1 \end{bmatrix}$ has only the single eigenvector $(1, 0)$ [191].

8.3.3.4. Eigenvalues Calculation

Eigenvalues are a special set of scalars associated with a linear system of equations (i.e., a matrix equation) that are sometimes also known as characteristic roots, characteristic values (Hoffman and Kunze 1971), proper values, or latent roots (Marcus and Minc 1988, p. 144).

The determination of the eigenvalues and eigenvectors of a system is extremely important in physics and engineering, where it is equivalent to matrix diagonalization and arises in such common applications as stability analysis, the physics of rotating bodies, and small oscillations of vibrating systems, to name only a few. Each eigenvalue is paired with a corresponding so-called eigenvector (or, in general, a corresponding right eigenvector and a corresponding left eigenvector; there is no analogous distinction between left and right for eigenvalues).

The decomposition of a square matrix into eigenvalues and eigenvectors is known in this work as eigen decomposition, and the fact that this decomposition is always possible as long as the matrix consisting of the eigenvectors of is square is known as the eigen decomposition theorem.

The Lanczos algorithm is an algorithm for computing the eigenvalues and eigenvectors for large symmetric sparse matrices.

Let A be a linear transformation represented by a matrix A . If there is a vector $X \in \mathbb{R}^n$ such that:

$$A X = \lambda X \quad 8.20$$

for some scalar λ , then λ is called the eigenvalue of A with corresponding (right) eigenvector X .

Letting A be a $k \times k$ square matrix

$$\begin{bmatrix} a_{11} & \cdots & a_{1k} \\ \vdots & \ddots & \vdots \\ a_{k1} & \cdots & a_{kk} \end{bmatrix} \quad 8.21$$

with eigenvalue λ , then the corresponding eigenvectors satisfy

$$\begin{bmatrix} a_{11} & \cdots & a_{1k} \\ \vdots & \ddots & \vdots \\ a_{k1} & \cdots & a_{kk} \end{bmatrix} \begin{bmatrix} x_1 \\ \dots \\ x_k \end{bmatrix} = \lambda \begin{bmatrix} x_1 \\ \dots \\ x_k \end{bmatrix} \quad 8.22$$

which is equivalent to the homogeneous system

$$\begin{bmatrix} a_{11} - \lambda & \cdots & a_{1k} \\ \vdots & \ddots & \vdots \\ a_{k1} & \cdots & a_{kk} - \lambda \end{bmatrix} \begin{bmatrix} x_1 \\ \dots \\ x_k \end{bmatrix} = \begin{bmatrix} 0 \\ \dots \\ 0 \end{bmatrix} \quad 8.23$$

Equation 8.23 can be written compactly as

$$(A - \lambda I)X = \mathbf{0} \quad 8.24$$

where I is the identity matrix. As shown in Cramer's rule, a linear system of equations has nontrivial solutions iff the determinant vanishes, so the solutions of equation 8.24 are given by

$$\det(A - \lambda I) = 0 \quad 8.25$$

This equation is known as the characteristic equation of A , and the left-hand side is known as the characteristic polynomial [192].

The eigenvalues of the covariance matrix, called Latent Roots, were grouped and used as input features for Neural Networks

8.3.4. Matlab Principal Components Analysis Computation

Syntax [193]

```
[COEFF, SCORE, latent] = princomp(X)
```

princomp(X) performs principal components analysis (PCA) on the n -by- p data matrix X , and returns the principal component coefficients, also known as loadings. Rows of X correspond to observations, columns to variables. **princomp** centers X by subtracting off column means.

COEFF is a p -by- p matrix, each column containing coefficients for one principal component. The columns are in order of decreasing component variance.

SCORE returns the principal component scores; that is, the representation of X in the principal component space. Rows of **SCORE** correspond to observations, columns to components.

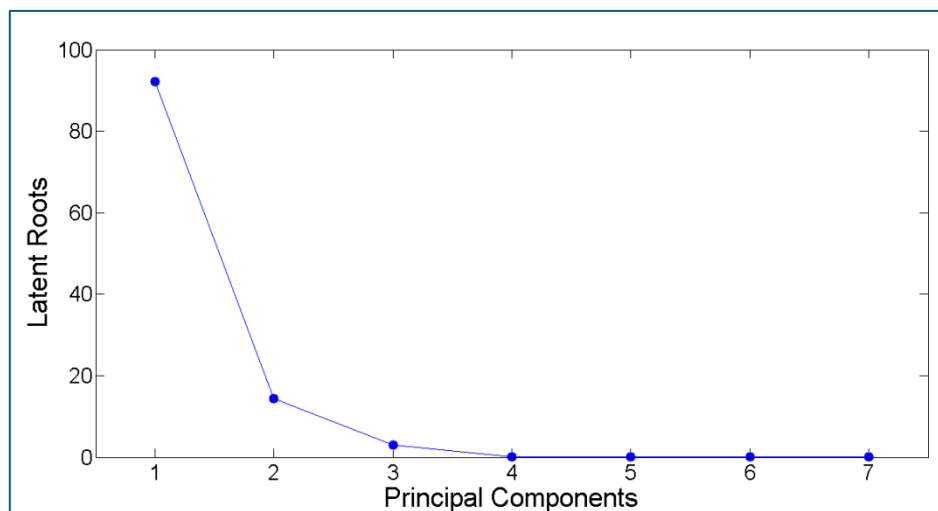
Latent returns a vector containing the eigenvalues of the covariance matrix of X .

The scores are the data formed by transforming the original data into the space of the principal components. The values of the vector **Latent** are the variance of the columns of **SCORE**. [194][195][196][197].

8.3.5. Plots

8.3.5.1. Scree Plot

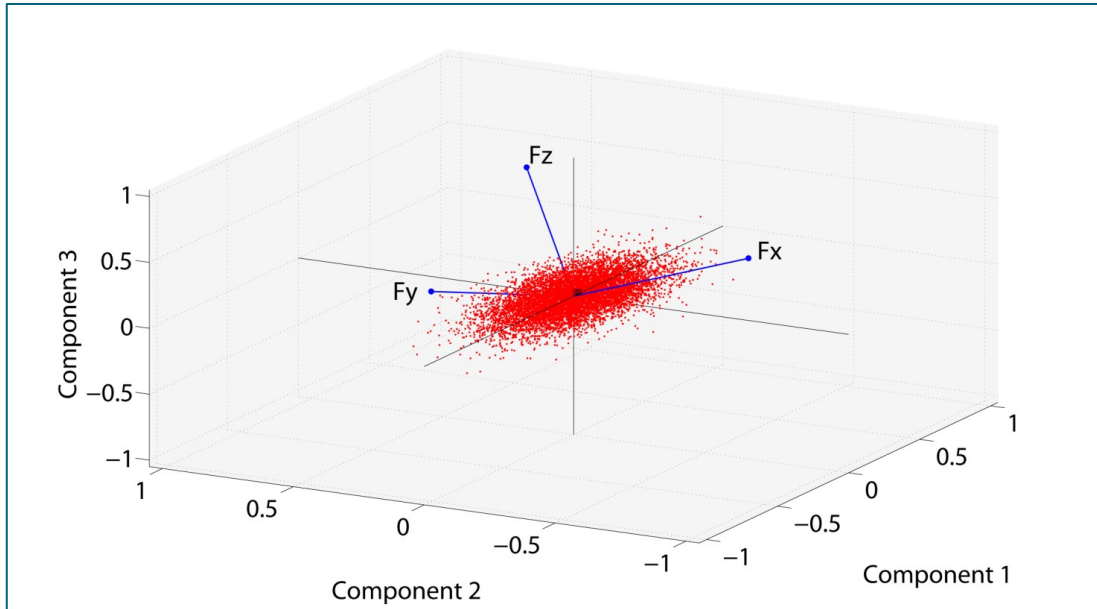
A Scree Plot is a simple line segment plot that shows the fraction of total variance in the data as explained or represented by each PC. The PCs are ordered by decreasing order of contribution to total variance.. Such a plot when read left-to-right across the abscissa can often show a clear separation in fraction of total variance where the “most important” components cease and the “least important” components begin. The point of separation is often called the “elbow”. In the PCA literature, the plot is called a “Scree” Plot because it often looks like a “scree” slope, where rocks have fallen down and accumulated on the side of a mountain [198].



8.5. Latent roots scree plot

8.3.5.2. Biplot

A biplot allows to visualize the magnitude and sign of each variable's contribution to the first three principal components, and how each observation is represented in terms of those components.



8.6. Principal Components Biplot

8.4. Results

The results of the PCA procedure applied to all sensor fusion data matrices (all test cases) are summarized in Table 8.4. The table values represent the sensor signal variable corresponding to the 1st, ..., 7th principal component, respectively.

Table 8.4. Table with correspondence

Principal Components	Original Variables
1 st	A_y
2 nd	A_x
3 rd	A_z
4 th	AE_{RMS}
5 th	F_y
6 th	F_z
7 th	F_x

Decision Making

9. Neural Network based Pattern Recognition

9.1. Pattern Recognition and Neural Networks

Pattern recognition can be defined as the categorization of input data into identifiable classes via the extraction of significant features or attributes of the data from a background of irrelevant detail. The historically most frequent areas of application are in spatial pattern recognition—3-D image processing, character and voice recognition, and in temporal pattern recognition—weather forecasting and financial time series forecasting [199] [200].

3-Layers Feedforward backpropagation Neural Networks were used for Pattern Recognition Purposes.

The first term, “feedforward” describes how this neural network processes and recalls patterns. In a feedforward neural network, neurons are only connected foreword. Each layer of the neural network contains connections to the next layer (for example, from the input to the hidden layer), but there are no connections back.

The term “backpropagation” describes how this type of neural network is trained. Backpropagation is a form of supervised training. When using a supervised training method, the network must be provided with both sample inputs and anticipated outputs. The anticipated outputs are compared against the actual outputs for given input. Using the anticipated outputs, the backpropagation training algorithm then takes a calculated error and adjusts the weights of the various layers backwards from the output layer to the input layer.

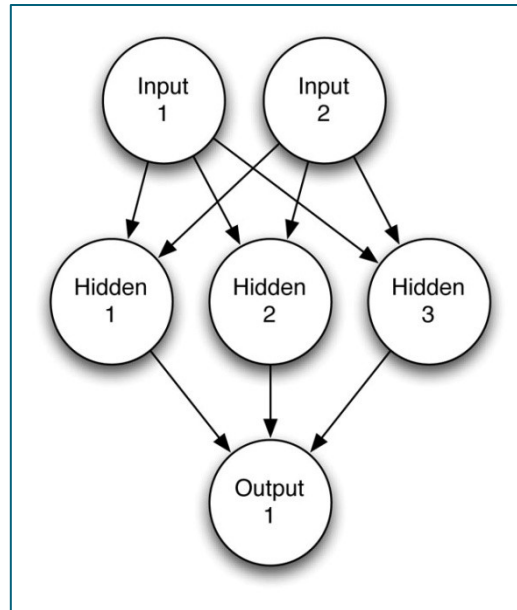
The backpropagation and feedforward algorithms are often used together. The feedforward neural network begins with an input layer. The input layer may be connected to a hidden layer or directly to the output layer. If it is connected to a hidden layer, the hidden layer can then be connected to another hidden layer or directly to the output layer. There can be any number of hidden layers, as long as there is at least one hidden layer or output layer provided. In common use, most neural networks will have one hidden layer, and it is very rare for a neural network to have more than two hidden layers [200].

Figure 9.1 illustrates a typical feedforward neural network with a single hidden layer.

The input layer is the conduit through which the external environment presents a pattern to the neural network. Once a pattern is presented to the input layer, the output layer will produce another pattern. In essence, this is all the neural network does. The input layer should represent the condition for which the neural network is trained. Every input neuron should represent some independent variable that has an influence over the output of the neural network.

The output layer of the neural network is what actually presents a pattern to the external environment. The pattern presented by the output layer can be directly traced back to the input layer. The number of output neurons should be directly related to the type of work that the neural network is to perform.

To determine the number of neurons to use in output layer, the intended use of the neural network should be considered. If the neural network is to be used to classify items into groups, then it is often preferable to have one output neuron for each group that input items are to be assigned into [200].



9.1. A typical feedforward neural network (single hidden layer)

Considerations about the number of hidden layer nodes

Statistical considerations based on several attempts of Neural Networks configurations shown that, on average, better results are obtained by setting a number of hidden layer nodes equal to 2 times (double) and 4 times (quadruple) the number of the input layer nodes. Hence, the two hidden layer nodes configuration mentioned above will be adopted for pattern recognition purposes in this thesis work, and they will be denoted by “2x” and “4x” respectively.

So, for example, the series of Neural Network configurations implemented by using SCG training algorithm and a number of hidden layer nodes equal to the double of Input Layer Nodes will be reported as SCG 2x, the quadruple as SCG 4x and so on...

9.2. Purposes

9.2.1. Tool State Identification

The first goal of pattern recognition neural networks is to identify the tool state, on the basis of features extracted in correspondence of both fresh tool and worn tool.

9.2.2. Residual Stress Assessment (worn tool)

For every experimental test, the signals related to the last step were considered., which are the steps in correspondence of which the residual stress measurement was carried out.

9.2.3. Residual Stress Assessment (fresh tool)

Signals related to the last step of every experimental turning test, by their definition, are acquired in correspondence of worn tool. The signals taken into account are hence the ones belonging to the first step of every experimental test.

9.3. Pattern Vectors

Features extracted both by conventional methodology and by advanced PCA based methodology were used as input pattern vectors for neural networks.

9.3.1. Pattern Vectors from Conventional Features

14 different pattern vectors made of different combinations of conventional features were utilized as input vectors for Neural Network decision making support systems, and reported in the table below.

Table 9.1. Pattern vectors from conventional features

# of features	Features
2	[Mean AE, Var AE]
3	[Var Ax, Var Ay, Var Az]
3	[Var Fx, Var Fy, Var Fz]
3	[Mean Fx, Mean Fy, Mean Fz]
6	[Mean Fx, Mean Fy, Mean Fz, Var Fx, Var Fy, Var Fz]
4	[Var Fx, Var Fy, Var Fz, Var AE]
4	[Mean Fx, Mean Fy, Mean Fz, Mean AE]
4	[Var AE, Var Ax, Var Ay, Var Az]
5	[Mean AE, Var AE, Var Ax, Var Ay, Var Az]
6	[Var Fx, Var Fy, Var Fz, Var Ax, Var Ay, Var Az,]
7	[Var Fx, Var Fy, Var Fz, Var AE, Var Ax, Var Ay, Var Az]
8	[Mean Fx, Mean Fy, Mean Fz, Var Fx, Var Fy, Var Fz, Mean AE, Var AE]
9	[Mean Fx, Mean Fy, Mean Fz, Var Fx, Var Fy, Var Fz, Var Ax, Var Ay, Var Az]
11	[Mean Fx, Mean Fy, Mean Fz, Var Fx, Var Fy, Var Fz, Mean AE, Var AE, Var Ax, Var Ay, Var Az]

9.3.2. Pattern Vectors from PCA based Features

6 different pattern vectors made of PCA based features were utilized as input vectors for Neural Network decision making support systems, and reported in the table below.

Table 9.2. Pattern vectors from PCA-based features

#of Features	Features
3	[Ay Ax Az]
3	[Fy Fz Fx]
4	[AErms Fy Fz Fx]
4	[Ay Ax Az AE _{RMS}]
6	[Ay Ax Az Fy Fz Fx]
7	[Ay Ax Az AE _{RMS} Fy Fz Fx]

9.4. Training Algorithms

9.4.1. Levenberg-Marquardt (LM)

Like the quasi-Newton methods, the Levenberg-Marquardt algorithm [201] was designed to approach second-order training speed without having to compute the Hessian matrix. When the performance function has the form of a sum of squares (as is typical in training feedforward networks), then the Hessian matrix can be approximated as

$$\mathbf{H} = \mathbf{J}^T \mathbf{J}$$

and the gradient can be computed as

$$\mathbf{g} = \mathbf{J}^T \mathbf{e}$$

Where \mathbf{J} is the Jacobian matrix that contains first derivatives of the network errors with respect to the weights and biases, and \mathbf{e} is a vector of network errors. The Jacobian matrix can be computed through a standard backpropagation technique (see [HaMe94]) that is much less complex than computing the Hessian matrix.

The Levenberg-Marquardt algorithm uses this approximation to the Hessian matrix in the following Newton-like update:

$$\mathbf{x}_{k+1} = \mathbf{x}_k - [\mathbf{J}^T \mathbf{J} + \mu \mathbf{I}]^{-1} \mathbf{J}^T \mathbf{e}$$

When the scalar μ is zero, this is just Newton's method, using the approximate Hessian matrix. When μ is large, this becomes gradient descent with a small step size. Newton's method is faster and more accurate near an error minimum, so the aim is to shift toward Newton's method as quickly as possible. Thus, μ is decreased after each successful step (reduction in performance function) and is increased only when a tentative step would increase the performance function. In this way, the performance function is always reduced at each iteration of the algorithm [203].

9.4.2. Scaled Conjugate Gradient (SCG)

Conjugate gradient is the most popular iterative method for solving large systems of linear equations [204]. In the first iteration usually the conjugate gradient algorithm will find the steep descent direction.

Approximate solution, \mathbf{x}_k for conjugate gradient iteration is described as formulas below [201]:

$$\mathbf{x}_k = \mathbf{x}_{k-1} + \alpha_k \mathbf{d}_{k-1} \tag{9.1}$$

k will always be the iteration index, α_k is the length of the step performed at iteration k , \mathbf{d}_k is search direction, \mathbf{r}_k is residual vector and β_k is improvement. Formula (9.2),(9.3),(9.4),(9.5) shows the relative component of approximate solution for conjugate gradient.

$$\alpha_k = \frac{(\mathbf{r}_{k-1}^T \mathbf{r}_{k-1})}{(\mathbf{d}_{k-1}^T \mathbf{A} \mathbf{d}_{k-1})} \tag{9.2}$$

$$\mathbf{d}_k = \mathbf{r}_k + \beta_k \mathbf{d}_{k-1} \tag{9.3}$$

$$\mathbf{r}_k = \mathbf{r}_{k-1} - \alpha_k \mathbf{A} \mathbf{d}_{k-1} \tag{9.4}$$

$$\beta_k = \frac{(r_k^T r_k)}{(r_k^T - 1r_{k-1})}$$

9-5

SCG is a second order Conjugate Gradient Algorithm that help minimize goal functions of several variables. This theoretical foundations was prove by Moller [201] which remains first order techniques in first derivatives like standard backpropogation and find the better way to a local minimum in second order techniques in second derivatives. SCG use a step size scaling mechanism avoids a time consuming line-search per learning iteration, which makes the algorithm faster than other second order algorithms recently proposed. Base on the Moller [201], SCG methods shows superlinear convergence on most problems [205].

9.4.3. Leave – k – Out (LKO)

In the leave-k-out method [1] [7] [9] [202] one homogeneous group of k patterns (here, k = 1), extracted from the full training set, was held back in turn for testing and the rest of the patterns was used for training. During testing, the NN output is correct if error $E = (O_a - O_d)$, where O_a = actual output and O_d = desired output, is $-0.5 \leq E \leq +0.5$; otherwise, a misclassification case occurs. The ratio of correct classifications over the total training cases yields the NN success rate (SR).

9.5. Matlab procedure

Input

The input matrix dimension is n x m, where:

- n rows, representing the number of samplings, 3000 for each dataset;
- m columns, representing the number of signal features;

Target

The target vector dimensions n x 1. The target elements are zeros and ones in function of the purposes:

- Tool state identification
 - Zero = fresh tool
 - One = worn tool
- Residual stress assessment
 - Zero = acceptable residual stress
 - One = unacceptable residual stress

Output

Output represent the classification resulting from the neural network implementation, and it must be compared to the target in order to find out the success rate.

Data division

Validation and test data sets are each set to 15% of the original data. With these settings, the input vectors and target vectors will be randomly divided into three sets as follows:

- 70% are used for training.
- 15% are used to validate that the network is generalizing and to stop training before overfitting.
- The last 15% are used as a completely independent test of network generalization.

The Matlab code for the neural network pattern recognition implementation is reported in the next page.

The example is referred to a number of hidden layer nodes equal to 12 and Levenberg-Marquardt as a training algorithm.

```

% Solve a Pattern Recognition Problem with a Neural Network
% Script generated by NPRTOOL

inputs = input'; %    input - input data
targets = target'; %    target - target data

% Create a Pattern Recognition Network
hiddenLayerSize = 12;
net = patternnet(hiddenLayerSize);

% Choose Input and Output Pre/Post-Processing Functions
% For a list of all processing functions type: help nprocess
net.inputs{1}.processFcns = {'removeconstantrows','mapminmax'};
net.outputs{2}.processFcns = {'removeconstantrows','mapminmax'};

% Setup Division of Data for Training, Validation, Testing
% For a list of all data division functions type: help nndivide
net.divideFcn = 'dividerand'; % Divide data randomly
net.divideMode = 'sample'; % Divide up every sample
net.divideParam.trainRatio = 70/100;
net.divideParam.valRatio = 15/100;
net.divideParam.testRatio = 15/100;

% For help on training function 'trainlm' type: help trainlm
% For a list of all training functions type: help ntrain
net.trainFcn = 'trainlm'; % Levenberg-Marquardt

% Choose a Performance Function
% For a list of all performance functions type: help nnperformance
net.performFcn = 'mse'; % Mean squared error

% Choose Plot Functions
% For a list of all plot functions type: help nnplot
net.plotFcns = {'plotconfusion','plotperform','plottrainstate','ploterrhist',
'plotregression','plotfit'};

% Train the Network
[net,tr] = train(net,inputs,targets);

% Test the Network
outputs = net(inputs);
errors = gsubtract(targets,outputs);
performance = perform(net,targets,outputs)

% Recalculate Training, Validation and Test Performance
trainTargets = targets .* tr.trainMask{1};
valTargets = targets .* tr.valMask{1};
testTargets = targets .* tr.testMask{1};
trainPerformance = perform(net,trainTargets,outputs)
valPerformance = perform(net,valTargets,outputs)
testPerformance = perform(net,testTargets,outputs)

view(net) % View the Network

% Plots
figure, plotperform(tr)
figure, plottrainstate(tr)
figure, plotconfusion(targets,outputs)
figure, ploterrhist(errors)

```

The results of the neural networks computations are organized in confusion matrices

The confusion matrix shows the percentages of correct and incorrect classifications. Correct classifications are the green squares on the matrices diagonal. Incorrect classifications form the red squares [206].

In Fig. 9.2 an example of confusion matrix is reported, for the configuration listed below:

- Tool State Identification
- Standard Tests only
- PCA Features
- Pattern features vector = [Ax Ay Az AERMS Fy Fz Fx]
- SCG Training algorithm
- Hidden layer nodes = 2 x input layer nodes

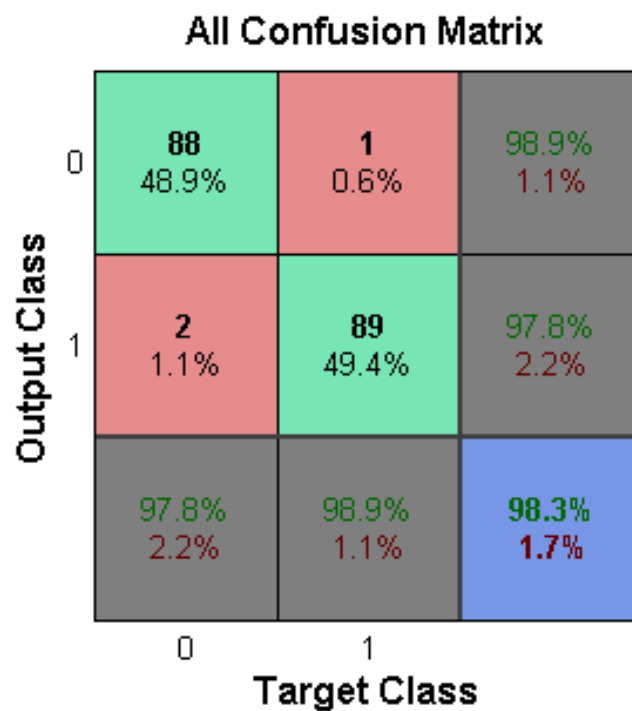


Fig. 9.2. Confusion Matrix example

10. Results

10.1. Tool State Identification

10.1.1. Standards Tests

Statistics Summary

Table 10.1. Statistics Summary

Statistics	
Total Average	90,76
Std dev.	10,46
Mode	100
Minimum	61,1
Conv vs PCA	
Conv	89,74
PCA	93,14
Difference	3,40
Training Algorithm	
LM	95,09
SCG	87,64
LKO	89,55
LM-SCG	7,45
LM-LKO	5,54
SCG-LKO	-1,91
Hidden Layer Nodes (4x - 2x)	
LM	2,83
SCG	3,51
LKO	-0,64

The results reported in Table 10.1 show that:

- It is possible to identify the tool state by extracting features from multi sensor signals with an average Success Rate (SR) = 90.76% , the minimum SR is 61.1%.
- The most frequent success rate is 100% showing an excellent reliability of features and neural network, for both Conventional and PCA features.

PCA vs. Conventional

Considering all the categories of NN Configurations, in terms of training algorithm and number of hidden layer nodes, the features extracted by PCA yield to a more successful pattern recognition than the ones obtained by conventional methodology, as shown in Table 10.2 and in Fig. 10.1. The difference in success rate between the two methodologies is 3.40%

The training algorithm that shows a clearer difference between the two features extraction methodologies is the SCG, where the gap ranges from 6.27 % (SCG-2x) to 6.32 % (SCG-4X).

Table 10.2

	LKO 2x	LKO 4x	SCG 2x	SCG 4x	LM 2x	LM 4x
Conventional	89.14	89.05	84,00	87,50	92,66	96,07
PCA	91.58	89.63	90,27	93,82	96,02	97,50

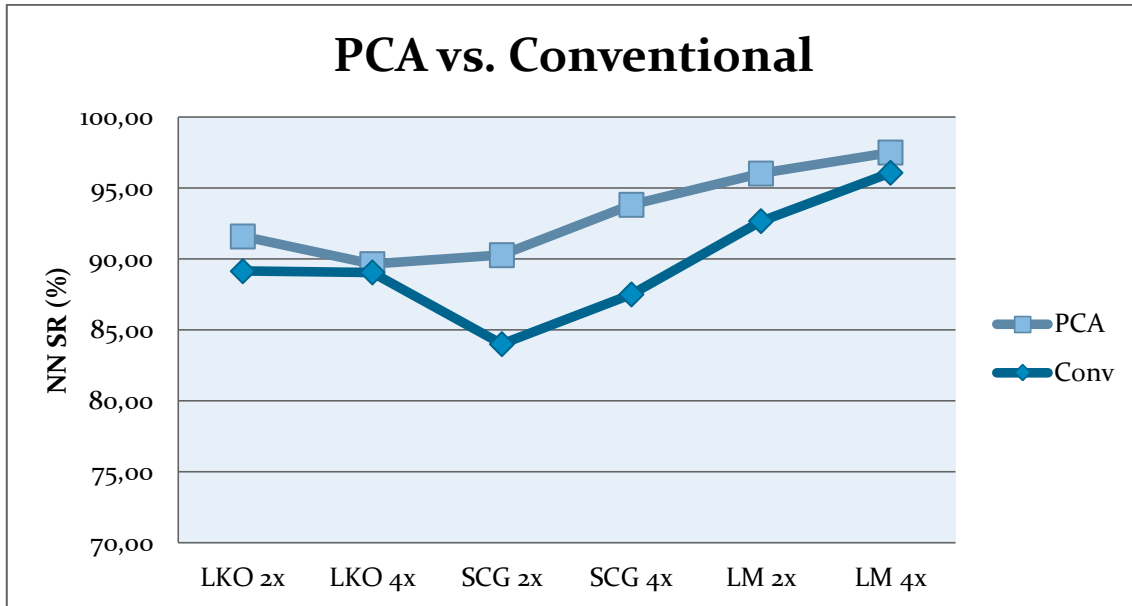


Fig. 10.1. PCA vs Conventional

Conventional Features Evaluation

In Figs. 10.2, 10.3 10.4 and 10.5 a conventional features evaluation is reported

Figures show that by increasing the number of features, the success rates increases too,

It is clear also that increasing the number of variables yields higher success rates.

This evaluation has been carried out for all the training algorithms and the trend mentioned above occurs for each training algorithm.

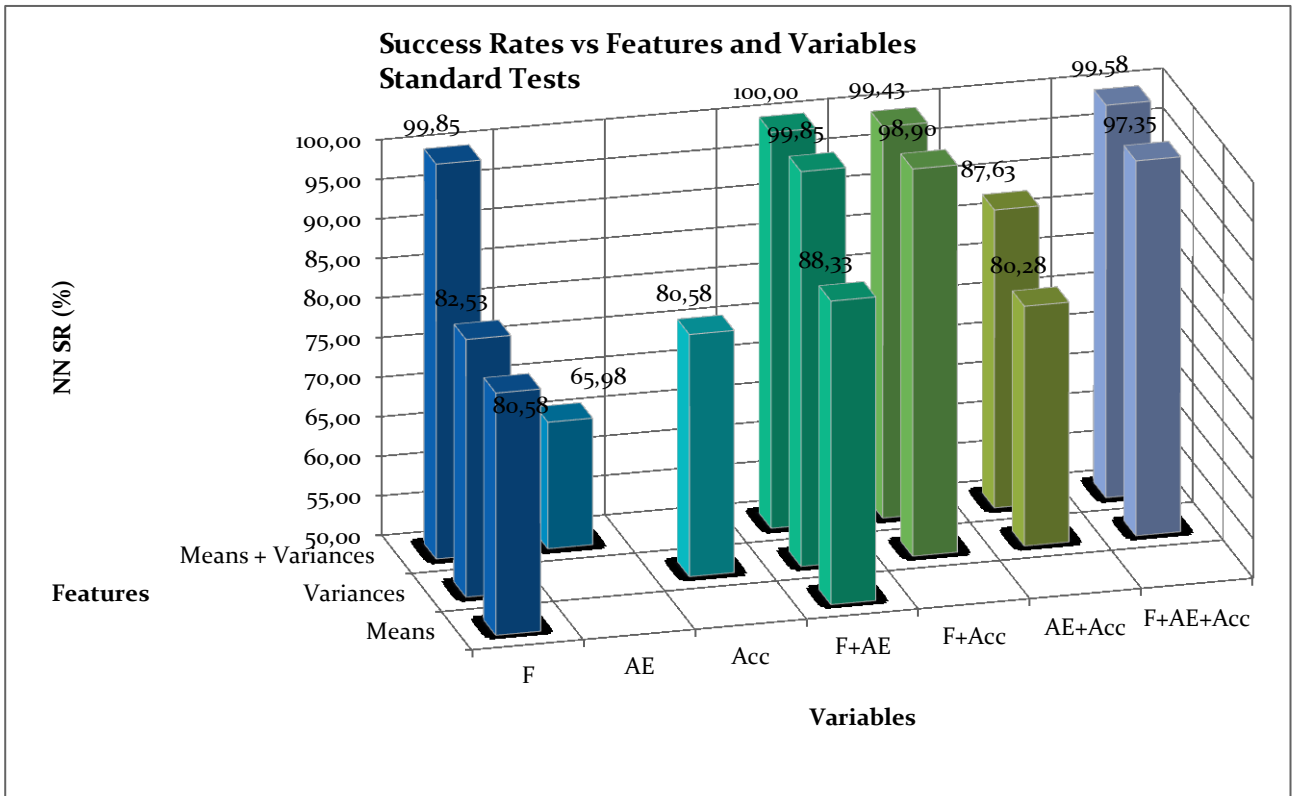


Fig. 10.2. Conventional features evaluation: overall average

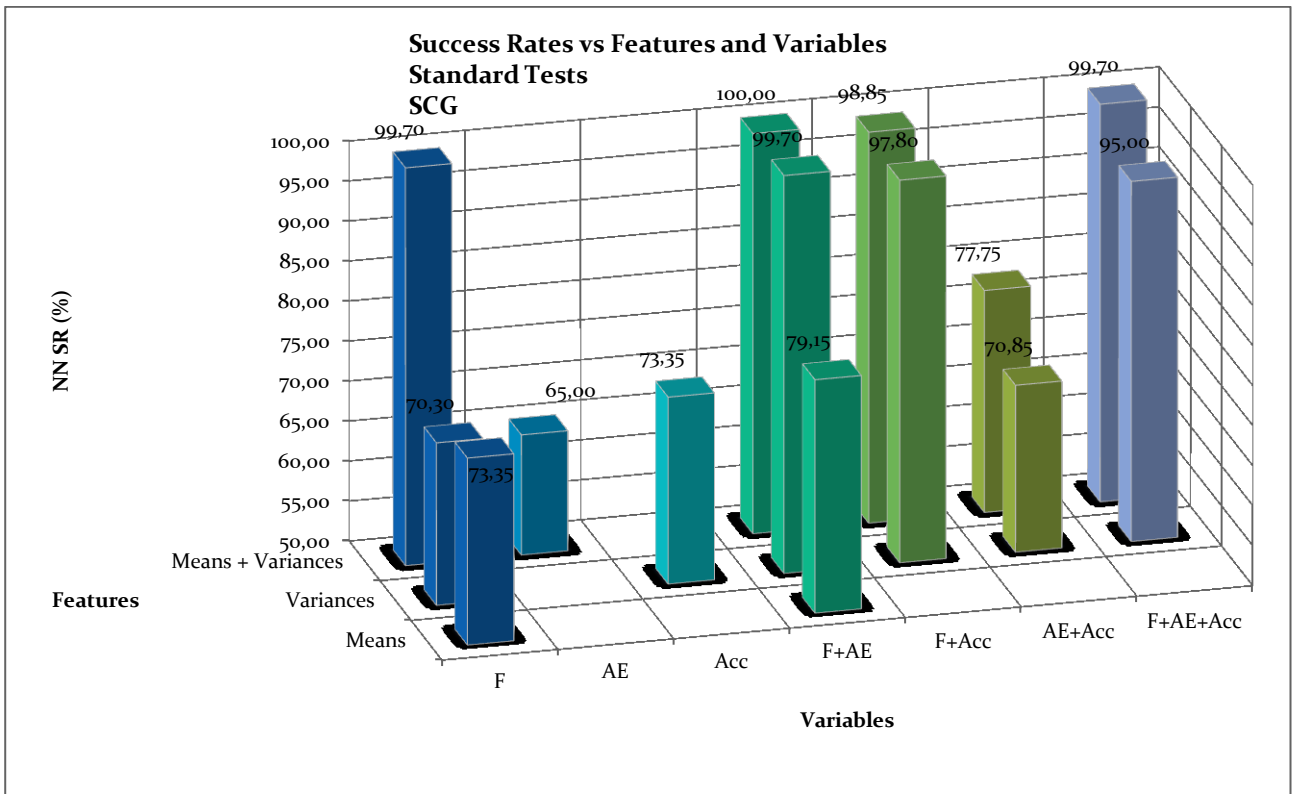


Fig. 10.3. Conventional features evaluation: SCG training algorithm

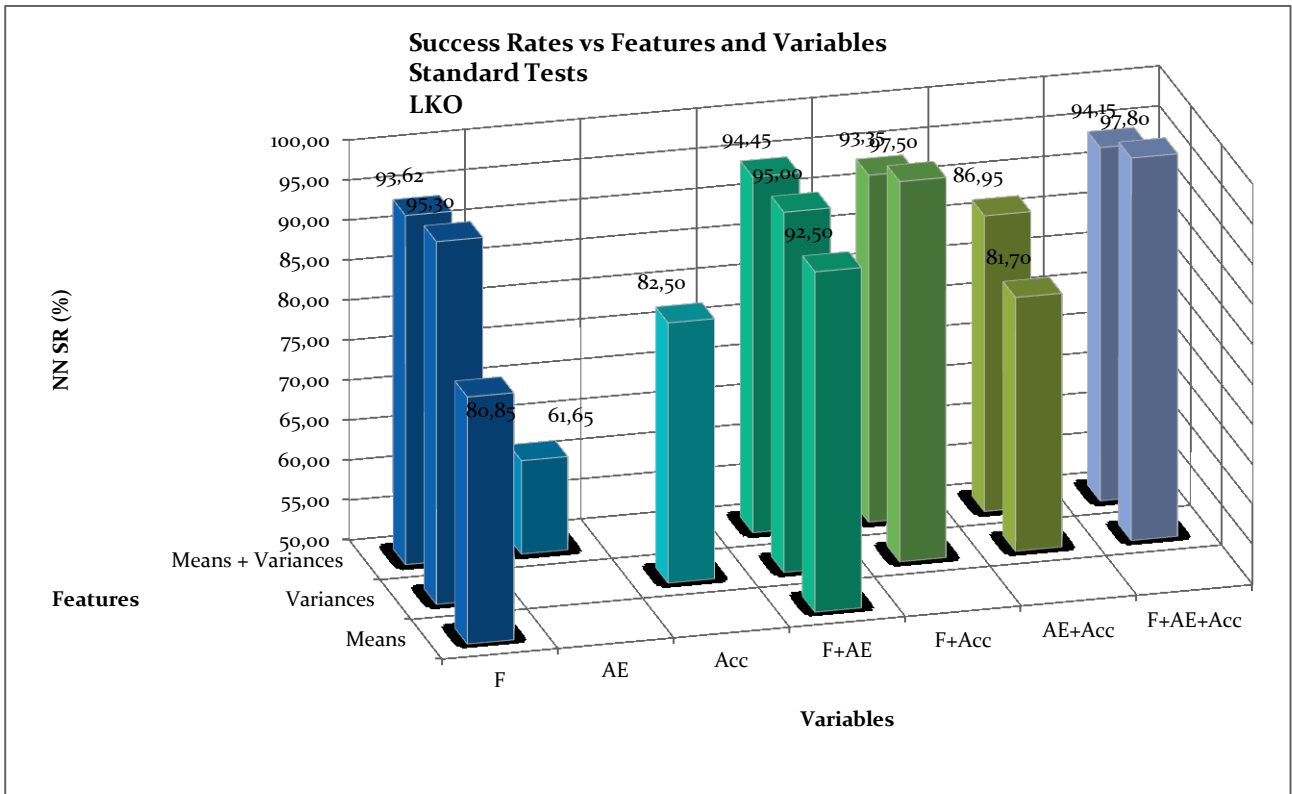


Fig. 10.4. Conventional features evaluation: LKO training algorithm

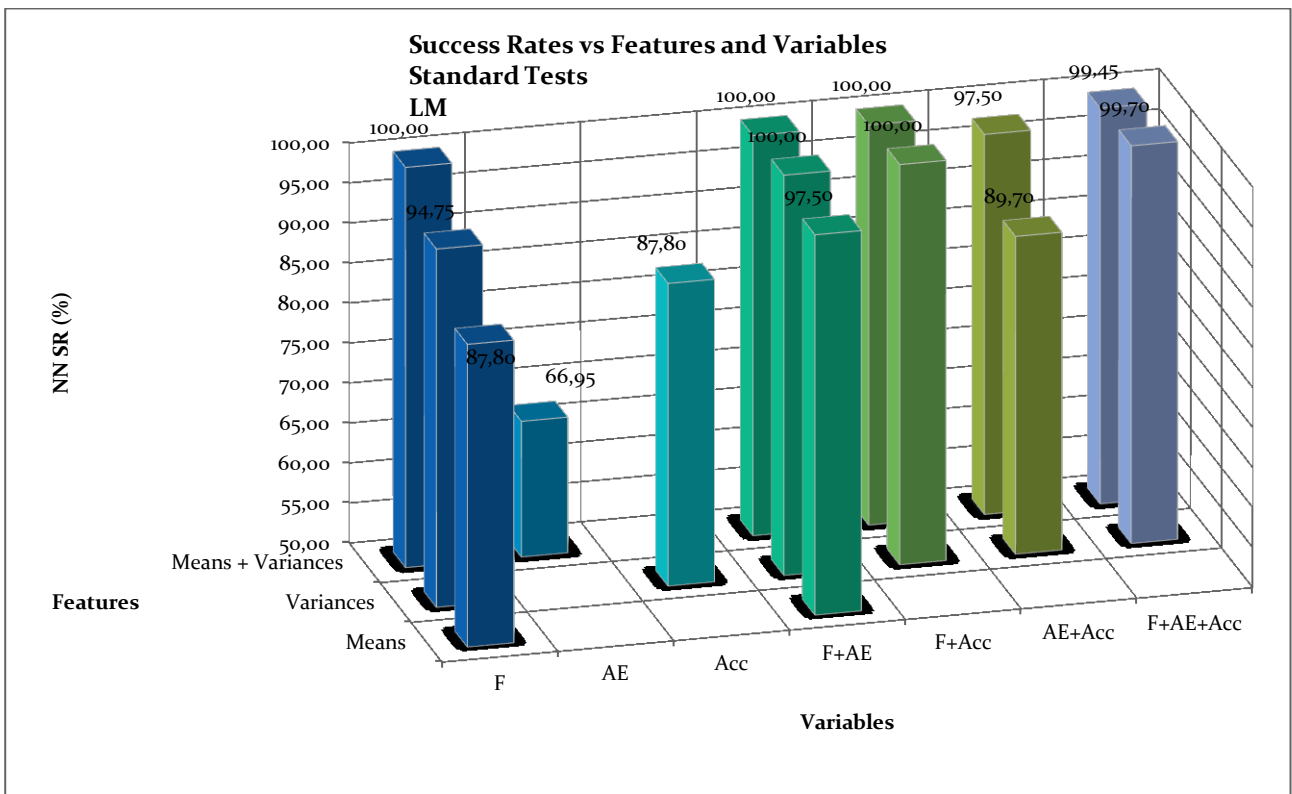


Fig. 10.5. Conventional features evaluation: LM training algorithm

Variables Comparison

Fig. 10.6. shows that as single group of variables, the cutting force components yield better results in terms of average success rate.

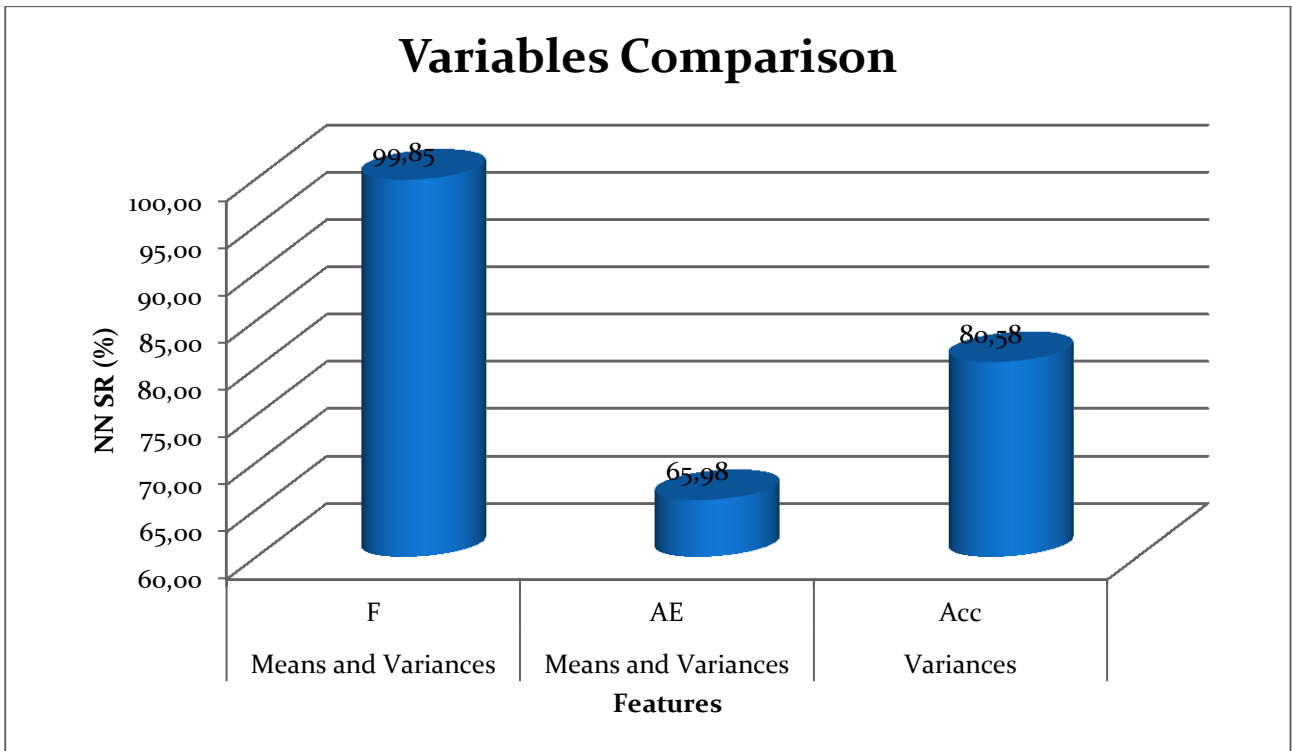


Fig. 10.6. Variables comparison

PCA Features Evaluation

Fig. 10.7. shows that by increasing the number of Principal Components, the success rates increases. By freezing the number of Principal Components utilized, the plot shows better results coming from cutting force components based PCA features.

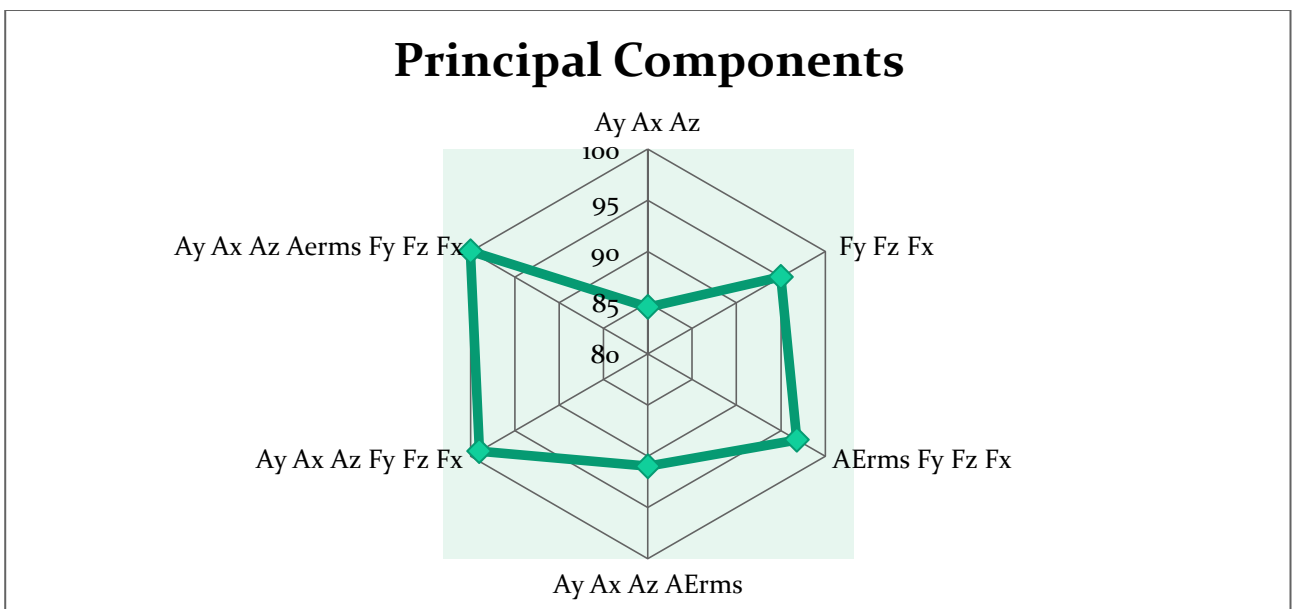


Fig. 10.7. PCA features evaluation

Success Rates vs. Training Algorithms

Levenberg-Marquardt training algorithm shows higher success rates compared to other algorithms both by adopting Conventional and PCA features, the differences in terms of success rates among the best (LM) and the worst (SCG) training algorithms is 7.45%. The results regarding the differences among the training algorithms are reported in Table 10.3 and in Fig. 10.6.

Table 10.3. Training algorithms comparison

	SCG	LKO	LM
Conventional	85,75	89,09	94,37
PCA	92,04	90,61	96,76

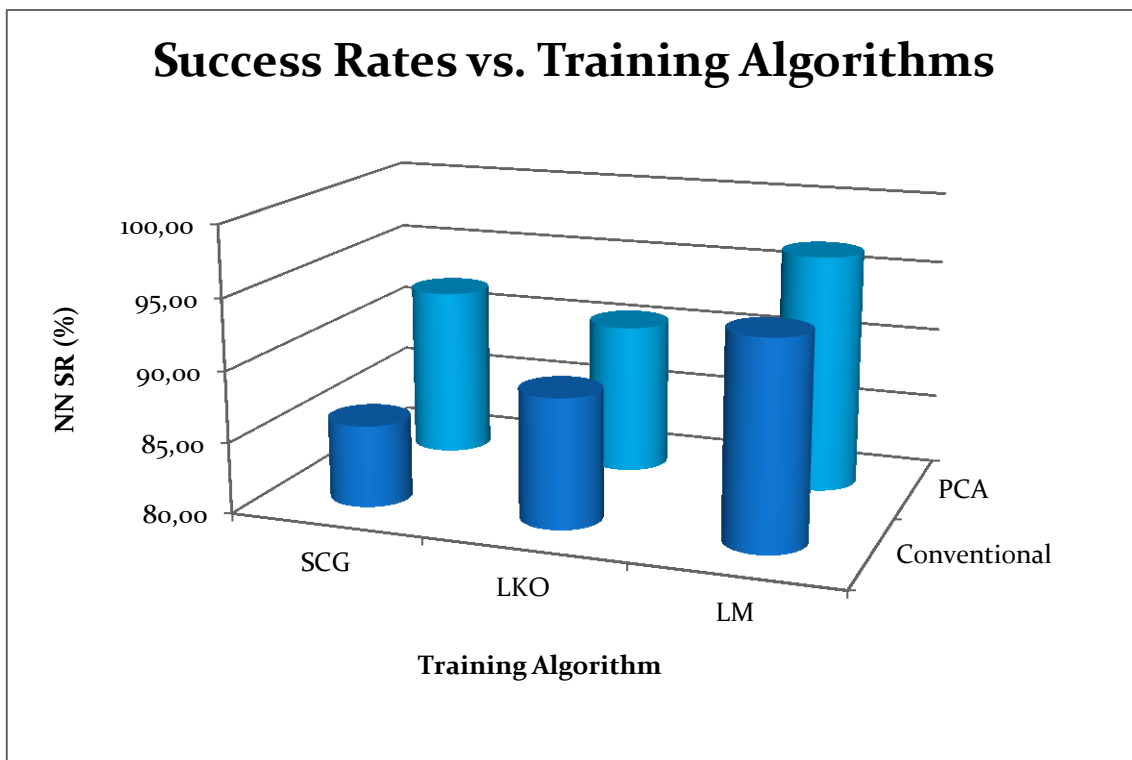


Fig. 10.8. Training algorithms comparison

Success Rates vs. Number of Hidden Layer Nodes

The general trend visible when increasing the number of hidden layer nodes, is an increasing of success rates. This occurs for both LM and SCG training algorithms but not for LKO, for which increasing hidden layer nodes yields a very small, not appreciable, decreasing trend, as reported in Fig. 10.9.

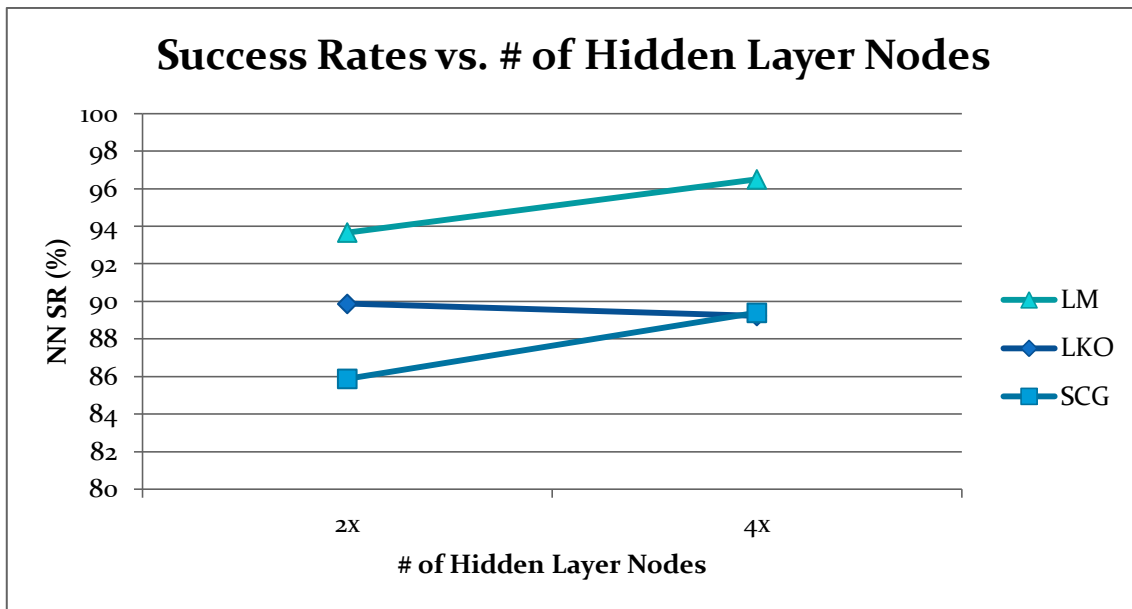


Fig. 10.9. Hidden layer nodes influence

10.1.2. Standard Tests + Severe Cutting Conditions Tests

Statistics Summary

Table 10.4. Statistics summary

Statistics	
Total Average	87,73
Std dev.	11,40
Mode	99,6
Minimum	59,6
Conv vs PCA	
Conv	88,81
PCA	85,19
Difference	-3,63
Training Algorithm	
LM	90,85
SCG	84,60
LKO	
LM-SCG	6,25
LM-LKO	90,85
SCG-LKO	84,60
Hidden Layer Nodes (4x - 2x)	
LM	2,31
SCG	2,44
LKO	2,12

The results reported in Table 10.1 show that:

- It is possible to identify the tool state by extracting features from multi sensor signals with an average Success Rate (SR) = 87.73% , the minimum SR is 59.6%.
- The most frequent success rate is 99.6% showing an excellent reliability of features and neural network, for both Conventional and PCA features.

PCA vs. Conventional

Considering all the categories of NN Configurations, in terms of training algorithm and number of hidden layer nodes, the features extracted by conventional methodology yield to a more successful pattern recognition than the ones obtained by PCA, as shown in Table 10.5 and in Fig. 10.10. The difference in success rate between the two methodologies is 3.63%

The training algorithm that shows a clearer difference between the two features extraction methodologies is the SCG, where the gap ranges from 5.86 % (SCG-2x) to 5.14 % (SCG-4X).

Table 10.5. Conventional vs. PCA

	LKO 2x	LKO 4x	SCG 2x	SCG 4x	LM 2x	LM 4x
Conventional	85,41	86,93	85,14	87,36	90,22	92,54
PCA	80,08	83,60	79,28	82,22	88,48	90,77

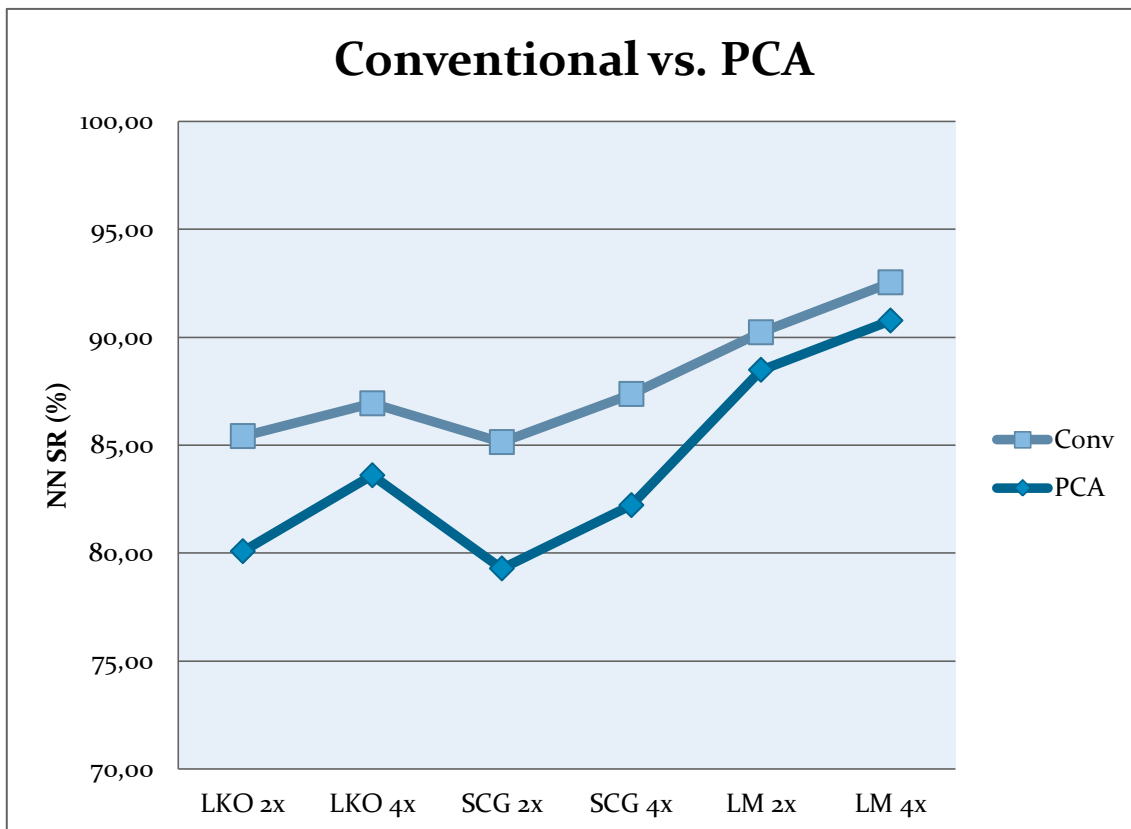


Fig. 10.10. Conventional vs. PCA

Conventional Features Evaluation

In Figs. 10.11, 10.12, 10.13 and 10.14 a conventional features evaluation is reported

Figures show that by increasing the number of features, the success rates increases too,

It is clear also that increasing the number of variables yields higher success rates.

This evaluation has been carried out for all the training algorithms and the trend mentioned above occurs for each training algorithm.

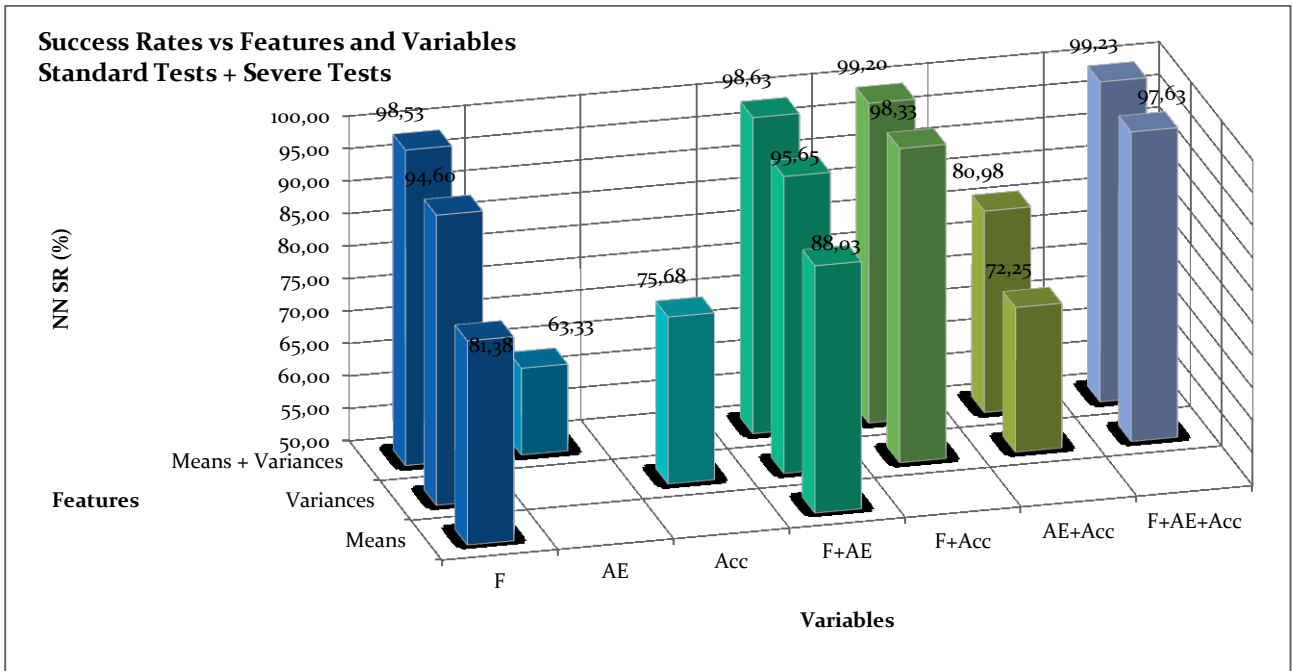


Fig. 10.11. Conventional features evaluation: overall average

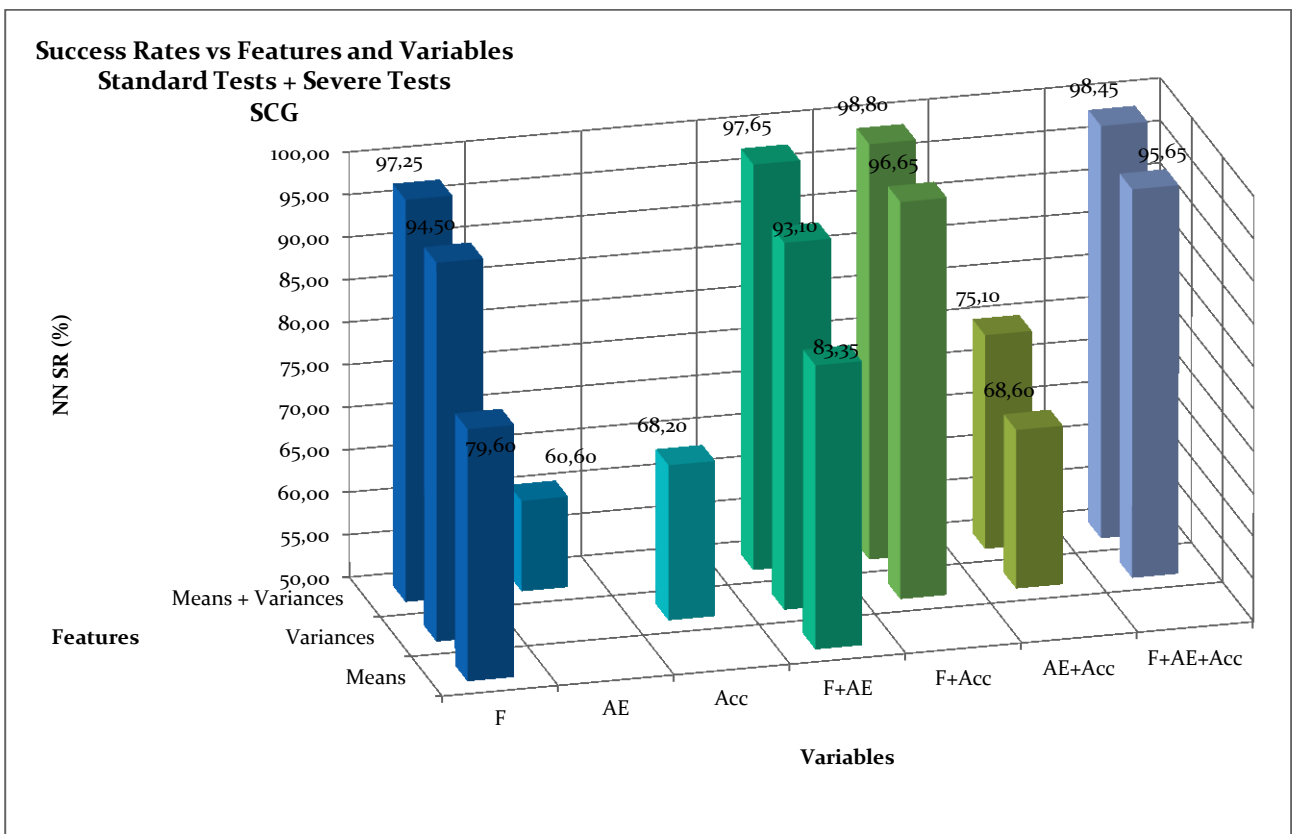


Fig. 10.12. Conventional features evaluation: SCG training algorithm

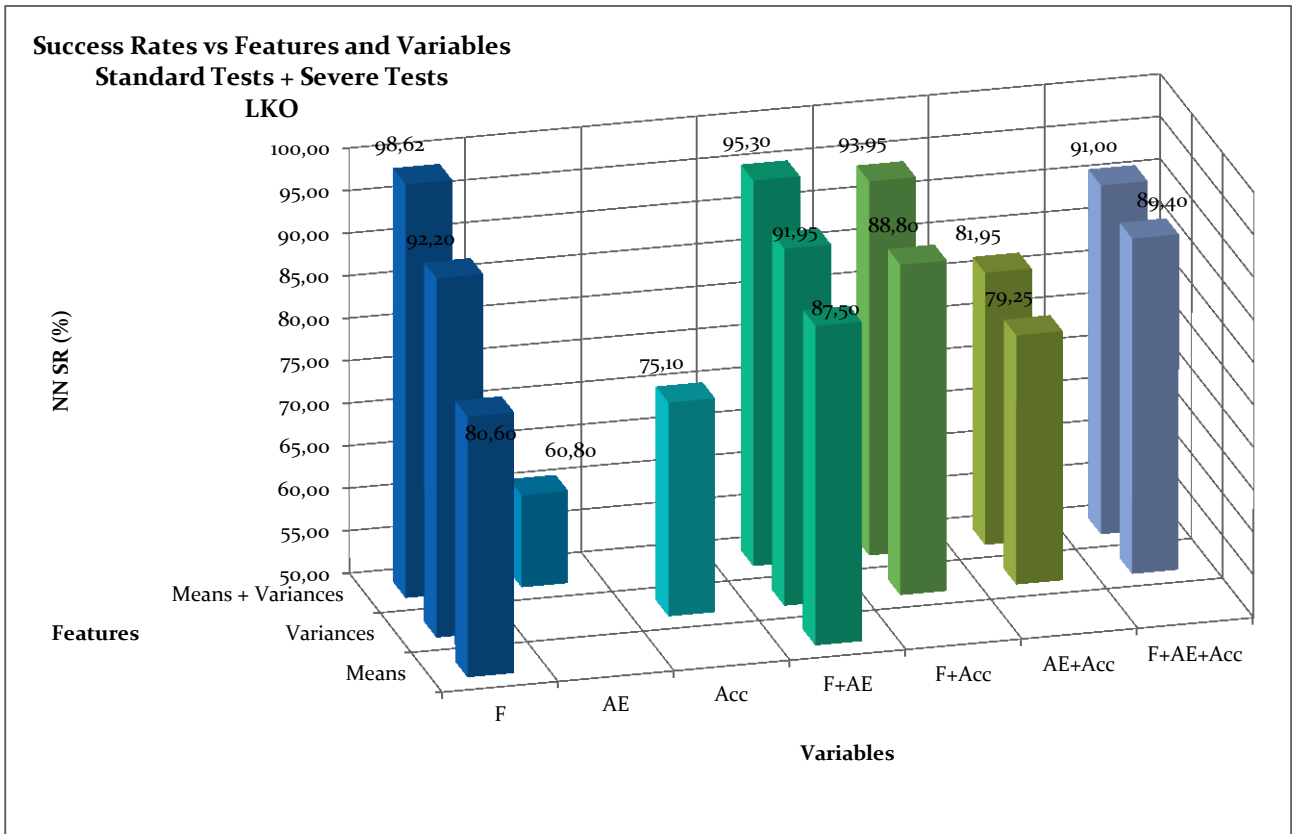


Fig. 10.13. Conventional features evaluation: LKO training algorithm

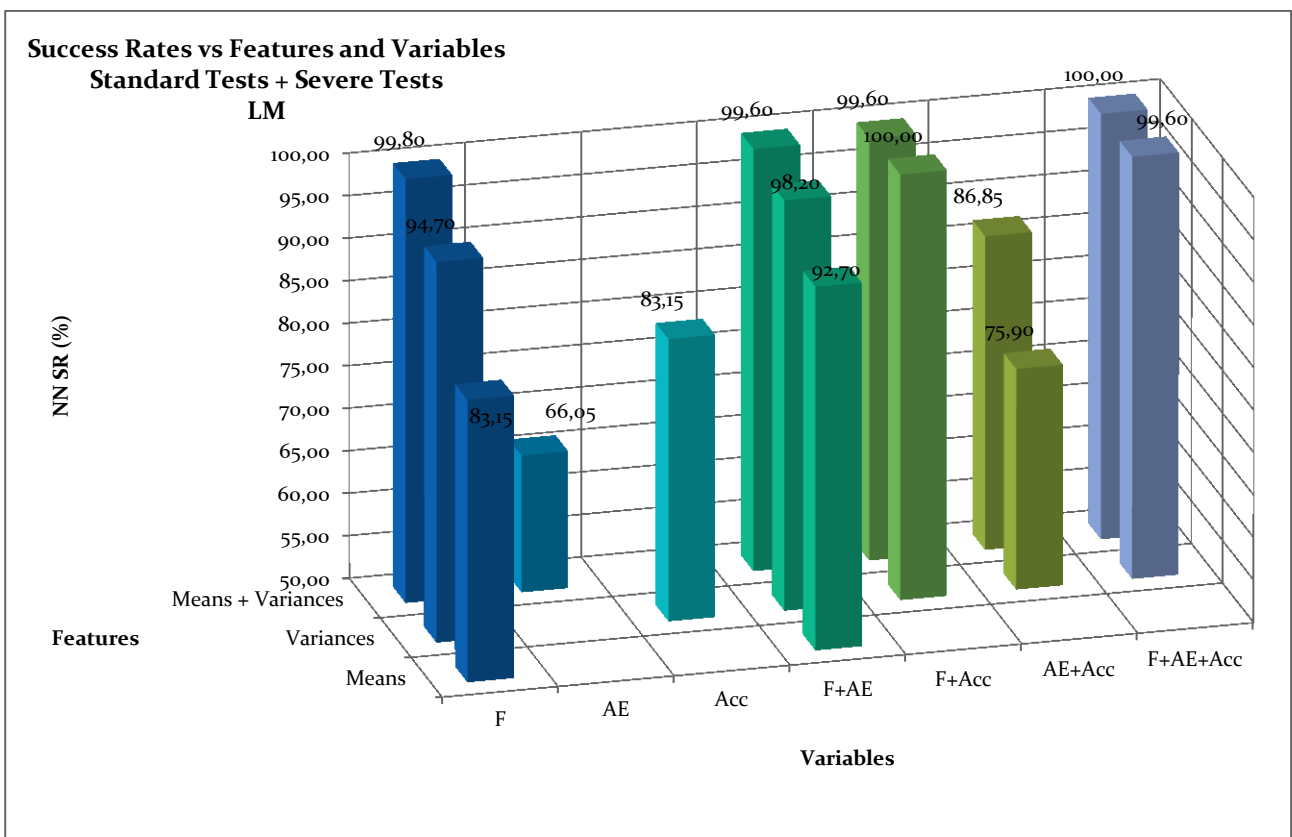


Fig. 10.14. Conventional features evaluation: LM training algorithm

Variables Comparison

Fig. 10.14. shows that as single group of variables, the cutting force components yield better results in terms of average success rate.

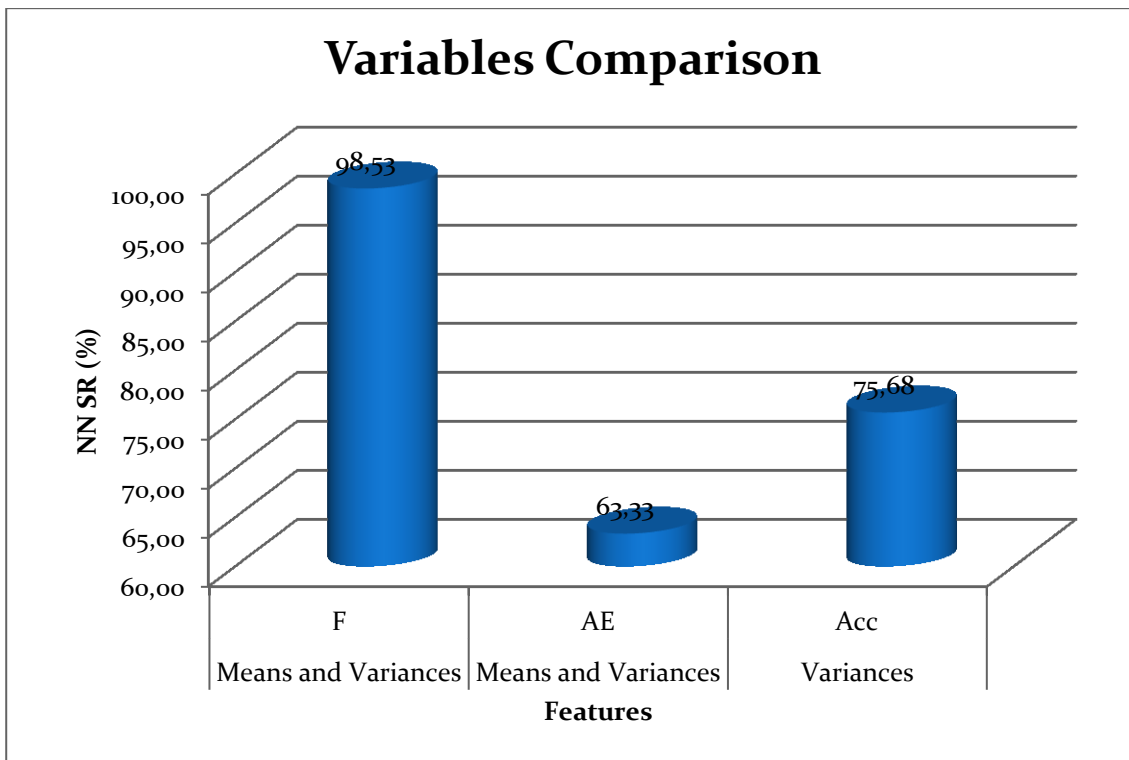


Fig. 10.15. Variables comparison

PCA Features Evaluation

Fig. 10.15. shows that by increasing the number of Principal Components, the success rates increases. By freezing the number of Principal Components utilized, the plot shows better results coming from cutting force components based PCA features.

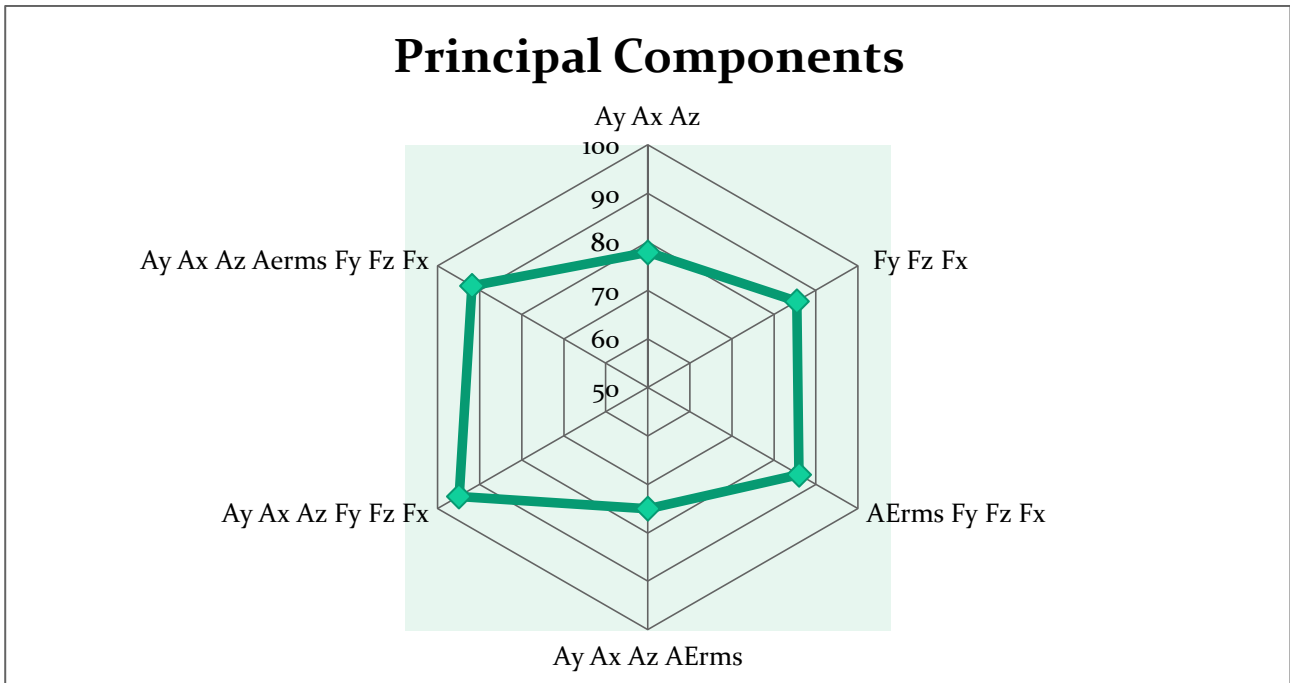


Fig. 10.16. PCA features evaluation

Success Rates vs. Training Algorithms

Levenberg-Marquardt training algorithm shows higher success rates compared to other algorithms both by adopting Conventional and PCA features, the differences in terms of success rates among the best (LM) and the worst (SCG) training algorithms is 7.45%. The results regarding the differences among the training algorithms are reported in Table 10.5 and in Fig. 10.16.

Table 10.6. Training algorithms comparison

	SCG	LKO	LM
Conventional	86,25	86,17	91,38
PCA	80,75	81,84	89,63

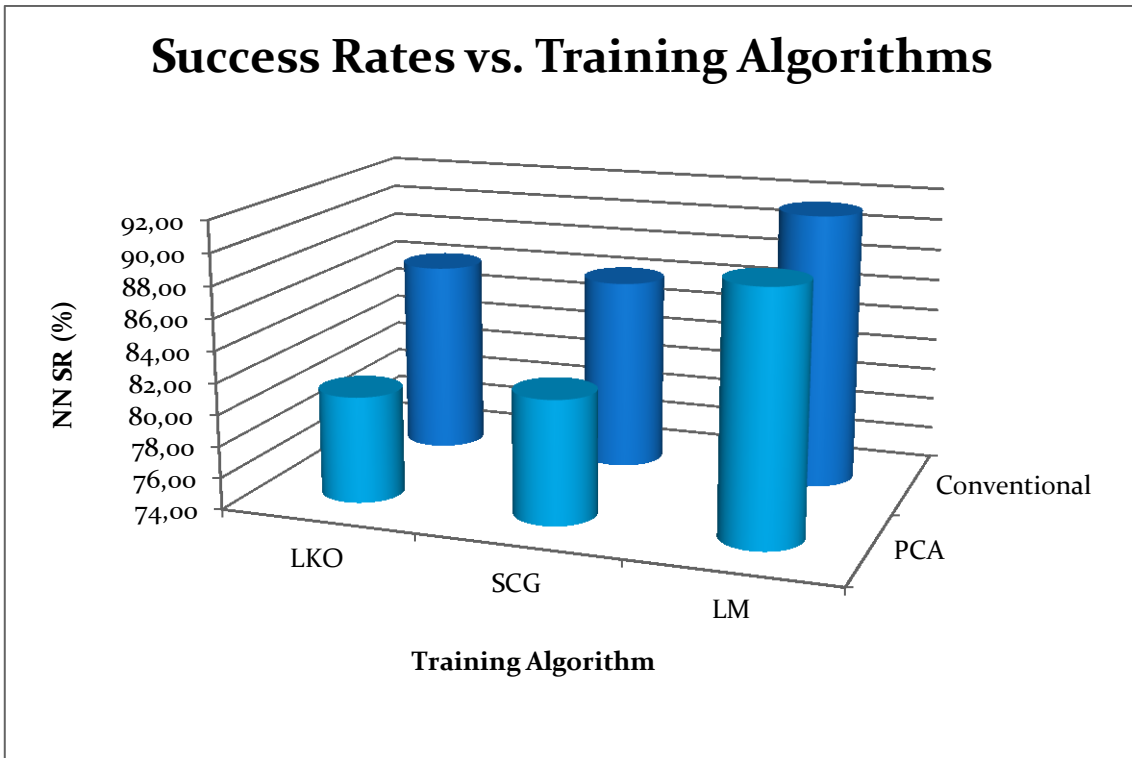


Fig. 10.17 Training algorithms comparison

Success Rates vs. Number of Hidden Layer Nodes

The general trend visible when increasing the number of hidden layer nodes, is an increasing of success rates. This occurs all the training algorithms, as reported in Fig. 10.17.

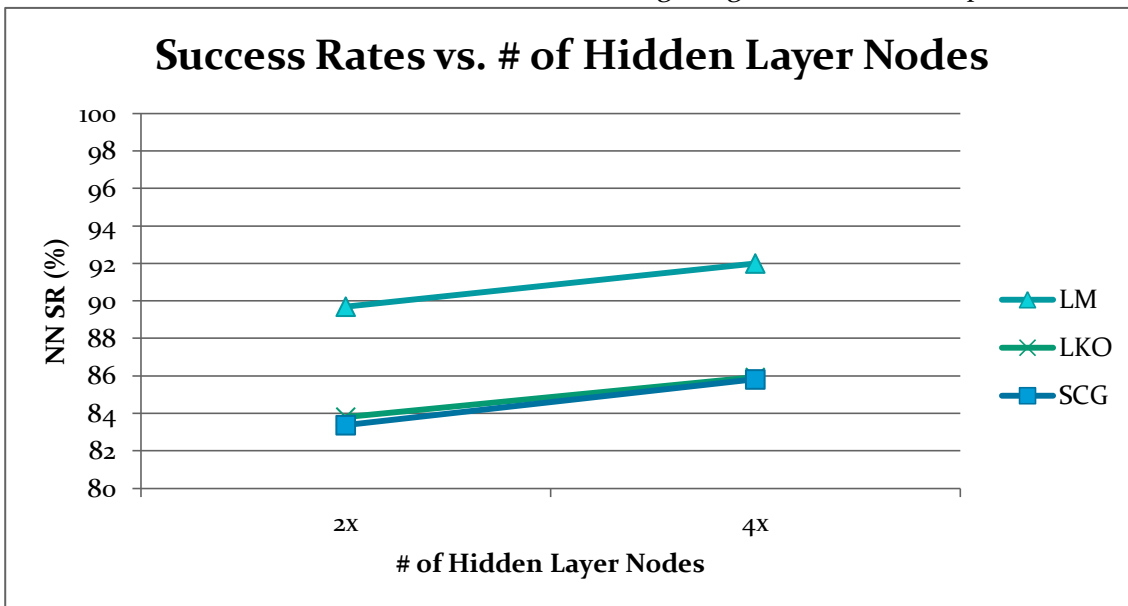


Fig. 10.18. Hidden layer nodes influence

10.2. Residual Stress Assessment (worn tool)

10.2.1. Standard Tests

Statistics Summary

Statistics	
Total Average	97,09
Std dev.	3,67
Mode	100
Minimum	84,4
Conv vs PCA	
Conv	97,70
PCA	95,66
Difference	-2,05
Training Algorithm	
LM	98,67
SCG	97,09
LKO	95,52
LM-SCG	1,59
LM-LKO	3,16
SCG-LKO	1,57
Hidden Layer Nodes (4x - 2x)	
LM	0,64
SCG	0,61
LKO	0,00

The results reported in Table 10.x show that:

- It is possible to distinguish favorable and unfavorable residual stresses by extracting features from signals acquired in correspondence of worn tool with an average Success Rate (SR) = 97.09% , the minimum SR is 84.4%.
- The most frequent success rate is 100% showing an excellent reliability of features and neural network, for both Conventional and PCA features.

PCA vs. Conventional

Considering all the categories of NN Configurations, in terms of training algorithm and number of hidden layer nodes, the features extracted by conventional methodology yield to a more successful pattern recognition than the ones obtained by PCA, as shown in Table 10.5 and in Fig. 10.19. The difference in success rate between the two methodologies is 2.05%

The training algorithm that shows a clearer difference between the two features extraction methodologies is the LKO, where the gap ranges from 2.55 % (LKO-2x) to 4.44 % (LKO-4X).

Table 10.7. Conventional vs PCA

	LKO 2x	LKO 4x	SCG 2x	SCG 4x	LM 2x	LM 4x
Conv	96,28	98,72	97,54	98,41	100,00	100,00
PCA	93,73	94,28	94,80	94,80	97,60	98,72

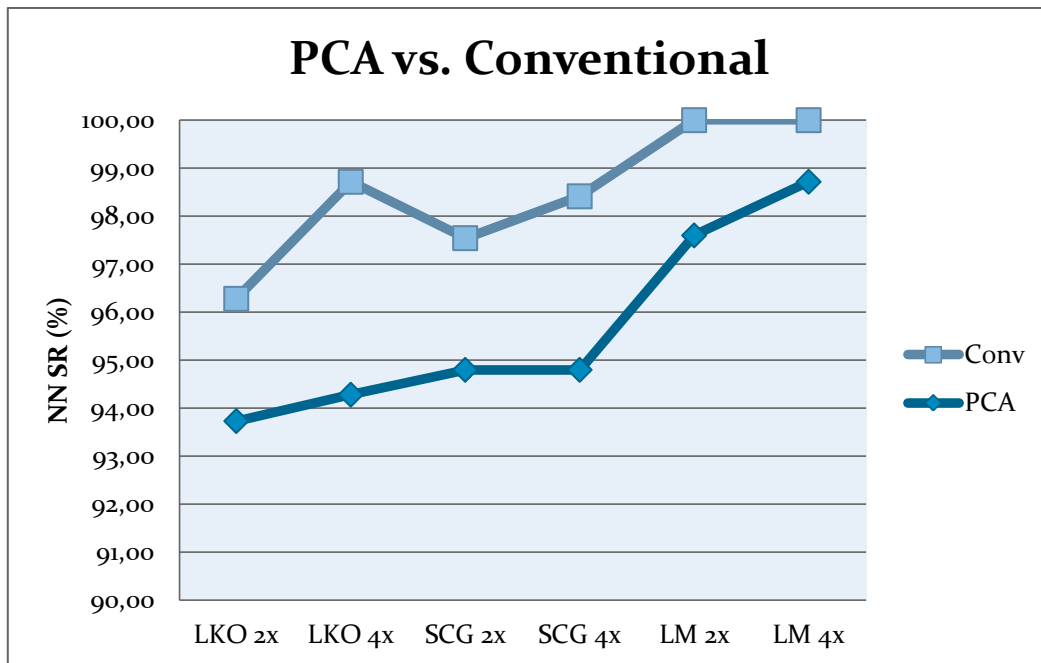


Fig. 10.19. Conventional vs PCA

Conventional Features Evaluation

In Figs. 10.20, 10.21, 10.22 and 10.23 a conventional features evaluation is reported

Figures show that by increasing the number of features, the success rates increase too,

It is clear also that increasing the number of variables yields higher success rates.

This evaluation has been carried out for all the training algorithms and the trend mentioned above occurs for each training algorithm.

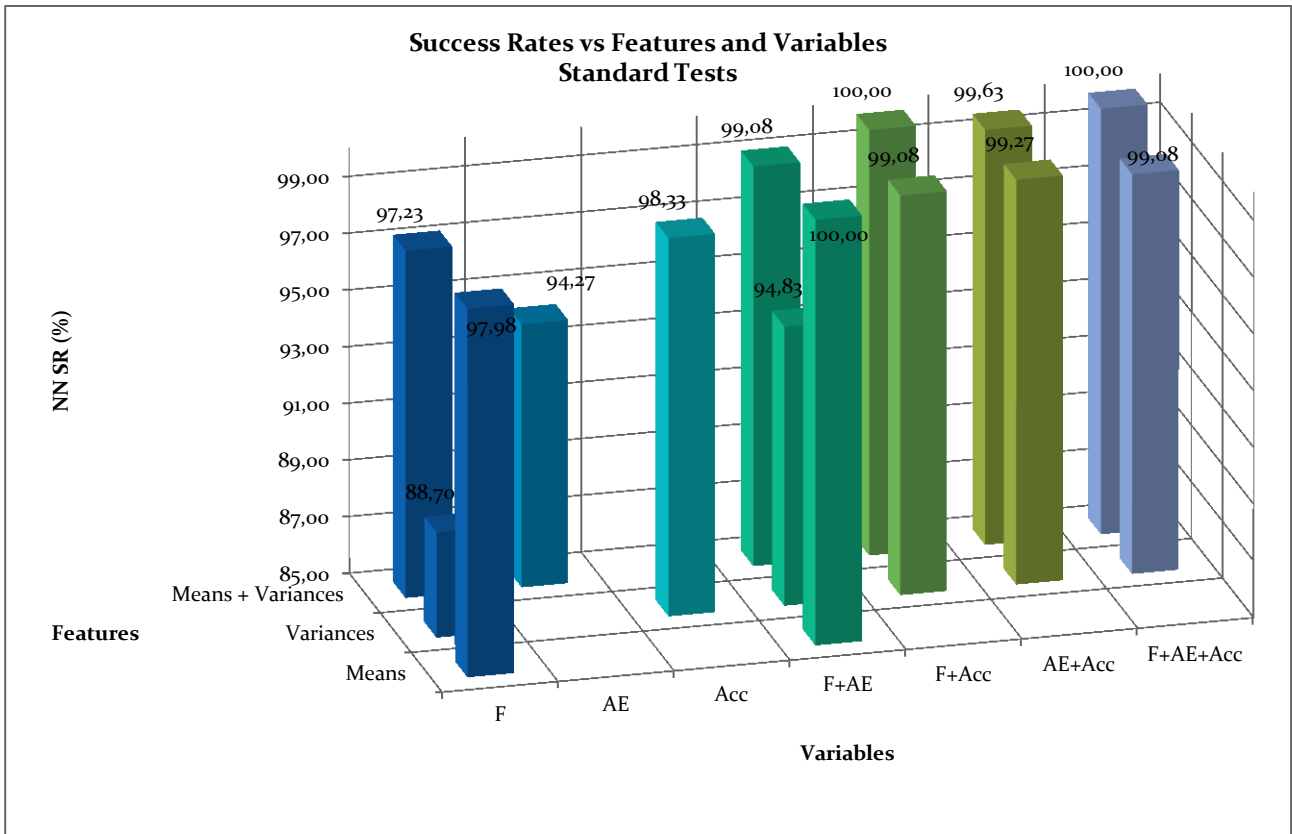


Fig. 10.20. Conventional features evaluation: overall average

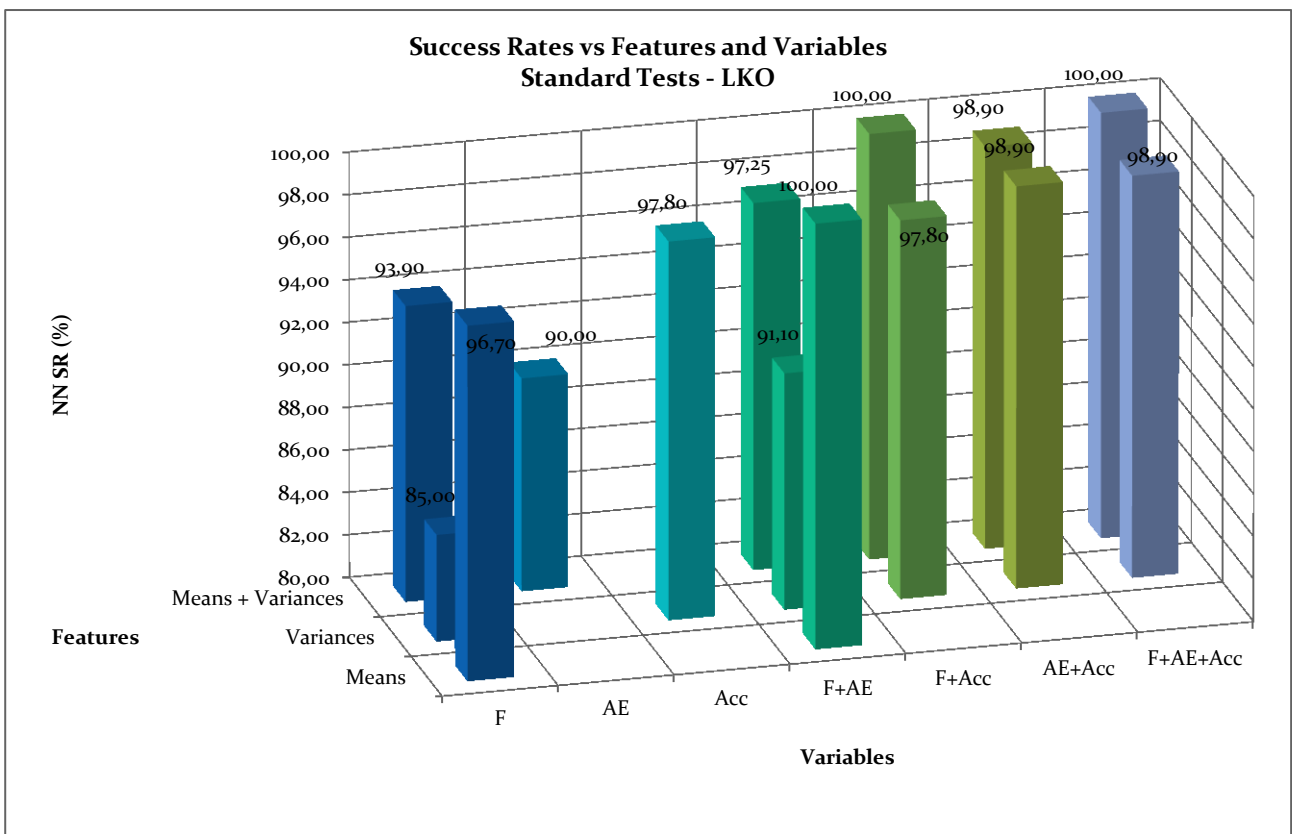


Fig. 10.21. Conventional features evaluation: LKO training algorithm

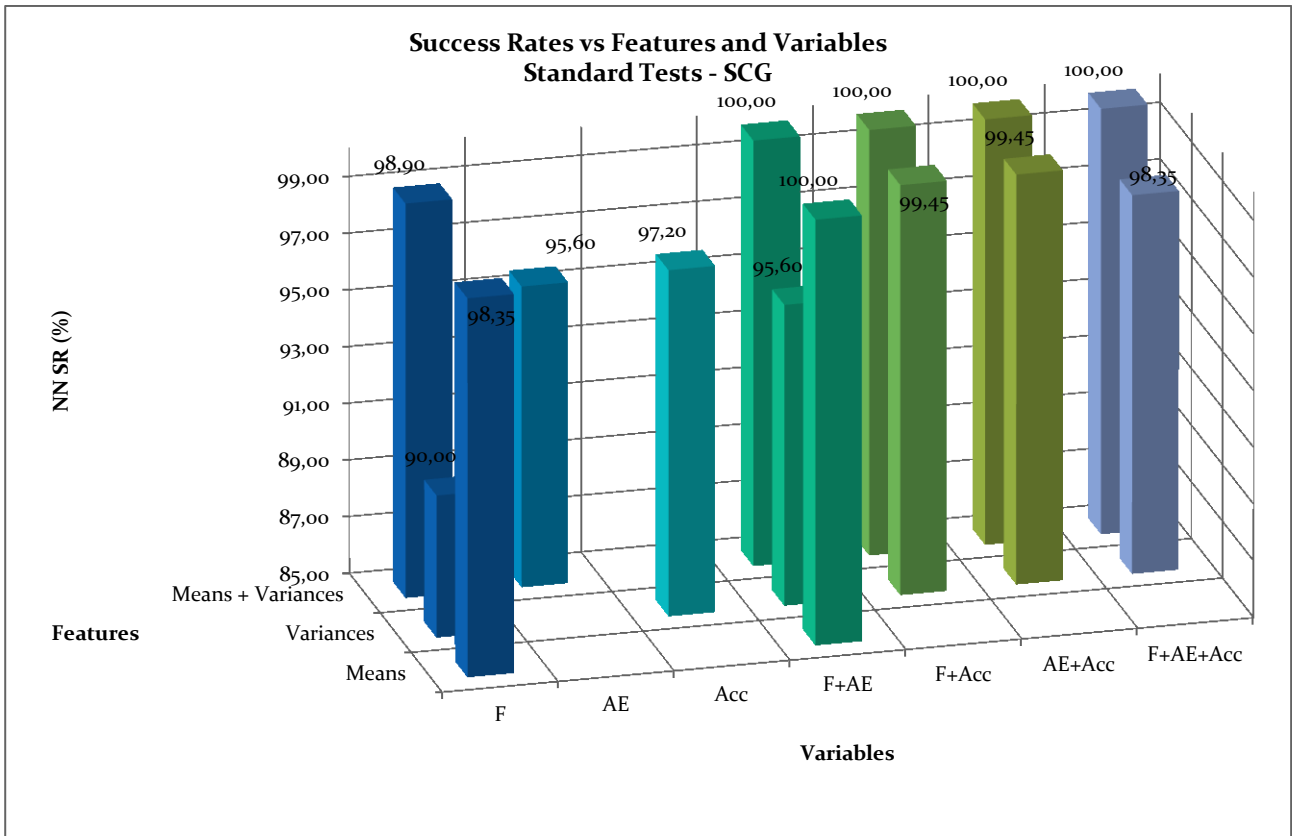


Fig. 10.22. Conventional features evaluation: SCG training algorithm

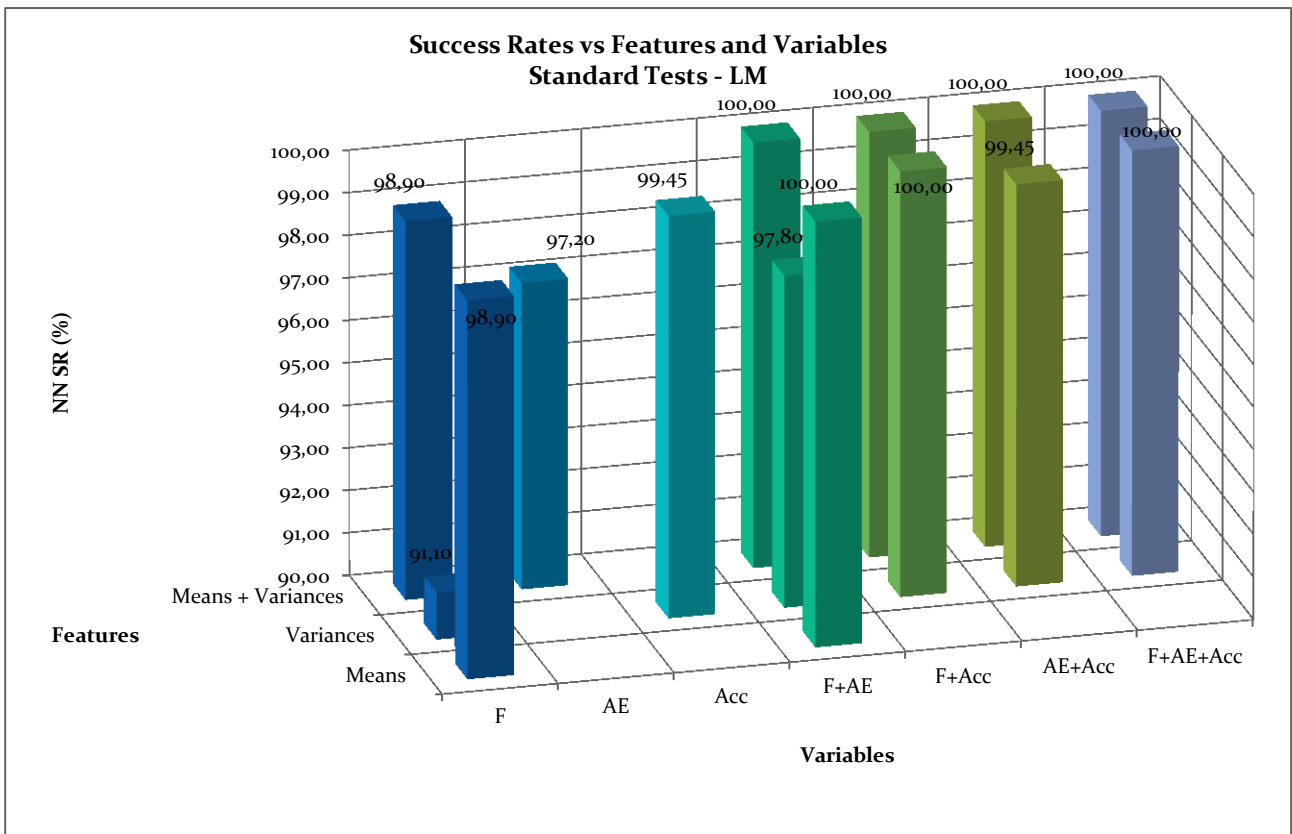


Fig. 10.23. Conventional features evaluation: SCG training algorithm

Variables Comparison

Fig. 10.23. shows that as single group of variables, the acceleration components yield better results in terms of average success rate.

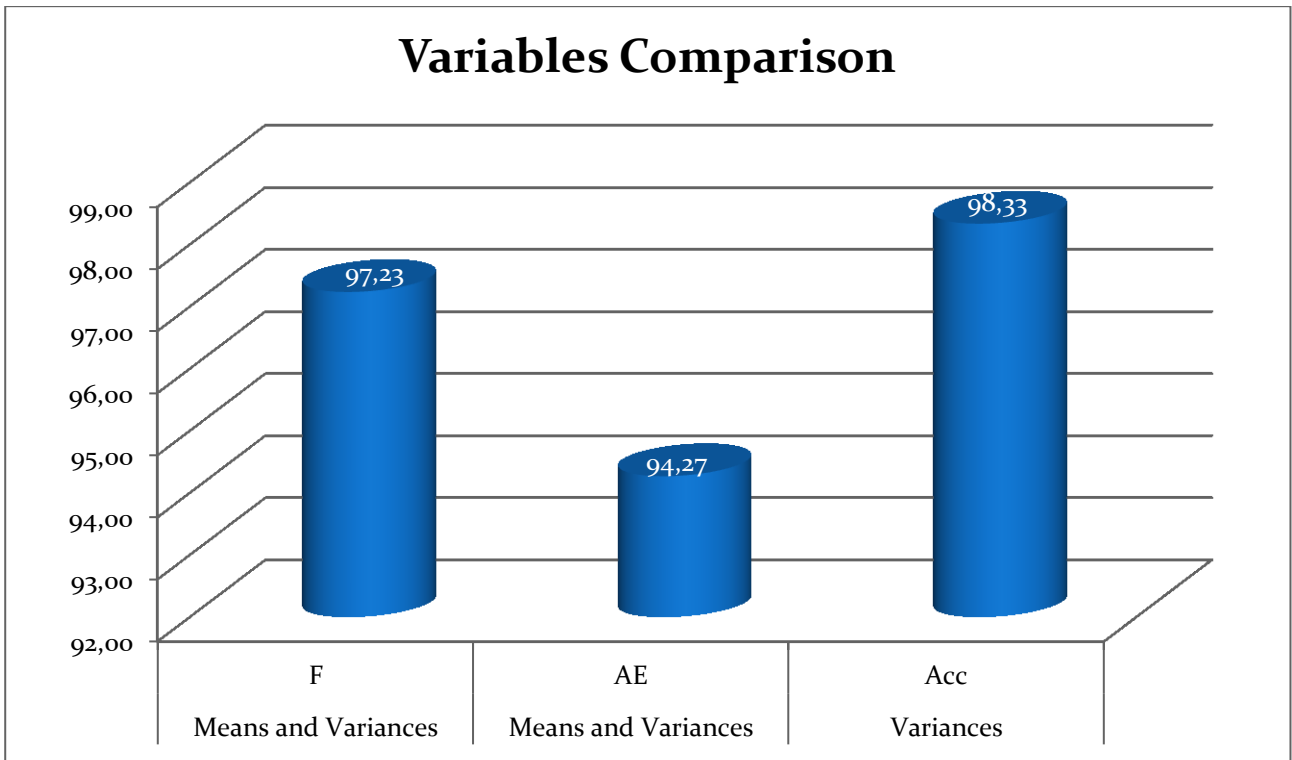


Fig. 10.24. Variables comparison

PCA Features Evaluation

Fig. 10.24. shows that by increasing the number of Principal Components, the success rates increases. By freezing the number of Principal Components utilized, the plot shows better results coming from cutting force components based PCA features.

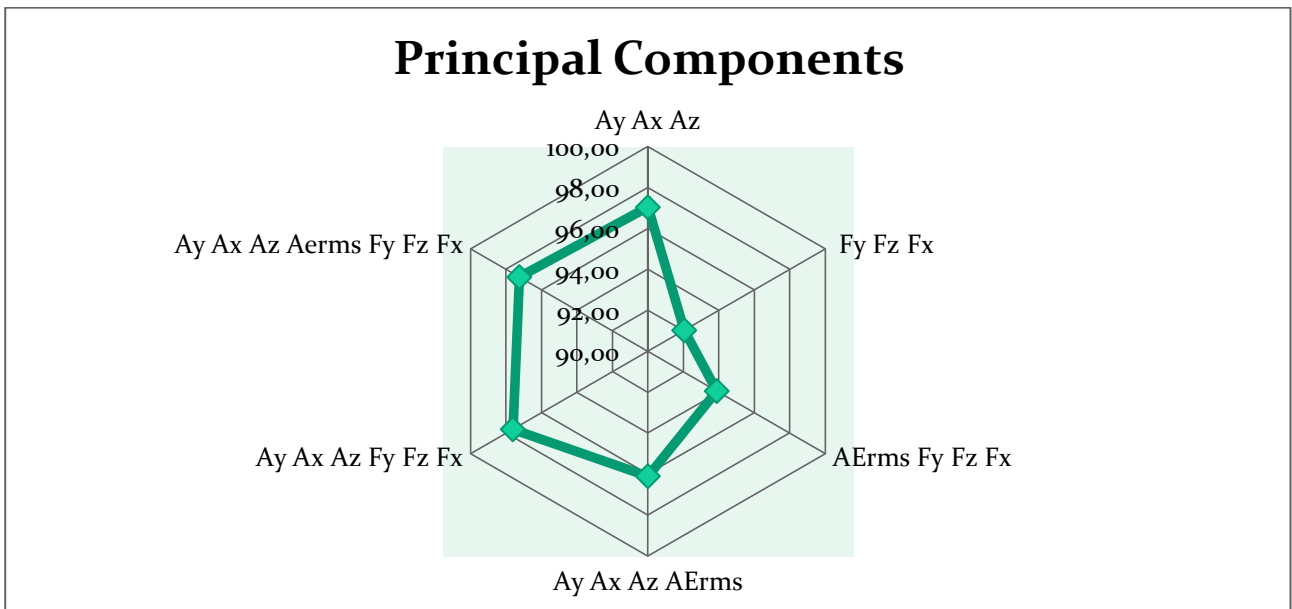


Fig. 10.25. PCA features evaluation

Success Rates vs. Training Algorithms

Levenberg-Marquardt training algorithm shows higher success rates compared to other algorithms both by adopting Conventional and PCA features, the differences in terms of success rates among the best (LM) and the worst (LKO) training algorithms is 5.99 %. The results regarding the differences among the training algorithms are reported in Table 10.7 and in Fig. 10.25.

10.8 Training algorithms comparison

	LKO	SCG	LM
Conventional	96,16	98,06	100,00
PCA	94,01	94,80	98,42

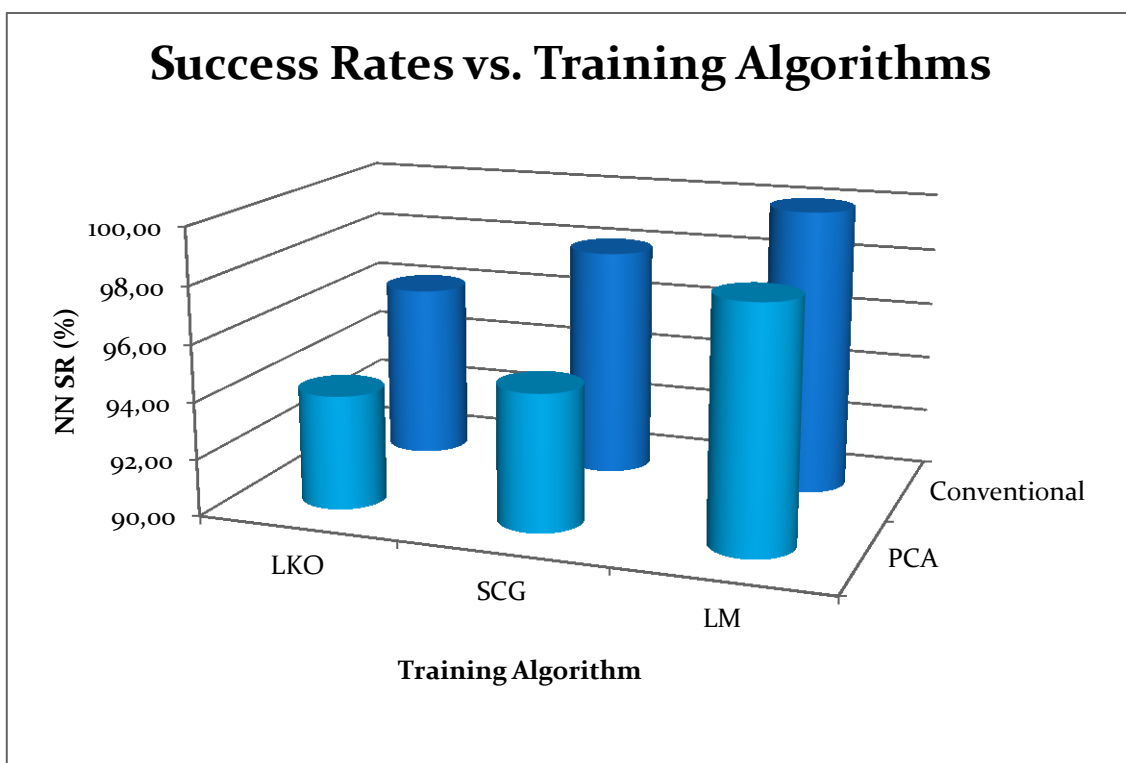


Fig. 10.26. Training algorithms comparison

Success Rates vs. Number of Hidden Layer Nodes

The general trend visible when increasing the number of hidden layer nodes, is an increasing of success rates. This occurs for both LM and SCG training algorithms but not for LKO, for which increasing hidden layer nodes yields a very small, not appreciable, decreasing trend, as reported in Fig. 10.26.

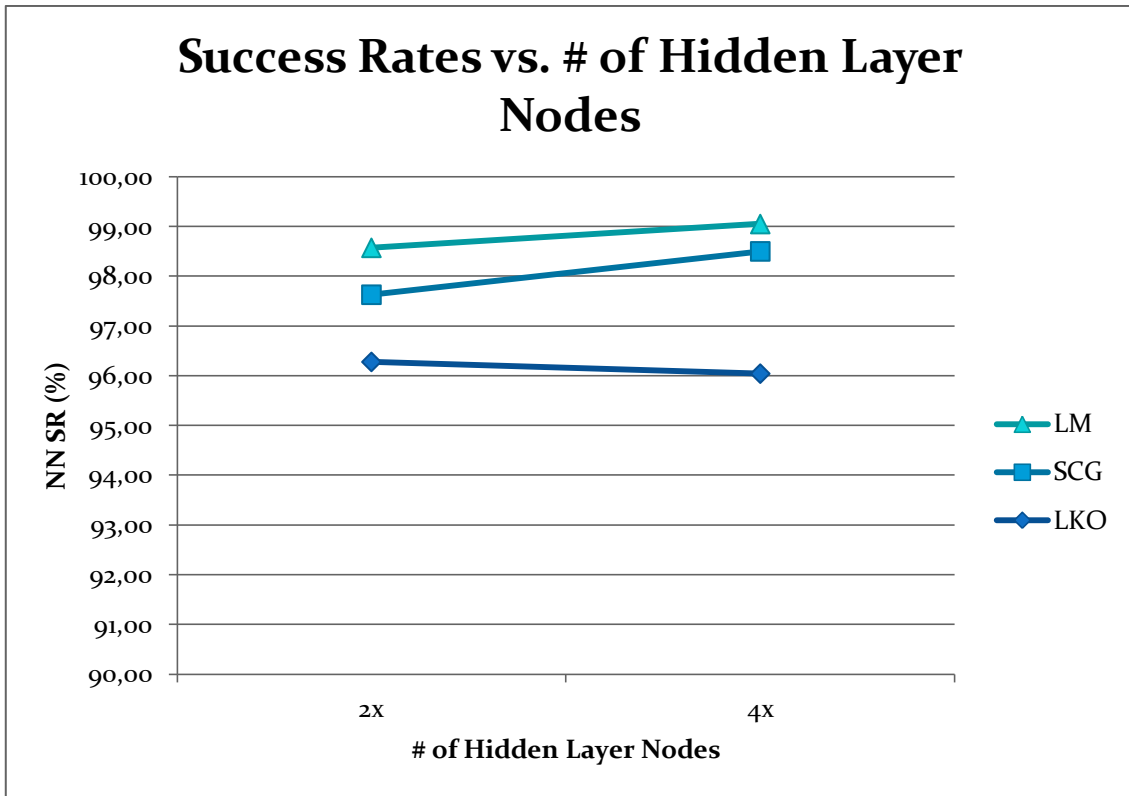


Fig. 10.27. Hidden layer nodes influence

10.2.2. Standard Tests + Severe Cutting Conditions Tests

Statistics Summary

Statistics	
Total Average	93,94
Std dev.	6,30
Mode	100
Minimum	71,5
Conv vs PCA	
Conv	96,31
PCA	88,40
Difference	-7,91
Training Algorithm	
LM	96,03
SCG	93,12
LKO	92,67
LM-SCG	2,91
LM-LKO	3,35
SCG-LKO	0,44
Hidden Layer Nodes (4x - 2x)	
LM	0,81
SCG	0,93
LKO	0,05

The results reported in Table 10.1 show that:

- It is possible to distinguish favorable and unfavorable residual stresses by extracting features from signals acquired in correspondence of fresh tool with an average Success Rate (SR) = 93.94% , the minimum SR is 71.5%.
- The most frequent success rate is 100% showing an excellent reliability of features and neural network, for both Conventional and PCA features.

PCA vs. Conventional

Considering all the categories of NN Configurations, in terms of training algorithm and number of hidden layer nodes, the features extracted by conventional methodology yield to a more successful pattern recognition than the ones obtained by PCA, as shown in Table 10.9 and in Fig. 10.28. The difference in success rate between the two methodologies is 7.91%

The training algorithm that shows a clearer difference between the two features extraction methodologies is the LKO, where the gap ranges from 9.12 % (LKO-2x) to 9.71 % (LKO-4X).

Table 10.9. Conventional vs PCA

	LKO 2x	LKO 4x	SCG 2x	SCG 4x	LM 2x	LM 4x
Conv	95,39	95,61	95,06	96,04	97,59	98,19
PCA	86,27	85,90	87,03	87,83	91,03	92,33

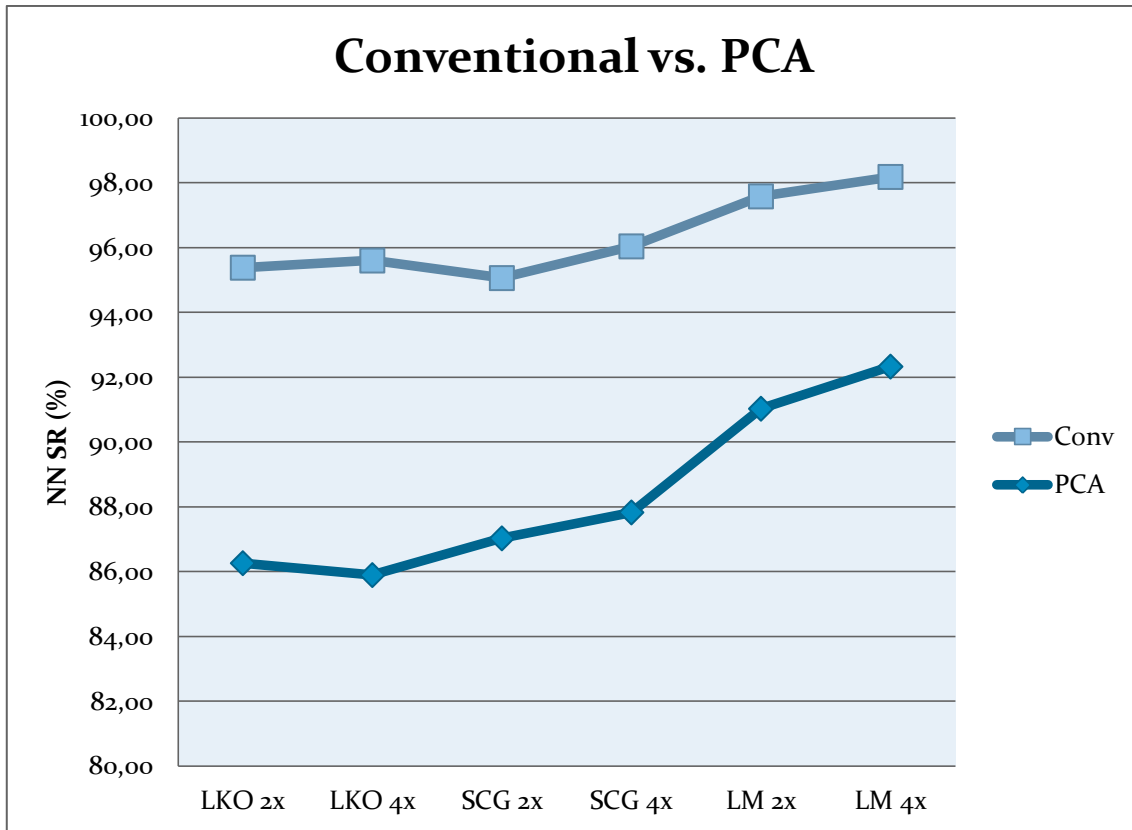


Fig. 10.28. Conventional vs. PCA

Conventional Features Evaluation

In Figs. 10.29, 10.30, 10.31 and 10.32 a conventional features evaluation is reported

Figures show that generally, by increasing the number of features, the success rates increase too,

It is clear also that, in most of cases, increasing the number of variables yields higher success rates.

This evaluation has been carried out for all the training algorithms and the trend mentioned above occurs for each training algorithm.

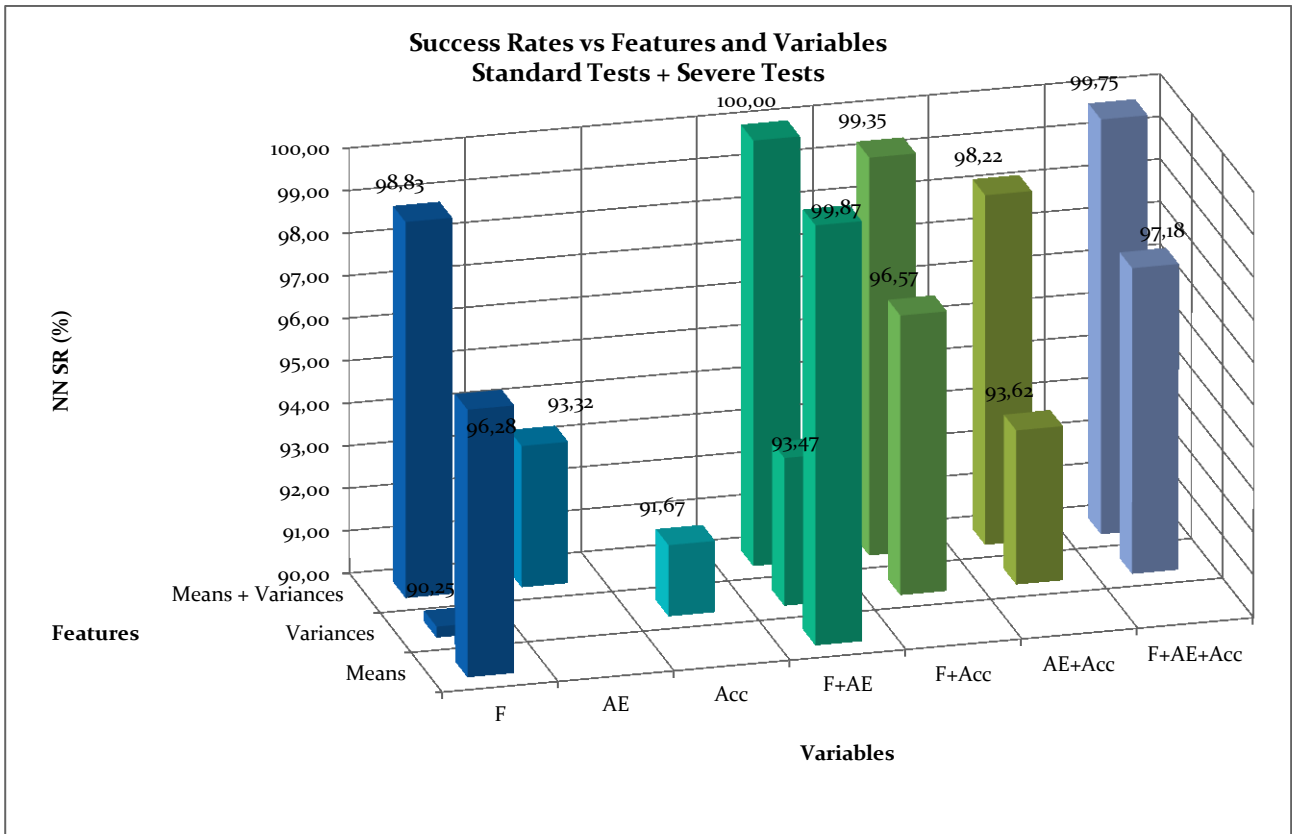


Fig. 10.29. Conventional features evaluation: overall average

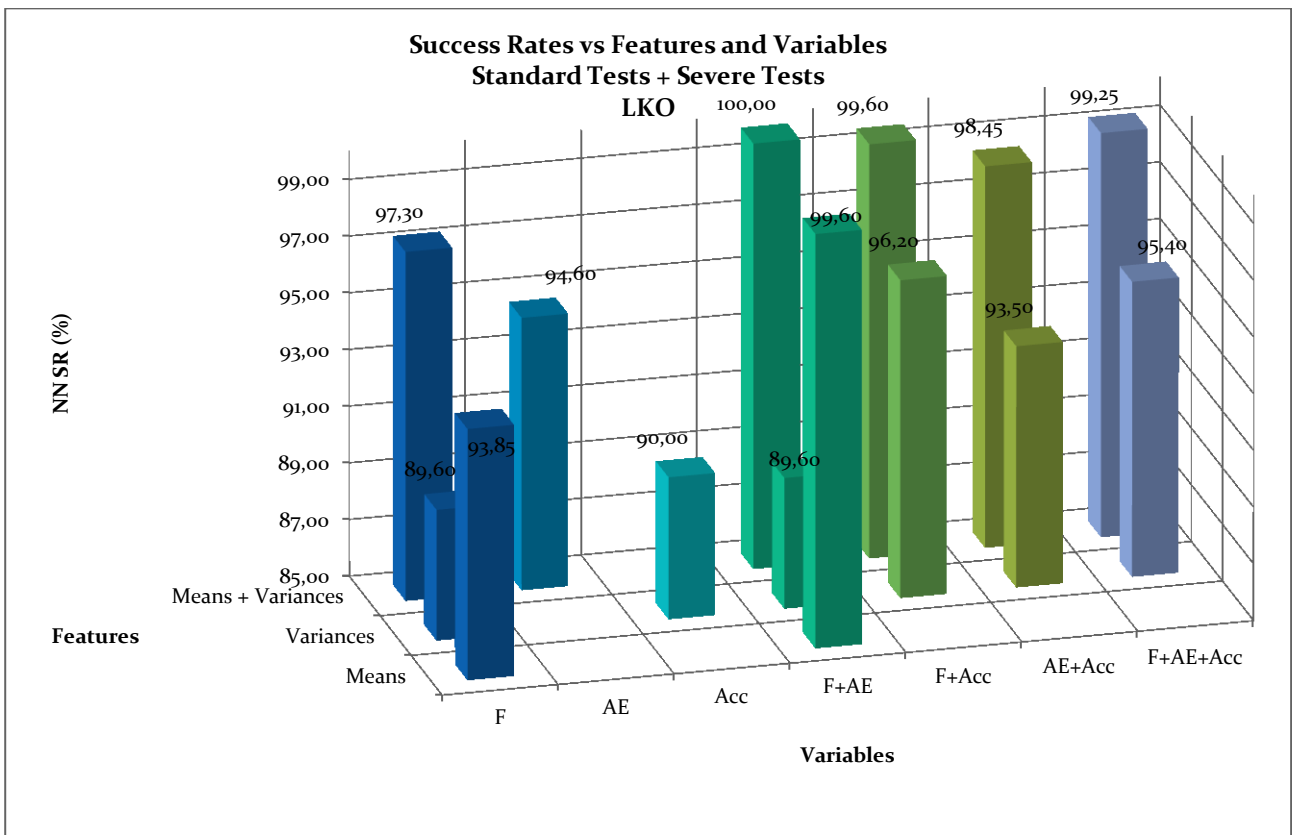


Fig. 10.30. Conventional features evaluation: LKO training algorithm

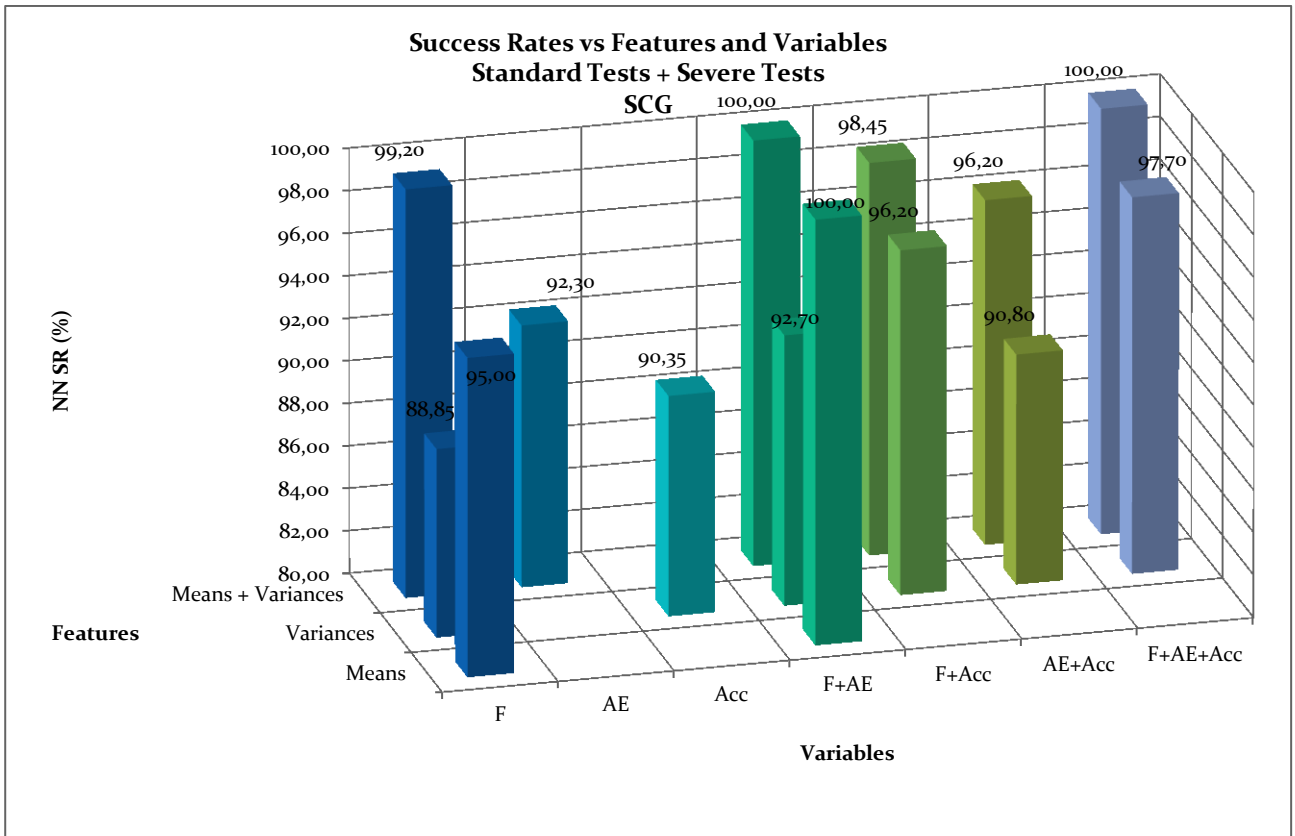


Fig. 10.31. Conventional features evaluation: SCG training algorithm

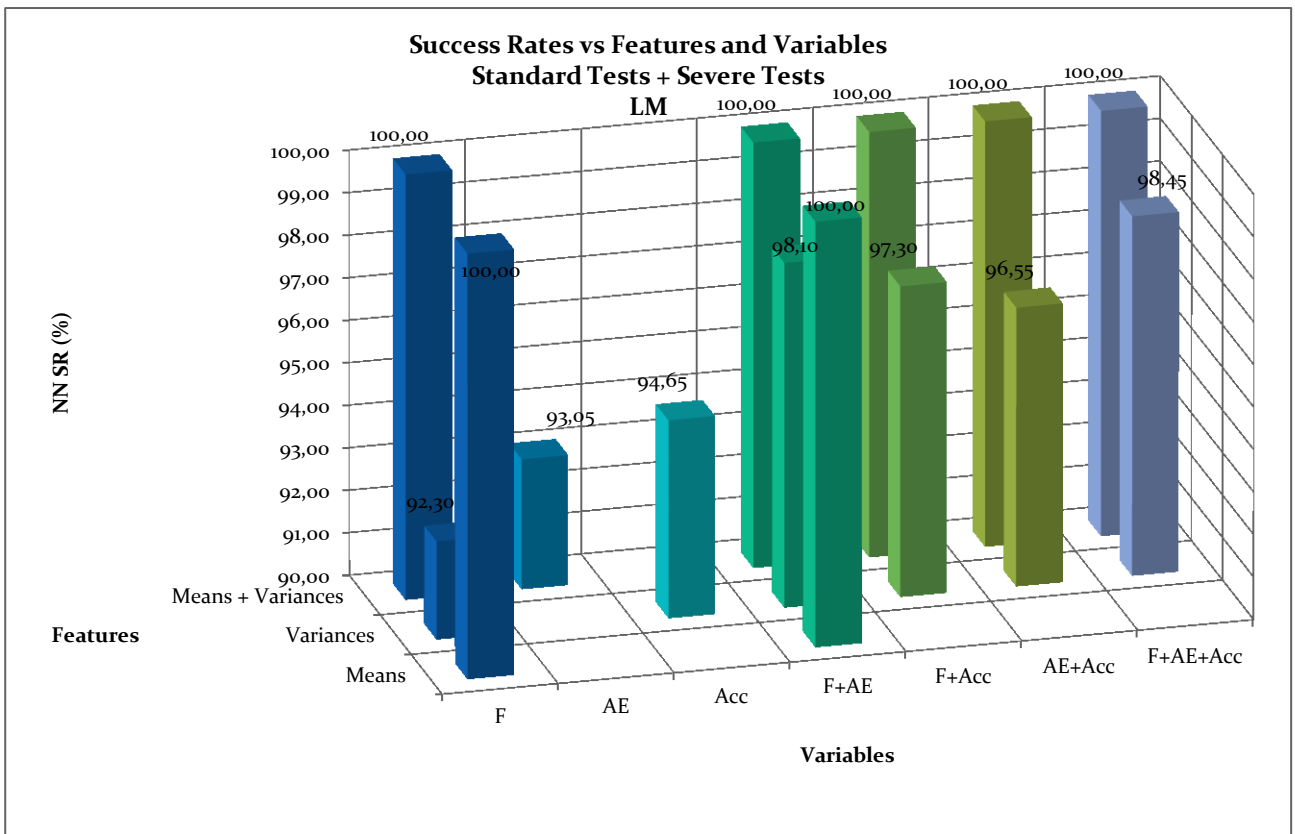


Fig. 10.32. Conventional features evaluation: LM training algorithm

Variables Comparison

Fig. 10.33. shows that as single group of variables, the cutting force components yield better results in terms of average success rate.

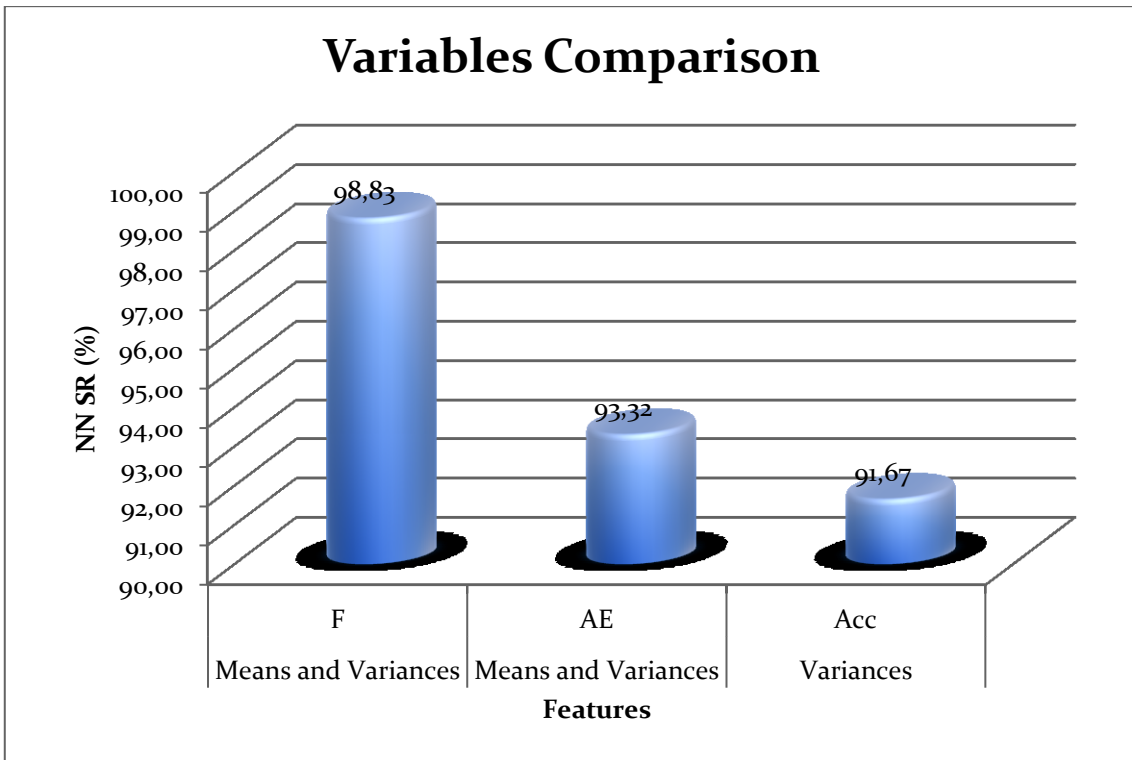


Fig. 10.33. Variables comparison

PCA Features Evaluation

Fig. 10.34. shows that by increasing the number of Principal Components, the success rates increases. By freezing the number of Principal Components utilized, the plot shows better results coming from acceleration components based PCA features.

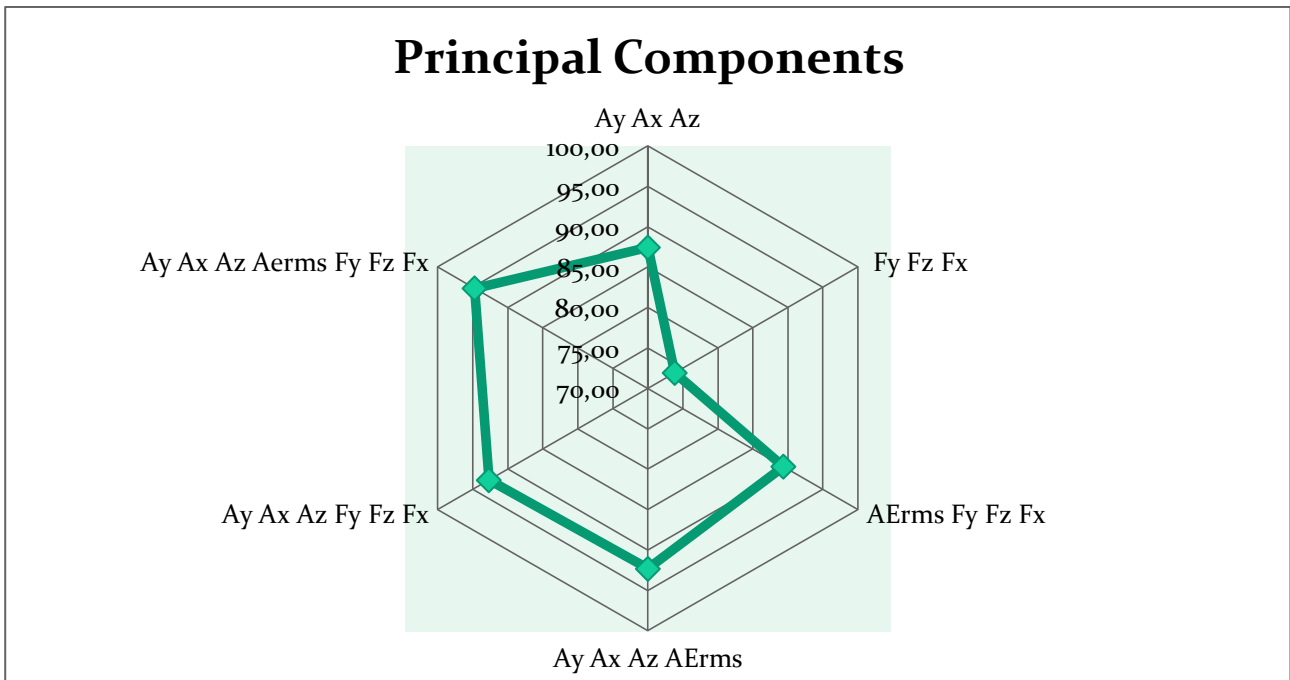


Fig. 10.34. PCA features evaluation

Success Rates vs. Training Algorithm

Levenberg-Marquardt training algorithm shows higher success rates compared to other algorithms both by adopting Conventional and PCA features, the differences in terms of success rates among the best (LM) and the worst (LKO) training algorithms is 7.45%. The results regarding the differences among the training algorithms are reported in Table 10.5 and in Fig. 10.16.

10.10. Training algorithms comparison

	LKO	SCG	LM
Conventional	95,50	95,55	97,89
PCA	86,08	87,43	91,68

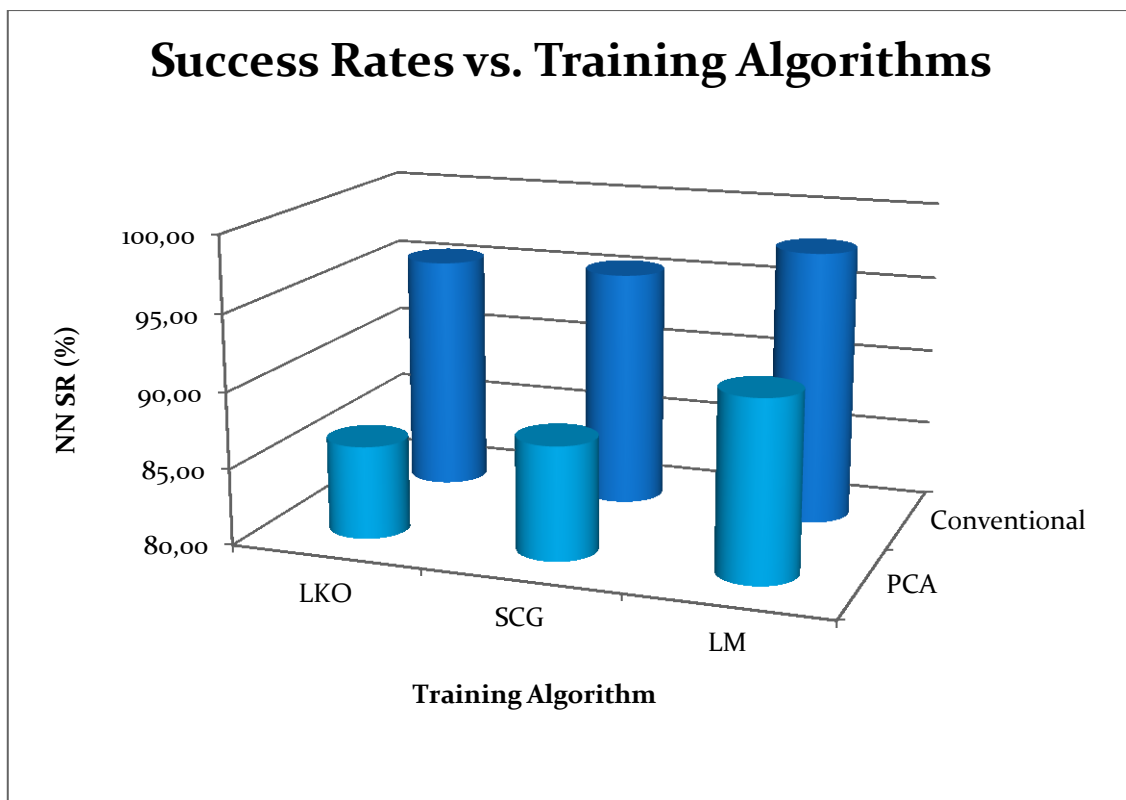


Fig. 10.35. Training algorithms comparison

Success Rates vs. Number of Hidden Layer Nodes

The general trend visible when increasing the number of hidden layer nodes, is an increasing of success rates. This occurs all the training algorithms, as reported in Fig. 10.36.

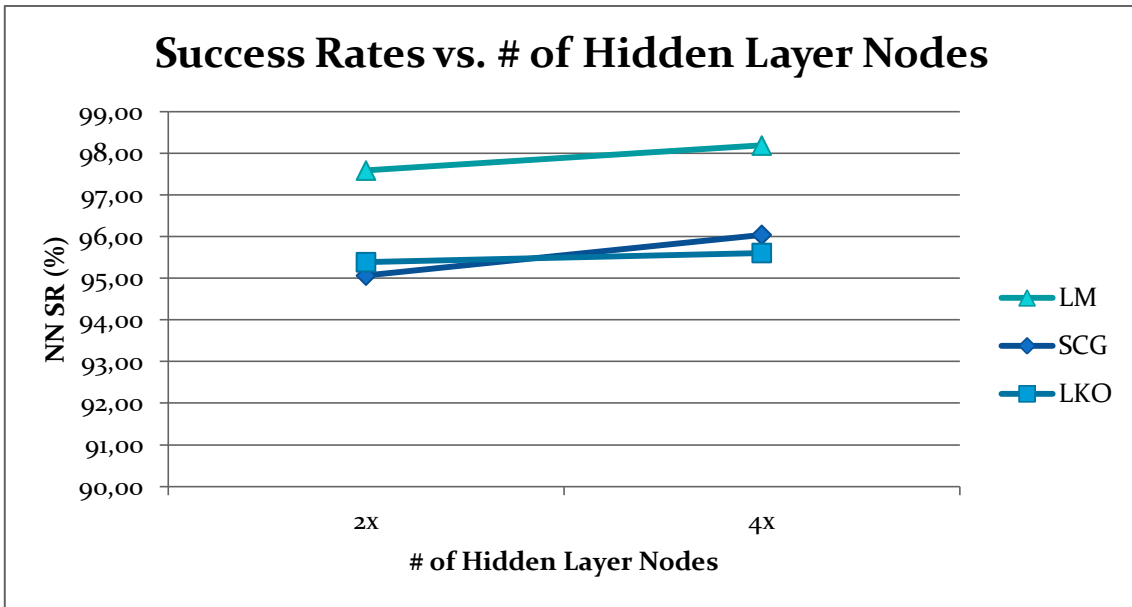


Fig. 10.36. Hidden layer nodes influence

10.3. Residual Stress Assessment (fresh tool)

10.3.1. Standard Tests

Statistics Summary

Table 10.11. Statistics summary

Statistics	
Total Average	98,71
Std dev.	1,88
Mode	100
Minimum	91,1
Conv vs PCA	
Conv	98,22
PCA	99,85
Difference	1,63
Training Algorithm	
LM	99,36
SCG	98,96
LKO	97,79
LM-SCG	0,40
LM-LKO	1,57
SCG-LKO	1,17
Hidden Layer Nodes (4x - 2x)	
LM	0,39
SCG	0,84
LKO	-0,45

The results reported in Table 10.11 show that:

- It is possible to distinguish favorable and unfavorable residual stresses by extracting features from signals acquired in correspondence of fresh tool with an average Success Rate (SR) = 98.71% , the minimum SR is 91.1%.
- The most frequent success rate is 100% showing an excellent reliability of features and neural network, for both Conventional and PCA features.

PCA vs. Conventional

Considering all the categories of NN Configurations, in terms of training algorithm and number of hidden layer nodes, the features extracted by PCA yield to a more successful pattern recognition than the ones obtained by conventional methodology, as shown in Table 10.12 and in Fig. 10.37. The difference in success rate between the two methodologies is 1.63%

The training algorithm that shows a clearer difference between the two features extraction methodologies is the LKO, where the gap ranges from 2.31 % (LKO-2x) to 2.69 % (LKO-4X).

Table 10.12

	LKO 2x	LKO 4x	SCG 2x	SCG 4x	LM 2x	LM 4x
Conventional	97,32	96,76	97,91	99,12	98,81	99,36
PCA	99,63	99,45	100,00	100,00	100,00	100,00

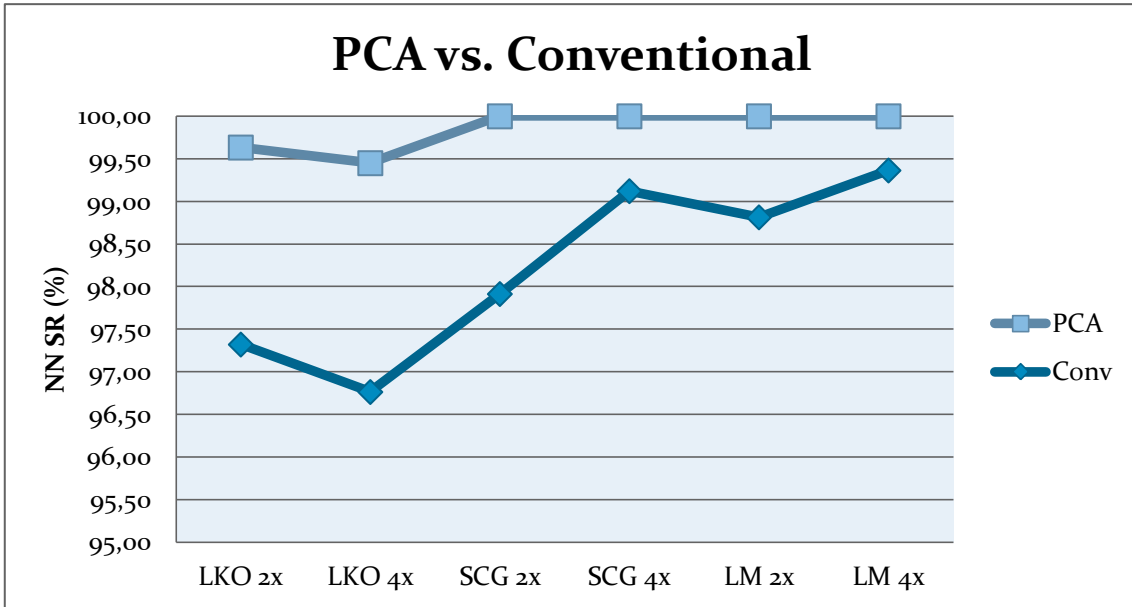


Fig. 10.37. PCA vs Conventional

Conventional Features Evaluation

In Figs. 10.38, 10.39 10.40 and 10.41 a conventional features evaluation is reported

Figures show that generally, by increasing the number of features, the success rates increases too,

It is clear also that, in most of cases, increasing the number of variables yields higher success rates.

This evaluation has been carried out for all the training algorithms and the trend mentioned above occurs for each training algorithm.

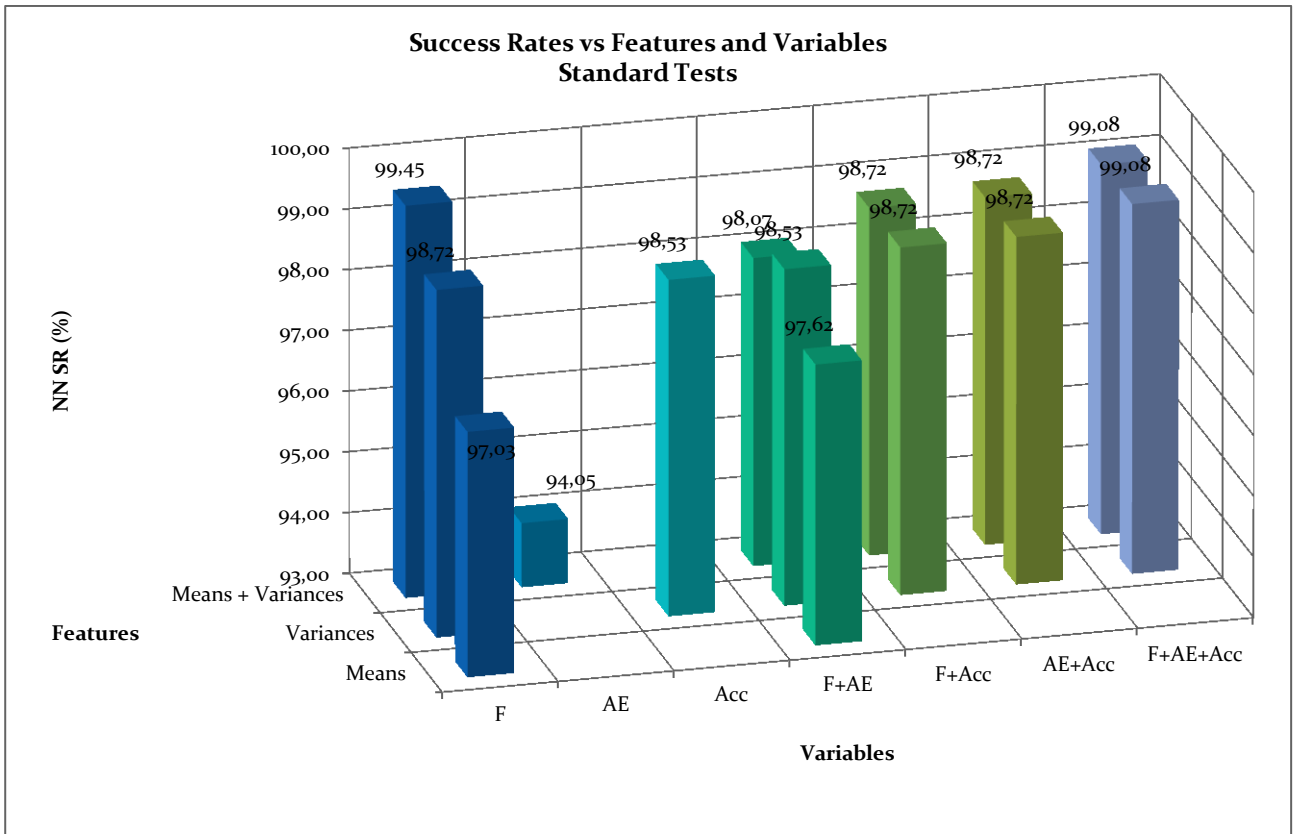


Fig. 10.38. Conventional features evaluation: overall average

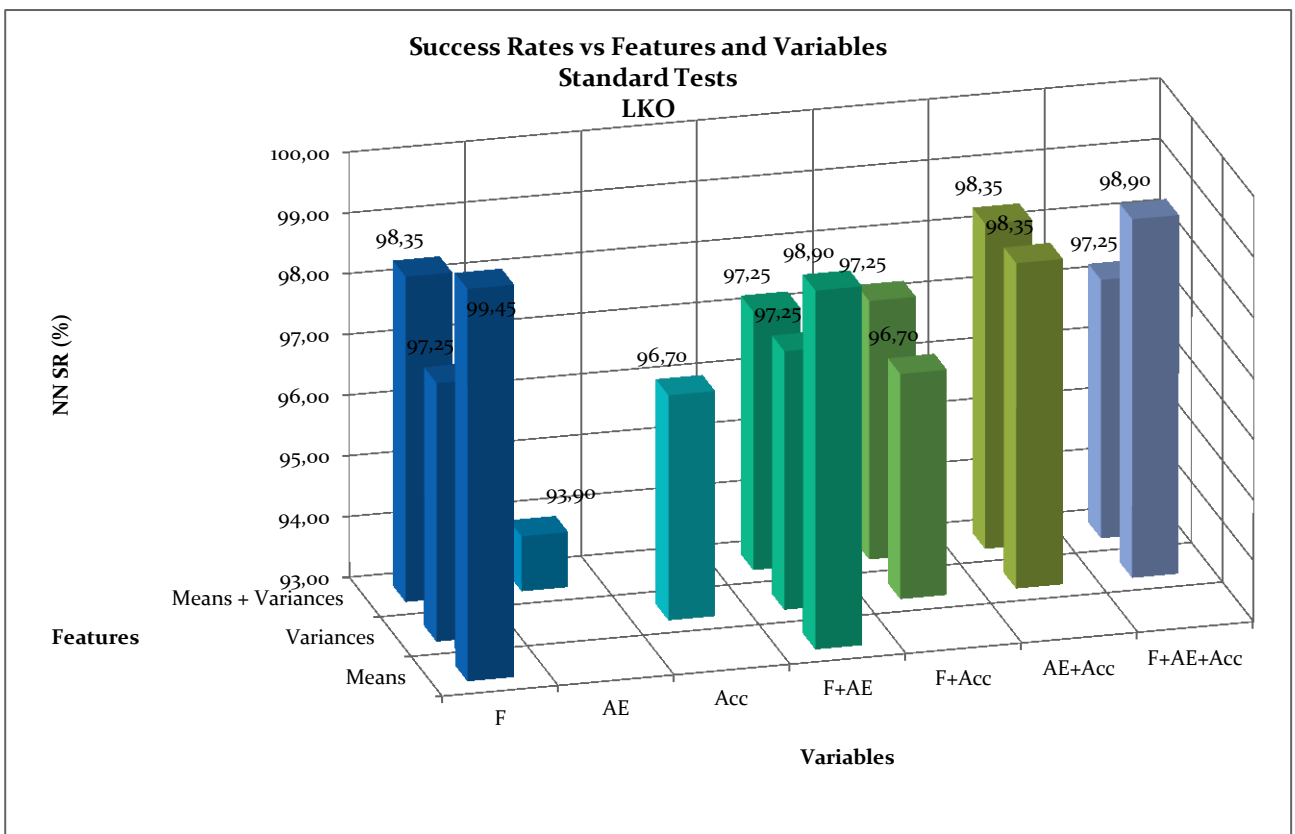


Fig. 10.39. Conventional features evaluation: LKO training algorithm

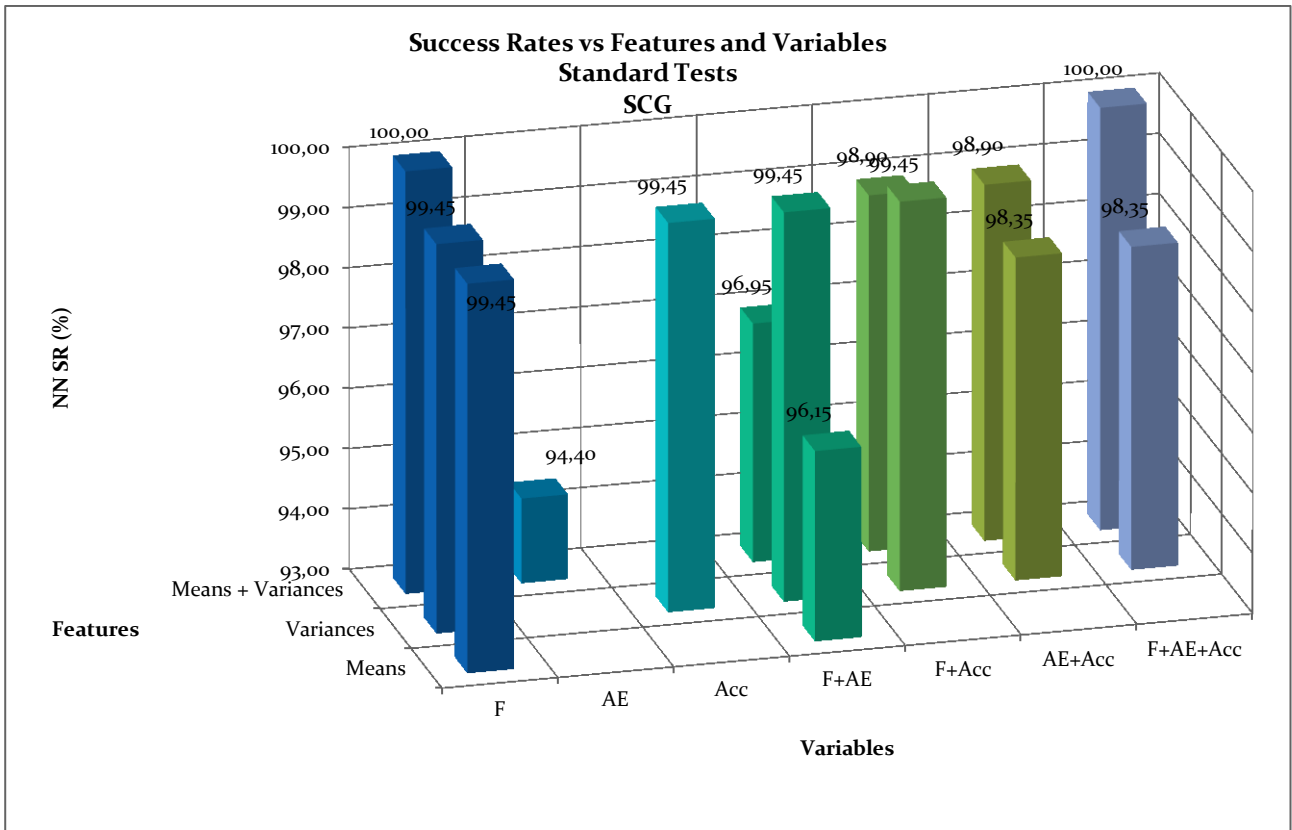


Fig. 10.40. Conventional features evaluation: SCG training algorithm

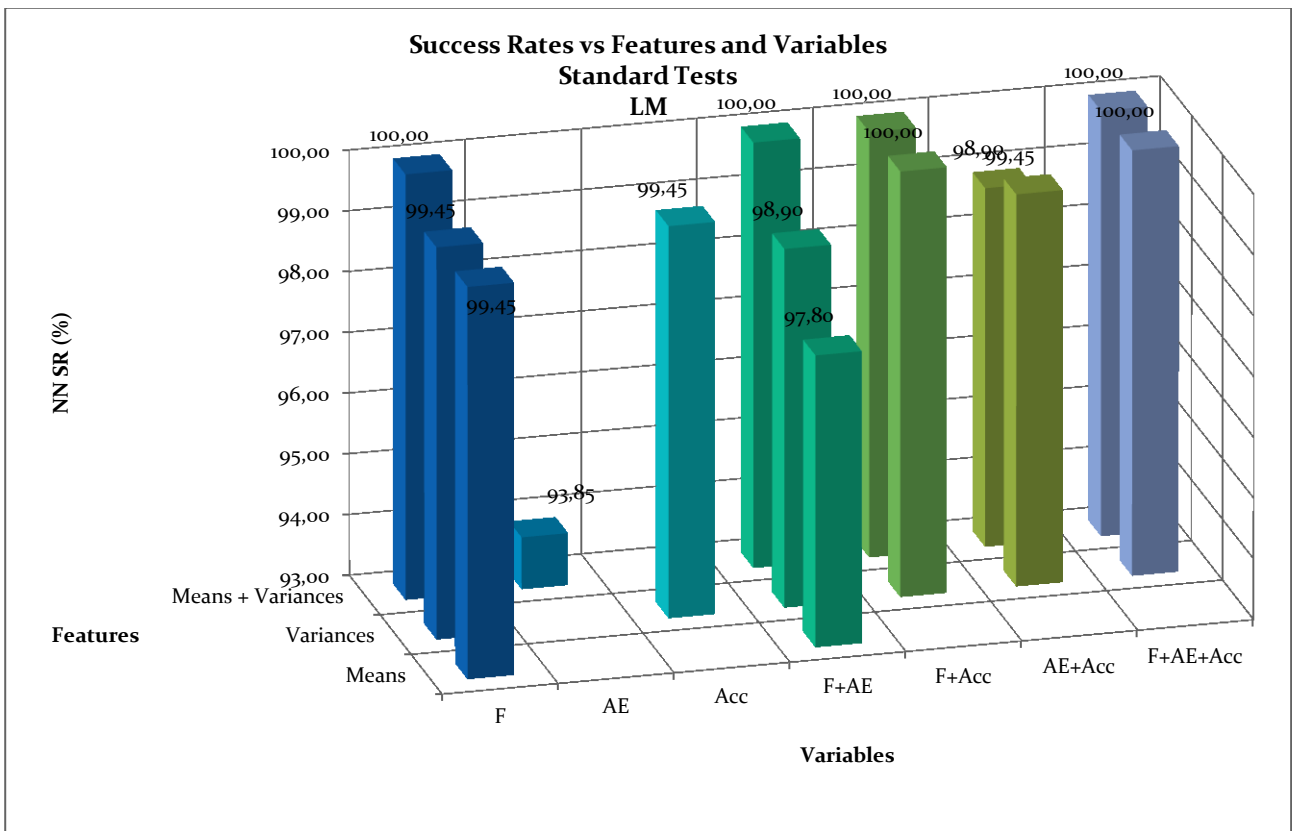


Fig. 10.41. Conventional features evaluation: LM training algorithm

Variables Comparison

Fig. 10.23. shows that as single group of variables, the cutting forces components yield better results in terms of average success rate.

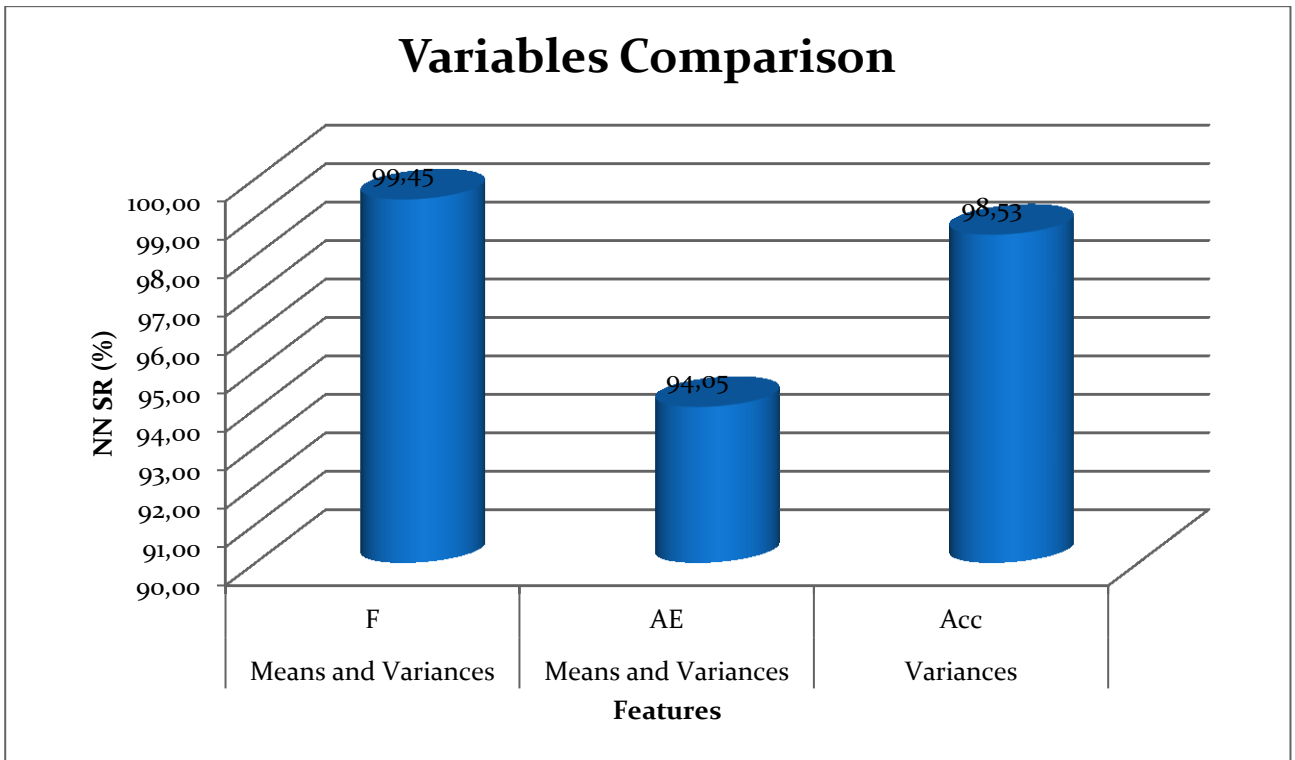


Fig. 10.42. Variables comparison

PCA Features Evaluation

Fig. 10.42. shows that the PCA based features produce success rates always higher than 99% demonstrating an excellent capability of PCA techniques in residual stress assessment.

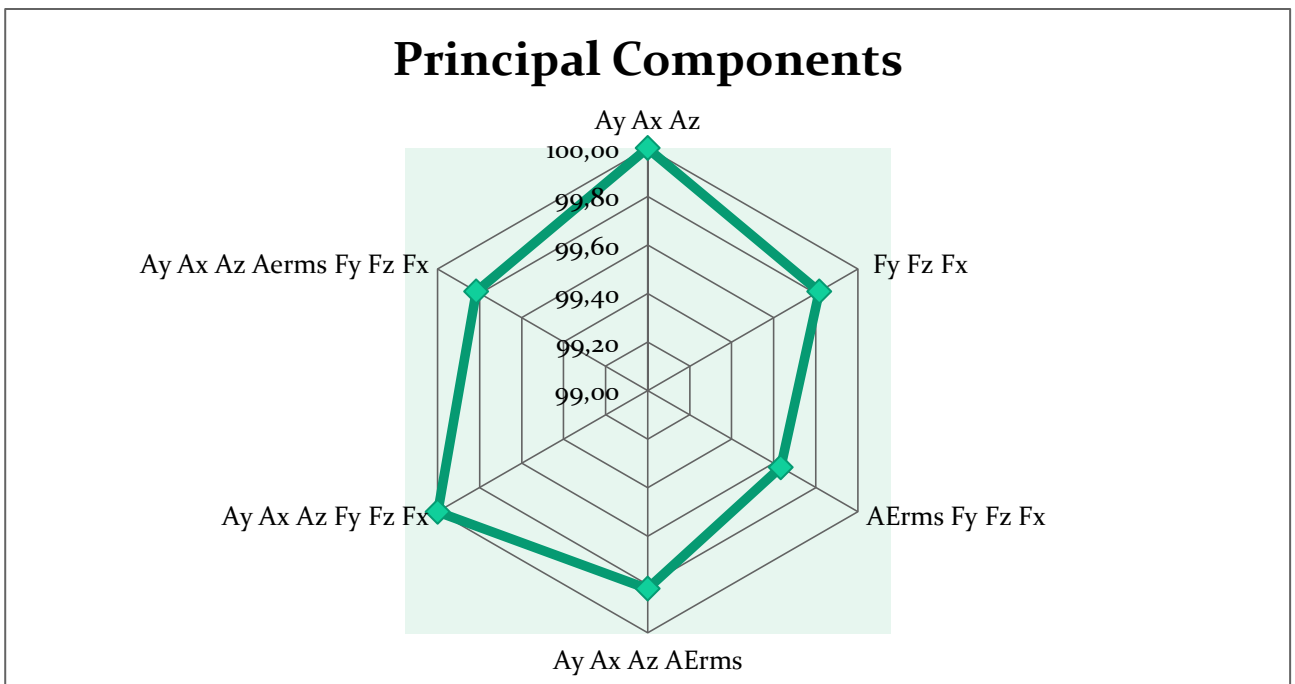


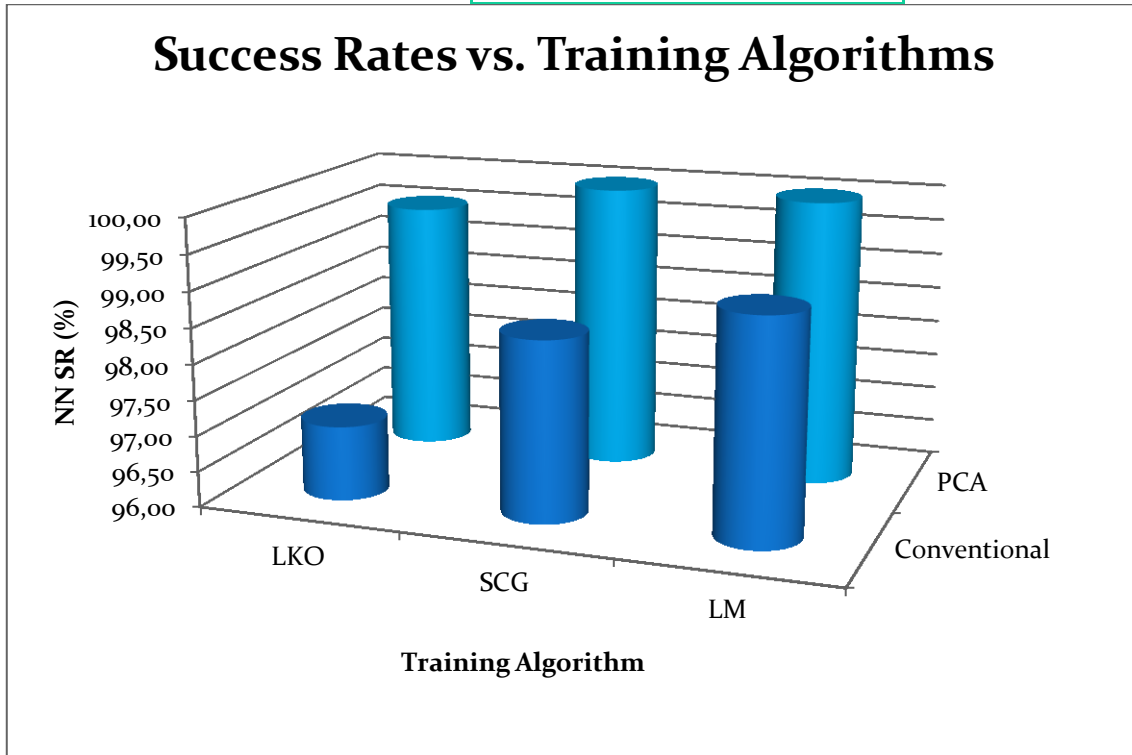
Fig. 10.43. PCA features evaluation

Success Rates vs Training Algorithms

Levenberg-Marquardt training algorithm shows higher success rates compared to other algorithms both by adopting Conventional and PCA features, the differences in terms of success rates among the best (LM) and the worst (LKO) training algorithms is 2.96%. The results regarding the differences among the training algorithms are reported in Table 10.5 and in Fig. 10.16.

Table 10.13 Training algorithms comparison

	LKO	SCG	LM
Conventional	97,04	98,52	99,09
PCA	99,54	100,00	100,00



10.44. Training algorithms comparison

Success Rates vs. Number of Hidden Layer Nodes

The general trend visible when increasing the number of hidden layer nodes, is an increasing of success rates. This occurs for both LM and SCG training algorithms but not for LKO, for which increasing hidden layer nodes yields a very small, decreasing trend, as reported in Fig. 10.44.

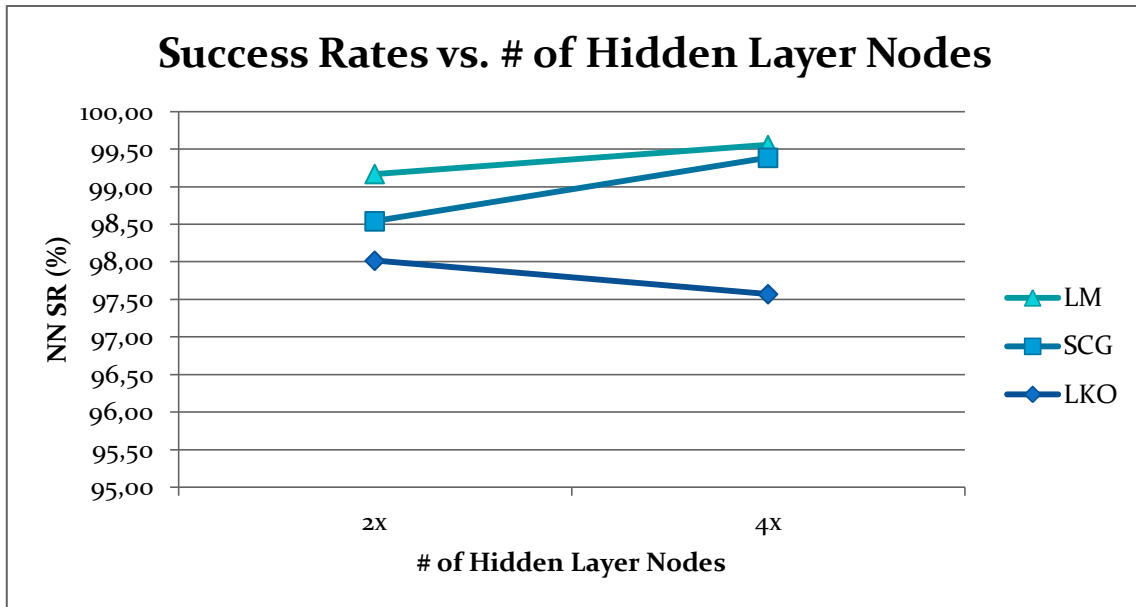


Fig. 10.45. Hidden layer nodes influence

10.3.2. Standard Tests + Severe Cutting Conditions Tests

Statistics Summary

Table 10.14. Statistics summary

Statistics	
Total Average	97,74
Std dev.	2,26
Mode	100
Minimum	91,5
Conv vs PCA	
Conv	97,62
PCA	97,99
Difference	0,37
Training Algorithm	
LM	99,48
SCG	97,26
LKO	96,47
LM-SCG	2,22
LM-LKO	3,01
SCG-LKO	0,78
Hidden Layer Nodes (4x - 2x)	
LM	0,35
SCG	1,42
LKO	0,00

The results reported in Table 10.12 show that:

- It is possible to distinguish favorable and unfavorable residual stresses by extracting features from signals acquired in correspondence of fresh tool with an average Success Rate (SR) = 97.04% , the minimum SR is 91.5%.
- The most frequent success rate is 100% showing an excellent reliability of features and neural network, for both Conventional and PCA features.

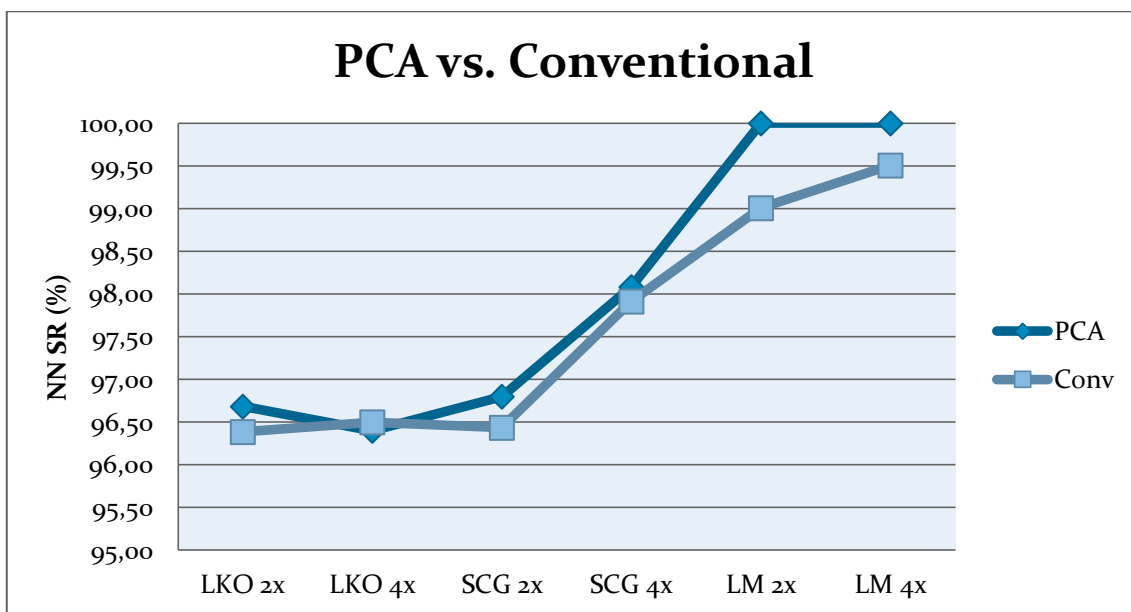
PCA vs. Conventional

Considering all the categories of NN Configurations, in terms of training algorithm and number of hidden layer nodes, the features extracted by PCA yield to a more successful pattern recognition than the ones obtained by conventional methodology, as shown in Table 10.15 and in Fig. 10.46. The difference in success rate between the two methodologies is 0.37%

The training algorithm that shows a clearer difference between the two features extraction methodologies is the LM, where the gap ranges from 0.99 % (LM-2x) to 0.49 % (LM-4X).

Table 10.15

	LKO 2x	LKO 4x	SCG 2x	SCG 4x	LM 2x	LM 4x
Conventional	96,39	96,50	96,44	97,91	99,01	99,51
PCA	96,68	96,40	96,80	98,08	100,00	100,00



10.46. PCA vs Conventional

Conventional Features Evaluation

In Figs. 10.47, 10.48 10.49 and 10.50 a conventional features evaluation is reported

Figures show that generally, by increasing the number of features, the success rates increases too,

It is clear also that, in most of cases, increasing the number of variables yields higher success rates.

This evaluation has been carried out for all the training algorithms and the trend mentioned above occurs for each training algorithm.

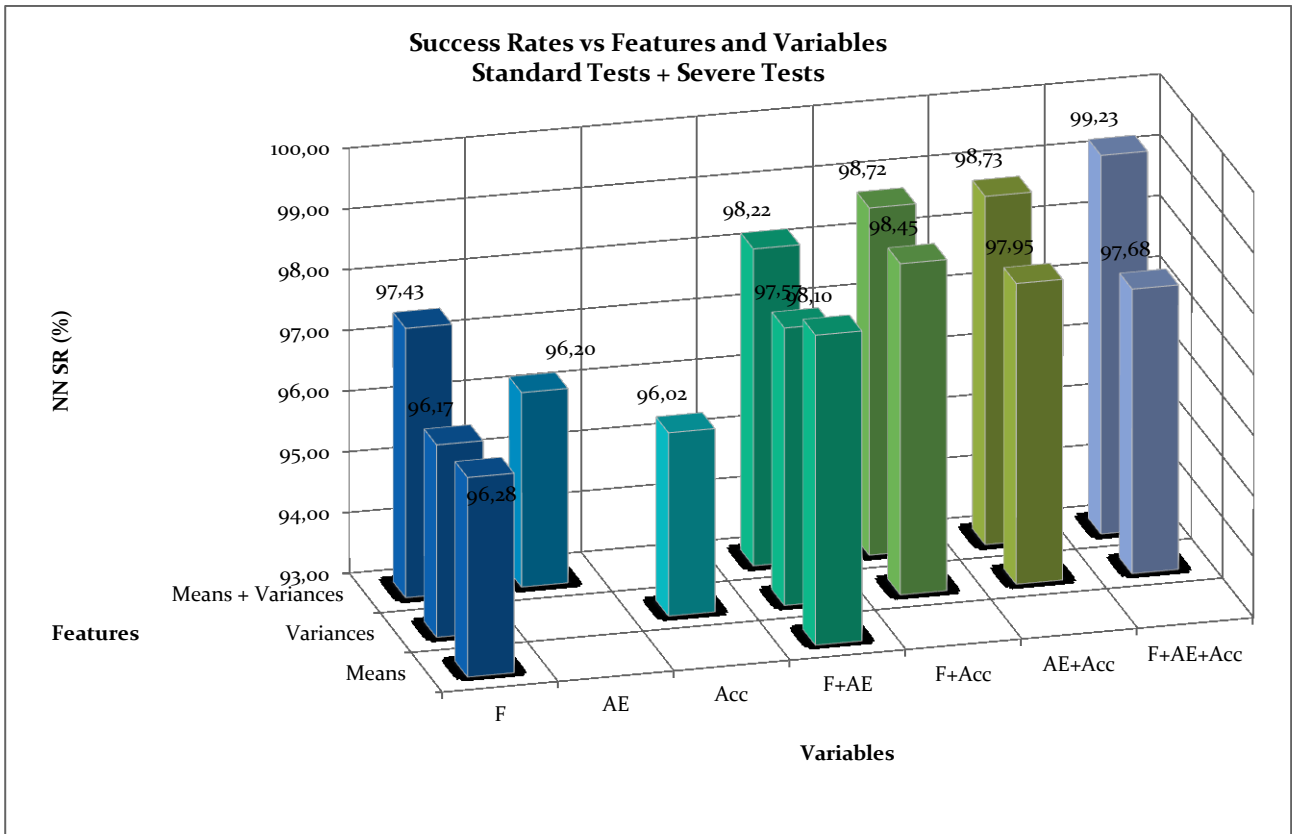


Fig. 10.47. Conventional features evaluation: overall average

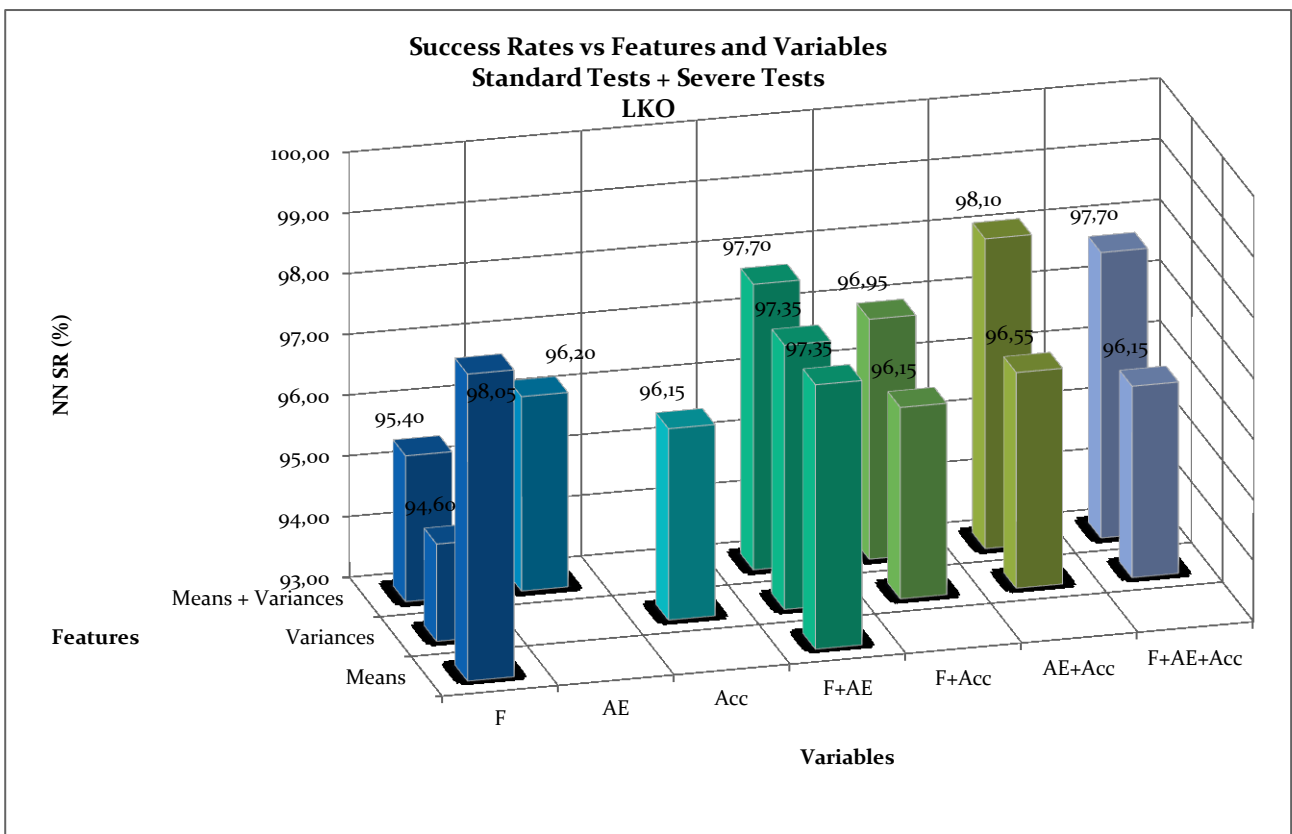


Fig. 10.48. Conventional features evaluation: LKO training algorithm

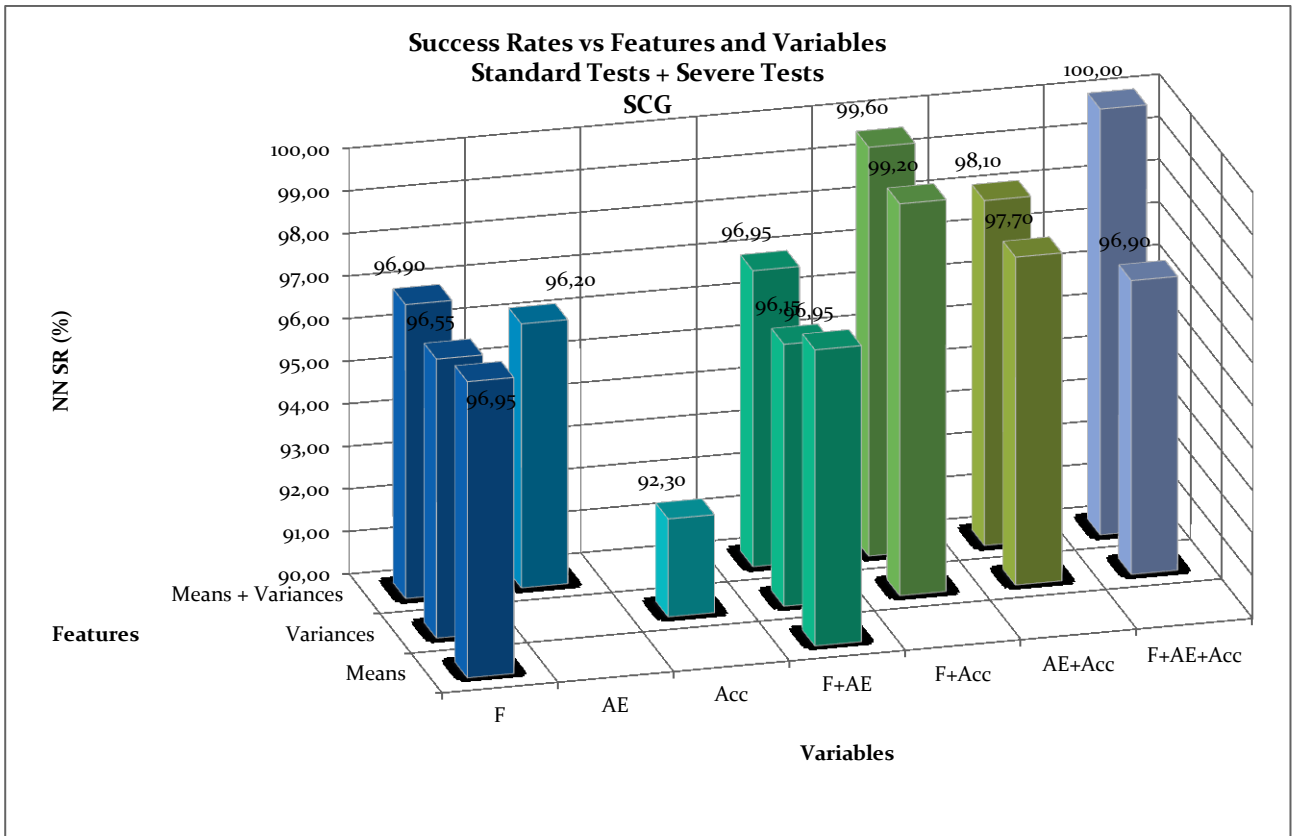


Fig. 10.49. Conventional features evaluation: SCG training algorithm

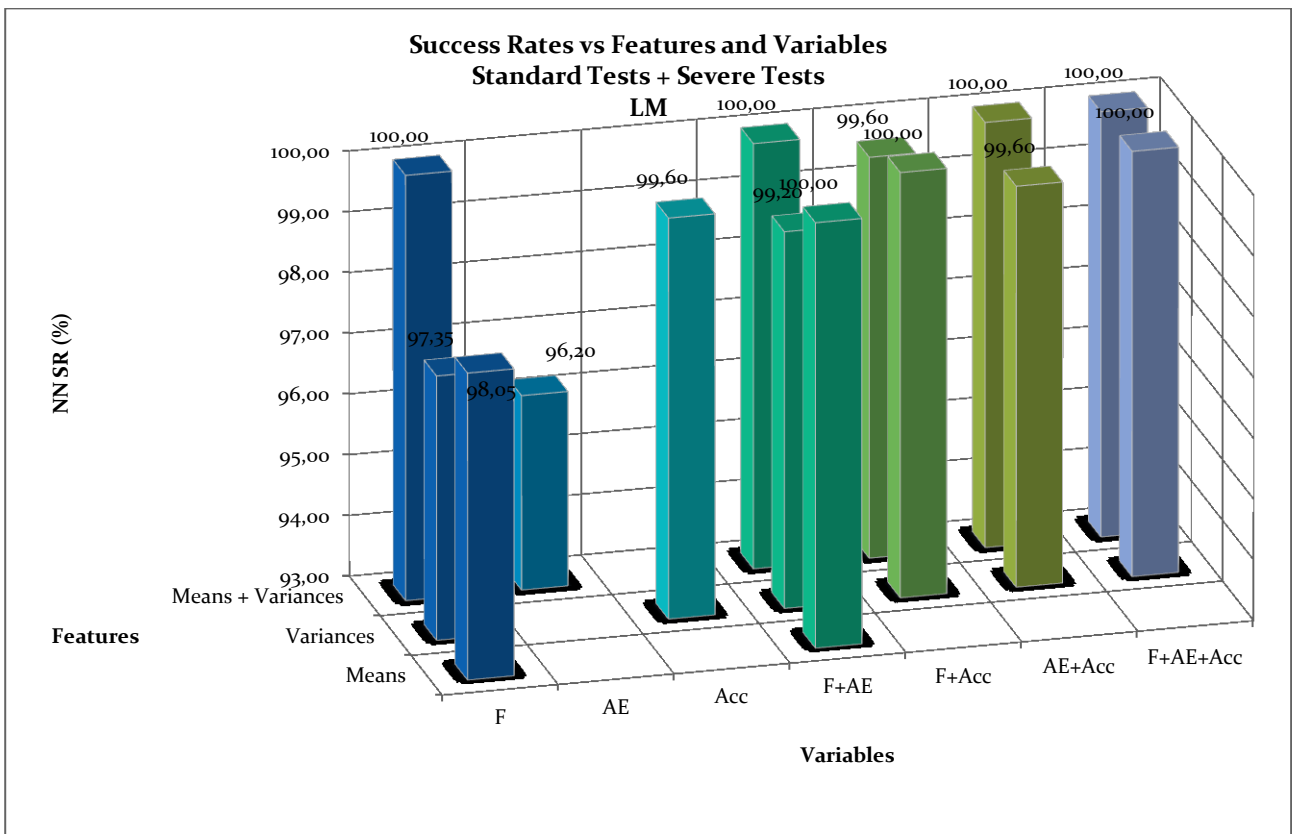


Fig. 10.50. Conventional features evaluation: LM training algorithm

Variables Comparison

Fig. 10.50. shows that as single group of variables, the cutting force components yield better results in terms of average success rate.

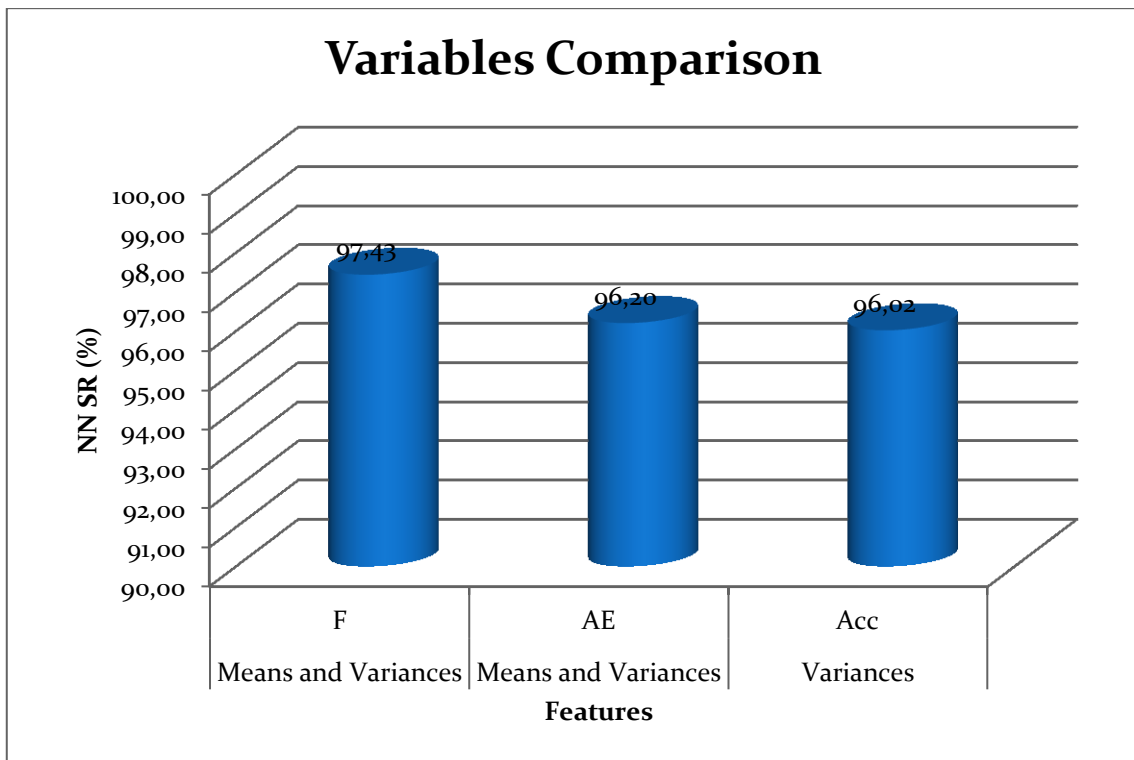


Fig. 10.51. Variables comparison

PCA Features Evaluation

Fig. 10.51. shows that success rates produced by PCA based features range from 96.17% to 99.1% . By freezing the number of Principal Components utilized, the plot shows better results coming from cutting force components based PCA features.

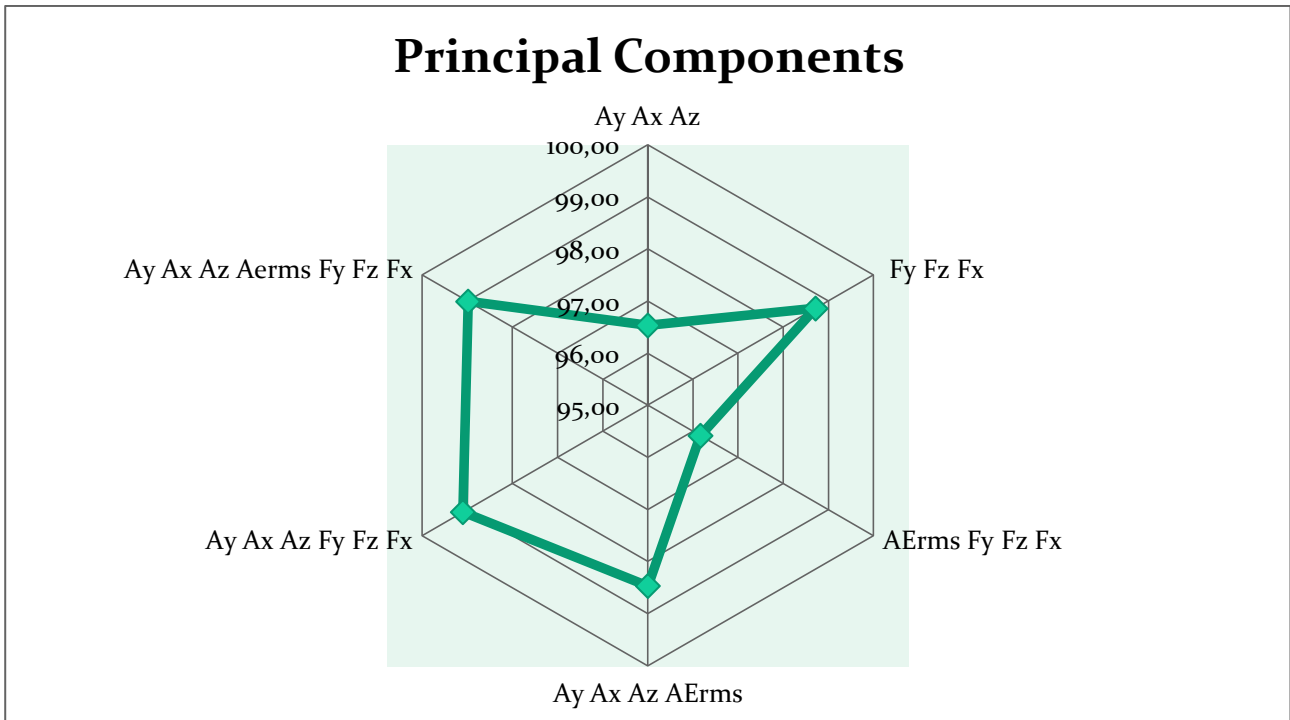


Fig. 10.52. PCA features evaluation

Success Rates vs. Training Algorithms

Levenberg-Marquardt training algorithm shows higher success rates compared to other algorithms both by adopting Conventional and PCA features, the differences in terms of success rates among the best (LM) and the worst (LKO) training algorithms is 3.46%. The results regarding the differences among the training algorithms are reported in Table 10.14 and in Fig. 10.52.

Table 10.16. Training algorithms comparison

	LKO	SCG	LM
Conventional	96,44	97,18	99,26
PCA	96,54	97,44	100,00

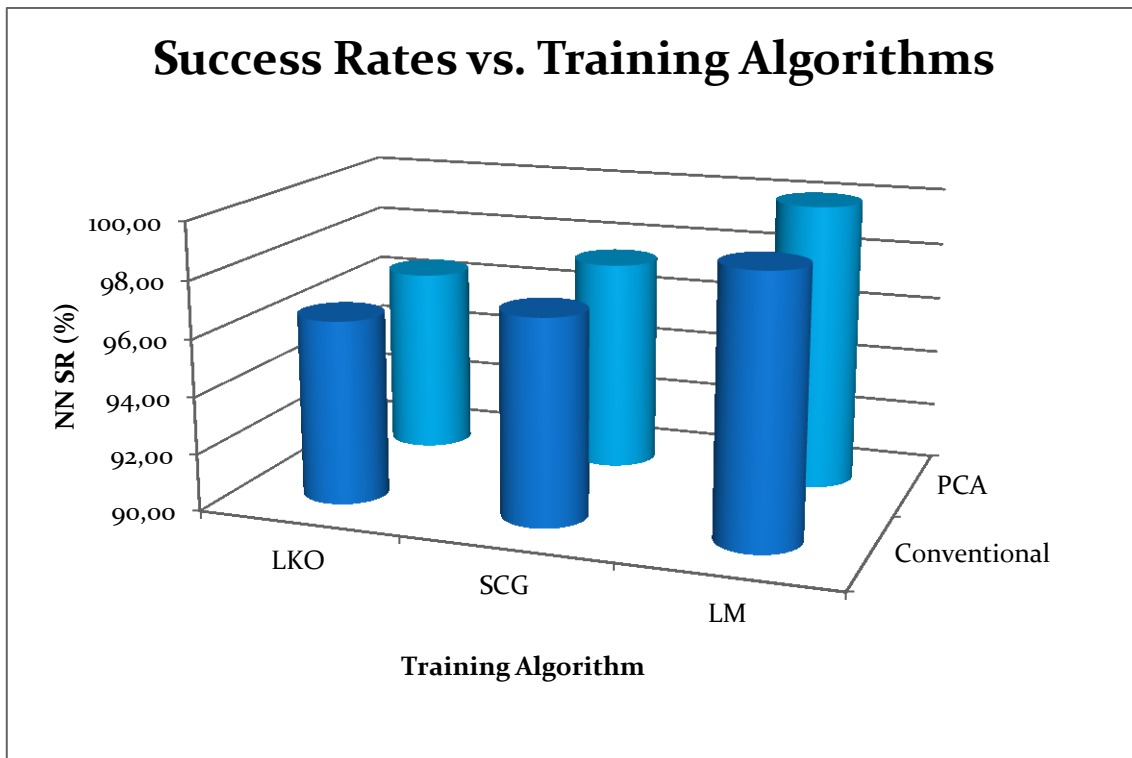


Fig. 10.53. Training algorithms comparison

Success Rates vs. Number of Hidden Layer Nodes

The general trend visible when increasing the number of hidden layer nodes, is an increasing of success rates. This occurs for both LM and SCG training algorithms but not for LKO, for which increasing hidden layer nodes yields a very small, not appreciable, decreasing trend, as reported in Fig. 10.53.

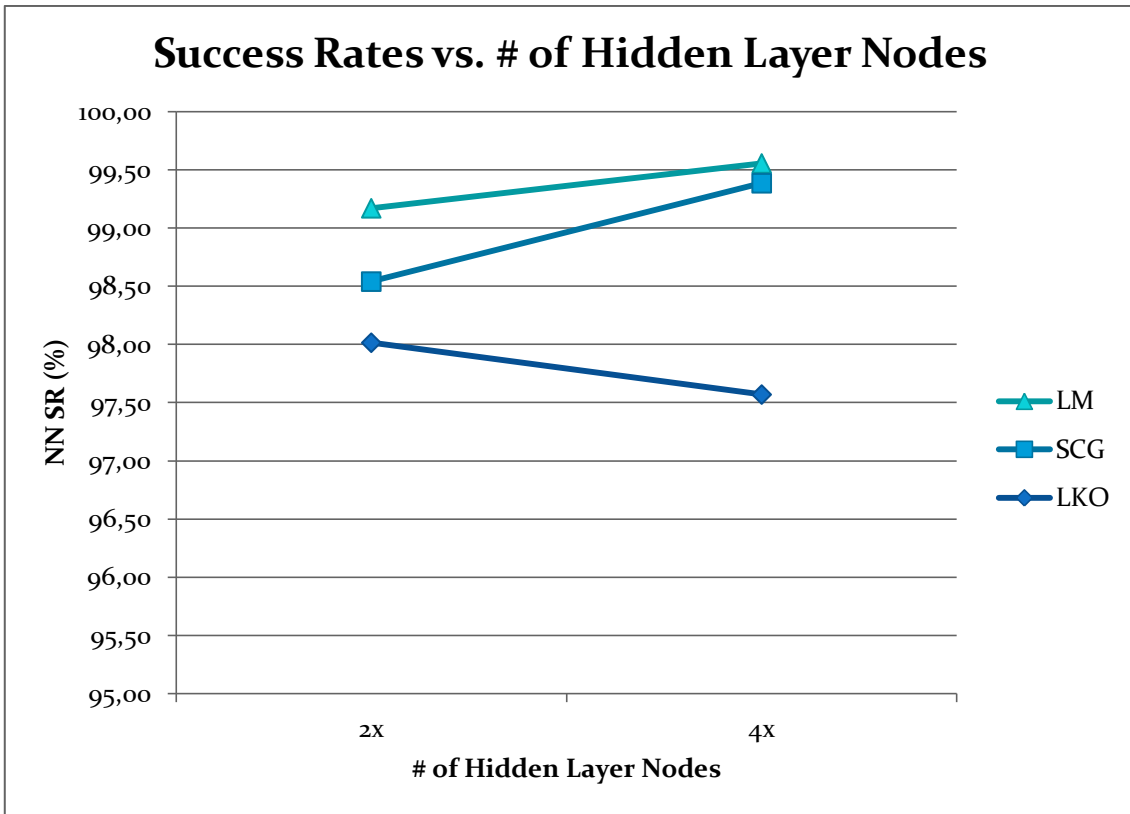


Fig. 10.54 Hidden layer nodes influence

10.4. Summary plots

From Figs. 10.54 to Fig 10.59 a summary plot, is reported for each purpose, both in case of Standard Tests only and for Standard Tests + Severe Cutting Conditions Tests.

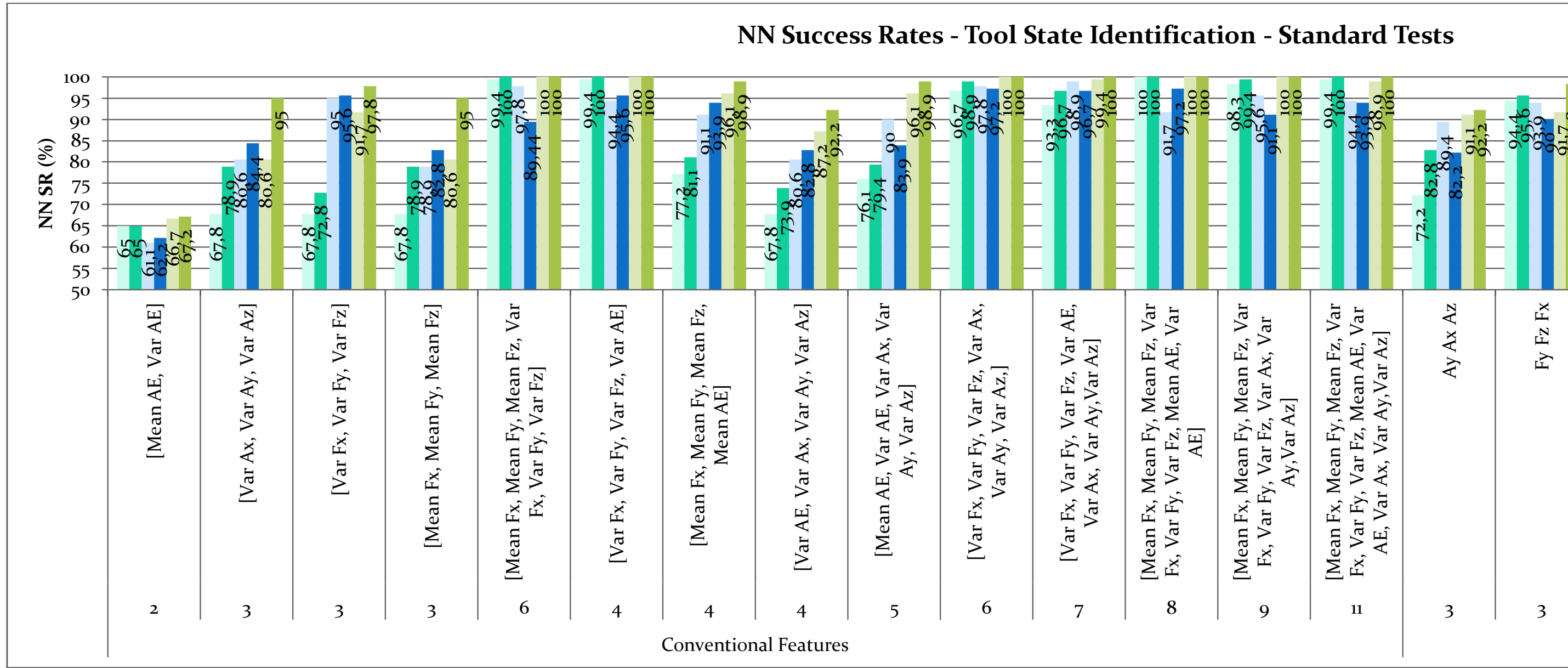
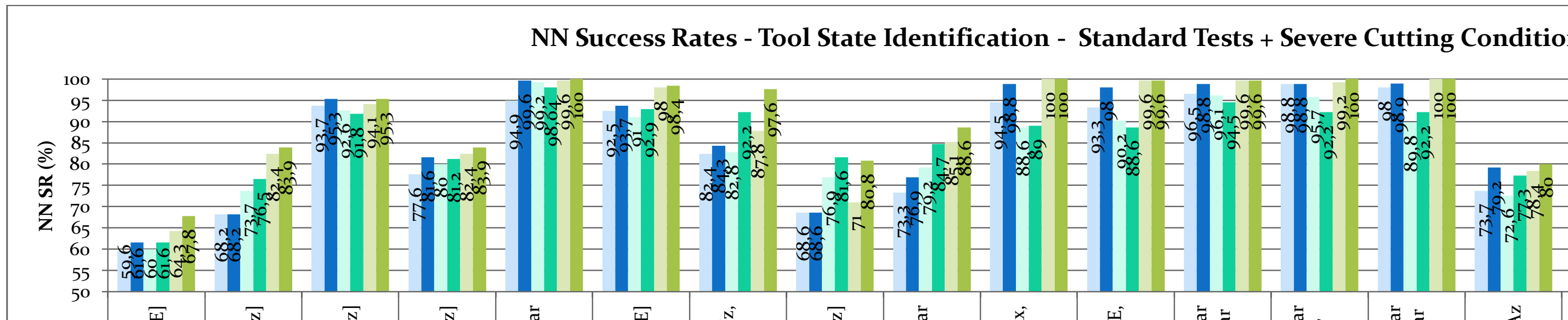


Fig. 10.55 Tool State Identification - Standard Tests



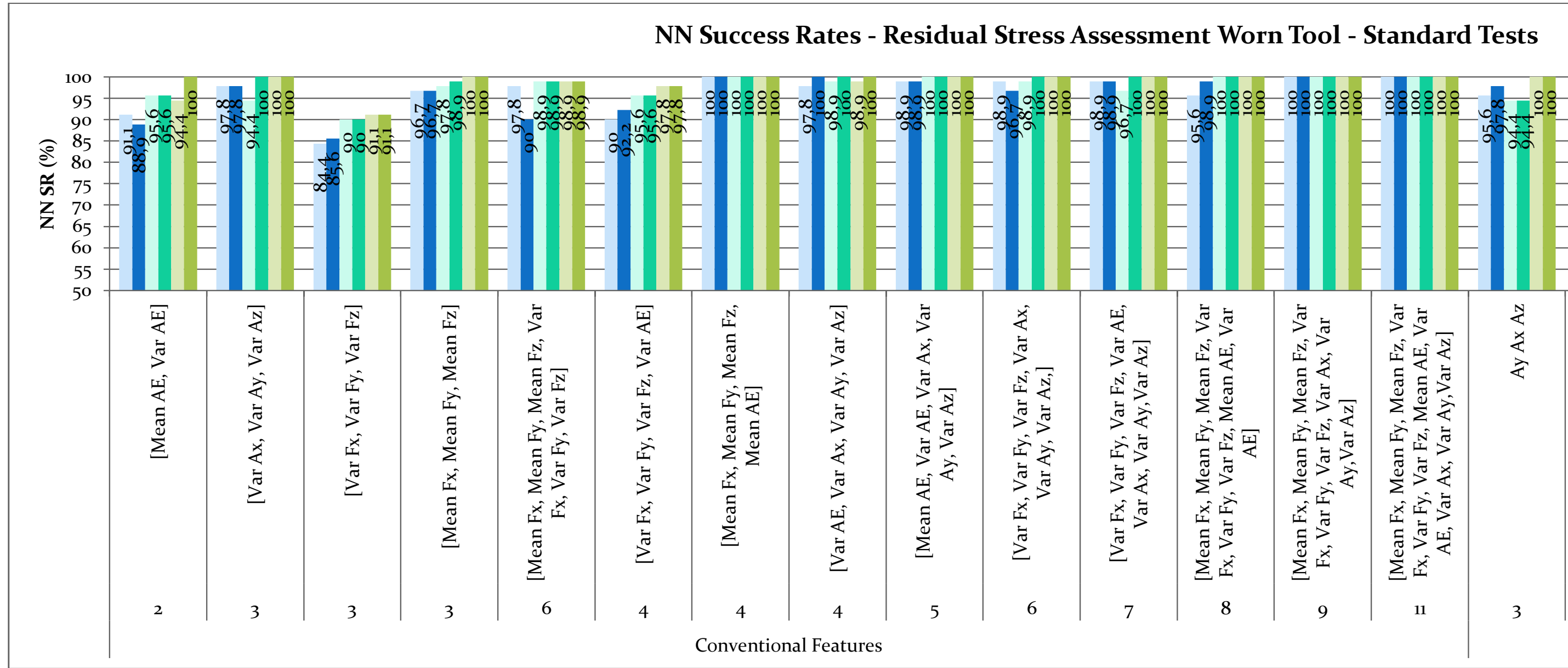
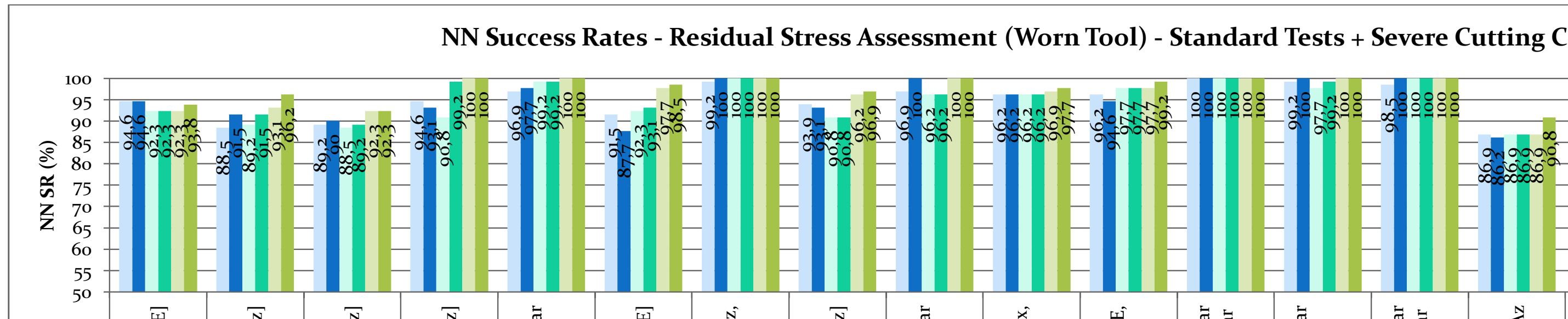


Fig. 10.57. Residual Stress Assessment (worn tool) - Standard Tests

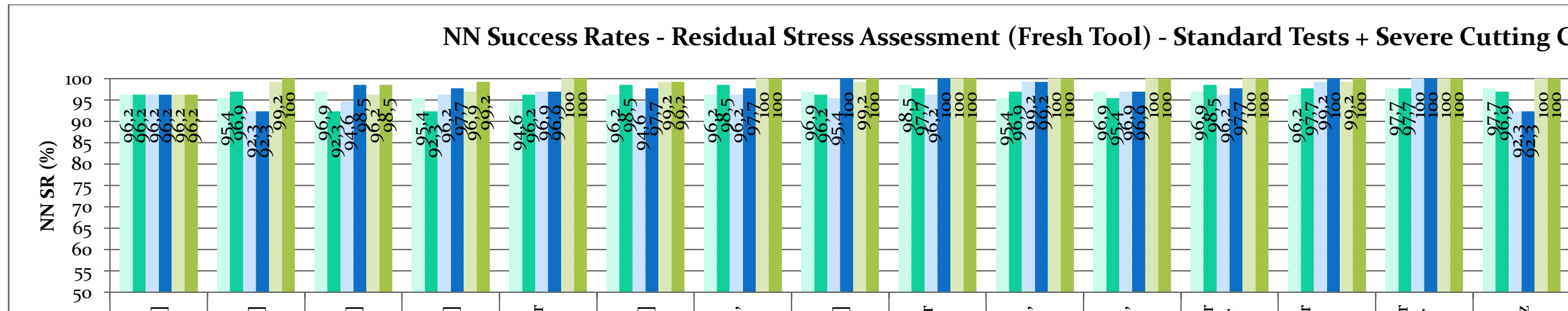


NN Success Rates - Residual Stress Assessment (Fresh Tool) - Standard Tests



10.59. Residual Stress Assessment (fresh tool) - Standard Tests

NN Success Rates - Residual Stress Assessment (Fresh Tool) - Standard Tests + Severe Cutting C



11. Conclusions / Considerations

A multi sensor monitoring system endowed with force, acoustic emission and vibration sensor was designed, assembled, calibrated and employed during machining operations.

An experimental campaign of turning tests on Inconel 718 cylindrical shafts was designed and carried out by considering standard cutting conditions as well as severe cutting conditions in order to increase the probability to generate surface defects on the workpiece.

For every cutting test, tool wear measurements were carried out in order to construct tool wear curves.

The surface defects were investigated by a series of material characterization tests including visual inspection, FPI, metallographic tests, microhardness and roughness measurements and residual stress measurements.

From the residual stress measurements it was possible to identify which turning tests yielded non acceptable residual stress values in the workpiece after machining.

Signal processing was performed for every cutting test on the detected sensor signals in order to generate homogeneous datasets, which were used to extract significant signal features.

Features extraction was carried out by adopting two methodologies, the former based on statistical conventional features and the latter based on an advanced paradigm based on Principal Components Analysis. Both signal features typologies were selected and grouped into pattern feature vectors and utilized as input for neural network based decision making pattern recognition.

Diverse neural network configurations were adopted for pattern recognition purposes, by changing the number of input layer nodes, the number of hidden layer nodes and the training algorithms.

All the configurations were applied to two different datasets, the first regarding the standard cutting conditions tests only and the second including the severe cutting conditions tests too.

The pattern recognition objectives regarded the Tool Wear Identification and the Residual Stress Assessment. The latter was subdivided into two precise purposes: discrimination of residual stress considering signals related to the worn tool (in correspondence of which the residual stress measurements were carried out) and signals related to the fresh tool.

List of references

- [1] D'Addona, D., Segreto, T., Simeone, A., Teti, R., 2011, ANN Tool Wear Modelling in the Machining of Nickel Superalloy Industrial Products, CIRP Journal of Manufacturing Science and Technology, Special Section on Innovative and Cognitive Manufacturing Engineering, DOI: 10.1016/j.cirpj.2011.07.003, 4/1: 33-37
- [2] Segreto, T., Simeone, A., Teti, R., 2012, Chip form Classification in Carbon Steel Turning through Cutting Force Measurement and Principal Component Analysis, Procedia CIRP, Volume 2, 2012, Pages 49-54, ISSN 2212-8271, 10.1016/j.procir.2012.05.038 July 2012.
- [3] Segreto, T., Simeone, A., Teti, R., 2011, Principal Component Analysis of Multiple Sensor Signals for Tool Wear Identification during Composite Materials Machining, X AITEM Conference, 12-14 sept, Naples, Italy, ISBN 978-88-906061-0-1.
- [4] Cedergren, S., Simeone, A., Wretland, A., 2010, Adaptive Process Monitoring of Holemaking Operations, 7th CIRP Int. Conference on Intelligent Computation in Manufacturing Engineering – CIRP ICME '10, 23-25 June, Capri, Italy.
- [5] Simeone, A., Segreto, T., Teti, R., 2012, Sensor Fusion for Tool State Classification in Nickel Superalloy High Performance Cutting, Procedia CIRP, Volume 1, 2012, Pages 593-598, ISSN 2212-8271, 10.1016/j.procir.2012.05.005 July 2012.
- [6] Segreto, Simeone, A., T., Teti, R., 2012, Multiple Sensor Monitoring in Nickel Alloy Turning for Tool Wear Assessment via Sensor Fusion, 8th CIRP Int. Conference on Intelligent Computation in Manufacturing Engineering – CIRP ICME '12, 18-20 July, Ischia, Italy.
- [7] D'Addona, D., Simeone, A., Teti, R., 2010, Neural Network Model for Tool Wear Curve Reconstruction during Turning of Inconel 718, 7th CIRP Int. Conference on Intelligent Computation in Manufacturing Engineering – CIRP ICME '10, 23-25 June, Capri, Italy
- [8] Simeone, A., Segreto, T., Teti, R., 2012, Residual Stress Condition Monitoring via Sensor Fusion in Turning of Inconel 718, 8th CIRP Int. Conference on Intelligent Computation in Manufacturing Engineering – CIRP ICME '12, 18-20 July, Ischia, Italy.
- [9] Teti, R., D'Addona, D., Segreto, T., Simeone, A., De Chiara, G. Gabriele, L., Marrone, R., 2008, Neural Network Tool Wear Prediction in Turning of Inconel 718, 6th CIRP Int. Conference on Intelligent Computation in Manufacturing Engineering – CIRP ICME '08, Naples, ISBN 978-88-900948-7-3: 23-25 July: 199-203.
- [10] Teti, R., Jemielniak, K., O'Donnell, G., Dornfeld, D., 2010, Advanced Monitoring of Machining Operations, STC-C Keynote Paper, Annals of the CIRP, Vol. 59/2, ISSN 0007-8506 (CIRP Annals), ISSN 1660-2773 (CD Rom): 717-739
- [11] Gregory RL. (1972) Seeing as Thinking – An Active Theory of Perception. Times Literary Supplement 707-708.
- [12] Gregory RL (1997) Knowledge in Perception and Illusion. Philosophical Transaction of Royal Society of London B 352:1121-1128.
- [13] Baicsy R (1995) From Active Perception to Active Cooperation: Fundamental Processes of Intelligent Behaviour, in Zangenmeister WH, et al. (Eds.) Visual Attention and Cognition: 309-321.
- [14] Byrne G, Dornfeld D, Denkena B (2004) Advancing Cutting Technology. CIRP Annals 52(2):483-507.
- [15] Byrne G, O'Donnell G (2007) An Integrated Force Sensor Solution for Process Monitoring of Drilling Operations. CIRP Annals 56(01):89-92.

- [16] Park S (2004) High Frequency Bandwidth Cutting Force Measurements in Milling Using the Spindle Force Sensor System, PhD Thesis, University of British Columbia, Vancouver, Canada.
- [17] Jun M, Ozdoganlar B, DeVor R, Kapoor S, Kirchheim K, Schaffner G (2002) Evaluation of a Spindle-based Force Sensor for Monitoring and Fault Diagnosis of Machining Operations. *International Journal of Machine Tools and Manufacture* 42:741-751.
- [18] O'Donnell GE, Kelly K, Byrne G (2000) Use of a Sensor Integrated Motor Spindle for Monitoring of a Flexible Machining Centre. 2nd CIRP Int. Sem. On ICME, Capri, Italy, 383-388.
- [19] Kim J-D, Kim D-S (1997) Development of a Combined Type Tool Dynamometer with a Piezo-film Accelerometer for an Ultra-Precision Lathe. *Journal of Materials Processing Technology* 71:360-366.
- [20] Bloa Korkut I (2003) A Dynamometer Design and Its Construction for Milling Operation. *Materials and Design* 24:631-637.
- [21] Smith DA, Smith S, Tlustý J (1998) High Performance Milling Torque Sensor. *Journal of Manufacturing Science and Engineering* 120:504-514.
- [22] Park S (2004) High Frequency Bandwidth Cutting Force Measurements in Milling Using the Spindle Force Sensor System, PhD Thesis, University of British Columbia, Vancouver, Canada.
- [23] ASTM. (1996) E 1316 Terminology for Non-destructive Testing, Annual Book of ASTM Standards; Non-destructive Testing, 03/03.
- [24] Rogers LM (1979) The Application of Vibration Analysis and Acoustic Emission Source Location to On-line Condition Monitoring of Anti-friction Bearings. *Tribology International* 51-59.
- [25] Karpuschewski B (2001) Sensoren zur Prozeßüberwachung beim Spanen, Habilitationsschrift. University of Hannover, Germany.
- [26] Hundt W, Leuenberger D, Rehsteiner F (1994) An Approach to Monitoring of the Grinding Process Using Acoustic Emission Techniques. *CIRP Annals* 43(1):295-298.
- [27] Nebel C, Pflug C (1996) Real Time Monitoring and Control of Chip Form in Turning with Acoustic Emission Using Thin Film Sensors, NAMRC XXIV, SME. University of Michigan, Ann Arbor, Michigan.
- [28] Caralon TA, Kidd SR, Hand DP, Wilcox SJ, Wilkinson P, Barton JS, Jones JDC, Reuben RL (1997) AE Monitoring of Tool Wear During the Face Milling of Steels and Aluminium Alloys Using a Fibre Optic Sensor, Part 1: Energy Analysis. *IMEchE* 211:299-309.
- [29] Caralon TA, Kidd SR, Hand DP, Wilcox SJ, Wilkinson P, Barton JS, Jones JDC, Reuben RL (1997) AE Monitoring of Tool Wear During the Face Milling of Steels and Aluminium Alloys Using a Fibre Optic Sensor, Part 2: Frequency Analysis. *IMEchE* 211:311-319
- [30] Inasaki I (1998) Application of Acoustic Emission Sensor for Monitoring Machining Processes. *Ultrasonics* 36:273-281.
- [31] Hutton DV, Hu F (1999) AE Monitoring of Tool Wear in End Milling Using Time Domain Averaging. *Journal of Manufacturing Science and Engineering* 121:8-12.
- [32] Li X, Dong S, Yuan Z (1999) Discrete Wavelet Transform for Tool Breakage Monitoring. *International Journal of Machine Tools and Manufacture* 39:1935-1944.
- [33] Karpuschewski B, Wehmeier M, Inasaki I (2000) Grinding Monitoring System Based on Power and AE Sensing. *CIRP Annals* 49(1):235-240.

- [34] Jemielniak K (2001) Some Aspects of Acoustic Emission Signal Pre-processing. *Journal of Material Processing Technology* 109:242–247.
- [35] Woulfe M (2000) On the Relationship Between Acoustic Emission and Surface Integrity in Machining, PhD Thesis, University of College Dublin, Ireland.
- [36] Dimla DE (2000) Sensor Signals for Tool-wear Monitoring in Metal Cutting: A Review of Methods. *International Journal of Machine Tools and Manufacture* 40:1073–1098.
- [37] Li X (2002) A Brief Review—Acoustic Emission Method for Tool Wear Monitoring in Turning. *International Journal of Machine Tools and Manufacture* 42:157–165.
- [38] Sick B (2002) On-line and Indirect Tool Wear Monitoring in Turning with Artificial Neural Networks: A Review of More Than a Decade of Research. *Mechanical Systems and Signal Processing* 16(4):487–546.
- [39] Jemielniak K, Bombin' ski S (2006) Hierarchical Strategies in Tool Wear Monitoring. *Proc. IMechE*, 220/B, 375–381.
- [40] Jemielniak K (2000) Some Aspects of AE Application in Tool Condition Monitoring. *Ultrasonics* 38:604–608.
- [41] Altintas Y, Park SS (2004) Dynamic Compensation of Spindle-integrated Force Sensors. *CIRP Annals* 53(1):305–308.
- [42] Scheffer C, Heyns PC (2004) An Industrial Tool Wear Monitoring System for Interrupted Turning. *Mechanical Systems and Signal Processing* 18:1219–1242.
- [43] Jemielniak K, Szafarczyk M (1992) Detection of Cutting Edge Breakage in Turning. *CIRP Annals* 41(1):97–100.
- [44] Ghosh N, Ravi A, Patra S, Mukhopadhyay S, Mohanty A, Chattopadhyay A (2007) Estimation of Tool Wear During CNC Milling Using NN-based Sensor Fusion. *Mechanical Systems and Signal Processing* 21:466–479.
- [45] Li X, Ouyang G, Liang Z (2008) Complexity Measure of Motor Current Signals for Tool Flute Breakage Detection in End Milling. *International Journal of Machine Tools and Manufacture* 48:371–379.
- [46] Bhattacharyya P, Sengupta D, Mukhopadhyay S (2007) Cutting Force-based Real-time Estimation of Tool Wear in Face Milling Using a Combination of Signal Processing Techniques. *Mechanical Systems and Signal Processing* 21:2665–2683
- [47] Marinescu I, Axinte D (2008) A Critical Analysis of Effectiveness of Acoustic Emission Signals to Detect Tool and Workpiece Malfunctions in Milling Operations. *International Journal of Machine Tools and Manufacture* 48:1148–1160.
- [48] Dong J, Subrahmanyam KVR, Wong YS, Hong GS, Mohanty AR (2006) Bayesian- inference-based Neural Networks for Tool Wear Estimation. *International Journal of Advanced Manufacturing Technology* 30:797–807.
- [49] Jemielniak K, Otman O (1998) Catastrophic Tool Failure Detection Based on AE Signal Analysis. *CIRP Annals* 47(1):31–34.
- [50] Jemielniak K, Bombinski S, Aristimuno PX (2008) Tool Condition Monitoring in Micromilling Based on Hierarchical Integration of Signal Measures. *CIRP Annals* 57(1):121–124.
- [51] Sick B (2002) On-line and Indirect Tool Wear Monitoring in Turning with Artificial Neural Networks: A Review of More Than a Decade of Research. *Mechanical Systems and Signal Processing* 16(4):487–546.

- [52] Kim H-Y, Ahn J-H (2002) Chip Disposal State Monitoring in Drilling Using Neural Network Based Spindle Motor Power Sensing. *International Journal of Machine Tools and Manufacture* 42:1113-1119.
- [53] Salgado D, Alonso F (2006) Tool Wear Detection in Turning Operations Using Singular Spectrum Analysis. *Journal of Materials Processing Technology* 171:451-458.
- [54] Scheffer C, Heyns PC (2001) Wear Monitoring in Turning Operations Using Vibration and Strain Measurements. *Mechanical Systems and Signal Processing* 15(6):1185-1202.
- [55] Sun J, Hong GS, Rahman M, Wong YS (2004) Identification of Feature Set for Effective Tool Condition Monitoring by AE Sensing. *International Journal of Production Research* 42(5):901-918.
- [56] Zhu K, Wong YS, Hong GS (2009) Multi-category Micro-milling Tool Wear Monitoring with Continuous Hidden Markov Models. *Mechanical Systems and Signal Processing* 23:547-560.
- [57] Binsaeid S, Asfoura S, Chob S, Onarc A (2009) Machine Ensemble Approach for Simultaneous Detection of Transient and Gradual Anomalies in Milling Using Multisensor Fusion. *Journal of Materials Processing Technology* 209:4728-4738
- [58] Huang B, Chen JC (2003) An In-process Neural Network-based Surface Roughness Prediction System Using a Dynamometer in End Milling Operations. *International Journal of Advanced Manufacturing Technology* 21:339-347.
- [59] Guo Y, Ammula S (2005) Real-time AE Monitoring for Surface Damage in Hard Machining. *International Journal of Machine Tools and Manufacture* 45:1622-1627.
- [60] Kwak JS, Song JB (2001) Trouble Diagnosis of the Grinding Process by Using AE Signals. *International Journal of Machine Tools and Manufacture* 41:899-913.
- [61] Al-Habaibeh A, Gindy N (2000) A New Approach for Systematic Design of Condition Monitoring Systems for Milling Processes. *Journal of Materials Processing Technology* 107:243-251.
- [62] El-Wardany TI, Gao D, Elbestawi MA (1996) Tool Condition Monitoring in Drilling Using Vibration Signature Analysis. *International Journal of Machine Tools and Manufacture* 36:687-711.
- [63] Rene de Jesus RT, Gilberto HR, Ivan TV, Carlos JCJ (2004) FPGA Based On-line Tool Breakage Detection System for CNC Milling Machines. *Mechatronics* 14:439-454.
- [64] Jemielniak K, Kwiatkowski L, Wrzosek P (1998) Diagnosis of Tool Wear Based on Cutting Forces and AE Measures as Inputs to Neural Network. *Journal of Intelligent Manufacturing* 9:447-455.
- [65] Kannatey-Asibu E, Dornfeld D (1982) A Study of Tool Wear Using Statistical Analysis of Metal Cutting Acoustic Emission. *Wear* 76:247-261.
- [66] Jemielniak K, Otman O (1998) Tool Failure Detection Based on Analysis of Acoustic Emission Signals. *Journal of Materials Processing Technology* 76:192-197.
- [67] Prickett PW, Johns C (1999) An Overview of Approaches to End Milling Tool Monitoring. *International Journal of Machine Tools and Manufacture* 39:105-122.
- [68] Christophe A, Suprock A, Piazza J, Roth JT (2007) Directionally Independent Failure Prediction of End-milling Tools During Pocketing Maneuvers. *Journal of Manufacturing Science and Engineering* 129(4):770-779.
- [69] Shi D, Gindy NN (2007) Tool Wear Predictive Model Based on Least Squares Support Vector Machines. *Mechanical Systems and Signal Processing* 21:1799-1814.

- [70] Abellan-Nebot JV, Subiro'n RF (2010) A Review of Machining Monitoring Systems Based on Artificial Intelligence Process Models. *International Journal of Advanced Manufacturing Technology* 47:237–257.
- [71] Kuljanic E, Sortino M, Totis G (2006) Application of Wavelet Transform of AE Signal for Tool Condition Monitoring in Face Milling. 39th CIRP Int. Sem. On Manuf. Systems, Ljubljana, 39–44
- [72] Axinte D, Gindy N (2003) Tool Condition Monitoring in Broaching. *Wear* 254(3-4):370–382.
- [73] Axinte D, Gindy N (2004) Assessment of the Effectiveness of a Spindle Power Signal for Tool Condition Monitoring in Machining Processes. *International Journal of Production Research* 42:2679–2691.
- [74] Teti R, Baciù IL (2004) Neural Network Processing of Audible Sound Signal Parameters for Sensor Monitoring of Tool Conditions. 4th CIRP Int. Sem. on ICME, Sorrento, 30 June–2 July, 385–390
- [75] Lee JM, Choi DK, Kim J, Chu CN (1995) Real-time Tool Breakage Detection for NC Milling Process. *CIRP Annals* 44(1):59–62.
- [76] Ryabov O, Mori K, Kasashima N (1996) An In-process Direct Monitoring Method for Milling Tool Failures Using a Laser Sensor. *CIRP Annals* 45(1):97–100.
- [77] Kim H, Ahn J, Kim S, Takata S (2002) Real Time Drill Wear Estimation Based on Spindle Motor Power. *Journal of Materials Processing Technology* 124(3):267–273.
- [78] Arrazola PJ, Arriola I, Davies MA, Cooke AL, Dutterer BS (2008) The Effect of Machinability on Thermal Fields in Orthogonal Cutting of AISI 4140 Steel. *CIRP Annals* 57(1):65–68
- [79] Gandarias E, Dimov S, Pham DT, Ivanov A, Popov K, Lizarralde R, Arrazola PJ (2006) New Methods for Tool Failure Detection in Micromilling. *Proceedings of IMechE* 220(2):137–144
- [80] Govekar E, Gradisek J, Grabec I (2000) Analysis of AE Signals and Monitoring of Machining Processes. *Ultrasonics* 38:598–603.
- [81] Teti R, Jawahir IS, Jemielniak K, Segreto T, Chen S, Kossakowska J (2006) Chip Form Monitoring through Advanced Processing of Cutting Force Sensor Signals. *CIRP Annals* 55(1):75–80.
- [82] Jemielniak K, Teti R, Kossakowska J, Segreto T (2006) Innovative Signal Processing for Cutting Force Based Chip Form Prediction. 2nd Virtual Int Conf. on IPROMS, 3–14 July, 7–12.
- [83] D'Addona D, Keshari A, Teti R (2008) Spectrum Estimation and Processing of Cutting Force Sensor Signals for Chip Form Monitoring and Classification. 4th Virtual Int. Conf. on IPROMS, 1–14 July, 555–560.
- [84] Venuvinod PK, Djordjevich A (1996) Towards Active Chip Control. *CIRP Annals* 45(1):83–86.
- [85] Andreasen JL, De Chiffre L (1998) An Automatic System for Elaboration of Chip Breaking Diagrams. *CIRP Annals* 47(1):35–40.
- [86] Brophy B, Kelly K, Byrne G (2002) AI-based Condition Monitoring of the Drilling Process. *Journal of Materials Processing Technology* 124:305–310
- [87] Mezentsev OA, Zhu R, DeVor RE, Kapoor SG, Kline WA (2002) Use of Radial Forces for Fault Detection in Tapping. *International Journal of Machine Tools and Manufacture* 42:479–488.
- [88] Shi D, Axinte D, Gindy N (2007) Development of an Online Machining Process Monitoring System: A Case Study of the Broaching Process. *International Journal of Advanced Manufacturing Technology* 34(1-2):34–46.

- [89] Rubio EM, Teti R (2009) Cutting Parameters Analysis for the Development of a Milling Process Monitoring System Based on Audible Energy Sound. *Journal of Intelligent Manufacturing* 20(1):43–54.
- [90] Teti R, Baciù IL, Rubio EM (2005) Sensor Monitoring of Machining Based on Audible Sound Detection and Analysis. 18th Int. Conf. on Production Research – ICPR 18, Salerno, 1–4 Ago, 47.
- [91] Teti R, Baciù IL, Rubio EM (2004) Neural Network Classification of Audible Sound Signals for Process Monitoring During Machining. 15th Int. DAAAM Symp. on Intelligent Manufact. Systems, 459–460.
- [92] Chen L, Bender P, Renton P, El-Wardany T (2002) Integrated Virtual Manufacturing Systems for Process Optimisation and Monitoring. *CIRP Annals* 51(1):409–412.
- [93] Ahn J, Kim S, Kim H, Kim S, Cho K (2005) Slicing Process Monitoring of Quartz Glass Ferrules with AE. *CIRP Annals* 54(1):297–300.
- [94] Ahn JH, Shen YF, Kim HY, Jeong HD, Cho KK (2001) Development of a Sensor Information Integrated Expert System for Optimizing Die Polishing. *Robotics and CIM* 17(4):269–276.
- [95] Pujana J, Arrazola P, Villar J (2008) In-process High-speed Photography Applied to Orthogonal Turning. *Journal of Materials Processing Technology* 202(1):475–485.
- [96] Azouzi R, Guillot M (1997) On-line Prediction of Surface Finish and Dimensional Deviation in Turning Using Neural Network Based Sensor Fusion. *International Journal of Machine Tools and Manufacture* 37(9):1201–1217.
- [97] Abouelatta O, Madl J (2001) Surface Roughness Prediction Based on Cutting Parameters and Tool Vibration in Turning. *Journal of Materials Processing Technology* 118:269–277.
- [98] Salgado DR, Alonso FJ, Cambero I, Marcelo A (2009) In-Process Surface Roughness Prediction System Using Cutting Vibrations in Turning. *International Journal of Advanced Manufacturing Technology* 43:40–51.
- [99] Song DY, Otani N, Aoki T, Kamakoshi Y, Ohara Y, Tamaki H (2005) A New Approach to Cutting State Monitoring in End-mill Machining. *International Journal of Machine Tools and Manufacture* 45:909–921.
- [100] Axinte D, Gindy N, Fox K, Unanue I (2004) Process Monitoring to Assist the Workpiece Surface Quality in Machining. *International Journal of Machine Tools and Manufacture* 44:1091–1098.
- [101] Chang HK, Kim JH, Kim H, Jang DY, Han DC (2007) In-process Surface Roughness Prediction Using Displacement Signals from Spindle Motion. *International Journal of Machine Tools and Manufacture* 47:1021–1026.
- [102] Axinte D, Boud F, Penny J, Gindy N, Williams DJ (2005) Broaching of Ti-6-4 – Detection of Workpiece Surface Anomalies on Dovetail Slots Through Process Monitoring. *CIRP Annals* 54(1):87–90.
- [103] Marinescu I, Axinte D (2009) A Time–frequency Acoustic Emission-based Monitoring Technique to Identify Workpiece Surface Malfunctions in Milling with Multiple Teeth Cutting Simultaneously. *International Journal of Machine Tools and Manufacture* 49(1):53–65.
- [104] Axinte D (2007) An Experimental Analysis of Damped Coupled Vibrations in Broaching. *International Journal of Machine Tools and Manufacture* 47(14):2182–2188.
- [105] Marinescu I, Axinte D (2008) A Critical Analysis of Effectiveness of AE Signals to Detect Tool and Workpiece Malfunctions in Milling Operations. *International Journal of Machine Tools and Manufacture* 48(10):1148–1160.

- [106] Axinte D, Natarajan D, Gindy NN (2005) An Approach to Use an Array of Three AE Sensors to Locate Uneven Events in Machining-Part 1: Method and Validation. *International Journal of Machine Tools and Manufacture* 45(14):1605–1613.
- [107] Rawat S, Attia H (2009) Characterization of the Dry High Speed Drilling Process of Woven Composites Using Machinability Maps Approach. *CIRP Annals* 58(1):105–108.
- [108] Teti R, Kumara SRT (1997) Intelligent Computing Methods for Manufacturing Systems, STC-O KN Paper. *CIRP Annals* 46(2):629–652.
- [109] Rumelhart DE, Hinton GE, Williams RJ (1986) Learning Internal Representations by Error in Propagation, in McClelland, Rumelhart, and the PDP Research Group (Eds.) *Parallel Distributed Processing: Exploration in the Microstructures of Cognition, Foundations*, vol 1.
- [110] Dreyfus G (2005) *Neural nets: Methodology & Applications*. Springer.
- [111] Haykin S (2008) *Neural Networks & Learning Machines*. Prentice-Hall.
- [112] Specht DF (1990) Probabilistic NN. *Neural Networks* 3(1):109–118.
- [113] Schmidhuber J, Wierstra D, Gagliolo M, Gomez F (2007) Training Recurrent Networks by Evolino. *Neural Computation* 19(3):757–779.
- [114] Schuster M, Paliwal KK (1997) Bidirectional Recurrent Neural Networks. *IEEE Transactions on Signal Processing* 45:2673–2681.
- [115] Pearlmutter BA (1995) Gradient Calculations for Dynamic Recurrent Neural Networks: A Survey. *IEEE Transactions on NNs* 6(5):1212–1228.
- [116] Daisuke H, Tomoharu N (2001) 2-D Artificial Cellular NN and Its Application to Chase Game. *Transactions on Institute of Electrical Engineers of Japan* 6:1071–1079.
- [117] Halgamuge SK, Glesner M (1984) NNs in Designing Fuzzy Systems for Real World Applications. *Fuzzy Sets and Systems* 65:1–12.
- [118] Kohonen T (1984) *Self-organisation and Associative Memory*. Springer-Verlag, Berlin.
- [119] Axinte D (2006) Approach into the Use of Probabilistic Neural Networks for Automated Classification of Tool Malfunctions in Broaching. *International Journal of Machine Tools and Manufacture* 46(12-13):1445–1448.
- [120] Kamarthi SV, Kumara SRT, Cohen PH (2000) Flank Wear Estimation in Turning through Wavelet Representation of Acoustic Emission Signals. *Journal of Manufacturing Science and Engineering* 122(1):12–19.
- [121] Kamarthi SV, Sankar GS, Cohen PH, Kumara SRT (1991) On-line Tool Wear Monitoring Using a Kohonen's Feature Map. *Int. Conf. on ANNIE'91, St. Louis, MO, November 10–13, 1*, 639–644.
- [122] Bukkapatnam S, Kumara S, Lakhtakia A (2000) Fractal Estimation of Flank Wear in Turning. *Journal of Dynamic System Measurements & Control* 122(1):89–94.
- [123] Bukkapatnam STS, Kumara SRT, Lakhtakia A (1994) Fractal Estimation of Flank Wear in Turning Using Time-delay Neural Networks. *ASME Press, New York*. pp.575–580.
- [124] Bukkapatnam STS, Kumara SRT, Lakhtakia A, Srinivasan P (2002) Neighborhood Method and Its Coupling with the Wavelet Method for Nonlinear Signal Separation of Contaminated Chaotic Time-series Data. *Signal Processing* 82(10):1351–1374.
- [125] Kim HY, Ahn JH (2002) Chip Disposal State Monitoring in Drilling Using Neural Network Based Spindle Motor Power Sensing. *International Journal of Machine Tools and Manufacture* 42(10):1113–1119.
- [126] Lu MC, Kannatey-Asibu Jr. (2000) Analysis of Sound Signal Generation Due to Flank Wear in Turning. *Int ME Congr & Exp, Orlando*.

- [127] Klein LA (2004) *Sensor and Data Fusion: A Tool for Information Assessment and Decision Making*. SPIE Press Book.
- [128] Hall D, Llinas J (2001) *Handbook of Multisensor Data Fusion*. CRC.
- [129] Mitchell HB (2007) *Multi-sensor Data Fusion: An Introduction*. Springer-Verlag, Berlin/Heidelberg.
- [130] Segreto T, Neugebauer R (2009) Sensor Fusion of Sensor Signals during Machining of Difficult-to-machine Metal Alloys. AITeM 2009, Torino, 7–9 September, 199.
- [131] Teti R, Segreto T (2008) Sensor Monitoring for Cutting Process Optimisation of Low Machinability Materials. 5th Chemnitz Colloq. on Prod. Techn. – CPK, Chemnitz, 21–22 October, 237–256.
- [132] Segreto T, Teti R (2008) Sensor Fusion of Acoustic Emission and Cutting Force for Tool Wear Monitoring during Composite Materials Machining. 6th CIRP Int. Conf. on ICME, Naples, 23–25 July, 221–226.
- [133] Teti R, Segreto T, Neugebauer R, Harzbecker C (2008) Sensor Monitoring Based Optimisation during Turning of Titanium Alloys. 4th Virtual Int. Conf. on IPROMS, 1–14 July, 547–554.
- [134] Teti R, Segreto T, Neugebauer R, Harzbecker C (2008) Process Acceptability in Turning of Ti alloys Based on Cutting Force Sensor Monitoring. 3rd Int. Conf. High Perf. Cutt, Dublin, 12–13 June, 241–250.
- [135] Byrne G, Dornfeld D, Inasaki I, König W, Teti R (1995) Tool Condition Monitoring – The Status of Research and Industrial Application. *CIRP Annals* 44(2):541–567.
- [136] Stearns SD, Hush DR (1990) *Digital Signal Analysis*. Prentice-Hall.
- [137] Rabiner RL, Shafer RW (1978) *Digital Signal Processing of Speech Signals*. Prentice-Hall, Englewood-Cliffs.
- [138] Teti R, Buonadonna P (1999) Round Robin on AE Monitoring of Machining. *Annals of the CIRP* 48(3):47–69.
- [139] Duda RO, Hart PE (1973) *Pattern Classification and Scene Analysis*. J. Wiley and Sons, New York.
- [140] Masters T (1993) *Practical Neural Network Recipes in C++*. Academic Press Inc., San Diego, CA.
- [141] Segreto T, Teti R, Neugebauer R, Schmidt G (2009) Machinability Assessment in Turning of NiTi Through Acceleration Sensor Monitoring. 2nd Int. Researchers Symp. on IPROMS, Ischia, 22–24 July, 75–80.
- [142] Teti A, Segreto T, Neugebauer R, Schmidt G (2009) Vibration Signal Detection and Conditioning for Machinability Analysis of Ti alloy Turning. 2nd Int. Resear. Symp. on IPROMS, Ischia, 22–24 July, 93–96.
- [143] Teti R (1995) A Review of Tool Condition Monitoring Literature Database. *CIRP Annals* 44(2):659–666.
- [144] Wang W, Hong G, Wong Y, Zhu K (2007) Sensor Fusion for On-line Tool Condition Monitoring in Milling. *International Journal of Production Research* 45(21):5095–5116.
- [145] ACCENT, *Adaptive Control of Manufacturing Processes for a New Generation of Jet Engine Components*, url: http://ec.europa.eu/research/transport/projects/items/accent_en.htm
- [146] <http://www.aviationmetals.net/inconel.php>
- [147] Bruno A. Olshausen, October 10, 2000, Aliasing, PSC 129 - Sensory Processes.
- [148] <http://www.thoughttechnology.com/pdf/MAR656-00%20Tech%20Note%20024.pdf>

- [149] Simeone, A., 2009, Sensor Monitoring in Drilling of Inconel 718, Report of experimental Activities at Volvo Aero Corporation, Trollhättan, Sweden.
- [150] Groover, M. P., 2010, Fundamentals of modern manufacturing: materials, processes and systems, 4th ed., John Wiley & Sons, Inc. USA, p 552-557.
- [151] International Standard ISO 3685/1993, "Tool-life testing with single point turning tools".
- [152] <http://www.itescam.edu.mx/principal/sylabus/fpdb/recursos/r49682.PDF>
- [153] Prevéy, P., 1986, "X-ray Diffraction Residual Stress Techniques," Metals Handbook, 10, pp 380-392.
- [154] M.E. Hilley, Ed., Residual Stress Measurement by XRay Diffraction, SAE J784a, Society of Automotive Engineers, Warrendale, PA, 1971, p 20.
- [155] A.L. Christenson and E.S. Rowland, Trans. ASM, Vol 45, 1953, p 638.
- [156] D.P. Koistinen and R.E. Marburger, Trans. ASM, Vol 51, 1959, p 537.
- [157] W.A. Rachinger, J. Sci. Instr., Vol 25, 1948, p 254.
- [158] S.K. Gupta and B.D. Cullity, Adv. X-Ray Anal., Vol 23, 1980, p 333.
- [159] P.S. Prevéy, Adv. X-Ray Anal., Vol 29.
- [160] <http://www.stresstechgroup.com> (<http://goo.gl/66h8c>).
- [161] <http://www.iprt.iastate.edu/nde/visual.html>
- [162] <http://www.iprt.iastate.edu/nde/liquidpenetrant.html>
- [163] <http://ndtd.org> (<http://goo.gl/z8QUo>)
- [164] Optical metallography m.r. louthan, jr., department of materials engineering, virginia polytechnic institute and state university, asm handbook, volume 10: materials characterizations r.e. whan, editor, p 299-308.
- [165] <http://www.taylor-hobson.com>
- [166] ASM Handbook, Volume 5: Surface Engineering, p.316.
- [167] J. Petrovic, L. Jacobson, P. Talty, and A. Vasudevan, J. Am. Ceram. Soc., Vol 58 (No. 3-4), 1975, p 113-116.
- [168] M. Mendiratta and J. Petrovic, J. Am. Ceram. Soc., Vol 61 (No. 5-6), 1978, p 226-230.
- [169] J. Petrovi and L. Jacobson, J. Am. Ceram. Soc., Vol 59 (No. 1-2), 1976, p 34-37.
- [170] J. Petrovic, R. Dirks, L. Jacobson, and M. Mendiratta, J. Am. Ceram. Soc., Vol 59, 1976, p 177-179.
- [171] http://www.nskamericas.com/cps/rde/xchg/na_en/hs.xsl/scoring.html
- [172] Surface engineering, ASM Metal Handbook, p. 2484.
- [173] FEIST, Wolf Dieter, Germany Johann H. HINKEN München, and Herbert WROBEL. "Detection and Characterization of Magnetic Anomalies in Gas Turbine Disks."
- [174] Beier HM (1999) Handbuch Entgrattechnik: Wegweiser zur Gratminimierung und Gratbeseitigung für Konstruktion und Fertigung. Hanser Verlag
- [175] Gillespie LK (1999) Deburring and Edge Finishing Handbook. Society of Manufacturing Engineers.
- [176] J.C. Aurich, D. Dornfeld, P.J. Arrazola, V. Franke, L. Leitz, S. Min, Burrs—Analysis, control and removal, CIRP Annals - Manufacturing Technology 58 (2009) 519-542.
- [177] http://nskeurope.com/cps/rde/xchg/eu_en/hs.xsl/flaking.html
- [178] <http://www.toolingu.com/definition-200325-87735-smearing.html>
- [179] <http://www.radical-departures.net/articles/advances-in-edm-for-aerospace>
- [180] Chao Xue, Wuyi Chen, Adhering layer formation and its effect on the wear of coated carbide tools during turning of a nickel-based alloy, Wear, Volume 270, Issues 11-12, 5 May 2011, Pages 895-902.

- [181] W. D. Feist, G. Mook, NDI for Manufacturing Anomalies in Aero-Engine Rotor Disks, ECNDT 2006 - We.4.1.2
- [182] Jie Meng, Tao Jin, Xiaofeng Sun, Zhuangqi Hu, Effect of surface recrystallization on the creep rupture properties of a nickel-base single crystal superalloy, *Materials Science and Engineering: A*, Volume 527, Issue 23, 15 September 2010, URL: <http://goo.gl/beiiQ>
- [183] TXT2MAT, url: <http://goo.gl/466BY>.
- [184] Nounou M.N., Bakshi, B. R., Goel, P.K., Shen, X., Bayesian Principal Component Analysis.
- [185] J. V. Kresta, J. F. MacGregor, and T. E. Marlin, *Can. J. Chem. Eng.*, 69, 35-47 (1991).
- [186] B. M. Wise, N. L. Ricker, D. F. Veltkamp, and B. R. Kowalski, *Proc. Cont. Qual.*, 1, 41(1990).
- [187] M. A. Kramer and R. S. H. Mah, *Proc. Int. Conf. On Foundations of Computer Aided Process Operations*, D. Rippin, J. Hale, J. Davis, eds. CACHE (1994).
- [188] Hervé Abdi, Lynne J. Williams, 2010, *Principal Component Analysis*, Wiley Interdisciplinary Reviews: Computational Statistics, 2.
- [189] Covariance matrix. A.V. Prokhorov (originator), *Encyclopedia of Mathematics*, url: <http://goo.gl/ooPUi>
- [190] Marcus and Minc 1988, p. 144.
- [191] Weisstein, Eric W. "Eigenvector." From MathWorld--A Wolfram Web Resource (<http://mathworld.wolfram.com/Eigenvector.html>).
- [192] Weisstein, Eric W. "Eigenvalue." From MathWorld--A Wolfram Web Resource. <http://mathworld.wolfram.com/Eigenvalue.html>
- [193] Principal Components Analysis (PCA) on data. MathWorks Documentation Center <http://www.mathworks.it/it/help/stats/princomp.html>
- [194] Jackson, J. E., *A User's Guide to Principal Components*, John Wiley and Sons, 1991, p.592.
- [195] Jolliffe, I. T., *Principal Component Analysis*, 2nd edition, Springer, 2002.
- [196] Krzanowski, W. J. *Principles of Multivariate Analysis: A User's Perspective*. New York: Oxford University Press, 1988.
- [197] Seber, G. A. F., *Multivariate Observations*, Wiley, 1984.
- [198] Creating a Scree Plot, Improved Outcomes Software, <http://goo.gl/XNm4d>
- [199] Pattern Recognition <http://goo.gl/pQvwz>
- [200] Feedforward Backpropagation Neural Networks <http://goo.gl/P9DzJ>
- [201] Martin Fodslette Moller. A Scaled Conjugate Gradient Algorithm For Fast Supervised Learning. *Neural Networks*, 6:525-533, 1993.
- [202] Hertz J, Krogh A, Palmer RG, *Introduction to the theory of neural computation*. Addison-Wesley, New York, 1991.
- [203] <http://www.mathworks.it/it/help/nnet/ref/trainlm.html>
- [204] Jonathan Richard Shewchuk, An Introduction to the Conjugate Gradient Method Without the Agonizing Pain, August 1994.
- [205] Zuhadi Zakaria, Nor Ashidi Mat Isa and Shahrel A. Suandi, A Study on Neural Network Training Algorithm for Multiface Detection in Static Images, *World Academy of Science, Engineering and Technology* 38 2010.
- [206] <http://goo.gl/Euca3>

